Infrared emissivity and reflectivity of sea surfaces with shadowing effect and surface reflections

Hongkun Li

▶ To cite this version:

Hongkun Li. Infrared emissivity and reflectivity of sea surfaces with shadowing effect and surface reflections. Electronics. UNIVERSITE DE NANTES, 2012. English. NNT : ED503-167 . tel-01104979

HAL Id: tel-01104979
https://hal.science/tel-01104979v1

Submitted on 19 Jan 2015

l'université
nantes
angers
le mans
PÔLE DE RECHERCHE ET D'ENSEIGNEMENT SUPÉRIEUR

UNIVERSITÉ DE NANTES

Thèse de Doctorat

Hongkun LI

Mémoire présenté en vue de l'obtention
du grade de Docteur de l'Université de Nantes
Sous le label de l'Université Nantes Angers Le Mans

Discipline : Electronique
Spécialité : Electromagnétisme
Laboratoire : IETR UMR 6164

Soutenance le 27 septembre 2012

École doctorale Sciences et Technologies de l'Information et Mathématiques (STIM)
Thèse N° ED503-167

ÉMISSIVITÉ ET RÉFLECTIVITÉ INFRAROUGES DE LA SURFACE DE MER AVEC OMBRE ET RÉFLEXIONS MULTIPLES

JURY

Président : **Mme Hélène ROUSSEL**, Professeur, L2E, Université Pierre et Marie Curie, Paris VI
Rapporteurs : **M. Richard DUSSÉAUX**, Professeur, LATMOS, Université de Versailles, St-Quentin-en-Yvelines
M. Charles-Antoine GUERIN, Professeur, MIO, Université du Sud Toulon Var
Examinateurs : **M. Yvonick HURTAUD**, Docteur, Ingénieur, DGA/MI, Bruz
Directeur de Thèse : **M. Christophe BOURLIER**, CR CNRS/HDR, IETR, Ecole polytechnique de l'université de Nantes
Co-encadrant : **M. Nicolas PINEL**, Docteur, Ingénieur de Recherche, IETR, Ecole polytechnique de l'université de Nantes
Invités : **M. Gérard BERGINC**, Directeur de la Recherche, THALES Optronique, Elancourt
M. Sandrine FAUQUEUX, Docteur, Ingénieur de Recherche, ONERA, Palaiseau

Remerciements

Je tiens tout d'abord à remercier les directeurs de l'IREENA et de l'IETR de m'avoir accueilli lors de ces trois années et de m'avoir permis de travailler dans de bonnes conditions.

Je tiens à remercier mon directeur de thèse Christophe BOURLIER et mon co-encadrant Nicolas PINEL pour avoir encadré mes travaux de thèse, et pour la confiance qu'ils m'ont donné au cours de cette étude.

Je souhaite également remercier l'ensemble des personnels du laboratoire IETR qui m'ont côtoyé et aidé au cours de ces trois années.

Enfin, je tiens à remercier tous mes proches, mes parents, mes soeurs, pour m'avoir accompagné, et pour leurs encouragements.

Résumé

1 Introduction

Lorsqu'on mesure le rayonnement infrarouge d'une surface de mer, le signal reçu est constitué de deux composantes. L'une de ces composantes est le rayonnement intrinsèque de la surface de la mer, qui est mesurée par son émissivité ε. L'autre est le rayonnement de l'atmosphère réfléchi par la surface de la mer, qui est mesurée par sa réflectivité ρ.

Tous les objets à des températures supérieures au zéro absolu émettent un rayonnement infrarouge. La puissance du rayonnement intrinsèque de la surface est obtenue en multipliant la puissance du rayonnement d'un corps noir $B(T)$ à la même température T que la surface par l'émissivité ε de la surface. Les capteurs du rayonnement thermique sont généralement étalonnés à l'aide du corps noir qui a une émissivité égale à 1.

L'émissivité ε d'un corps est une mesure de sa capacité à absorber et à réémettre l'énergie rayonnée. Elle est le rapport entre l'énergie qu'elle rayonne et celle qu'un corps noir rayonnerait à la même température. C'est un nombre sans dimension, compris entre 0 (parfait réflecteur) et 1 (parfait émetteur, corps noir).

La connaissance de l'émissivité est importante pour la télédétection de la température d'un objet quelconque. Les capteurs thermiques sont généralement étalonnés à l'aide du corps noir comme une source de référence, qui ont une émissivité égale à 1. Puisqu'un objet réel a une émissivité inférieure à 1, un rayonnement thermique moins important que celui d'un corps noir à la même température sera reçu par le thermomètre. En conséquence, cet objet apparaîtra plus froid qu'il ne l'est en réalité. Pour estimer la température réelle de cet objet, la prise en compte de l'émissivité de cet objet est donc essentielle. Cependant, l'émissivité d'un objet dépend des propriétés du matériau, de la direction d'observation, etc. Il est donc nécessaire de la mesurer ou la calculer précisément.

L'émissivité infrarouge d'une surface de mer joue un rôle clé dans des domaines liés à l'environnement, comme la mesure de la température apparente de la mer, les prévisions météorologiques, la détection de pollutions, etc. Elles sont quasi constantes lorsque l'angle d'observation est faible (proche du zénith). En revanche, pour des angles d'observation rasants (proches de l'horizon), elles dépendent fortement de la rugosité de la surface de la mer. Pour les angles d'observation rasants, l'effet d'ombrage et les réflexions multiples sont significatifs, augmentant la difficulté de prévoir l'émissivité avec précision. De plus, la connaissance précise de l'émissivité est importante. D'un point de vue applicatif, l'erreur sur le calcul de l'émissivité infrarouge doit être inférieure à 5×10^{-3} pour estimer la température apparente de la surface de mer avec une précision de 0.3 K [1]. En conséquence, il est important de calculer l'émissivité avec précision, ce qui implique que les phénomènes d'ombrage et de réflexions de la surface doivent être pris en compte.

La connaissance précise de la réflectivité d'une surface de mer est aussi essentielle. La réflectivité ρ d'un objet est une mesure de sa capacité à réfléchir l'énergie incidente. Elle est le rapport de l'énergie réfléchie sur l'énergie incidente. C'est un nombre sans dimension, compris entre 0 et 1 (parfait réflecteur).

La réflectivité dépend des directions d'incidence et d'observation (bidirectionnelle). La réflectivité hémisphérique est aussi souvent calculée par l'intégration de la réflectivité bidirectionnelle sur une des deux directions (d'incidence ou d'observation).

La réflectivité d'une surface de mer fait l'objet de nombreuses études depuis les années 60, par exemple pour le calcul du scintillement du soleil d'une surface de mer, pour la télédétection radar, etc. Les modèles de la réflectivité d'une surface de mer prennent souvent en compte une réflexion par la surface. Pour la calculer plus précisément, les réflexions multiples doivent être prises en compte.

Cette thèse a pour but de modéliser l'émissivité ε et la réflectivité ρ infrarouges d'une surface de mer avec précision. En effet, les phénomènes d'ombrage et de réflexions multiples par la surface sont pris en compte dans les modèles. Comme cette thèse s'intéresse au domaine infrarouge, l'approximation de l'optique géométrique (OG) est utilisée, parce que les longueurs d'onde infrarouges sont suffisamment faibles par rapport à la rugosité de la surface de la mer. La surface de la mer est modélisée comme étant bijective (en particulier, elle ne possède pas plusieurs hauteurs pour une même abscisse), ce qui signifie que les vagues déferlantes ne sont pas prises en compte. En outre, les "whitecaps" (moutons) ne sont pas traités. Sous l'approximation de l'optique géométrique, seules les réflexions spéculaires sont considérées.

Le chapitre 1 introduit les concepts de l'émissivité et de la réflectivité d'une surface de mer. La surface de mer est décrite par un processus stochastique stationnaire et ergodique. Ensuite, une bibliographie des modèles de la littérature est donnée, bibliographie qui montre que les phénomènes d'ombrage et des réflexions par la surface sont les facteurs clés dans la modélisation de l'émissivité et de la réflectivité d'une surface de mer. Pour prendre en compte ces deux phénomènes, les fonctions d'illumination monostatique (pour l'émissivité) et bistatique (pour la réflectivité) doivent être mises en oeuvre.

Le chapitre 2 introduit la fonction d'illumination monostatique, qui est la paramètre clé pour calculer l'émissivité de la surface de mer. La configuration "monostatique" implique le fait que seul un récepteur apparaît. Dans cette thèse, la fonction d'illumination statistique est utilisée. Les fonctions d'illumination d'ordre zéro (sans réflexion, qui traitent l'effet d'ombrage) sont bien connues. Ainsi, une fonction d'illumination d'ordre un (qui prend en compte une réflexion par la surface) est développée, en se basant sur celle d'ordre zéro.

Dans le chapitre 3, l'émissivité infrarouge de la surface de mer est calculée. En effet, les phénomènes d'ombrage et d'une réflexion par la surface sont pris en compte dans la modélisation de l'émissivité, via les fonctions d'illumination monostatiques développées dans le chapitre 2. La polarisation de l'onde est prise en compte. Les résultats du modèle sont comparés avec ceux d'une méthode de tracé de rayons de Monte Carlo et avec des mesures de la littérature.

Le chapitre 4 introduit la fonction d'illumination bistatique, qui est la paramètre clé pour le calcul de la réflectivité de la surface de mer. La configuration "bistatique" implique le fait qu'un récepteur et un émetteur apparaissent, et qu'ils sont dans des directions différentes. La fonction d'illumination d'ordre un, qui prend en compte une réflexion, est rappelée. Ensuite, celle d'ordre deux, qui prend en compte deux réflexions, est développée. Les résultats sont comparés avec ceux d'une méthode de tracé de rayons de Monte Carlo.

Dans le chapitre 5, la réflectivité infrarouge de la surface de la mer est calculée. Une et deux réflexions par la surface sont prises en compte via les fonctions d'illumination bistatiques d'ordre un et deux. La polarisation de l'onde est prise en compte. Enfin le critère de conservation d'énergie est examiné.

2 État de l'art

Lorsqu'on mesure le rayonnement infrarouge d'une surface de mer, dans les fenêtres de transmission atmosphérique infrarouges ($\lambda \in [3;5]$ et $\lambda \in [8;12]$ μm), le signal reçu par un récepteur est constitué de deux composantes, comme illustré dans la figure 1. L'un est le rayonnement intrinsèque de la surface de mer en infrarouge, qui est mesuré par son émissivité ε. L'autre est le rayonnement de l'atmosphère en infrarouge, réfléchi par la surface de mer, qui est mesuré par sa réflectivité ρ. Pour estimer le signal reçu, la connaissance de l'émissivité et de la réflectivité est nécessaire.

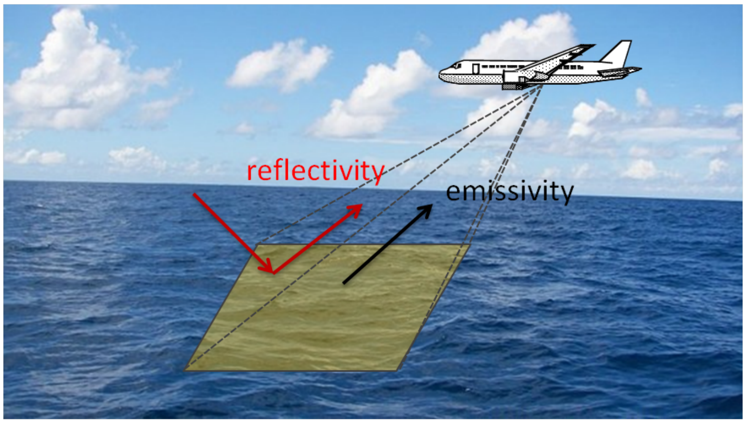

Figure 1: Illustration du rayonnement d'une surface de mer.

Ce travail de thèse a pour but de modéliser l'émissivité ε et la réflectivité ρ infrarouges d'une surface de mer avec précision. En effet, les phénomènes d'ombrage et de réflexions multiples par la surface sont pris en compte dans les modèles. La figure 2 illustre les phénomènes importants pour modéliser l'émissivité et la réflectivité.

Les figures 2 (a) et (b) correspondent au rayonnement intrinsèque de la surface de mer. La figure 2 (a) illustre le rayonnement intrinsèque de la surface de mer se propageant directement vers le récepteur. A cause de la rugosité de la surface, une partie de la surface est dans l'ombre du récepteur, comme illustré en ligne discontinue dans la figure 2 (a). Ce phénomène est appelé l'effet d'ombrage. Il est aussi possible que le rayon d'émission intercepte la surface à un autre point, où il est réfléchi spéculairement dans la direction d'observation. Cette partie de l'énergie reçue par le capteur est plus faible que celle se propageant directement vers le récepteur, mais elle contribue au signal reçu par celui-ci. De plus, elle augmente lorsque l'angle d'observation θ est grand (direction d'observation proche de l'horizon). En

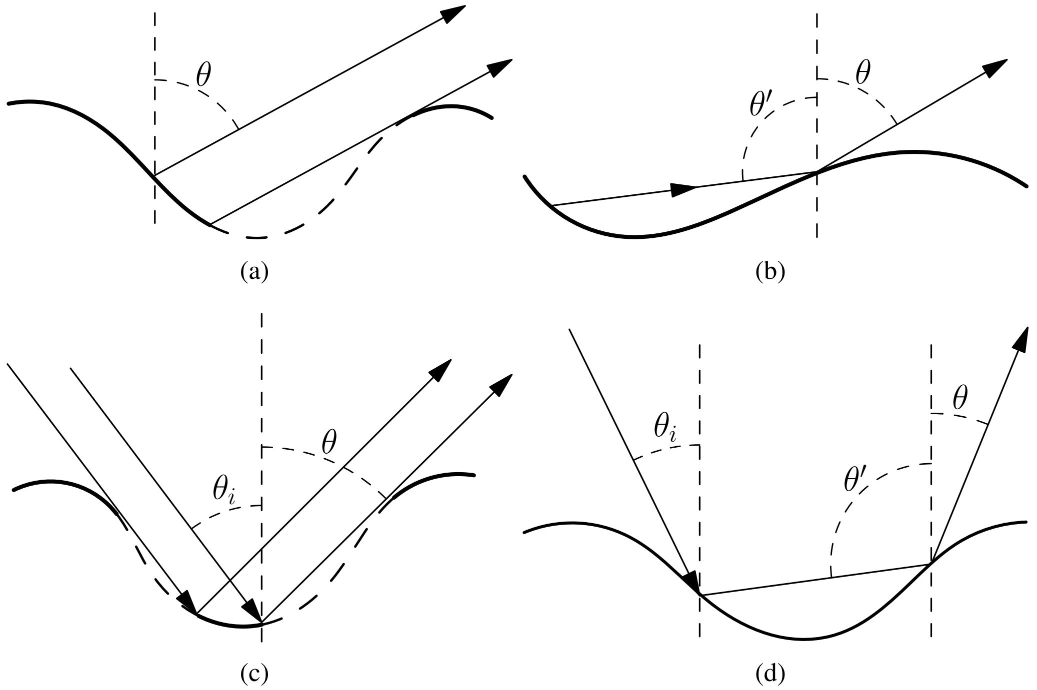

(a) (b) (c) (d)

Figure 2: Phénomènes physiques pour la modélisation du rayonnement de la surface de mer : (a) rayonnement intrinsèque de la surface de mer se propageant directement vers le récepteur, (b) rayonnement intrinsèque de la surface de mer qui est réfléchi une fois par la surface ; (a) et (b) correspondent donc à l'émissivité de la surface de mer ; (c) rayonnement de l'atmosphère réfléchi une fois par la surface, (d) rayonnement de l'atmosphère réfléchi deux fois par la surface ; (c) et (d) correspondent donc à la réflectivité de la surface de mer.

conséquence, il est important de la prendre en compte. Des réflexions multiples peuvent se produire. Quand le nombre de réflexions augmente, l'énergie du rayon reçu associé diminue.

Les figures 2 (c) et (d) correspondent au rayonnement de l'atmosphère réfléchi par la surface. La figure 2 (c) illustre un rayon d'incidence réfléchi une fois par la surface. L'effet d'ombrage apparaît [2–4]. Une partie de la surface est dans l'ombre du récepteur ou de celui de l'émetteur. La figure 2 (d) illustre un rayon d'incidence réfléchi deux fois par la surface. Plus de réflexions peuvent avoir lieu, mais comme le nombre de réflexions augmente, l'énergie du rayon associé reçu diminue.

La modélisation de l'émissivité et de la réflectivité de la surface de mer est basée sur les phénomène d'ombrage et de réflexions par la surface. Dans les fenêtres de transmission atmosphérique infrarouges ($\lambda \in [3, 5]$ et $\lambda \in [8, 12]$ μm), l'approximation de l'optique géométrique est employée. L'approximation de l'optique géométrique est valide si [5] :

$$2\pi\rho_c \cos^3 \chi \gg \lambda \tag{1}$$

où λ est la longueur d'onde du rayonnement et ρ_c est le rayon de courbure local de la surface. χ est l'angle d'incidence local, qui est celui entre la normale locale de la surface et la direction d'observation (voir figure 3). Dans les fenêtres de transmission atmosphérique infrarouges, la longueur d'onde est de l'ordre de 10 μm. Le rayon de courbure moyen des vagues capillaires (les rayons de courbure plus faibles) est de l'ordre de quelques millimètres à quelques centimètres [6]. Pour $\rho_c = 1$ cm, l'équation (1) est valide pour $\cos\chi \gg 0.025$, correspondant à un angle d'incidence très proche de $90°$ ($\cos 88.5° \approx 0.025$). En conséquence, l'approximation de l'optique géométrique est souvent utilisée dans la modélisation de l'émissivité et de la réflectivité infrarouges [7, 6, 1, 8–13].

Dans cette section, l'état de l'art de la modélisation de l'émissivité et la réflectivité est rappelé. Comme la surface est décrite par un processus stochastique, les caractères statistiques de la surface de mer sont rappelés. Ensuite, les modèles de l'émissivité et de la réflectivité de la littérature sont donnés.

2.1 Caractéristiques statistiques de la surface de mer

2.1.1 Vagues océaniques

La surface de mer est rugueuse à cause de l'apparition de vagues, qui sont générées par du vent sur la surface de mer. Les vagues océaniques sont constituées de vagues de gravité et de capillarité. Les vagues de gravité ont des grandes longueur d'onde (de l'ordre du mètre), qui sont déterminées par la distance horizontale entre deux crêtes ou deux creux. Les vagues capillaires ont des longueurs d'onde beaucoup plus petites, de l'ordre de quelques millimètres à quelques centimètres.

Parce qu'il est difficile de prévoir l'état d'un point quelconque de la surface (hauteur, pente, etc.), la surface de mer est modélisée comme un processus stochastique [4]. Pour des vitesses du vent importantes, les vagues déferlantes et des "whitecaps" (moutons) apparaissent. Cependant, ils ne sont pas pris en compte dans cette thèse, ce qui restreint la validité de cette étude à des vents modérés.

2.1.2 DDPs des hauteurs et des pentes de la surface de mer

Les études de la littérature ont montré qu'une surface naturelle a une distribution des hauteurs proche d'une gaussienne [14]. En conséquence, la densité de probabilité (DDP) des hauteurs de la surface est supposée gaussienne centrée, donnée par :

$$p_\zeta(\zeta) = \frac{1}{\sqrt{2\pi}\sigma_\zeta} \exp\left(-\frac{\zeta^2}{2\sigma_\zeta^2}\right), \tag{2}$$

où σ_ζ est l'écart type des hauteurs de la surface.

Théoriquement, lorsque la densité de probabilité des hauteurs est gaussienne centrée, la densité de probabilité des pentes est aussi gaussienne centrée, donnée par [10, 13, 15] :

$$p_\gamma^{\mathrm{G}}(\gamma_x, \gamma_y) = \frac{1}{2\pi\sigma_{\gamma_x}\sigma_{\gamma_y}} \exp\left(-\frac{\gamma_x^2}{2\sigma_{\gamma_x}^2} - \frac{\gamma_y^2}{2\sigma_{\gamma_y}^2}\right), \tag{3}$$

où σ_{γ_x} et σ_{γ_y} sont les écarts types des pentes de la surface dans les directions x et y.

Il y a différentes méthodes dans la littérature pour calculer l'écart type des pentes de la surface de mer [16, 17]. Dans cette thèse, le modèle de Cox & Munk [17] est utilisé. Les écarts type des pentes de la surface de mer sont liés à la vitesse du vent à 12.5 m au dessus de la surface de mer, donnés par :

$$\begin{aligned} \sigma_{\gamma_x}^2 &= 3.16 \times 10^{-3} u_{12} \pm 0.004, \\ \sigma_{\gamma_y}^2 &= 1.92 \times 10^{-3} u_{12} + 0.003 \pm 0.004, \end{aligned} \tag{4}$$

où “±” correspond aux erreurs de mesure. Dans les calculs de cette thèse, l’erreur de mesure n’est pas prise en compte.

Cependant, Cox & Munk [17] ont montré que la densité de probabilité des pentes de la surface de mer est différente d’une gaussienne centrée. La densité de probabilité des pentes est décrite comme la somme d’une série de Gram-Charlier jusqu’à l’ordre quatre. Elle s’écrit [17] :

$$\begin{aligned}
p_\gamma^{\mathrm{non-G}}(\gamma_x,\gamma_y) &= \frac{1}{2\pi\sigma_{\gamma_x}\sigma_{\gamma_y}}\exp\left(-\frac{\gamma_x^2}{2\sigma_{\gamma_x}^2}-\frac{\gamma_y^2}{2\sigma_{\gamma_y}^2}\right)\\
&\times\Big[1+\frac{c_{21}}{2}(\Gamma_y^2-1)\Gamma_x+\frac{c_{03}}{6}(\Gamma_x^2-3)\Gamma_x\\
&+\frac{c_{22}}{4}(\Gamma_x^2-1)(\Gamma_y^2-1)+\frac{c_{40}}{4}(\Gamma_y^4-6\Gamma_y^2+3)\\
&+\frac{c_{04}}{24}(\Gamma_x^4-6\Gamma_x^2+3)\Big],
\end{aligned} \tag{5}$$

où

$$\begin{aligned}
\Gamma_{x,y} &= \frac{\gamma_{x,y}}{\sigma_{\gamma_x,\gamma_y}},\\
c_{21} &= (0.86u_{12}-1\pm 3)10^{-2},\\
c_{03} &= (3.3u_{12}-4\pm 12)10^{-2},\\
c_{04} &= 0.23\pm 0.41,\\
c_{40} &= 0.40\pm 0.23,\\
c_{22} &= 0.12\pm 0.06,
\end{aligned} \tag{6}$$

Les termes $\{c_{21}, c_{03}\}$ (moments statistiques impairs, liés au skewness) provoquent alors une asymétrie sur les vagues et $\{c_{04}, c_{40}, c_{22}\}$ (moments statistiques pairs, liés au kurtosis) impliquent des fronts montants et descendants des vagues plus pentus et des creux plus adoucis. Les effets du skewness et du kurtosis sont étudiés dans cette thèse.

2.1.3 Autocorrélation des hauteurs d’une surface de mer

La connaissance des densités de probabilité des hauteurs et de pentes ne sont pas suffisantes pour décrire le comportement de la surface de mer, parce que les hauteurs et les pentes des différents points de la surface peuvent être liés lorsqu’ils sont proches. Ceci implique la connaissance de la fonction d’autocorrélation de la surface.

La fonction d’autocorrélation de la surface de mer est calculée par le spectre de la surface [4]. L’étude du spectre de la surface de mer a fait l’objet de nombreuses études [18, 16, 19]. Le spectre de Elfouhaily *et al.* [16], très utilisé pour les fréquences microondes, a l’avantage de prendre en compte à la fois les vagues de gravité et de capillarité.

Cependant, le spectre de mer n’est pas utilisé dans cette thèse. Pour des raisons de simplicité, la fonction d’autocorrélation de la surface de la mer est supposée gaussienne [20, 4], donnée par :

$$R(\tau) = \sigma_\zeta^2 \exp\left(-\frac{\tau^2}{L_c^2}\right), \tag{7}$$

où σ_ζ est l'écart type des hauteurs de la surface de mer et L_c la longueur de corrélation, correspondant à la distance horizontale entre deux points de la surface telle que leur corrélation est diminuée de e^{-1}.

Pour être plus général, l'équation (7) normalisée est donnée par :

$$R_{\text{nor}}(\tau) = \frac{R(\tau)}{\sigma_\zeta^2} = \exp\left(-y^2\right), \tag{8}$$

où

$$y = \frac{\tau}{L_c}. \tag{9}$$

Pour $|y| > 3$, $R_{\text{nor}} \approx 0$. Ainsi, pour deux points quelconques de la surface, la corrélation entre leurs hauteurs est négligeable lorsque leur distance horizontale est supérieure à 3 fois la longueur de corrélation L_c (voir figure 1.4 pour plus d'informations).

La fonction d'autocorrélation gaussienne est utilisée pour générer des surfaces rugueuses, afin de mettre en oeuvre une méthode de tracé de rayons. Elle est aussi utilisée pour calculer la densité de probabilité corrélée des pentes de la surface de mer. Un spectre de surface de mer plus réaliste n'est pas utilisé parce que la fonction d'autocorrélation gaussienne est simple à prendre en compte, tandis qu'un spectre de mer réaliste nécessite de calculer des intégrales numériques pour calculer la densité de probabilité corrélée des pentes [21]. De plus, il est important de souligner que les résultats de l'émissivité de la surface de mer ont montré que la fonction d'autocorrélation gaussienne est une bonne approximation [22].

2.1.4 Densité de probabilité corrélée

Puisque les hauteurs des points de la surface sont corrélées, la densité de probabilité des hauteurs et des pentes $p(\zeta, \gamma|\zeta_0, \gamma_0; \tau)$ est calculée. C'est un paramètre important pour le calcul de la fonction d'illumination corrélée.

Pour un processus corrélé gaussien centré et d'après le théorème de Bayes, la probabilité conditionnelle des hauteurs et des pentes de deux points séparés par une distance horizontale τ est donnée par [4, 20] :

$$\begin{aligned} p(\zeta, \gamma|\zeta_0, \gamma_0; \tau) &= \frac{p(\zeta, \gamma, \zeta_0, \gamma_0; \tau)}{p(\zeta_0, \gamma_0)} \\ &= \frac{\sigma_\zeta \sigma_\gamma}{2\pi\sqrt{|[C]|}} \exp\left[-\frac{1}{2}\boldsymbol{V}^T [C]^{-1} \boldsymbol{V} + \frac{\zeta^2}{2\sigma_\zeta^2} + \frac{\gamma^2}{2\sigma_\gamma^2}\right], \end{aligned} \tag{10}$$

où $\boldsymbol{V}$ est le vecteur de composantes

$$\boldsymbol{V}^T = [\zeta_0, \zeta, \gamma_0, \gamma], \tag{11}$$

et $[C]$ est la matrice de covariance du vecteur $\boldsymbol{V}$

$$[C] = \begin{bmatrix} \sigma_\zeta^2 & R_0(\tau) & 0 & R_1(\tau) \\ R_0(\tau) & \sigma_\zeta^2 & -R_1(\tau) & 0 \\ 0 & -R_1(\tau) & \sigma_\gamma^2 & -R_2(\tau) \\ R_1(\tau) & 0 & -R_2(\tau) & \sigma_\gamma^2 \end{bmatrix}. \tag{12}$$

R_0 est la fonction d'autocorrélation des hauteurs de la surface ($\sigma_\zeta^2 = R_0(0)$), $R_1 = \mathrm{d}R_0\,\mathrm{d}\tau$ et $R_2 = \mathrm{d}R_1\,\mathrm{d}\tau$ sont ses premier et deuxième dérivées, données par [20] :

$$\begin{aligned} R_1(\tau) &= -\frac{2\sigma_\zeta^2}{L_c^2}\tau \exp\left(-\frac{\tau^2}{L_c}\right), \\ R_2(\tau) &= -\frac{2\sigma_\zeta^2}{L_c^2}\left(1-2\frac{\tau^2}{L_c^2}\right)\exp\left(-\frac{\tau^2}{L_c}\right). \end{aligned} \tag{13}$$

Pour $\tau = 0$ (les deux points sont superposés), la matrice de covariance s'écrit :

$$[C]_{\tau=0} = \begin{bmatrix} \sigma_\zeta^2 & \sigma_\zeta^2 & 0 & 0 \\ \sigma_\zeta^2 & \sigma_\zeta^2 & 0 & 0 \\ 0 & 0 & \sigma_\gamma^2 & \sigma_\gamma^2 \\ 0 & 0 & \sigma_\gamma^2 & \sigma_\gamma^2 \end{bmatrix}. \tag{14}$$

On trouve que $[C]_{\tau=0}$ n'est pas inversible. En conséquence, la hauteur et la pente d'un point quelconque de la surface sont supposées décorrélées.

2.2 Définitions de l'émissivité et de la réflectivité

Le rayonnement thermique intrinsèque d'un objet est caractérisé par deux paramètres : son émissivité et le rayonnement du corps noir correspondant. Pour un matériau quelconque, la puissance de son rayonnement intrinsèque $L(\lambda, T, \theta)$ est égale à celle d'un corps noir à la même température $B(\lambda, T)$ multipliée par son émissivité $\varepsilon(\lambda, T, \theta)$. Elle s'écrit :

$$L(\lambda, T, \theta) = \varepsilon(\lambda, T, \theta)B(\lambda, T). \tag{15}$$

L'émissivité de la surface de mer dépend de la longueur d'onde de son rayonnement, de l'état de la surface (température T, rugosité, etc.), et de la direction d'observation. Puisque celle-ci est toujours inférieure à 1, la puissance d'un objet réel est inférieure à celle d'un corps noir à la même température.

La puissance d'un rayon d'incidence est divisée en trois parties : la puissance réfléchie E_r, la puissance absorbée E_a, et la puissance transmise E_t. Le critère de conservation de l'énergie implique que :

$$\rho = \frac{E_r}{E_i}, \qquad \alpha = \frac{E_a}{E_i}, \qquad t = \frac{E_t}{E_i}. \tag{16}$$

En conséquence :

$$\rho + \alpha + t = 1. \tag{17}$$

Le corps noir est défini par $\alpha = 1$. Ceci se traduit physiquement par le fait que toute l'énergie incidente est absorbée.

En équilibre thermique, l'émissivité d'un objet est égale à son absorptivité (loi de Kirchoff) :

$$\varepsilon = \alpha. \tag{18}$$

Ainsi, l'émissivité d'un objet opaque (l'énergie ne peut être transmise dans cet objet) est donnée par :

$$\varepsilon = 1 - \rho. \tag{19}$$

Sous l'approximation de l'optique géométrique, seules les réflexions spéculaires sont considérées. La figure 3 illustre une réflexion spéculaire par une surface lisse.

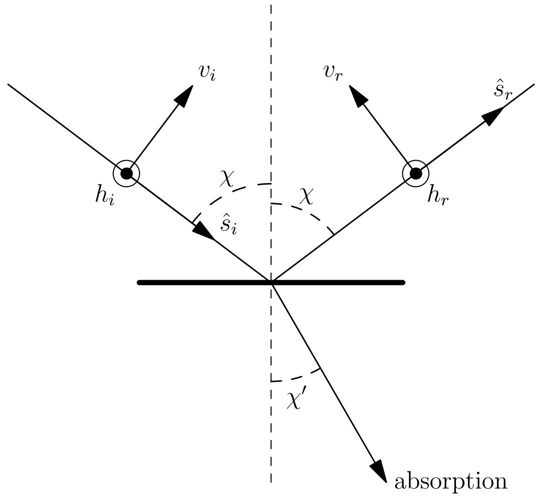

Figure 3: Réflexion spéculaire sur une surface lisse.

La surface est supposée opaque. Ceci implique que toute l'énergie du rayon de réfraction est absorbée.

La normale à la surface et la direction d'incidence définissent le plan d'incidence. La puissance du rayon réfléchi est reliée à celle du rayon d'incident par la relation :

$$L_r = |r_{H,V}(\chi)|^2 L_i, \tag{20}$$

où χ est l'angle d'incidence local et $r_{H,V}$ sont les coefficients de Fresnel en polarisations horizontale (H, le vecteur électrique est perpendiculaire au plan d'incidence) et verticale (H, le vecteur électrique est dans le plan d'incidence). Ces derniers s'écrivent :

$$\begin{aligned} r_H(\chi) &= \frac{\cos\chi - \widetilde{n}\cos\chi'}{\cos\chi + \widetilde{n}\cos\chi'}, \\ r_V(\chi) &= \frac{\widetilde{n}\cos\chi - \cos\chi'}{\widetilde{n}\cos\chi + \cos\chi'}, \end{aligned} \tag{21}$$

où $\widetilde{n}$ est l'indice de réfraction de la surface de la mer. χ' est angle de réfraction local, donné par la loi de Snell-Descartes :

$$\sin(\chi') = \frac{\sin(\chi)}{\widetilde{n}}. \tag{22}$$

L'émissivité et la réflectivité d'une surface est donc donnée par [23, 10, 9, 6] :

$$\begin{aligned} \varepsilon(\chi) &= 1 - |r_{H,V}(\chi)|^2 \\ \rho(\chi) &= |r_{H,V}(\chi)|^2 \end{aligned} \tag{23}$$

L'équation (23) donne l'émissivité ε et la réflectivité ρ d'une surface lisse. L'émissivité et la réflectivité d'une surface de mer sont calculées en suivant l'équation (23), qui sont rappelées dans les sections suivantes.

2.3 Modèle de l'émissivité d'une surface de mer

L'émissivité infrarouge d'une surface de mer dans les fenêtres de transmission atmosphériques est un paramètre important pour la télédétection océanique. Elle joue un rôle important dans les domaines de l'environnement, tels que la mesure de la température de la surface de mer, la prévision météorologique et la télédétection de la pollution. Comme un récepteur infrarouge passif reçoit uniquement le rayonnement de la cible (il n'y a pas de signal émis), il est très furtif, et peut donc être utilisé à des fins militaires.

D'un point de vue applicatif, il est important de calculer l'émissivité avec précision, ce qui implique que les phénomènes d'ombrage et de réflexions de la surface doivent être pris en compte, et ce, de manière précise.

2.3.1 Emissivité directe avec ombrage

Les premiers modèles de l'émissivité infrarouge d'une surface de mer calcule l'émissivité sans tenir compte des réflexions sur la surface de la mer (nommée émissivité directe, ou contribution de l'émissivité d'ordre zéro). En revanche, l'effet de l'ombrage a généralement été considéré.

Comme la surface de la mer varie dans le temps et dans l'espace, sa prévisibilité est limitée. En conséquence, les surfaces de mer sont généralement modélisées comme des processus aléatoires. Sous l'approximation de l'optique géométrique, l'émissivité moyenne du point d'intérêt de la surface est généralement estimée par l'émissivité moyenne de toute la surface, donnée par [23, 24, 10, 6] :

$$\varepsilon_0(\theta) = \left\langle [1 - |r|^2] g_0 \right\rangle , \tag{24}$$

où $\langle \cdots \rangle$ représente la moyenne statistique sur les variables aléatoires. Le terme $1 - |r|^2$ est l'émissivité locale du point d'intérêt, et g_0 correspond à la projection de la zone autour de ce point sur la direction orthogonale à la direction d'observation. L'équation (24) résume le principe de base de la modélisation de l'émissivité infrarouge d'une surface de mer.

Cependant, le problème principal de l'équation (24) est que l'effet d'ombrage (voir la figure 2.(a)) n'est pas considéré. L'émissivité de la surface de mer sans ombre, donnée par l'équation (24), est supérieure à 1 et tend vers l'infini pour des angles d'observation par rapport au zénith θ grands (voir la figure 3.2 du manuscrit) [10], ce qui n'est pas physique. Ceci est dû au fait que le rayonnement des points dans l'ombre est inclus dans l'équation (24), alors que ces points ne contribuent pas physiquement au rayonnement de la surface dans la direction considérée.

Beaucoup d'efforts ont été consacrés à la construction d'une fonction d'illumination [1] pour prendre en compte l'effet d'ombrage. La fonction d'illumination qui prend en compte l'effet d'ombrage est appelée fonction d'illumination monostatique d'ordre zéro [26], notée S^0_{M}, où l'indice "M" représente la configuration monostatique (seul un récepteur est utilisé), et l'exposant "0" traduit le fait qu'aucune réflexion par la surface n'est considérée. Elle donne la probabilité qu'un point arbitraire de la surface soit vu par le récepteur. Avec la fonction d'illumination monostatique, l'émissivité directe de la surface de mer est donnée par la relation :

$$\varepsilon_0(\theta) = \left\langle [1 - |r|^2] g_0 S^0_{\mathrm{M}} \right\rangle . \tag{25}$$

Certaines propriétés de la fonction d'illumination peuvent être prédites. Pour une direction d'observation normale ($\theta = 0°$), tous les points de la surface sont

---

[1] La fonction d'illumination a été appelée "fonction d'ombre" [3, 25]. Comme le terme "ombrage" est confus lorsque les réflexions par la surface sont considérées, cette fonction est plutôt nommée "fonction d'illumination" par les modèles récents.

vus par le récepteur, ce qui signifie que la fonction d'illumination monostatique d'ordre zéro est égale à un : $S_{\mathrm{M}}^{0} = 1$. Par contre, si le récepteur est situé à l'horizon ($\theta \to 90°$), alors $S_{\mathrm{M}}^{0} = 0$, parce que toute la surface est dans l'ombre du récepteur.

L'effet d'ombre a été étudié à partir du début des années 60. Plusieurs modèles peuvent être rencontrés dans la littérature, modèles qui sont résumés ci-après.

Modèles de tracé de rayons Le modèle le plus direct est celui de Brockelman & Hagfors [27], qui est un modèle numérique de tracé de rayons de Monte-Carlo. Dans cette méthode, un grand nombre (de l'ordre de 100 à 1000) de surfaces rugueuses aléatoires sont générées, surfaces sur lesquelles un tracé de rayons est réalisé. Les rayons incidents sont envoyés dans une direction d'observation donnée (θ) et sont retracés pour trouver les points de la surface dans l'ombre et ceux vus par le récepteur (voir la figure 2.7 du manuscrit, par exemple). La fonction d'illumination monostatique S_{M}^{0} est alors donnée par (la définition des symboles est modifiée) :

$$S_{\mathrm{M}}^{0}(\theta) = \frac{N_j}{N_s}, \tag{26}$$

où N_j est le nombre des points vus par le récepteur, N_s est celui de la surface totale ; S_{M}^{0} n'est pas la probabilité qu'un point arbitraire soit vu par le récepteur, mais la proportion de la surface vue par le récepteur.

Cette idée a été reprise et développée par Bourlier *et al.* [20, 26]. Bourlier *et al.* utilisent le même algorithme de tracé de rayons pour trouver les points vus par le récepteur. Cependant, au lieu simplement de calculer la proportion de la surface vue par le récepteur, les histogrammes des hauteurs et des pentes des points vus par le récepteur sont également calculés.

Les méthodes de Brockelman & Hagfors [27] et de Bourlier *et al.* [20, 26] sont généralement utilisés comme référence pour vérifier l'exactitude de méthodes analytiques [25, 3, 28].

Modèles statistiques Le modèle de Beckmann [29] est l'un des premiers modèles de fonction d'illumination statistique. La fonction d'illumination S_{M}^{0} est résolue par une équation différentielle qui donne la probabilité que le point d'intérêt soit vu par le récepteur.

Ricciardi & Sato [30, 31] ont montré que la fonction d'illumination peut être définie rigoureusement par une série de Rice, série dans laquelle des intégrations doivent être résolues. Pour un processus gaussien décorrélé, une expression analytique de la série peut être obtenue, mais les résultats sont non physiques pour des angles rasants, car la corrélation est négligée [26]. La prise en compte de la corrélation pourrait surmonter ce problème, mais il est impossible d'obtenir une solution analytique de la série (nécessite un calcul numérique).

Le modèle de Wagner [3] correspond au premier terme de la série de Ricciardi & Sato [30, 31], qui est physique pour des angles rasants. Le modèle de Smith [25] a été développé sur la base du modèle de Wagner [3], mais il est plus rigoureux mathématiquement et physiquement.

Bourlier *et al.* [26] ont comparé les modèles de Ricciardi & Sato [30, 31], de Wagner [3] et de Smith [25]. Ils ont conclu que le modèle de Ricciardi & Sato est le moins précis, car il n'est pas physique pour des angles d'observation rasants. Le modèle de Smith est le plus précis parce que de très bons accords sont obtenus entre les résultats de la fonction d'illumination de Smith et ceux du modèle de tracé de rayon de Monte-Carlo.

De nombreux modèles d'émissivité infrarouge d'une surface de mer avec les fonctions d'illumination monostatiques analytiques S_{M}^{0} ont été développés. Le modèle de Yoshimori *et al.* [6, 7] calcule l'émissivité infrarouge d'une surface de mer, où l'effet d'ombrage est pris en compte à l'aide de la fonction d'illumination de Smith [25]. Dans le modèle de Bourlier *et al.* [32], la fonction d'illumination de Smith [25] est utilisé. Ils ont de plus considéré une distribution des pentes de la surface non gaussienne, introduite par Cox & Munk [17], qui prend en compte les effets du skewness et du kurtosis. Caillault *et al.* [33] et Fauqueux *et al.* [24] ont développé des modèles multi-résolution de l'émissivité infrarouge d'une surface de mer, dans lesquels la fonction d'illumination de Smith a été utilisée.

Modèles avec facteur de normalisation Au lieu d'utiliser une fonction statistique, Saunders [34] et Masuda *et al.* [10] ont introduit des facteurs de normalisation pour prendre en compte l'effet d'ombrage. Ces deux facteurs de normalisation sont pratiquement les mêmes, et sont beaucoup utilisés en raison de leur simplicité.

Masuda *et al.* [10] ont calculé l'émissivité infrarouge non polarisée d'une surface de mer. La densité de probabilité des pentes de la surface est supposée gaussienne centrée. Du fait que sans ombre, l'équation (24) tend vers l'infini lorsque θ est égale à $90°$, Masuda *et al.* ont calculé l'émissivité d'une surface de mer en divisant l'équation (24) par un facteur de normalisation :

$$\varepsilon_0(\theta) = \frac{\langle [1 - |r|^2] g_0 \rangle}{\langle g_0 \rangle}. \tag{27}$$

Le facteur de normalisation $\langle g_0 \rangle$ est utilisé pour estimer l'effet d'ombrage, donc :

$$p(\theta) = \frac{1}{\langle g_0 \rangle} \tag{28}$$

joue le rôle de fonction d'illumination.

Le facteur de normalisation de Masuda *et al.* [10] est très utilisé. Freund *et al.* [35] a suivi la même idée que Masuda *et al.* [10] et a utilisé un facteur de normalisation pour estimer l'influence de l'ombrage. L'émissivité d'une surface de mer a été calculée par une moyenne d'ensemble hémisphérique. Shaw et Marston [36] ont calculé l'émissivité infrarouge polarisée d'une surface de mer suivant le modèle de Masuda *et al.* [10].

D un point de vue applicatif, la précision dans l'estimation de l'émissivité d'une surface de mer est importante. Des travaux de la littérature ont montré qu'une différence de 3×10^{-3} dans l'émissivité induit une différence de 0.5 K dans l'estimation de la température de la surface [1]. Toutefois, cette précision n'est pas atteinte par des modèles de l'émissivité directe. En effet, les comparaisons avec les mesures ont montré que le modèle de l'émissivité directe de Masuda *et al.* [10] a sous-estimé l'émissivité de la surface de mer de $2 \sim 3 \times 10^{-2}$ pour les angles d'observation grands ($\theta \gtrsim 60°$) [37, 38]. En conséquence, il est nécessaire de prendre en compte les réflexions multiples par la surface de mer dans la modélisation.

2.3.2 Emissivité avec réflexion par la surface

L'émissivité avec réflexion par la surface de mer est illustrée sur la figure 2(b). Pour calculer l'émissivité infrarouge d'une surface de mer avec précision, plusieurs auteurs ont essayé d'inclure les réflexions par la surface dans leur modèle de l'émissivité. La difficulté principale dans la prise en compte de cet effet est le calcul de la probabilité d'observer des réflexions par la surface. Dans ce qui suit, les principaux modèles sont rappelés.

Modèles de tracé de rayons Le modèle de Henderson *et al.* [13] est un modèle numérique de tracé de rayons de Monte-Carlo. Dans ce modèle, un algorithme de tracé de rayons est utilisé pour calculer l'émissivité de surface de mer avec jusqu'à 10 réflexions par la surface. Beaucoup de surfaces rugueuses aléatoires sont générées, surfaces sur lesquelles des tracés de rayons sont réalisés. Les points de la surface conduisant à des réflexions sont trouvés (voir la figure 2.15 du manuscrit pour plus d'informations). L'émissivité de la surface avec des réflexions est ainsi calculée.

Cette méthode est très semblable à celle de Hagfors & Brockelman [27], sauf que les réflexions par la surface sont considérées. Cette méthode donne des résultats fiables et constitue une référence pour la validation de modèles analytiques [15, 11]. Son désavantage est que le temps de calcul est long (généralement, plusieurs heures sur un PC ordinaire, pour une direction d'observation donnée).

Modèle empirique Watts *et al.* [39] et Wu & Smith [1] ont défini empiriquement la probabilité d'observer une réflexion par surface, en définissant un angle de seuil mesuré à partir du zénith, comme illustré sur la figure 4.

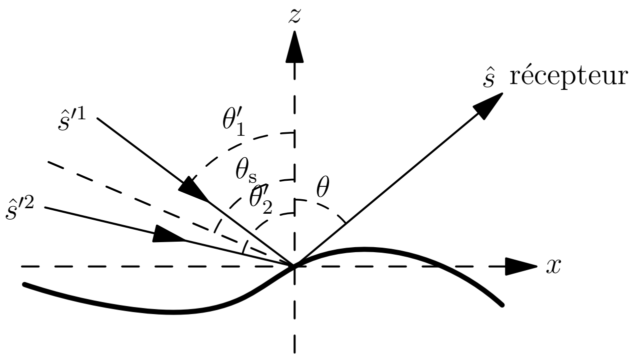

Figure 4: Réflexion et angle de seuil.

La figure 4 montre deux rayons incidents, $\hat{s}'^1$ et $\hat{s}'^2$, réfléchis par la surface dans la direction du récepteur. Pour un rayon incident émis par un point de la surface et réfléchi spéculairement par un autre point, le rayon réfléchi $\hat{s}$ dans la direction d'observation contribue à l'émissivité de la surface. La tâche principale est la détermination de la probabilité P que le rayon partant d'un point de la surface dans la direction d'observation provienne d'un autre point de la surface de la mer (par une réflexion spéculaire).

Dans ce but, Watts *et al.* [39] ont défini un angle de seuil θ_s (équation (2.8) de [39]) pour calculer la probabilité P. Pour un angle d'incidence inférieur à θ_s, Watts *et al.* ont défini que le rayon d'incidence provient du ciel (la lumière du soleil, le rayonnement de l'atmosphère, etc), par exemple, le rayon incident $\hat{s}'^1$ dans la figure 4. Sinon, le rayon d'incidence provient de la surface, par exemple, le rayon incident $\hat{s}'^2$ dans la figure 4.

Watts *et al.* ont calculé l'angle de seuil délimitant ces deux zones en fonction de la hauteur et de la longueur d'onde des vagues de la surface de mer. Ils ont mis en évidence que θ_s est compris entre $79°$ et $89,9°$.

Wu & Smith [1] ont utilisé presque la même méthode pour calculer P. La seule différence est que deux angles de seuil ont été définis, l'un étant $90°$ et l'autre étant $85°$. Ils ont défini que les rayons avec $\theta' < 85°$ proviennent du ciel, et les rayons avec $\theta' > 90°$ proviennent de la surface. Pour les rayons avec $85° \leq \theta' \leq 90°$, la probabilité qu'ils proviennent de la surface P a été donnée empiriquement.

Il est difficile de définir précisément les angles de seuil. L'émissivité obtenue dépend alors fortement de la définition des angles de seuil. Watts *et al.* ont montré que l'émissivité de la surface de mer avec une réflexion pour $\theta_\mathrm{s} = 85°$ et $90°$ diffèrent de $2,5 \times 10^{-3}$ pour des vitesses de vent modérées. Cette différence croît avec la vitesse du vent (voir la figure 5 de [39] pour plus de détail).

Modèle avec fonction de poids Pour éviter d'avoir à déterminer un angle de seuil avec précision, Masuda [11] a calculé l'émissivité d'ordre un (avec une réflexion) à l'aide d'une fonction de poids. Cette fonction de poids pondère la probabilité qu'un rayon d'incidence $\hat{s}'$ avec un angle d'incidence θ' provienne de la surface. Elle a été développée sur la base du facteur de normalisation de Masuda *et al.* [10], donnée par (la définition des symboles est modifiée) :

$$P = \begin{cases} 1, & \text{if} \quad \theta' \geq 90° \\ 1 - p(\theta'), & \text{if} \quad \theta' < 90° \end{cases}, \tag{29}$$

où $p(\theta')$ est la fonction d'illumination de Masuda *et al.* donnée par l'équation (28) [10].

Dans la région où $\theta' < 90°$, la fonction d'illumination de Masuda *et al.* $p(\theta')$ représente approximativement la probabilité qu'un point de la surface soit vu par le récepteur. Ainsi, la fonction de poids donne approximativement la probabilité que le rayon $\hat{s}$ provienne de la surface.

Cependant, comme la fonction d'illumination de Masuda *et al.* ne représente pas la probabilité statistique, $p(\theta')$ n'est plus valide pour $\theta' > 90°$, et la performance de la fonction de poids peut être mise en doute. En fait, de mauvais accords sont observés entre l'émissivité d'ordre un obtenue par le modèle de Masuda *et al.* [11] et les résultats de la méthode de tracé de rayons de Monte-Carlo [22]. Nous avons calculé l'émissivité d'une surface de la mer d'ordre un avec une méthode de tracé de rayons de Monte-Carlo, et avons constaté que l'émissivité d'ordre un tend vers 0 lorsque l'angle d'observation θ tend vers $90°$. Le résultat de Masuda *et al.* pour $\theta = 90°$ est d'environ $0,02$, ce qui représente une erreur beaucoup plus élevé que la précision demandée $(0,3 \times 10^{-3})$ [22].

Modèles statistiques Plus rigoureusement, Bourlier *et al.* [15, 26] ont évalué la contribution de l'émissivité d'ordre un en développant une fonction d'illumination statistiques d'ordre un S^1_M (avec une réflexion), afin d'estimer la probabilité qu'un rayon émis par surface a été réfléchi une fois par un autre point de la surface dans la direction d'observation considérée.

Cependant, les résultats du modèle [15] ne sont pas en bon accord avec les résultats de Henderson *et al.* [13] (méthode tracé de rayons de Monte-Carlo). Bourlier *et al.* [15] ont souligné que ceci pouvait être attribué au fait que la fonction d'illumination S^1_M n'a pas bien été évaluée.

Pour calculer l'émissivité d'une surface de mer avec précision, une fonction d'illumination avec réflexions par la surface plus précise doit être développée, ce qui constitue l'un des apports principaux de cette thèse.

2.4 Modèle de réflectivité

La réflectivité d'une surface de la mer ρ correspond au rayonnement de l'atmosphère réfléchi par la surface dans la direction d'observation θ, comme illustré dans la figure 2 (c) avec une réflexion et dans la figure 2 (d) avec deux réflexions.

La réflectivité de la surface de mer ρ est une fonction directionnelle qui dépend de la direction d'incidence $\hat{s}_i(\theta_i, \phi_i)$ et de la direction de réflexion $\hat{s}(\theta, \phi)$. Toutefois, il est courant de la moyenner sur l'hémisphère selon la direction d'incidence ou de réflexion pour obtenir la réflectivité moyennée hémisphérique [12, 6], donnée par :

$$\rho^{\mathrm{hemi}}(\theta, \phi) = \int_0^{2\pi} \int_0^{\pi/2} \rho(\theta, \phi, \theta_i, \phi_i) \, \mathrm{d}\theta_i \, \mathrm{d}\phi_i. \tag{30}$$

Dans le domaine infrarouge, l'approximation de l'optique géométrique est supposée valide, ce qui signifie que seules les réflexions spéculaires sont prises en compte dans le processus de diffusion. Dans la littérature, une réflexion par la surface est souvent considérée. Les réflexions multiples par la surface sont généralement ignorées, en raison de la complexité du problème.

2.4.1 Réflectivité avec une réflexion

Sous l'approximation de l'optique géométrique, la réflectivité d'un point de la surface est obtenue par la réflectivité moyenne de la surface entière, donnée par :

$$\rho_1 = \left\langle |r|^2 g_0 \right\rangle, \tag{31}$$

où le symbole $\langle \cdots \rangle$ correspond à la moyenne statistique sur les variables aléatoires. Le terme $|r|^2$ représente la réflectivité locale du point d'intérêt, et g_0 correspond à la projection de la zone autour de ce point sur la direction orthogonale à la direction d'observation. L'équation (31) résume le principe de base de la modélisation de la réflectivité infrarouge d'une surface de mer.

Comme montré dans la figure 2 (c), certaines parties de la surface sont dans l'ombre de l'émetteur (atmosphère) ou du récepteur, en particulier pour des angles d'incidence θ_i ou d'observation θ par rapport aux zénith importants. En conséquence, une fonction d'illumination bistatique d'ordre un, S_{B}^1, est employée pour tenir compte de ce phénomène. L'indice "B" représente la configuration bistatique (l'émetteur et le récepteur sont situés dans des endroits différents), et l'exposant "1" signifie qu'une réflexion par la surface est considérée.

Dans le modèle de Wagner [3], la fonction d'illumination monostatique S_{M}^0 est étendue à la configuration bistatique. Bourlier *et al.* [4] ont étendu la fonction d'illumination de Smith [25] à la configuration bistatique de la même façon que Wagner. Ces fonctions d'illumination bistatiques d'ordre un sont très utilisées pour calculer la réflectivité d'une surface de mer [6, 8, 23, 33, 40]. La fonction d'illumination bistatique est utilisée dans cette thèse pour calculer la réflectivité d'une surface de mer avec une réflexion.

2.4.2 Réflectivité avec réflexions multiples

Il est également possible que le rayon d'incidence soit réfléchi plusieurs fois par la surface avant l'arrivée dans la direction d'observation, comme illustré dans la figure 2 (d) pour deux réflexions. Ainsi, pour être plus précis dans l'estimation de la réflectivité, les réflexions multiples par la surface doivent être considérées. Cependant, comme il faut déduire une fonction d'illumination bistatique d'ordre n, où n désigne le nombre des réflexions, cela constitue un problème difficile à résoudre, donc elles ne sont pas prises en compte dans cette thèse.

Lynch $\&$ Wagner [12] ont construit une fonction d'illumination bistatique avec deux réflexions par la surface. Ils ont supposé que la surface était un réflecteur parfait. La réflectivité non polarisée de la surface a alors été calculée. Ils ont ainsi mis en évidence que le critère de conservation de l'énergie était mieux satisfait après la prise en compte de la seconde réflexion.

Bourlier *et al.* [41] ont développé une fonction d'illumination bistatique avec réflexions multiples, qui est le produit des fonctions monostatiques d'ordre zéro. Les résultats associés n'ont pas été comparés avec des résultats numériques ou avec des mesures.

Dans le modèle de Schott *et al.* [42], une méthode de tracé de rayons de Monte-Carlo a été développée pour calculer la réflectivité d'une surface de mer avec réflexions multiples. Ils ont obtenu la même conclusion que le critère de conservation de l'énergie était mieux satisfait après la prise en compte de la seconde réflexion.

Ce travail de thèse a pour but de modéliser l'émissivité ε et la réflectivité ρ infrarouges d'une surface de mer avec précision. Dans cette thèse, les phénomènes d'ombrage et de réflexions multiples par la surface sont pris en compte. Le travail de cette thèse est résumé ci-dessous.

3 Contribution

3.1 Fonction d'illumination monostatique

Pour calculer l'émissivité d'une surface de mer avec précision, les phénomènes d'ombrage et de réflexions multiples par la surface doivent être pris en compte. Ainsi, les fonctions d'illumination monostatiques sans réflexion S^0_{M} et celles avec n réflexions S^n_{M} sont étudiées, fonctions qui permettent d'évaluer l'effet d'ombrage et des réflexions par la surface. Les exposants "0" et "n" désignent le nombre de réflexions. L'indice "M" représente la configuration monostatique.

3.1.1 Fonction d'illumination sans réflexion

La figure 5 illustre un récepteur mesurant le rayonnement d'une surface rugueuse. Le récepteur se trouve dans la direction d'observation $\hat{s}(\theta, \phi)$, qui forme un angle $\theta \in [0°; 90°]$ avec le zénith, et un angle azimutal $\phi \in [0°; 360°]$ avec la direction du vent. La direction X correspond à la direction horizontale du récepteur. A cause de la rugosité de la surface, certaines parties de la surface se trouvent dans l'ombre du récepteur, qui sont indiquées par les lignes en pointillés sur la figure 5. Ce phénomène est appelé l'effet d'ombrage.

Évidemment, l'effet d'ombrage dépend de la direction d'observation $\hat{s}$ et de la rugosité de la surface (en particulier, des pentes de surface). Par exemple, une

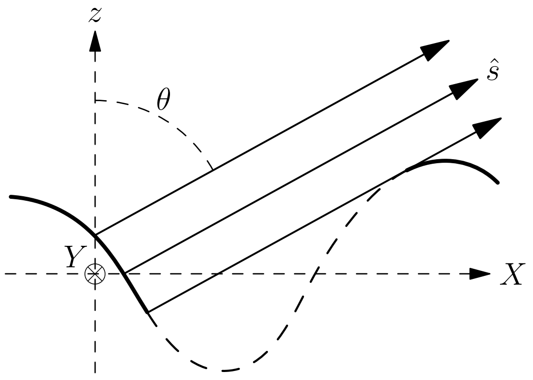

Figure 5: Effet d'ombrage d'une surface rugueuse. La direction d'observation forme un angle en élévation θ avec le zénith. La direction X correspond à la direction horizontale du récepteur. La partie de la surface en pointillés se situe dans l'ombre du récepteur, tandis que la partie de la surface en ligne continue est vue par le récepteur.

surface lisse est toujours entièrement vue, quelle que soit la direction d'observation $0^\circ \leq \theta < 90^\circ$. Les caractéristiques physiques suivantes peuvent être prédites (pour plus d'informations, voir la figure 2.2 du manuscrit) :

1. Dans le cas où $\theta = 0^\circ$, ce qui correspond au fait que les rayons d'émission se propagent verticalement vers le haut, aucun rayon d'émission n'est bloqué. Ceci implique que $S_{\mathrm{M}}^0 = 1$.
2. Dans le cas où $\theta = 90^\circ$, ce qui correspond au fait que les rayons d'émission se propagent horizontalement vers le récepteur situé au niveau de l'horizon, tous les rayons d'émission sont bloqués. Ceci implique que $S_{\mathrm{M}}^0 = 0$.
3. Plus le point de la surface considéré est élevé, plus la probabilité qu'il soit vu est proche de 1. Le point culminant de la surface est vu, quand il n'y a pas d'autre point de la surface qui peut l'ombrager. En effet, pour qu'un point de la surface soit dans l'ombre du récepteur, son rayon d'émission dans la direction d'observation $\hat{s}$ doit atteindre la surface en un autre point.
4. Les points de la surface possédant des pentes γ_{X_0} dans la direction X (correspondant à la direction horizontale du récepteur) qui sont supérieures à la pente $\mu = \cot\theta$ du rayon d'émission se trouvent dans l'ombre du récepteur; sinon, l'angle d'incidence local (entre la normale $\hat{n}$ au point considéré et la direction d'émission) $|\chi| > 90^\circ$, ce qui n'est pas physique.

Comme prévu par les caractéristiques 1 et 2 de la liste ci-dessus, l'effet d'ombrage devient de plus en plus significatif lorsque l'angle d'observation θ augmente. Dans la mesure du rayonnement d'une surface de mer, les récepteurs situés proches de la surface de la mer (par exemple, sur un navire ou un avion) ont des angles d'observation importants. Ceci implique que l'effet d'ombrage ne peut pas être négligé pour ce type de configuration. Ce phénomène est renforcé par l'augmentation de la vitesse du vent au-dessus de la surface de mer. En conséquence, l'estimation de l'effet d'ombrage (nommé fonction d'illumination ou fonction d'ombre) doit être faite avec précision.

Beaucoup d'efforts ont été consacrés à l'évaluation de l'effet d'ombrage [3, 10, 25, 30, 31, 34, 26]. Ces modèles sont appelés fonctions d'illumination d'ordre zéro, car ils ne considèrent pas les réflexions par la surface.

Dans cette thèse, le modèle de Smith est utilisé, car il est le plus précis. La fonction d'illumination monostatique de Smith donne la probabilité qu'un point quelconque de la surface soit vu par le récepteur. Pour une surface de longueur infinie, elle est donnée par :

$$S_{\mathrm{M}}^{0,\mathrm{unco}}(\mu, \gamma_{X_0}, \zeta_0) = \Upsilon(\mu - \gamma_{X_0}) F(\zeta_0)^{\Lambda(\mu)}, \tag{32}$$

où γ_{X_0} est la pente du point considéré dans la direction X, ζ_0 sa hauteur, $\mu = \cot\theta$ est la pente du rayon d'émission, et F est la fonction de répartition des hauteurs de la surface, donnée par :

$$F(\zeta) = \int_{-\infty}^{\zeta} p_\zeta(t)\mathrm{d}t, \tag{33}$$

où p_ζ est la densité de probabilité des hauteurs de la surface. La fonction $\Lambda(\mu)$ est liée à la pente du rayon d'émission, donnée par :

$$\Lambda(\mu) = \frac{1}{\mu} \int_{\mu}^{+\infty} (\gamma - \mu) p_\gamma(\gamma)\,\mathrm{d}\gamma. \tag{34}$$

La moyenne de la fonction d'illumination sans réflexion donne le pourcentage de la surface vue par le récepteur. Pour une surface avec une densité de probabilité des pentes p_γ gaussienne centrée, elle est donnée par :

$$\begin{aligned} \overline{\overline{S}}_{\mathrm{M}}^{0,\mathrm{unco}}(\mu) &= \int_{\infty}^{\infty} \int_{\infty}^{\infty} \Upsilon(\mu - \gamma_{X_0}) F(\zeta_0)^{\Lambda(\mu)} p_{\gamma_X}(\gamma_{X_0}) p_\zeta(\zeta_0)\,\mathrm{d}\gamma_{X_0}\,\mathrm{d}\zeta_0 \\ &= \left[1 - \frac{1}{2}\mathrm{erfc}\left(\frac{\mu}{\sigma_{\gamma_{X_0}}\sqrt{2}}\right)\right] \frac{1}{\Lambda(\mu)+1}, \end{aligned} \tag{35}$$

où σ_{γ_X} est l'écart type des pentes dans la direction X. erfc est la fonction erreur complémentaire.

Les équations (32) et (35) n'ont pas pris en compte la corrélation entre les hauteurs et les pentes de la surface. La fonction d'illumination de Smith avec corrélation est également étudiée dans cette thèse. Elle n'est pas présentée ici à cause de la complexité de son expression mathématique.

Les résultats de la fonction d'illumination sans réflexion sont présentés dans la section 2.1.6 du manuscrit. Une méthode de tracé de rayons de Monte-Carlo est utilisée comme méthode de référence. La densité de probabilité des pentes de la surface est supposée gaussienne centrée. La corrélation des hauteurs et des pentes de la surface est prise en compte en considérant une fonction d'autocorrélation des hauteurs gaussienne.

Les résultats des fonctions d'illumination de Smith et de Wagner sont comparés avec ceux de la méthode de tracé de rayons de Monte-Carlo. De meilleurs accords généraux sont observés entre la méthode de tracé de rayons de Monte Carlo et le modèle de Smith. Cela indique le modèle de Smith est plus précis. En conséquence, le modèle de Smith est utilisé dans toute la suite pour calculer l'émissivité d'une surface de mer. Le modèle de Smith décorrélé surestime un peu l'effet d'illumination. Cependant, de meilleurs accords sont observés après la prise en compte de la corrélation.

L'ombrage est négligeable pour des angles d'observation par rapport au zénith faibles : par exemple, $\theta < 60°$ pour une surface avec un écart type des pentes $\sigma_\gamma = 0.2$. Pour θ plus grand, l'effet d'ombrage apparaît et augmente rapidement.

Pour $\theta = 90°$, la fonction d'illumination moyenne est égale à zéro, ce qui signifie que toute la surface est dans l'ombre du récepteur. Les résultats montrent que pour $\nu = \mu/(\sigma_\gamma\sqrt{2})$ inférieur à 2, l'effet d'ombrage est négligeable (pour plus d'informations, voir les figures 2.10 et 2.11 du manuscrit).

La fonction d'illumination de Smith est également étudiée en fonction de la direction du vent. Il est montré que l'effet d'ombrage varie de manière significative en fonction de la direction du vent. De manière générale, cet effet est maximal dans les directions traverses au vent ($\phi = \{90°, 270°\}$), parce que l'écart type des pentes est le plus faible dans ces directions.

La fonction d'illumination de Smith moyennée est symétrique par rapport aux directions face, traverse, et dos au vent ($\phi = \{0°, 90°, 180°, 270°\}$) pour une densité de probabilité des pentes gaussienne. Après la prise en compte de l'effet de skewness, elle est symétrique par rapport aux directions face et dos au vent ($\phi = \{0°, 180°\}$), ce qui vérifie la définition de l'effet de skewness. En règle générale, la fonction d'illumination moyennée de Smith augmente pour $\theta = 85°$ après la prise en compte des effets de skewness et de kurtosis.

3.1.2 Fonction d'illumination avec une réflexion

Pour calculer l'émissivité d'une surface de mer avec précision, les réflexions par la surface doivent être considérées. La clé de ce problème réside dans la résolution de la fonction d'illumination avec réflexions par la surface.

Dans cette thèse, une réflexion par la surface est considérée. Nous rappelons que l'approximation de l'optique géométrique est employée, ce qui implique que seules les réflexions spéculaires sont considérées. Une fonction d'illumination monostatique statistique avec une réflexion par la surface est développée dans cette section, fonction qui donne la probabilité que le rayon d'émission d'un point arbitraire M_1 de la surface arrive au récepteur après avoir s'être réfléchi une fois en un autre point M_0 de la surface.

La figure 6 illustre une réflexion par la surface. Un rayon est émis par le point M_1 et se propage dans la direction $\hat{s}'$. Il intercepte la surface au point M_0, où il est réfléchi spéculairement dans la direction d'observation $\hat{s}$.

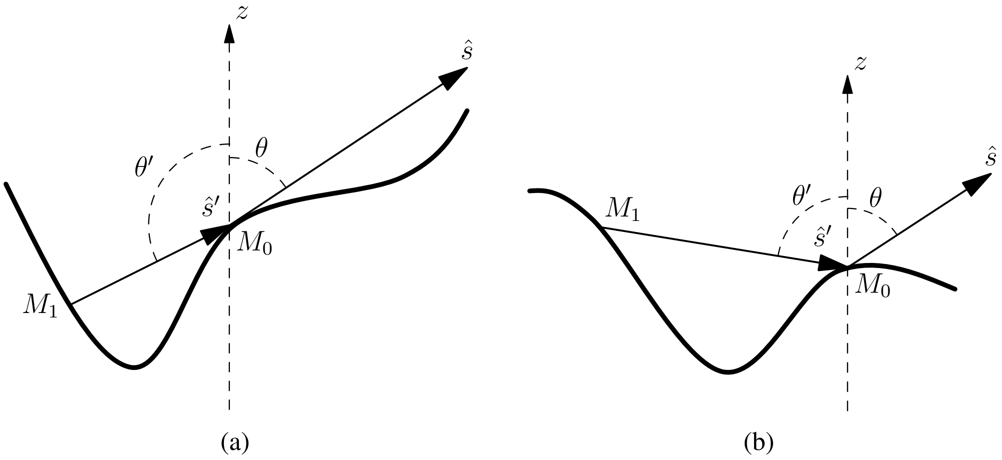

(a) (b)

Figure 6: Une réflexion par la surface : (a) cas 1, $\theta' > 90°$; (b) cas 2, $\theta' < 90°$.

La fonction d'illumination avec une réflexion peut également être exprimée par la probabilité que le rayon allant de M_0 au récepteur (notée $M_0(\hat{s})$) n'intercepte pas la surface, tandis que le rayon allant de M_0 à M_1 (noté $M_0(-\hat{s}')$) intercepte la surface. Cette probabilité est donnée par la relation :

$$\begin{aligned} S_{\mathrm{M}}^1 &= p(M_0(\hat{s}) \text{ n'intercepte pas } \cap M_0(-\hat{s}') \text{ intercepte}), \\ &= p(M_0(\hat{s}) \text{ n'intercepte pas}) \\ &\quad \times p(M_0(-\hat{s}') \text{ intercepte } | \ M_0(\hat{s}) \text{ n'intercepte pas}), \\ &= p(M_0(\hat{s}) \text{ n'intercepte pas}) \\ &\quad \times [1 - p(M_0(-\hat{s}') \text{ n'intercepte pas } | \ M_0(\hat{s}) \text{ n'intercepte pas})] \\ &= p(a)[1 - p(b|a)], \end{aligned} \tag{36}$$

où "$M_0(\hat{s})$ *n'intercepte pas la surface*" est noté "a" et "$M_0(-\hat{s}')$ *n'intercepte pas la surface*" est noté "b".

La probabilité $p(a)$ correspond à la fonction d'illumination monostatique sans réflexion S_{M}^0. Dans cette thèse, la fonction d'illumination de Smith est employée. Elle est donnée par

$$p(a) = S_{\mathrm{M}}^0 = \Upsilon(\mu - \gamma_{X_0}) F(\zeta_0)^{\Lambda(\mu)}, \tag{37}$$

où X est la direction horizontale de $\hat{s}$.

La probabilité conditionnelle $p(b|a)$ est calculée par rapport aux cas illustré sur la figure 6. Dans le cas 1 où le rayon $M_0(-\hat{s}')$ se propage vers le bas ($|\theta'| > 90°$), la probabilité conditionnelle $p(b|a) = 0$. La raison physique est qu'un rayon se propageant vers le bas intercepte obligatoirement la surface. Ainsi, sa probabilité complémentaire est égale à 0.

Dans le cas 2 où le rayon $M_0(-\hat{s}')$ se propage vers le haut ($|\theta'| < 90°$), la probabilité conditionnelle $p(b|a)$ est donnée par :

$$p(b|a) = F(\zeta_0)^{\Lambda^-(\mu_1)}, \qquad \text{si} \qquad \theta' < 90°. \tag{38}$$

où μ_1 est la pente du rayon $\hat{s}'$ dans la direction X'. X' est défini par la direction horizontale du vecteur $\hat{s}'$. La fonction $\Lambda^-(\mu_1)$ est donnée par :

$$\Lambda^-(\mu_1) = \frac{1}{\mu_1} \int_{-\infty}^{\mu_1} (\gamma - \mu_1) p_{\gamma_{X'}}(\gamma) \, \mathrm{d}\gamma, \tag{39}$$

où $p_{\gamma_{X'}}$ est la densité de probabilité des pentes de la surface dans la direction X'.

Pour conclure, la fonction d'illumination statistique avec une réflexion par la surface (dite d'ordre un) est donnée par :

$$\begin{aligned} S_{\mathrm{M}}^{1,\mathrm{unco}}(\theta, \gamma_{x_0}, \gamma_{y_0}, \zeta_0) &= \Upsilon(\mu - \gamma_{X_0}) F(\zeta_0)^{\Lambda(\mu)} \\ &\quad \times \left\{ \begin{array}{ll} 1 & \text{si} \quad |\theta'| > 90° \\ 1 - F(\zeta_0)^{\Lambda^-(\mu_1)} & \text{si} \quad |\theta'| < 90° \end{array} \right. . \end{aligned} \tag{40}$$

Rappelons que la fonction d'illumination sans réflexion (dite d'ordre zéro) dépend de la pente de M_0 via la fonction de Heaviside $\Upsilon(\mu - \gamma_{X_0})$, ce qui ne donne que deux possibilités : l'éventualité que la facette soit vue par le capteur est ou possible ($\Upsilon = 1$), ou impossible ($\Upsilon = 0$). Cependant, la fonction d'illumination avec une réflexion est plus compliquée, car elle implique un rayon d'incidence et un rayon de réflexion. La pente du rayon réfléchi affecte grandement la fonction d'illumination. En conséquence, les points vus par le capteur sont divisés en deux parties. La première partie correspond au cas 1, où le rayon réfléchi se propage vers le bas et intercepte (de manière certaine) la surface. Ainsi, la fonction d'illumination monostatique d'ordre un correspond à la probabilité que le point M_0 soit vu par le récepteur, ce qui est égal à $F(\zeta_0)^{\Lambda(\mu)}$. L'autre partie correspond au cas 2, où le rayon réfléchi se propage vers le haut. Il faut considérer la probabilité que le rayon réfléchi $M_0(-\hat{s}')$ intercepte la surface au cours de sa propagation. En conséquence, un terme supplémentaire $1 - F(\zeta_0)^{\Lambda(\mu_1)}$ apparaît.

L'équation (40) ne prend pas en compte la corrélation des hauteurs et des pentes de la surface. La fonction d'illumination d'ordre un corrélée a également été étudiée. Cependant, elle n'est pas montrée ici, à cause de la complexité de sa forme.

Les résultats de la fonction d'illumination d'ordre un sont présentés dans la section 2.2.2 du manuscrit. Pour valider le modèle, une méthode de tracé de rayons de Monte-Carlo est utilisée. La densité de probabilité de la surface est supposée gaussienne centrée.

Les histogrammes marginaux d'ordre un des hauteurs et des pentes constituent un moyen supplémentaire de vérifier la validité du modèle. Ils sont définis par :

$$\begin{aligned} \widetilde{p}^1_\gamma(\mu,\gamma_0) &= p_\gamma(\gamma_0)\int_{-\infty}^{+\infty} S^1_{\mathrm{M}}(\mu,\gamma_0,\zeta_0)p_\zeta(\zeta_0)\,\mathrm{d}\zeta_0, \\ \widetilde{p}^1_\zeta(\mu,\zeta_0) &= p_\zeta(\zeta_0)\int_{-\infty}^{+\infty} S^1_{\mathrm{M}}(\mu,\gamma_0,\zeta_0)p_\gamma(\gamma_0)\,\mathrm{d}\gamma_0. \end{aligned} \tag{41}$$

Ils correspondent à la distribution des hauteurs et des pentes de la surface qui conduisent à une réflexion. Les résultats sont comparés avec ceux de la méthode de tracé de rayons de Monte-Carlo, et sont présentés dans la figure 2.16 du manuscrit. De manière générale, nous pouvons observer que le modèle surestime légèrement les réflexions par la surface. De meilleurs accords sont obtenus après la prise en compte de la corrélation des hauteurs et des pentes de la surface. Les comparaisons des résultats pour des surfaces avec différents écarts types des pentes ont montré que la contribution des réflexions par la surface augmente lorsque l'écarte type des pentes augmente.

Pour vérifier la validité du modèle présenté, la fonction d'illumination monostatique avec une réflexion moyennée est étudiée. Elle est obtenue par l'intégrale de S^1_{M} sur les hauteurs et les pentes de M_0, donnée par :

$$\overline{\overline{S}}^1_{\mathrm{M}}(\theta) = \int_{-\infty}^{+\infty}\int_{-\infty}^{+\infty} S^1_{\mathrm{M}}(\theta,\gamma_0,\zeta_0)p(\gamma_0,\zeta_0)\,\mathrm{d}\zeta_0\,\mathrm{d}\gamma_0. \tag{42}$$

Les résultats sont donnés dans la figure 2.18 du manuscrit. La fonction d'illumination monostatique avec une réflexion moyennée est calculée et présentée pour des surfaces avec des écarts type des pentes $\sigma_\gamma = 0.2$ et $\sigma_\gamma = 0.5$. De bons accords entre le modèle décorrélé et la méthode de tracé de rayons Monte-Carlo sont observés. La surestimation est significative pour des angles d'observation par rapport au zénith importants : par exemple, $\theta > 60°$ pour des surfaces avec un écart type des pentes $\sigma_\gamma = 0.2$. Après la prise en compte de la corrélation, la surestimation diminue. Malheureusement, le modèle corrélé est trop complexe à calculer et prend un temps de calcul trop long.

Les simulations ont montré que la fonction d'illumination d'ordre un est toujours importante pour des angles d'observation par rapport au zénith θ grands, avec un maximum de plus de $0,2$ à $\theta \approx 75°$ pour des surfaces avec $\sigma_\gamma = 0,2$ et à $\theta \approx 50°$ pour des surfaces avec $\sigma_\gamma = 0,5$, ce qui signifie que les réflexions par la surface ont lieu sur 20 $\%$ de l'aire totale de la surface pour ces angles d'observation. Les recherches existantes sur l'émissivité infrarouge d'une surface de mer [1, 13] ont montré que les modèles qui ne tiennent pas compte des réflexions par la surface sous-estiment l'émissivité de la surface pour des angles d'observation par rapport au zénith θ grands. Lorsque les réflexions par la surface sont significatives pour ces angles, la prise en compte d'une réflexion par la surface améliore l'accord entre le modèle analytique et les mesures.

La fonction d'illumination monostatique avec une réflexion moyennée est également calculée par rapport à la direction du vent. Les simulations ne montré qu'elle dépend de la direction du vent. Elle est symétrique par rapport aux directions face, traverse, et dos au vent ($\phi = \{0°, 90°, 180°, 270°\}$) pour la densité de probabilité des pentes gaussienne. Après la prise en compte de l'effet du skewness, elle est symétrique par rapport aux directions face et dos au vent ($\phi = \{0°, 180°\}$).

La fonction d'illumination corrélée est plus précise, mais son temps de calcul est long. Ainsi, un facteur empirique est développé pour améliorer la performance du modèle décorrélé, tout en conservant un temps de calcul très faible. La fonction d'illumination sans réflexion par la surface est multipliée par ce facteur empirique. De très bons accords sont observés entre la fonction d'illumination empirique, sans et avec une réflexion, et la méthode de tracé de rayons de Monte-Carlo.

Pour conclure, les fonctions d'illumination monostatique sans et avec une réflexion sont étudiées. Les simulations montrent que la fonction d'illumination de Smith est la plus précise. Les réflexions par la surface sont importantes pour des angles d'observation rasants.

Dans ce qui suit, l'émissivité infrarouge de la surface de mer est étudiée, où l'ombrage et des réflexions par la surface sont pris en compte à l'aide des fonctions d'illumination développées dans cette section. La fonction d'illumination d'ordre un constitue une des contributions principales de cette thèse.

3.2 Emissivité d'une surface de mer

L'émissivité infrarouge d'une surface de mer dans les fenêtres de transmission atmosphériques est un paramètre important pour la télédétection océanique, par exemple, pour le calcul de la température de la surface de la mer. D'un point de vue applicatif, il est important de calculer l'émissivité avec précision, ce qui implique que les phénomènes d'ombrage et de réflexions par la surface doivent être pris en compte.

Les premiers modèles de l'émissivité infrarouge d'une surface de mer ont pris en compte l'effet de l'ombrage. Cependant, les réflexions par la surface sont difficiles à considérer. Les modèles de la littérature de l'émissivité d'une surface de mer avec réflexions ne sont pas satisfaisants, à cause du défaut de la construction de la fonction d'illumination avec réflexion(s). Dans cette thèse, l'émissivité d'une surface de mer avec une réflexion par la surface est calculée à l'aide de la fonction d'illumination d'ordre un présentée précédemment.

3.2.1 Emissivité directe avec ombrage

L'émissivité infrarouge directe d'une surface de mer, qui est illustrée sur la figure 7, correspond au rayonnement intrinsèque de la surface se propageant directement vers le récepteur situé dans la direction d'observation $\hat{s}$. Elle est également appelée émissivité d'ordre zéro, car aucune réflexion par la surface n'est considérée. Les modèles de l'émissivité infrarouge d'une surface de mer d'ordre zéro sont bien connus [10, 32, 6, 7, 35]. Cette section se base sur les travaux de Bourlier *et al.* [32] pour calculer l'émissivité infrarouge directe (dite d'ordre zéro) d'une surface de mer. De plus, la polarisation est prise en compte.

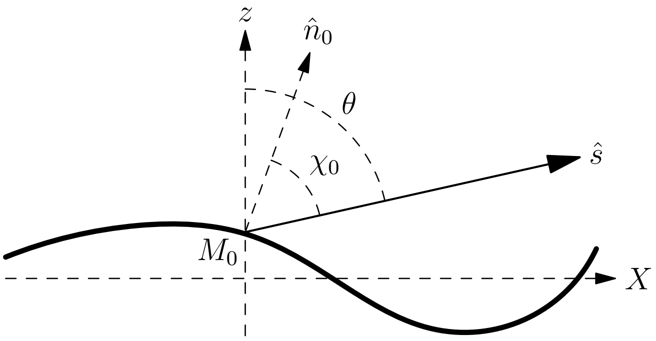

Figure 7: Emissivité infrarouge directe d'une surface de mer. Le rayon d'émission se propage directement vers le récepteur situé dans la direction $\hat{s}$.

L'émissivité directe ε_0 est calculée tout d'abord pour des surfaces à une dimension (problème 2D), pour plus de simplicité. Ensuite, des surfaces bidimensionnelles (problème 3D) sont considérées pour étudier l'effet de polarisation croisée. A cause de la rugosité de la surface, l'effet d'ombrage doit être pris en compte dans la modélisation électromagnétique.

Nous supposons que la mer est opaque pour les longueurs d'onde infrarouges, ce qui signifie que toute l'énergie de réfraction est absorbée. Nous supposons également que la surface de mer est dans un équilibre thermique. L'émissivité locale d'un point arbitraire de la surface M_0 est donnée par [10] :

$$\varepsilon_{0,H,V}^{\text{local}}(\chi_0) = 1 - |r_{H,V}(\chi_0)|^2, \tag{43}$$

où $r_{H,V}$ sont les coefficients de Fresnel respectivement en polarisations horizontale H et verticale V.

L'émissivité infrarouge directe ε_0 d'une surface de mer ε_0 est obtenue par la moyenne de l'émissivité locale $\varepsilon_{0,H,V}^{\text{local}}$ des points vus par le récepteur, donnés par [32] :

$$\varepsilon_{0,H,V} = \left\langle \left[1 - |r_{H,V}(\chi_0)|^2\right] g_0 \; S_{\text{M}}^0 \right\rangle_0 , \tag{44}$$

où g_0 correspond à la projection de la zone autour du point M_0 sur la direction orthogonale à la direction d'observation. Le symbole $\langle \cdots \rangle_0$ représente la moyenne statistique sur les pentes et les hauteurs de la surface. S_{M}^0 est la fonction d'illumination sans réflexion par la surface. Dans cette thèse, le modèle de Smith est employé.

Emissivité directe L'émissivité infrarouge sans réflexion d'une surface de mer est calculée pour des vitesses du vent à 12.5 m u_{12} de 5 et 10 m/s, et pour des longueurs d'onde λ de 4 et 10 μm. Les résultats sont présentés dans les figures 3.3-3.5 du manuscrit. Les résultats sans effet d'ombrage montrent que, pour $\theta > 85°$, l'émissivité d'ordre zéro ε_0 dépasse 1 et tend vers l'infini lorsque θ tend vers 90°, ce qui n'est pas physique. Ceci est dû au fait que pour les angles d'observation par rapport au zénith importants, le modèle sans ombrage prend en compte tous les points de la surface pour calculer l'émissivité de la surface, y compris les points dans l'ombre du récepteur qui ne contribuent pas à la radiation de la surface.

L'émissivité infrarouge directe d'une surface lisse est calculée et comparée avec ceux des surfaces de mer. Il est montré que l'émissivité infrarouge directe ε_0 est proche de 1 lorsque θ est faible ($\theta < 40°$). L'émissivité infrarouge directe d'une surface lisse est égale à 0 pour $\theta = 90°$. En outre, lorsque la vitesse du vent augmente, l'émissivité infrarouge directe ε_0 diminue légèrement pour les angles par rapport au zénith modérés (par exemple, $50° \lesssim \theta \lesssim 70°$), et augmente significativement pour des angles importants (par exemple $\theta \gtrsim 70°$).

Les résultats du modèle sont comparés avec ceux de la méthode de tracé de rayons de Monte-Carlo pour des surfaces avec une densité de probabilité des pentes gaussienne centrée. De très bons accords sont observés entre le modèle et la méthode de tracé de rayons de Monte-Carlo pour $\theta \lesssim 85°$. En général, le modèle corrélé donne un meilleur accord avec la méthode de tracé de rayons. De petites différences apparaissent pour $\theta > 85°$. Dans cette région, l'erreur de calcul dans l'intégration numérique de la fonction d'illumination corrélée devient importante, ce qui est la raison principale de cet écart.

Les effets du skewness et du kurtosis sont également étudiés. Lorsque la mer est relativement calme, par exemple pour $u_{12} = 5$ m/s, les émissivités directes avec une densité de probabilité des pentes gaussienne et non-gaussienne (avec skewness et kurtosis compris) sont très semblables, ce qui signifie que les effets du skewness et du kurtosis sont faibles. Lorsque la vitesse du vent augmente, les effets du skewness et du kurtosis deviennent plus importants.

Degré de polarisation Le rayonnement infrarouge intrinsèque d'une surface rugueuse est partiellement polarisée pour des grands angles d'observation [36, 43]. Le degré de polarisation (DP) de l'émissivité est donc calculé. Il est donné par :

$$DP = \frac{\varepsilon_H - \varepsilon_V}{\varepsilon_H + \varepsilon_V}, \tag{45}$$

où ε_H et ε_V sont les émissivités en polarisations horizontale H et verticale V.

Le module du DP décrit la fraction de la puissance polarisée par rapport à la puissance totale, tandis que son signe traduit la direction de polarisation dominante. Un DP positif indique que la polarisation horizontale (H) est dominante, et vice-versa.

Les résultats de DP de l'émissivité directe ε_0 sont montrés dans les figures 3.6 et 3.12 du manuscrit. Les simulations montrent que le DP est toujours négatif, ce qui signifie que la polarisation V est toujours la polarisation dominante. Lorsque la vitesse du vent augmente, la valeur absolue du DP diminue, ce qui signifie que l'augmentation de la vitesse du vent induit une diminution des caractéristiques de polarisation de l'émissivité directe.

Polarisation croisée Pour des surfaces 1D (problèmes 2D), la direction d'observation $\hat{s}$ et la normale locale du point considéré $\hat{n}_0$ sont dans le même plan contenant la surface. Ceci signifie que les directions de polarisation locales horizontale et verticale des différents points de la surface sont identiques. En conséquence, il n'y a pas de polarisation croisée.

Cependant, pour des surface 2D (problèmes 3D), les directions de polarisation locales sont différentes d'un point de la surface à un autre. Pour décrire l'état de polarisation de l'émissivité infrarouge d'une surface de mer, la surface moyenne de la mer, qui est parallèle au plan horizontal, est considérée. Les directions de polarisation globales sont définies par la direction d'observation $\hat{s}$ et le zénith. Lorsque le plan tangent au point considéré est différent de la surface moyenne de la mer, il y a un angle de rotation α entre les directions de polarisation globales et locales. Nous appelons cet effet la "polarisation croisée".

L'effet de la polarisation croisée de l'émissivité directe est étudiée dans la figure 3.8 du manuscrit. Il est montré que les termes de polarisation croisée (h_0V et v_0H) ne sont significatifs que pour des petits angles d'observation par rapport au zénith θ ; par exemple, $\theta < 30°$ pour la vitesse du vent $u_{12} = 5$ m/s et $\theta < 35°$ pour $u_{12} = 10$ m/s. Nous pouvons alors conclure que l'augmentation de la vitesse du vent induit une augmentation de l'effet de polarisation croisée pour des petits angles d'observation θ, ce qui est conforme à la physique.

Les contributions des polarisations croisées diminuent rapidement avec l'augmentation de l'angle θ et deviennent faibles pour les grandes valeurs de θ : par exemple, $\varepsilon_{0,h_0V} \approx 0,0068$ et $\varepsilon_{0,v_0H} \approx 0,0093$ pour $\theta = 85°$. D'autre part, les contributions ε_{0,h_0H} et ε_{0,v_0V} sont toujours significatives, quel que soit l'angle d'observation θ.

Pour étudier la diminution rapide des contributions des polarisations croisées, la moyenne de l'angle de rotation α, donnée par $\langle \alpha S_{\mathrm{M}}^0 \rangle_0$, est calculée pour des densités de probabilité des pentes de la surface gaussienne et non gaussienne. La fonction d'illumination S_{M}^0 est prise en compte pour éliminer l'influence des points dans l'ombre du récepteur, qui ne contribuent pas à l'émissivité observée.

Les résultats montrent que la moyenne de α est un peu plus de $40°$ pour $\theta = 0°$ pour les vitesses du vent $u_{12} = 5$ et 10 m/s. Cela explique que les termes en polarisations parallèles (h_0H, v_0V) et ceux en polarisations croisées (h_0V et v_0H) sont similaires pour $\theta = 0°$, car α est proche de $45°$.

La moyenne de α décroît avec l'augmentation de θ, d'un peu plus de $40°$ pour $\theta = 0°$ à environ $0°$ pour $\theta = 90°$. Ceci implique que les directions de polarisation globales et locales sont proches. Par conséquent, l'influence des polarisations croisées devient négligeable.

3.2.2 Emissivité avec une réflexion

Des comparaisons avec des mesures ont montré que les modèles d'ordre zéro ont sous-estimé l'émissivité infrarouge d'une surface de mer pour des angles d'observation θ importants [39, 1, 22]. Une raison à cette observation est que les réflexions par la surface n'ont pas été prises en compte.

Dans cette thèse, l'émissivité infrarouge d'une surface de mer avec une réflexion (d'ordre un) est calculée analytiquement. La fonction d'illumination avec une réflexion S_{M}^1 est utilisée. La fig. 8 illustre l'émissivité d'une surface avec une réflexion.

L'émissivité d'ordre un ε_1 correspond à l'énergie émise par un point de la surface M_1 et réfléchie par un autre point M_0 de la surface dans la direction d'observation $\hat{s}$. L'émissivité d'ordre un locale d'un point arbitraire est donnée par [15] :

$$\varepsilon_1^{\text{local}} = \left[1 - |r(\chi_1)_{H,V}|^2\right] |r(\chi_0)_{H,V}|^2. \tag{46}$$

L'émissivité d'une surface de mer avec une réflexion ε_1 est obtenue par la moyenne des émissivités locales $\varepsilon_1^{\text{local}}$ des points de la surface, donnée par :

$$\varepsilon_1 = \left\langle \varepsilon_1^{\text{local}} g_0 S_{\mathrm{M}}^1 \right\rangle_1 , \tag{47}$$

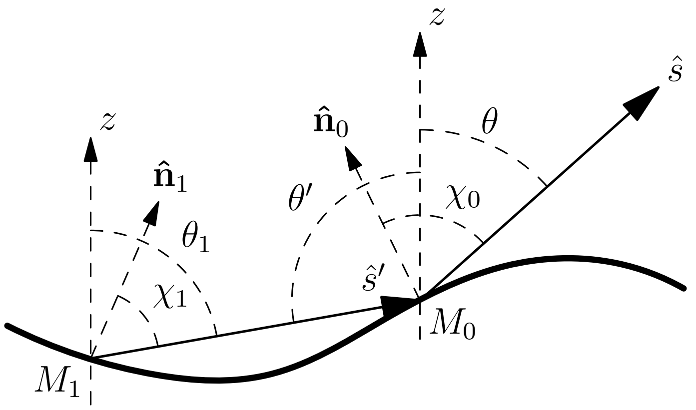

Figure 8: Emissivité d'une surface de mer avec une réflexion. Le rayon d'émission du point M_1 de la surface intercepte la surface au point M_0, où il est réfléchi spéculairement à la direction d'observation $\hat{s}$.

où g_0 correspond à la projection de la zone autour du point considéré sur la direction orthogonale à la direction d'observation. Le symbole $\langle \cdots \rangle_1$ représente la moyenne statistique sur les pentes et les hauteurs de la surface. S^1_{M} est la fonction d'illumination avec une réflexion par la surface.

Comparaison avec la méthode de tracé de rayons L'émissivité infrarouge d'une surface de mer avec une réflexion ε_1 est calculée et comparée avec la méthode de tracé de rayons de Monte-Carlo dans les fig. 3.15 et 3.16. La DDP des pentes de la surface est supposée gaussienne centrée.

Les simulations montrent que l'émissivité avec une réflexion ε_1 contribue aux angles d'observation importants. Avec la fonction d'illumination d'ordre un décorrélée, de bons accords sont observés entre le modèle et la méthode de tracé de rayons. Le modèle décorrélé surestime l'émissivité d'ordre un pour $\theta > 80°$. De meilleurs accords sont obtenus par la prise en compte de la corrélation des hauteurs et des pentes de la surface. L'émissivité avec une réflexion a un maximum d'environ $2,5 \times 10^{-2}$ et tend vers zéro à $\theta = 90°$.

Les résultats de la méthode de tracé de rayons de Monte-Carlo de l'émissivité infrarouge avec deux réflexions sont également présentés, afin de voir s'il est nécessaire de pousser la modélisation à l'ordre deux ou plus. Un maximum d'environ $2,5 \times 10^{-3}$ pour $80°$ est observé en polarisations H et V, ce qui est très inférieur (10%) à celui de l'émissivité avec une réflexion. Les calculs de la méthode de tracé de rayons de Monte-Carlo avec trois réflexions ont également été menés : un maximum d'environ 4×10^{-4} a alors été obtenu (non représenté dans la thèse). En conséquence, deux réflexions et plus sont négligeables dans l'émissivité par la surface de mer.

Polarisation croisée Pour des surfaces 2D, les directions de polarisation locales sont différentes d'un point de la surface à un autre. Lorsque les normales des points M_0 et M_1 ne sont pas identiques, il y a un angle de rotation β entre leurs directions de polarisation locales. Rappelons qu'il y a un angle de rotation α entre la direction de polarisation locale du point M_0 et la direction de polarisation globale. Cela signifie que la polarisation croisée se produit.

Les termes de l'émissivité d'une surface de mer avec une réflexion en polarisations parallèles et croisées sont présentés dans les figures 3.20 et 3.21 du manuscrit. Les contributions des polarisations croisées sont très faibles $u_{12} = 5$ m/s et faibles pour $u_{12} = 10$ m/s. On peut conclure que, comme attendu, l'augmentation de la vitesse du vent augmente l'effet des polarisations croisées.

Les angles de rotation moyennés α et β, donnés par $\langle \alpha \S^1_{\mathrm{M}} \rangle_1$ et $\langle \beta S^1_{\mathrm{M}} \rangle_1$, sont calculés. La fonction d'illumination d'ordre un est prise en compte pour pondérer chaque α et β, selon la probabilité d'observer une réflexion. Les résultats montrent que les moyennes des angles α et β sont très petites : par exemple, le maximum de β est d'environ $3°$, et celui de α est $1°$ pour une vitesse du vent $u_{12} = 5$ m/s. En d'autres termes, cela signifie que les directions de polarisation globales et locales des points M_0 et M_1, sont presque les mêmes. Ainsi, les termes en polarisations croisées sont faibles.

Emissivité totale et comparaison avec mesures L'émissivité totale de la surface de mer peut être évaluée par la somme de l'émissivité directe et de celle avec une réflexion, car nous avons mis en évidence que les émissivités avec deux réflexions et plus étaient négligeables.

Les simulations montrent que l'émissivité totale d'une surface de mer diminue avec l'augmentation de l'angle d'observation θ. Par rapport à l'émissivité directe, l'émissivité totale est significativement augmentée pour des angles d'observation importants après la prise en compte de la contribution de l'émissivité d'ordre un. Le degré de polarisation (DP) de l'émissivité totale est également étudiée. On trouve que le DP de l'émissivité totale est toujours négatif, ce qui signifie que la polarisation globale verticale est la dominante. La prise en compte de l'émissivité avec une réflexion diminue le module du DP, ce qui signifie qu'une réflexion par la surface diminue les caractéristiques de polarisation de l'émissivité d'une surface de mer.

L'émissivité totale obtenue par le modèle développé dans cette thèse est comparée avec les mesures de Smith *et al.* [37] et ceux de Niclòs *et al.* [38]. Les comparaisons montrent que les résultats du modèle et les mesures ont la même forme. De très bons accords sont observés pour des angles d'observation θ faibles à modérés ($\theta = \{25°, 35°, 36.5°, 45°, 55°, 56.5°\}$). Le modèle sous-estime l'émissivité de la surface de mer pour les angles $65°$ et $73.5°$. De plus, de meilleurs accords sont obtenus après la prise en compte de l'émissivité avec une réflexion.

L'émissivité infrarouge d'ordre un d'une surface de mer est une des principales contributions de cette thèse. Les résultats pour des surfaces 1D ont fait l'objet d'une publication en revue en 2011 dans *Applied Optics* [22], et ceux pour des surfaces 2D ont été publiés très récemment dans *Remote Sensing of Environment* [44].

Pour prédire le signal reçu par le récepteur mesurant le rayonnement infrarouge d'une surface de mer, la connaissance de l'émissivité ε et de la réflectivité ρ de la surface sont nécessaires. Ainsi, dans ce qui suit, la fonction d'illumination bistatique, qui est un paramètre clé du calcul de la réflectivité, est étudiée.

3.3 Fonction d'illumination bistatique

Lorsqu'on calcule la réflectivité d'une surface de mer ρ, l'ombrage de l'émetteur et du récepteur doit être étudié, en particulier lorsque l'émetteur et le récepteur sont proches de l'horizon (θ_i et θ tendent vers $90°$). D'autre part, la contribution des réflexions multiples doit être prise en compte.

Pour évaluer les phénomènes de l'ombrage et des réflexions multiples, une fonction d'illumination bistatique S_{B}^{n} est utilisée, où $n = 1, 2, 3, \ldots$ désigne le nombre de réflexions. L'indice "B" correspond à la configuration bistatique, ce qui signifie que l'émetteur et le récepteur sont situés dans des endroits différents.

3.3.1 Fonction d'illumination bistatique avec une réflexion

La figure 9 illustre un rayon d'incidence $\hat{s}_i$ réfléchi par la surface dans la direction d'observation $\hat{s}$. En raison de la rugosité de la surface, une partie de la surface se trouve dans l'ombre de l'émetteur, comme indiqué par la ligne discontinue bleu sur la figure. De même, une partie de la surface se trouve dans l'ombre du récepteur, notée en rouge. Ce phénomène est appelé effet d'ombrage bistatique. Les directions X et X' correspondent aux composantes horizontales de $\hat{s}$ et $\hat{s}_i$.

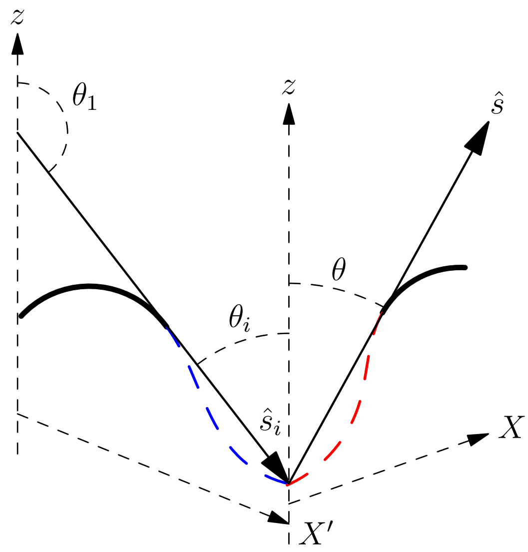

Figure 9: Effet d'ombrage bistatique : une partie de la surface se trouve dans l'ombre de l'émetteur (zone en bleu) ou du récepteur (zone en rouge).

Pour évaluer l'effet d'ombrage bistatique, une fonction d'illumination bistatique avec une réflexion est utilisée. Dans cette thèse, le modèle de Smith [4] est employé.

Les résultats de la fonction d'illumination bistatique sont comparés avec ceux d'une méthode de tracé de rayons de Monte-Carlo. La densité de probabilité des pentes de la surface est supposée gaussienne centrée.

Les histogrammes des hauteurs et des pentes de la surface vues par le récepteur et l'émetteur sont d'abord étudiés. On trouve que la fonction d'illumination prédit bien les hauteurs et les pentes de la surface vues dans les deux directions. Le modèle décorrélé surestime les résultats, ainsi que celui avec corrélation, qui donne de meilleurs accords.

La fonction d'illumination bistatique moyennée $\overline{\overline{S}}_{\mathrm{B}}^{2}$ donne le pourcentage de la surface vue par le récepteur et l'émetteur. Les résultats sont comparés avec ceux de la méthode de tracé de rayons de Monte-Carlo. Comme prévu par les résultats des histogrammes, la fonction d'illumination bistatique moyennée donne de bons accords avec la référence. De meilleurs accords sont obtenus après la prise en compte de la corrélation.

Ensuite, le fait que les directions d'observation et d'incidence sont liées par une réflexion spéculaire est pris en compte dans la modélisation. Tout d'abord, pour une direction d'observation θ donnée, la distribution de la direction d'incidence θ_i est étudiée. Les résultats sont présentés et comparés avec ceux de la méthode de tracé de rayons de Monte-Carlo, pour des surface avec un écart type des pentes $\sigma_\gamma = 0.2$ et $\sigma_\gamma = 0.5$. Les angles d'observation faible $\theta = 30°$, modéré $\theta = 60°$ et grand $\theta = 80°$ sont étudiés. De très bons accords sont alors observés pour ces 3 angles entre le modèle et la méthode de tracé de rayons de Monte Carlo.

Les résultats montrent que la largeur des lobes de la distribution selon la direction d'incidence θ_i deviennent plus faible lorsque l'angle d'observation par rapport au zénith θ augmente, ce qui signifie que l'énergie de réflexion est plus concentrée angulairement.

Pour des surfaces avec un écart type des pentes $\sigma_\gamma = 0.2$, les largeurs des lobes sont plus étroits que ceux pour $\sigma_\gamma = 0.5$. Pour des surfaces avec $\sigma_\gamma = 0.2$, les distributions selon θ_i, pour les trois directions angulaires d'observation $\theta = \{30°, 60°, 80°\}$ étudiées, ont un maximum autour de la direction de réflexion spéculaire globale $\theta_i = \{-30°, -60°, -80°\}$, ce qui signifie qu'il est plus probable que le rayon réfléchi quitte la surface dans la direction de réflexion spéculaire globale. Pour des surfaces avec $\sigma_\gamma = 0.5$, les lobes sont plus étalés, comme attendu.

La moyenne hémisphérique de la fonction d'illumination bistatique avec une réflexion $\overline{\overline{S}}_{\mathrm{B}}^{1,\mathrm{hemi}}$ est calculée et comparée avec la méthode de tracé de rayons de Monte-Carlo. Elle donne la proportion de la surface vue par le récepteur dans la direction θ, et où le rayon réfléchi quitte la surface après une réflexion par la surface (chemin inverse). De bons accords sont observés, avec une surestimation. On trouve que $\overline{\overline{S}}_{\mathrm{B}}^{1,\mathrm{hemi}}$ diminue de façon monotone avec l'augmentation de l'angle d'observation θ. Pour des surfaces avec $\sigma_\gamma = 0.2$, $\overline{\overline{S}}_{\mathrm{B}}^{1,\mathrm{hemi}}$ est proche de 1 lorsque $\theta < 40°$, ce qui signifie que toute la surface est vue par le capteur, et tous les rayons réfléchis quittent la surface (sans la rencontrer à nouveau) après une réflexion. Pour des surfaces avec $\sigma_\gamma = 0.5$, $\overline{\overline{S}}_{\mathrm{B}}^{1,\mathrm{hemi}} \approx 0.9$, ce qui signifie que 90% de la surface est vue et les rayons réfléchis quittent la surface (sans la rencontrer à nouveau) après une réflexion. Pour $\theta = 90°$, $\overline{\overline{S}}_{\mathrm{B}}^{1,\mathrm{hemi}}$ tend vers zéro.

3.3.2 Fonction d'illumination bistatique avec deux réflexions

Pour prendre en compte deux réflexions par la surface, une fonction d'illumination bistatique avec deux réflexions S_{B}^2 est développée suivant le modèle de Lynch & Wagner [12]. La figure 10 illustre deux réflexions par la surface.

Un rayon d'incidence $\hat{s}_i$ intercepte la surface au point M_1, où il est réfléchi spéculairement dans la direction $\hat{s}'$. Ensuite, le rayon $\hat{s}'$ intercepte la surface en M_0, où il est réfléchi spéculairement dans la direction d'observation $\hat{s}$.

Pour évaluer la probabilité que les réflexions double soient observées, 4 événements sont définis, donnés par :

- "le rayon $\hat{s}$ n'intercepte pas la surface" est noté a ;
- "le rayon $\hat{s}'^-$ intercepte la surface au point M_1" est noté b ;
- "M_0 réfléchi $\hat{s}'^-$ à la direction $\hat{s}_i^-$" est noté c ;
- "le rayon $\hat{s}_i^-$ n'intercepte pas la surface" est noté d.

La fonction d'illumination bistatique avec deux réflexions S_{B}^2 est donc donnée par :

$$S_{\mathrm{B}}^2 = p(abcd) = p(a)p(b|a)p(c|ab)p(d|abc). \tag{48}$$

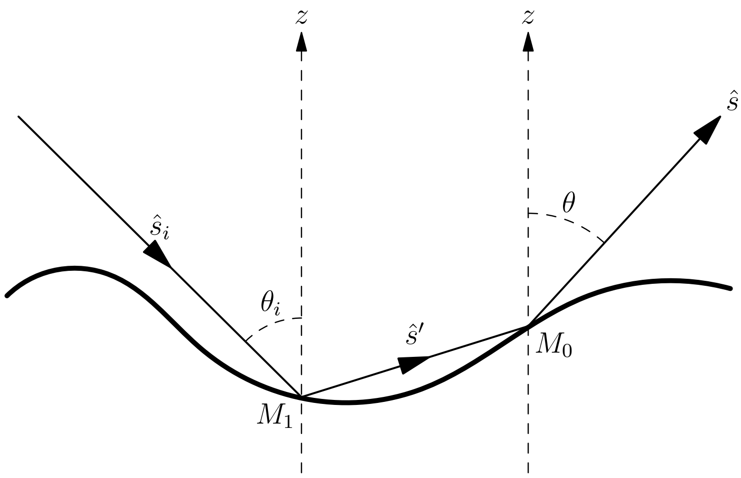

Figure 10: Deux réflexions par la surface : le rayon d'incidence $\hat{s}_i$ est réfléchi spéculairement deux fois par la surface, au point M_1 puis au point M_0, dans la direction d'observation $\hat{s}$.

S_{B}^{2} est basée sur les fonctions d'illumination monostatiques sans et avec une réflexion.

La fonction d'illumination bistatique avec deux réflexions moyennée $\overline{\overline{S}}_{\text{B}}^{2,\text{spe}}$, qui correspond à la distribution de θ_i (ou θ) pour un θ (ou θ_i) donné, est calculée pour des surfaces avec un écart type des pentes $\sigma_\gamma = 0.2$ et $\sigma_\gamma = 0.5$, et pour des angles d'observation $\theta = \{30°, 60°, 80°\}$. Les résultats sont comparés avec ceux de la méthode de tracé de rayons de Monte-Carlo.

Des différences apparaissent entre les résultats du modèle et ceux de la méthode de tracé de rayons de Monte-Carlo, en particulier pour le plus faible angle d'observation $\theta = 30°$. Le maximum de $\overline{\overline{S}}_{\text{B}}^{2,\text{spe}}$ du modèle est situé presque pour le même $\theta_i \approx -80°$ pour les différentes valeurs de θ, tandis que les résultats de tracé de rayons de Monte-Carlo montrent que sa position dépend de l'angle θ. Une raison possible de cette différence est que la densité de probabilité de la pente M_1 n'est pas bien calculée dans le modèle. Mis à part ce décalage, les résultats du modèle sont généralement au même niveau que ceux de la méthode tracé de rayons de Monte-Carlo.

La moyenne hémisphérique de la fonction d'illumination avec deux réflexions $\overline{\overline{S}}_{\text{B}}^{2,\text{hemi}}$ donne la proportion de la surface vue par le récepteur (chemin inverse) pour deux réflexions par la surface. Elle est obtenue par la moyenne de $\overline{\overline{S}}_{\text{B}}^{2,\text{spe}}$ sur l'angle d'incidence $\theta_i \in [-90°; 90°]$.

Les résultats de $\overline{\overline{S}}_{\text{B}}^{2,\text{hemi}}$ sont présentés pour des surfaces avec un écart type des pentes $\sigma_\gamma = 0.2$ et $\sigma_\gamma = 0.5$. Bon accord général est obtenu entre le modèle et la méthode de tracé de rayons de Monte Carlo. Le modèle décorrélé surestime les résultats pour des angles d'observation importants. En règle générale, la prise en compte d'une réflexion donne un meilleur accord avec la méthode de tracé de rayons. On observe que les réflexions doubles contribuent plus fortement lorsque l'écart type des pentes de la surface augmente.

3.4 Réflectivité d'une surface de mer

La réflectivité d'une surface de mer est un paramètre important dans le domaine océanique, par exemple, pour estimer le scintillement du soleil sur la surface de la mer. Habituellement, une seule réflexion par la surface est considérée [23, 8, 45, 6]. Pourtant, pour calculer la réflectivité avec précision, il faut prendre en compte les réflexions multiples dans la modélisation électromagnétique [9, 12]. Dans cette section, la réflectivité d'une surface de mer avec une et deux réflexions par la surface est calculée, à l'aide des fonctions d'illumination bistatiques associées décrites précédemment.

3.4.1 Réflectivité avec une réflexion

La réflectivité infrarouge d'ordre un d'une surface de mer correspond au rayonnement de l'atmosphère réfléchi une fois par la surface dans la direction d'observation. La figure 11 illustre la réflectivité avec une réflexion.

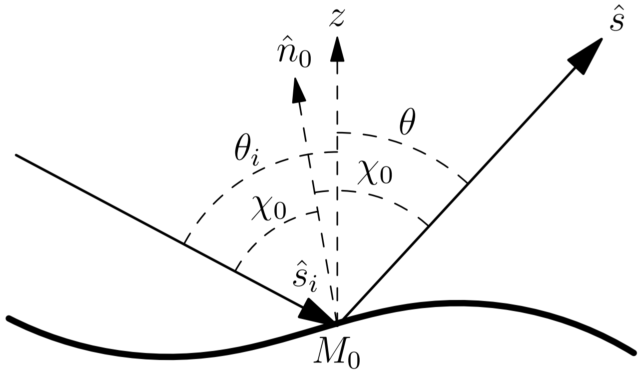

Figure 11: Un rayon d'incidence $\hat{s}_i$ intercepte la surface au point M_0, où il est réfléchi spéculairement dans la direction d'observation $\hat{s}$.

La réflectivité (locale) d'un point arbitraire M_0 de la surface est donnée par :

$$\rho^{\text{local}}_{1,H,V}(\chi_0) = |r_{H,V}(\chi_0)|^2, \tag{49}$$

où $r_{H,V}$ sont les coefficients de réflexion de Fresnel en polarisations horizontale H et verticale V.

La réflectivité d'une surface de mer est obtenue par la moyenne de la réflectivité locale sur les points vus par le récepteur et l'émetteur, donnée par :

$$\rho_{0,H,V} = \left\langle |r_{H,V}(\chi_0)|^2 g_0 \; S^{1,\text{spe}}_{\text{B}} \right\rangle_0, \tag{50}$$

où g_0 correspond à la projection de la zone autour de ce point sur la direction orthogonale à la direction d'observation. Le symbole $\langle \cdots \rangle_0$ représente la moyenne statistique sur les pentes et les hauteurs de la surface. $S^{1,\text{spe}}_{\text{B}}$ est la fonction d'illumination bistatique avec une réflexion par la surface. Dans cette thèse, la fonction de Smith [4] est utilisée.

La réflectivité d'une surface de mer est calculée pour des vitesses du vent u_{12} de 5 et 10 m/s. Pour simplifier le problème, des surfaces 1D sont considérées. Pour des surfaces 1D, les directions de polarisation globales et locales sont identiques, ce qui signifie qu'il n'y a pas de polarisation croisée.

Tout d'abord, la réflectivité avec une réflexion moyennée ρ_1^{spe} est calculée, ce qui donne la distribution bidirectionnelle de la réflectivité de la surface. Trois angles d'observation $\theta = \{30°, 60°, 80°\}$ sont considérés. Les résultats sont comparés avec une méthode de tracé de rayons de Monte-Carlo.

De très bons accords sont observés entre le modèle et la méthode de tracé de rayons de Monte-Carlo. Les résultats montrent que les réflectivités avec un réflexion ρ_1^{spe} en polarisations H et V sont très différentes. La réflectivité en polarisation V est toujours plus faible, ce qui signifie que l'état de polarisation du rayon d'incidence est modifié après la réflexion par la surface. Le rayon réfléchi d'un rayon non polarisé est partiellement polarisé, la polarisation H étant la plus significative.

On trouve que les maxima de ρ_1^{spe} en polarisation H et V sont différents. De plus, ils ne sont pas dans la direction de réflexion spéculaire globale. Les positions des maxima sont déplacés vers l'horizon ($|\theta_i|$ plus grand). Cet effet est rapporté dans la littérature [8, 45].

La moyenne hémisphérique de la réflectivité avec une réflexion ρ_1^{hemi} est également étudiée. Elle est obtenue par la moyenne de la réflectivité bidirectionnelle ρ_1^{spe} sur l'angle d'incidence $\theta_i \in [-90°; 90°]$. Les résultats sont comparés avec ceux d'une méthode de tracé de rayons de Monte-Carlo, où de bons accords sont observés.

3.4.2 Réflectivité avec deux réflexions

La réflectivité infrarouge d'ordre deux d'une surface de mer correspond au rayonnement de l'atmosphère réfléchi deux fois par la surface dans la direction d'observation. La figure 12 illustre la réflectivité avec deux réflexions.

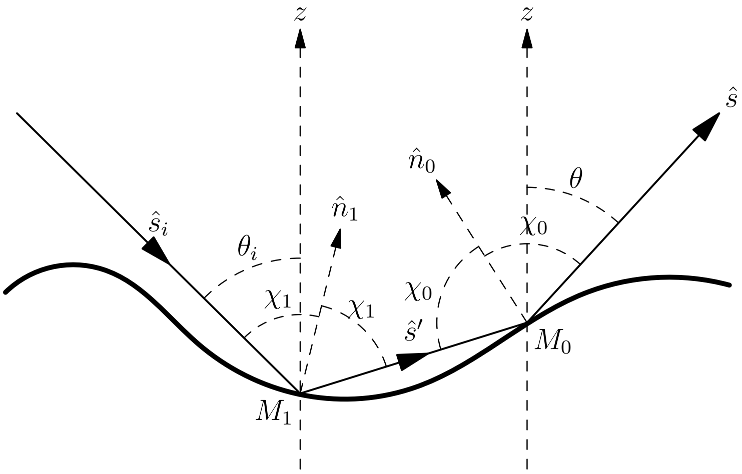

Figure 12: Un rayon d'incidence intercepte la surface au point M_1, où il est réfléchi dans la direction $\hat{s}'$. Ce rayon intercepte alors la surface au point M_0, où il est réfléchi dans la direction $\hat{s}$.

La réflectivité locale d'un point arbitraire de la surface est donnée par :

$$\rho_{2,H,V}^{\text{local}} = |r_{H_1,V_1}(\chi_1)|^2 |r_{H,V}(\chi_0)|^2, \tag{51}$$

où r_{H_1,V_1} correspond à la réflexion au point M_1 et $r_{H,V}$ correspond à celle au point M_0. La réflectivité de la surface de mer est obtenue par :

$$\rho_{2,H,V} = \left\langle \rho_{2,H,V}^{\text{local}} g_0 S_{\mathrm{B}}^{2,\text{spe}} \right\rangle_1 , \tag{52}$$

où g_0 correspond à la projection de la zone autour du point considéré sur la direction orthogonale à la direction d'observation. Le symbole $\langle \cdots \rangle_1$ représente la moyenne statistique sur les pentes et les hauteurs de la surface. $S_{\mathrm{B}}^{2,\mathrm{spe}}$ est la fonction d'illumination bistatique avec deux réflexions par la surface.

La réflectivité d'une surface de mer est calculée et comparée avec les résultats d'une méthode de tracé de rayons de Monte-Carlo. Pour simplifier le problème, des surfaces 1D sont considérées. Pour des surfaces 1D, les directions de polarisation globales et locales sont identiques, ce qui signifie qu'il n'y a pas de polarisation croisée.

D'abord, la réflectivité avec deux réflexions moyennée est étudiée, ce qui donne la distribution bidirectionnelle de la réflectivité. Trois angles d'observation $\theta = \{30°, 60°, 80°\}$ sont considérés. Des différences entre les résultats du modèle et ceux de la méthode de tracé de rayons de Monte-Carlo sont observées, en particulier pour les angles d'observation $\theta = 30°$ et $\theta = 60°$. Les positions des maxima sont déplacées. De meilleurs accords sont observés pour $\theta = 80°$. Ce désaccord est lié à celui de la fonction d'illumination bistatique avec deux réflexions. Heureusement, la réflectivité avec deux réflexions pour $\theta = 30°$ et $\theta = 60°$ est faible par rapport à celle avec une réflexion.

De plus, on trouve que les maxima de la réflectivité avec deux réflexions ne sont pas situés dans la direction de réflexion spéculaire globale : ils sont déplacés vers l'horizon, c'est-à-dire pour des angles θ plus grands.

La moyenne hémisphérique de la réflectivité avec deux réflexions ρ_2^{hemi} est également étudiée. Elle est obtenue par la moyenne de la réflectivité bidirectionnelle ρ_2^{spe} sur l'angle d'incidence $\theta_i \in [-90°; 90°]$. Les résultats sont comparés avec ceux d'une méthode de tracé de rayons de Monte-Carlo. De bons accords généraux sont observés. Le modèle décorrélé surestime la réflectivité avec deux réflexions. De meilleurs accords sont observées après la prise en compte de la corrélation. En règle générale, on observe que la réflectivité augmente avec la vitesse du vent.

3.4.3 Conservation d'énergie

La loi de conservation de l'énergie implique que, à l'équilibre thermique, l'énergie absorbée par une surface de mer est égale à son énergie rayonnée. Nous supposons que la surface de la mer est opaque, ce qui signifie que toute l'énergie du rayon de réfraction est absorbée par la mer. La loi de conservation de l'énergie est exprimée par la relation :

$$\varepsilon + \rho = 1. \tag{53}$$

Yoshimori *et al.* ont rapporté que l'équation (53) n'est pas vérifiée lorsque seules l'émissivité directe ε_0 et la réflectivité d'ordre un ρ_1^{hemi} sont considérées [6], avec $\varepsilon_0 + \rho_1^{\mathrm{hemi}} \leq 1$. Ainsi, l'équation (53) est examinée, en prenant en compte à la fois l'émissivité d'ordre un ε_1 et la réflectivité d'ordre deux ρ_2^{hemi}.

Les résultats montrent que le critère de conservation de l'énergie est satisfait pour des angles d'observation modérés $\theta < 60°$. Pour $\theta > 60°$, une perte d'énergie est observée lorsque seules l'émissivité directe ε_0 et la réflectivité d'ordre un ρ_1^{hemi} sont considérés. Après la prise en compte de l'émissivité d'ordre un ε_1 et de la réflectivité d'ordre deux ρ_2^{hemi}, le critère de conservation de l'énergie est mieux satisfait. Une surestimation est cependant obtenue par le modèle.

4 Conclusion

L'émissivité ε et la réflectivité ρ sont des paramètres sans dimension, compris entre 0 et 1. L'émissivité est la mesure de la capacité d'un objet à réémettre l'énergie absorbée. La réflectivité ρ d'un objet est une mesure de sa capacité à réfléchir l'énergie incidente. Le critère de conservation de l'énergie impose que la somme de l'énergie absorbée et de l'énergie réfléchie soit égale à l'énergie incidente, ce qui implique :

$$\varepsilon + \rho^{\text{hemi}} = 1.$$

L'émissivité et la réflectivité d'une surface de mer sont des paramètres importants dans le domaine océanique. La connaissance de l'émissivité et de la réflectivité est essentielle. Cette thèse a pour but de modéliser l'émissivité ε et la réflectivité ρ infrarouges d'une surface de mer avec précision. En effet, les phénomènes d'ombrage et de réflexions multiples par la surface sont pris en compte dans les modèles.

Cette thèse s'intéresse au domaine infrarouge, et l'approximation de l'optique géométrique (OG) est utilisée. La surface de la mer est modélisée comme étant bijective (en particulier, pour une abscisse donnée, elle ne possède pas plusieurs hauteurs), ce qui signifie que les vagues déferlantes ne sont pas prises en compte. En outre, des "whitecaps" (moutons) ne sont pas traités. Sous l'approximation de l'optique géométrique, seule la réflexion spéculaire par la surface est considérée dans le processus de diffusion électromagnétique.

Dans le chapitre 2, les fonctions d'illumination monostatiques sans réflexion par la surface de la littérature sont rappelées. Une fonction d'illumination avec une réflexion par la surface est développée. De très bons accords sont observés entre le modèle et la méthode de tracé de rayons de Monte-Carlo. Nous avons montré que la réflexion par la surface est significative pour des angles d'observation importants. La fonction d'illumination d'ordre un est une des contributions principales de cette thèse.

Dans le chapitre 3, l'émissivité d'une surface de mer est étudiée. Une réflexion par la surface est prise en compte à l'aide de la fonction d'illumination avec une réflexion développée dans le chapitre 2. De très bons accords entre le modèle et la méthode de tracé de rayons de Monte-Carlo sont observés. De plus, l'accord avec des mesures est amélioré après la prise en compte de l'émissivité avec une réflexion par la surface. Les modèles de l'émissivité avec une réflexion pour des surfaces 1D et 2D ont fait l'objet de publications dans 2 revues [22, 44]. Nous avons montré également que les émissivités avec deux réflexions et plus sont négligeables.

Dans le chapitre 4, la fonction d'illumination bistatique est étudiée. Une fonction d'illumination bistatique avec deux réflexions par la surface est développée. De bons accords généraux entre le modèle et la méthode de tracé de rayons de Monte-Carlo sont observés.

Dans le chapitre 5, la réflectivité d'une surface de mer est calculée. Tout d'abord, une réflexion est prise en compte à l'aide de la fonction d'illumination d'ordre un. Dans cette thèse, le modèle de Smith est employé. La réflectivité avec deux réflexion est également calculée, à l'aide de la fonction d'illumination d'ordre deux développée dans le chapitre 4. De bons accords entre le modèle et la méthode de tracé de rayons de Monte-Carlo sont observés.

Le critère de conservation de l'énergie est enfin examiné. Nous avons montré que le critère de conservation de l'énergie est satisfait pour des angles d'observation modérés. Pour des angles d'observation plus grands, une perte d'énergie est observée lorsque seules l'émissivité directe ε_0 et la réflectivité d'ordre un ρ_1^{hemi} sont considérées. Après la prise en compte de l'émissivité d'ordre un ε_1 et de la réflectivité d'ordre deux ρ_2^{hemi}, le critère de conservation de l'énergie est mieux satisfait.

Quelques perspectives à ce travail peuvent être énumérées. Tout d'abord, la polarisation croisée de la réflectivité de la surface peut être étudiée en considérant des surfaces 2D, ce qui peut être intéressant. Elle n'a pas été étudiée dans cette thèse à cause du manque de temps.

Par ailleurs, une étude plus approfondie de la fonction d'illumination bistatique avec deux réflexions doit être faite. En effet, le modèle présenté ici ne prédit pas bien la distribution de la direction du rayon réfléchi après deux réflexions.

Les vagues déferlantes et des "whitecaps" (moutons) ne sont pas pris en compte dans cette thèse, ce qui signifie que ce modèle est valide pour des vents faibles à modérés.

Enfin, l'erreur de calcul de la fonction d'ombre avec corrélation est importante pour des angles d'observation $\theta > 85°$. Il faut retravailler les équations (afin, notamment, de s'affranchir des problèmes de formes indéterminées) et modifier les codes de calcul en conséquence.

Introduction

When measuring the radiance of the sea surface, or named surface leaving radiance, in the infrared atmospheric transmission windows ($\lambda \in [3, 5]$ and $[8, 12]$ μm), as illustrated in Fig. 1.1, the signal received by a downlooking receiver consists of two components. The first one is the contribution of the intrinsic thermal radiance of the sea surface L_e, which is characterized by its ***emissivity*** ε. The other one is the contribution of the downwelling atmospheric radiance reflected by the surface L_r, which is characterized by its ***reflectivity*** ρ.

All objects at temperatures above absolute zero emit thermal radiation in infrared wavelength. The intrinsic sea surface infrared emission intensity L_e can be obtained by multiplying the emission intensity $B(T)$ of a black body at the same temperature as the sea surface T with the emissivity ε of the sea surface: $L_\mathrm{e} = B(T)\varepsilon$.

Emissivity ε is defined as the ratio of the energy radiated from a material surface to that radiated from a blackbody (a perfect emitter) at the same temperature and wavelength, and under the same viewing conditions. It is a dimensionless quantity ranging from 0 (for a perfect reflector) to 1 (for a perfect emitter).

The knowledge of surface emissivity is important both for accurate non-contact temperature measurement and for heat transfer calculations. Radiation thermometers detect the thermal radiation emitted by a surface. They are generally calibrated using blackbody reference sources that have an emissivity close to 1. When viewing real surfaces, which have a lower emissivity, less thermal radiation will be received by the thermometer than from a blackbody at the same temperature and so the surface will appear colder than it is, unless the thermometer is adjusted to take into account the material surface emissivity. Unfortunately, because the emissivity of a material surface depends on many chemical and physical properties, it is often difficult to estimate it. It must either be measured or determined in some way, for example by modeling.

Sea surface infrared emissivity in the atmospheric transmission windows, for $\lambda \in [3, 5]$ and $[8, 12]$ μm, is an important parameter in oceanic remote sensing, e.g. for deriving the sea surface temperature. Sea surface infrared emissivity is nearly constant for observation directions near zenith, but it varies largely for high grazing angles (that is, near the horizon). In these observation directions, shadowing and surface reflections become significant, increasing the difficulty in predicting the sea surface emissivity accurately. Besides, an error of 3×10^{-3} in emissivity leads to an error of 0.5 K when calculating the sea surface temperature, which is well above the sensitivity of common sensors of remote sensing. As a result, it is of great interest to calculate the sea surface infrared emissivity with accuracy, which implies that the phenomena of shadowing and surface reflections must be both taken into account.

Given the downwelling atmospheric radiation intensity L_a, the intensity of the reflected ray can be obtained as:

$$L_{\mathrm{r}} = L_{\mathrm{a}}\rho,$$

where ρ is the reflectivity of the sea surface.

Reflectivity ρ is the fraction of incident radiation reflected by a surface. In general, reflectivity is treated as a directional property which is a function of the incident and reflected directions. By definition, it is a dimensionless quantity ranging from 0 to 1 (perfect reflector).

Sea surface reflectivity gained wide attention in the early 1960s, for example in the study of the sun glitter on the sea surfaces and in the radar detection of the background of sea surfaces. The reflectivity can be measured by sensors, but commonly it is calculated by models. Usually, one surface reflection is considered. It would be more accurate to take more reflections into account. Modeling correctly the surface reflectivity is essential in application.

The aim of this research is to accurately model the sea surface infrared emissivity ε and reflectivity ρ. As this thesis is interested in the infrared domain, the Geometric Optics approximation (GO) is assumed to be valid, because the infrared wavelengths are small enough compared with the sea surface roughness. The sea surface is modeled as being single valued, which means that breaking waves are not taken into account. Also, white caps are not dealt with. Besides, as the Geometric Optics approximation is assumed to be valid, the surface is assumed to be composed of a series of continuous smooth facets with continuous first derivatives between adjacent facets. Under the Geometric Optics approximation, reflections of the surface are replaced by the reflections on the tangent plane of the surface point, and specular reflection is considered.

In chapter 1, a general introduction of modeling of the surface emissivity and reflectivity is given, and the main difficulties are addressed. Then, a through literature review is given. The sea surface is modeled as an ergodic random process, and some important statistical characteristics are also reviewed.

In chapter 2, the monostatic illumination function is studied, which is the key parameter in the modeling of sea surface emissivity. The monostatic configuration here means that only a receiver appears. The surface is assumed to be a random process, and the illumination functions are studied statistically. Firstly, the zero-order monostatic illumination function (without surface reflection) is reviewed, which deals with the shadowing effect. Then, the one with one surface reflection (first-order) is derived analytically. The results of the Model are compared with a Monte Carlo ray-tracing method.

In chapter 3, the sea surface infrared emissivity is calculated using the monostatic illumination functions developed in chapter 2. Polarization is taken into account, and the degree of polarization (DOP) is calculated. The direct emissivity (without surface reflection) is firstly calculated with the zero-order monostatic illumination function, then the emissivity with one surface reflection (surface-emitted surface-reflected) is calculated with the first-order monostatic illumination function derived in chapter 2. The sea surface infrared emissivity obtained by the model is compared firstly with a Monte Carlo ray-tracing method and then with measurements.

In chapter 4, the bistatic illumination function is studied, which is the key parameter in the modeling of sea surface reflectivity. The bistatic configuration means that the transmitter and the receiver are in different locations. The bistatic illumination function with one surface reflection is reviewed. Then, the one with two reflections is derived. The results are compared with a Monte Carlo ray-tracing method.

In chapter 5, the sea surface infrared reflectivity is calculated using the bistatic illumination function developed in chapter 4. The surface reflectivity with one surface reflection and the one with two reflections are calculated. Polarization is also considered. Last, energy conservation of the developped model is studied by comparison with a Monte Carlo ray-tracing method, by calculating the sum of the sea surface emissivity and the hemispherical average reflectivity.

1

Research background

When measuring the radiance of a wind-roughened sea surface in the infrared atmospheric transmission windows ($\lambda \in [3,5]$ and $\lambda \in [8,12]$ μm), or named surface-leaving radiance as illustrated in Fig. 1.1, the signal received by a down-looking receiver consists of two components. The first one is the contribution of the intrinsic thermal radiation (in infrared wavelengths) of the sea surface L_{e}, which is characterized by its emissivity ε. The other one is the contribution of the down-welling atmospheric radiation reflected by the surface L_{r}, which is characterized by its reflectivity ρ. To predict the surface-leaving radiance, both the emissivity and the reflectivity of the surface have to be derived.

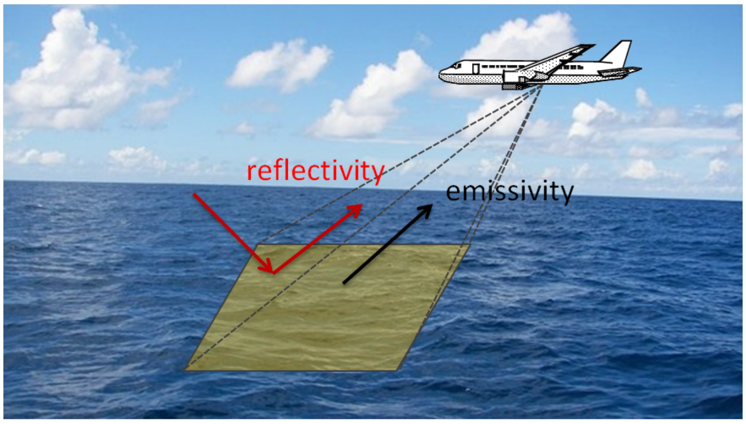

Figure 1.1: Illustration of a receiver measuring the sea surface-leaving radiance.

This thesis is intended to accurately model the sea surface infrared emissivity and reflectivity in the infrared atmospheric transmission windows. Fig. 1.2 shows the major physical phenomena which affect the surface-leaving radiance for a given observation direction θ.

Fig. 1.2 (a) and (b) corresponds to the surface intrinsic radiation. Fig. 1.2 (a) shows the direct radiation of the surface in the direction θ. Because of the roughness of the surface, some parts of the surface lie in shadow, shown as the dashed lines for a given θ in Fig. 1.2 (a). This is called the shadowing effect [3, 25]. It is also possible that the radiation ray intersects the surface at some other point where it is

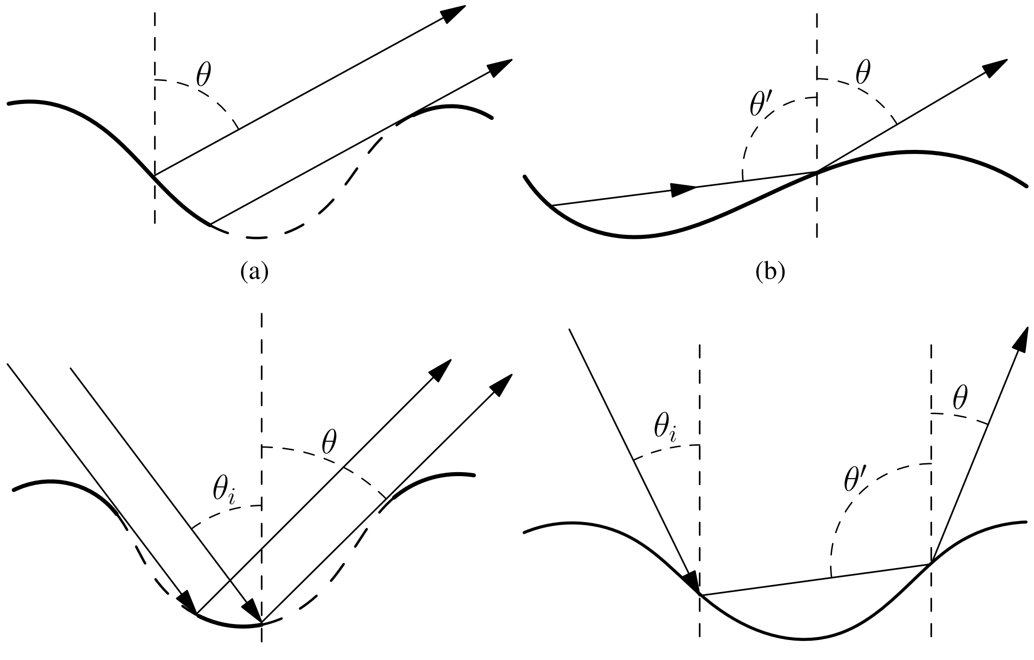

(a) (b)

(c) (d)

Figure 1.2: Major physical phenomena affecting the surface-leaving radiance for a given observation direction. The first row corresponds to the surface intrinsic radiation: (a) direct radiation and shadowing, and (b) surface-emitted surface-reflected radiation. The second row corresponds to atmospheric radiation reflected by the surface: (c) surface-reflected radiation and shadowing, and (d) surface-reflected surface-reflected radiation.

then reflected to the receiver. This part of energy is smaller than the direct radiation, but it also contributes to the final radiation field. This is called the surface-emitted surface-reflected (SESR) radiation [39]. Fig. 1.2 (b) shows one surface reflection as an example. As the number of reflection increases, the SESR radiation becomes smaller and smaller.

Fig. 1.2 (c) and (d) corresponds to the atmospheric radiation reflected by the surface. Fig. 1.2 (c) shows that the incident ray is reflected once by the surface to the receiver. Shadowing occurs again [2–4]. Except from shadowing from the receiver, shadowing form the transmitter should be also considered. Fig. 1.2 (d) shows that the emission ray of the atmosphere is reflected twice by the surface (SRSR). More surface reflections can be considered, but the SRSR radiation contribution reduces as the number of reflection increases .

The models of the sea surface emissivity and reflectivity are built based on these phenomena. In the infrared atmospheric transmission windows ($\lambda \in [3, 5]$ and $[8, 12]$ μm), the Geometric Optics approximation (GO) is usually employed. The geometric optics approximation (GO) is valid if [5]:

$$2\pi\rho_c \cos^3 \chi \gg \lambda \tag{1.1}$$

with λ being the studied wavelength and ρ_c being the surface local radius of curvature. χ is the local angle of incidence, corresponding to the angle between the normal to the facet and the observation direction (see Fig. 1.5). In the infrared domain, λ is of the order of 10 μm. The surface local radius of curvature ρ_c of capillary waves of the sea surface is of the order of several millimeter to several centimeter [6]. Take $\rho_c = 1$ cm for example, Eq. (1.1) is valid for $\cos\chi \gg 0.025$, which corresponds to a local incidence angle close to $90°$ ($\cos 88.5° \approx 0.025$). As a result, Geometrical Optics approximation is widely used in the modeling of the sea surface infrared emissivity and reflectivity [7, 6, 1, 8–13].

In this chapter, the research background of sea surface infrared emissivity and reflectivity is reviewed. As the sea surface is modeled as a random process, in section 1.1, the statistical characteristics of the sea surface are summarized. In section 1.3, the study of the sea surface infrared emissivity is summarized, and in section 1.4, the models of the sea surface infrared reflectivity are reviewed.

1.1 Statistical characteristics of sea surfaces

1.1.1 Sea surface waves

Sea surface waves are the movement of the ocean's water due to the oscillation of water particles by the friction of the wind over the water surface.

On a perfectly calm sea, the wind has almost no grip. As the wind slides over the water surface film, the water moves, and small ripples (wave with small wavelength, or capillary wave) are formed. The ripples make the water's surface rough, giving the wind a better grip. They grow with the increase of the wind speed. The rougher the water becomes, the easier it is for the wind to transfer its energy. When the wind blows a sufficiently long distance (called fetch) along the same direction, the waves it created reach maximum size, speed and wavelength. This is called a fully developed sea. In this area, the waves have long wavelength, and are called gravity waves.

To sum up, the sea surface waves consist of gravity waves and capillary waves. Gravity waves have large wavelengths (of the order of meters), which is determined by the horizontal distance between two crests or two troughs. Capillary waves have much smaller wavelengths, which is of the order of several millimeters to several centimeters [6].

Wind waves have a certain amount of randomness: subsequent waves differ in height, duration and shape, with a limited predictability. They are usually described as a random process [4]. For very high wind speeds, white caps and breaking waves appear. These phenomena increase the difficulty in modeling the sea surface, but these are ignored in this thesis.

1.1.2 Review on random process

The sea surface is usually model as a random process. A random process can be represented as a collection of random variables $x(t, \xi)$ on the evolution over time [46]. If $\xi = \xi_i$ is fixed, $x(t, \xi) = x(t, \xi_i)$ is a time function. If $t = t_i$ is fixed, $x(t, \xi) = x(t_i, \xi)$ is a random variable. For example, a sea surface can be modeled as a collection of surface heights, which are random variables of their location, changing over time. This subsection reviews some of the properties of statistics used later in this thesis.

1.1.2.1 Expected value

As opposed to other mathematical variables, a random variable conceptually does not have a single, fixed value. Instead, it can take on a set of possible different values, each with an associated probability. The expected value of a random variable is obtained by:

$$E(x) = \langle x_i \rangle \,, \tag{1.2}$$

where $\langle \cdots \rangle$ represents the statistical average.

1.1.2.2 Autocorrelation

The autocorrelation of a random process describes the correlation between values of the process at different points in time. Let x_i be the realization of a run of the process at time t_i. The autocorrelation of the random process between times t_1 and t_2 is given by [4]:

$$R(t_1, t_2) = E(x_1(t_1, \xi) x_2(t_2, \xi)) = \int\int x_1 x_2 p(x_1, t_1, x_2, t_2) \, \mathrm{d}x_1 \, \mathrm{d}x_2 . \tag{1.3}$$

A random process is call stationary if its autocorrelation function does not depend on both t_1 and t_2, but only on their time difference $\tau = t_1 - t_2$.

1.1.2.3 Ergodicity

A random process $x(t, \xi)$ is called ergodic if the time average equals to the statistical mean [4]:

$$\overline{x} = \lim_{T\to\infty} \frac{1}{2T} \int_{-T}^{T} x(t, \xi_i) \, \mathrm{d}t = \int x(t_i, \xi) p(x) \, \mathrm{d}x \tag{1.4}$$

The sea surface is usually modeled as a stationary ergodic random process, whose behavior is mainly determined by its spectrum or autocorrelation function, and its slope probability density [47]. In what follows, the studies of the sea surface height and slope probability density, and the autocorrelation function are summarized.

1.1.3 Surface height and slope PDFs

1.1.3.1 Gaussian distribution

Because of the limited predictability of the ocean surface, the sea surface is modeled as a random process. It is reported that a natural surface has a height distribution very close to a Gaussian distribution [14]. The probability density function (PDF) of the sea surface height ζ is usually assumed to be Gaussian with zero mean:

$$p_\zeta(\zeta) = \frac{1}{\sqrt{2\pi}\sigma_\zeta} \exp\left(-\frac{\zeta^2}{2\sigma_\zeta^2} \right) , \tag{1.5}$$

where σ_ζ is the Root Mean Square (RMS) of the surface height.

As the surface height distribution is Gaussian, the surface slope, which is the derivative of the surface height, has also a Gaussian PDF with zero mean, given by [10, 13, 15]:

$$p_\gamma^{\mathrm{G}}(\gamma_x,\gamma_y)=\frac{1}{2\pi\sigma_{\gamma_x}\sigma_{\gamma_y}}\exp\left(-\frac{\gamma_x^2}{2\sigma_{\gamma_x}^2}-\frac{\gamma_y^2}{2\sigma_{\gamma_y}^2}\right), \tag{1.6}$$

where σ_{γ_x} and σ_{γ_y} are the RMS slope in the up-wind and cross-wind directions, respectively. For 1D surfaces, the Gaussian slope PDF with zero mean is given by:

$$p_\gamma^{\mathrm{G}}(\gamma)=\frac{1}{\sqrt{2\pi}\sigma_\gamma}\exp\left(-\frac{\gamma^2}{2\sigma_\gamma^2}\right), \tag{1.7}$$

There are several researches [16, 17] in the literature that calculate the surface RMS slopes. In this thesis, the result of Cox & Munk is used, which relates the surface RMS slope to the wind speed u_{12} at 12.5 m above the sea surface as [17]:

$$\begin{array}{rcl}\sigma_{\gamma_x}^2 &=& 3.16\times10^{-3}u_{12}\pm0.004,\\ \sigma_{\gamma_y}^2 &=& 1.92\times10^{-3}u_{12}+0.003\pm0.004,\end{array} \tag{1.8}$$

where "±" corresponds to the error of measurement. In the simulations of this thesis, the measurement error is not considered.

1.1.3.2 Non-Gaussian slope distribution

By measuring the sun glitter of the sea surface, Cox & Munk [17] pointed out that the real sea surface slope PDF is slightly different from a Gaussian zero mean distribution.

Cox & Munk derived the non-Gaussian surface slope PDF as the successive sums of Gram-Charlier series up to the fourth order. It is expressed as [17]:

$$\begin{array}{rcl}p_\gamma^{\mathrm{non-G}}(\gamma_x,\gamma_y) &=& \dfrac{1}{2\pi\sigma_{\gamma_x}\sigma_{\gamma_y}}\exp\left(-\dfrac{\gamma_x^2}{2\sigma_{\gamma_x}^2}-\dfrac{\gamma_y^2}{2\sigma_{\gamma_y}^2}\right)\\ && \times\Big[1+\dfrac{c_{21}}{2}(\Gamma_y^2-1)\Gamma_x+\dfrac{c_{03}}{6}(\Gamma_x^2-3)\Gamma_x\\ && +\dfrac{c_{22}}{4}(\Gamma_x^2-1)(\Gamma_y^2-1)+\dfrac{c_{40}}{4}(\Gamma_y^4-6\Gamma_y^2+3)\\ && +\dfrac{c_{04}}{24}(\Gamma_x^4-6\Gamma_x^2+3)\Big],\end{array} \tag{1.9}$$

where

$$\begin{array}{rcl}\Gamma_{x,y} &=& \dfrac{\gamma_{x,y}}{\sigma_{\gamma_x,\gamma_y}},\\ c_{21} &=& (0.86u_{12}-1\pm3)10^{-2},\\ c_{03} &=& (3.3u_{12}-4\pm12)10^{-2},\\ c_{04} &=& 0.23\pm0.41,\\ c_{40} &=& 0.40\pm0.23,\\ c_{22} &=& 0.12\pm0.06,\end{array} \tag{1.10}$$

in which "±" corresponds to the error of measurement. In the simulations of this thesis, the error of measurement will not be considered.

The parameters c_{21}, c_{03} are the skewness coefficients, and c_{04}, c_{40}, c_{22} are the kurtosis coefficients. These parameters were calculated from the data of the measurements of the sun glitter on the sea surface [17].

The skewness coefficients correspond to the asymmetry of the distribution of the sea surface slope PDF. It means that the sea surface is anisotropic. The properties of the sea surface depends on the observation direction. The asymmetry of the surface slope distribution is called the skewness effect in the following of this thesis.

Kurtosis is another parameter in measuring of the distribution shape. It correspond to the "peakedness" of the probability distribution [48]. A high kurtosis distribution has a sharper peak, while a low kurtosis distribution has a more rounded peak. The "peakedness" is called the kurtosis effect in the following of this thesis.

Basing on the non-Gaussian slope PDF derived by Cox and Munk, Bourlier *et al.* [32] derived the marginal slope PDF of the sea surface along the direction X which forms an angle ϕ with the up-wind direction (x direction). It is given by [32]:

$$\begin{aligned} p_\gamma(\gamma_X) &= \frac{1}{\sigma_{\gamma_X}\sqrt{2\pi}} \exp\left(-\frac{\gamma_X^2}{2\sigma_{\gamma_X}}\right) \\ &\times \left[1 + \alpha_K\left(1 - 2\frac{\gamma_X^2}{\sigma_{\gamma_X}^2} + \frac{\gamma_X^4}{3\sigma_{\gamma_X}^4}\right) + \alpha_S\left(\frac{\gamma_X}{3\sigma_{\gamma_X}} - \frac{\gamma_X^3}{3\sigma_{\gamma_X}^3}\right)\right], \end{aligned} \tag{1.11}$$

where γ_X is the surface slope along the X direction and σ_{γ_X} is the RMS slope along the X direction. The parameters α_S and α_K relate to the skewness and kurtosis effects, respectively. They are given by:

$$\left\{ \begin{aligned} \alpha_S(\phi) &= \frac{-\sigma_X \cos\phi}{2\sigma_X^3}\left[c_{03}(\sigma_x\cos\phi)^2 + 3c_{21}(\sigma_y \sin\phi)^2\right], \\ \alpha_K(\phi) &= \frac{1}{8\sigma_X^4}\left[c_{04}(\sigma_x\cos\phi)^4 + c_{40}(\sigma_y\sin\phi)^4 + \frac{3}{2}c_{22}\sigma_x^2\sigma_y^2\sin^2(2\phi)\right], \\ \sigma_{\gamma_X}^2(\phi) &= (\sigma_{\gamma_x}\cos\phi)^2 + (\sigma_{\gamma_y}\sin\phi)^2. \end{aligned} \right. \tag{1.12}$$

From Eqs. (1.11) and (1.12), it is notable that the skewness effect relates to the odd-order terms and the kurtosis effect relates to the even-order terms. In other words, the skewness effect corresponds to the asymmetry of the sea slope PDF about the axis $\gamma_X = 0$. Taking into account the kurtosis effect does not change the symmetry of the shape of the distribution about $\gamma_X = 0$ [32]. This is consistent with the definition of skewness and kurtosis.

Fig. 1.3 shows the sea surface marginal slope PDF in the up-wind direction ($\phi = 0°$). Gaussian PDF (G), Gaussian PDF plus skewness effect (GS), Gaussian PDF plus kurtosis effect (GK), and Gaussian PDF plus skewness and kurtosis effects (GSK) are compared. The wind speed at 12.5 m above the sea surface is set to $u_{12} = 10$ m/s.

It is shown in Fig. 1.3 that the GK PDF is symmetrical about $\gamma_X = 0$. Besides, the slope distribution is sharper around $\gamma_X = 0$. After taking the skewness effect into account, the slope PDF is no longer symmetry, which checks the definition of the skewness effect (see the GS and GSK curves).

For a Gaussian slope PDF, $\alpha_S = 0$, $\alpha_K = 0$, and $\sigma_{\gamma_X}(n\pi/2+\phi) = \sigma_{\gamma_X}(n\pi/2-\phi)$ hold for $n = 0, 1, 2, \cdots$. As a result, the Gaussian slope PDF is symmetrical about the up-wind, down-wind and cross-wind directions ($\phi = \{0°, 90°, 180°, 270°\}$).

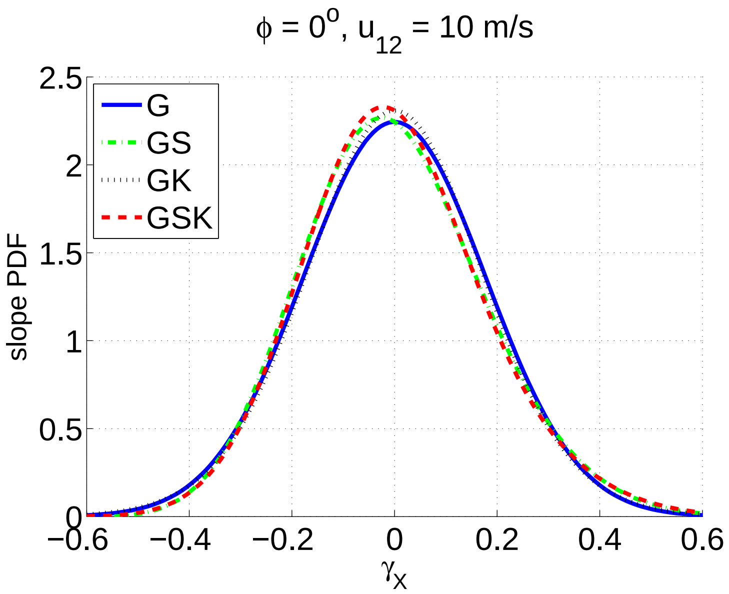

Figure 1.3: Gaussian and non-Gaussian slope of a sea surface. The skewness effect corresponds to the asymmetry and the kurtosis effect corresponds to the peakedness.

For a non-Gaussian slope PDF, it is notable that $\alpha_{S,K}(n\pi+\phi)=\alpha_{S,K}(n\pi-\phi)$ and $\sigma_{\gamma_X}(n\pi+\phi)=\sigma_{\gamma_X}(n\pi-\phi)$ hold for $n=0,1,2,\cdot$, implying that the non-Gaussian slope PDF is symmetrical about the up-wind and down-wind directions ($\phi=\{0°,180°\}$).

1.1.4 Surface autocorrelation

1.1.4.1 Surface height autocorrelation function

Knowing the PDF of the heights and slopes of the surface is usually not sufficient, as the heights and slopes of two points of the surface may affect each other (correlated) if they are close enough. The aim of this subsection is to define the height autocorrelation function of the sea surface which completes the modeling of the sea surface.

For a stationary random surface, the surface height autocorrelation function is defined as:

$$R(\tau)=E(X_iX_{i+\tau}), \tag{1.13}$$

where τ is the distance between any two surface points.

The height autocorrelation function of the sea surface can be calculated by the sea surface spectrum [4]. The study of sea surface spectrum has received wide attention [18, 16, 19]. The spectrum of Elfouhaily *et al.* [16] took into account both gravity and capillary waves of the sea surface, and it may be the most widely used in domains related to sea surface.

To be more simple, it is also assumed that the surface height autocorrelation function is Gaussian or Lorentzian [20, 4]. In this thesis, the surface height autocorrelation function is assumed to be Gaussian, given by:

$$R(\tau)=\sigma_\zeta^2\exp\left(-\frac{\tau^2}{L_c^2}\right), \tag{1.14}$$

where σ_ζ is the surface Root Mean Square (RMS) height, and L_c is the surface correlation length which corresponds to the horizontal distance that the correlation between the heights of two points is reduced by e^{-1}.

To be more general, Eq. (1.14) is normalized as:

$$R_{\text{nor}}(\tau) = \frac{R(\tau)}{\sigma_\zeta^2} = \exp\left(-y^2\right), \tag{1.15}$$

where

$$y = \frac{\tau}{L_c}. \tag{1.16}$$

Fig. 1.4 shows the normalized Gaussian autocorrelation function. It is shown that R_{nor} decreases with the increase of $|y|$. For $|y| > 3$, $R_{\text{nor}} \approx 0$, which means that any two surface points of horizontal distance larger than 3 times the correlation length can be assumed to be uncorrelated.

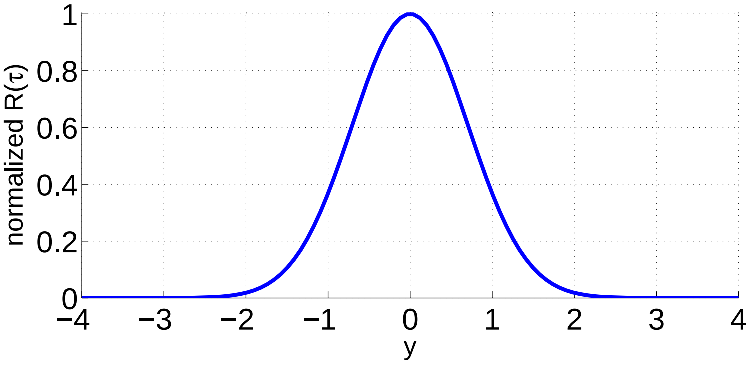

Figure 1.4: Normalized Gaussian height autocorrelation function. For $y > 3$, $R_{\text{nor}} \approx 0$, thus the correlation can be ignored.

This Gaussian height autocorrelation function is used to generate random rough sea surfaces which are used later in a Monte Carlo ray-tracing method. It is also used to determined the correlated height and slope PDF of the sea surface. With a sea spectrum, the sea surface height autocorrelation function and the correlated height and slope PDF can also be derived, as shown by Bourlier & Berginc [21]. A sea spectrum is not used in this thesis. Firstly, because the Gaussian height autocorrelation function is simpler in form, while the use of the sea spectrum requires additional numerical integrations to calculate the correlated illumination function. Secondly, it is proved that the model of sea surface emissivity with Gaussian height autocorrelation function agreed well with measurements [22], showing that Gaussian height autocorrelation function is a good approximation.

1.1.4.2 Correlated PDF of heights and slopes

As the surface heights of two surface points are correlated, the correlated PDF of the surface heights and slopes $p(\zeta, \gamma | \zeta_0, \gamma_0; \tau)$ has to be derived in order to take into account this correlation. This is an important parameter in the calculation of the illumination function (see Chap. 2).

It is assumed that the sea surface is modeled as a stationary Gaussian correlated process. The conditional probability of the heights and slopes of two points separated by a horizontal distance τ is given by [4, 20]:

$$\begin{aligned} p(\zeta,\gamma|\zeta_0,\gamma_0;\tau) &= \frac{p(\zeta,\gamma,\zeta_0,\gamma_0;\tau)}{p(\zeta_0,\gamma_0)} \\ &= \frac{\sigma_\zeta\sigma_\gamma}{2\pi\sqrt{|[C]|}}\exp\left[-\frac{1}{2}\boldsymbol{V}^T[C]^{-1}\boldsymbol{V}+\frac{\zeta^2}{2\sigma_\zeta^2}+\frac{\gamma^2}{2\sigma_\gamma^2}\right], \end{aligned} \tag{1.17}$$

where $\boldsymbol{V}$ is the vector containing all the variables

$$\boldsymbol{V}^T = [\zeta_0,\zeta,\gamma_0,\gamma], \tag{1.18}$$

and $[C]$ is the covariance matrix

$$[C] = \begin{bmatrix} \sigma_\zeta^2 & R_0(\tau) & 0 & R_1(\tau) \\ R_0(\tau) & \sigma_\zeta^2 & -R_1(\tau) & 0 \\ 0 & -R_1(\tau) & \sigma_\gamma^2 & -R_2(\tau) \\ R_1(\tau) & 0 & -R_2(\tau) & \sigma_\gamma^2 \end{bmatrix}, \tag{1.19}$$

in which $R_0(\tau)$ is the autocorrelation function of the surface heights. Here the Gaussian autocorrelation function (Eq. (1.14)) is employed. $R_1(\tau)$ and $R_2(\tau)$ are the first and second derivatives of $R_0(\tau)$, respectively, given by[20]:

$$\begin{aligned} R_1(\tau) &= -\frac{2\sigma_\zeta^2}{L_c^2}\tau\exp\left(-\frac{\tau^2}{L_c}\right), \\ R_2(\tau) &= -\frac{2\sigma_\zeta^2}{L_c^2}\left(1-2\frac{\tau^2}{L_c^2}\right)\exp\left(-\frac{\tau^2}{L_c}\right). \end{aligned} \tag{1.20}$$

For a Gaussian autocorrelation function $R(\tau)$, the surface slope variance relates to the surface height variance by:

$$\sigma_\gamma^2 = -R_2(0) = \frac{2\sigma_\zeta^2}{L_c}. \tag{1.21}$$

For $\tau = 0$ (the two points overlap), the covariance matrix is simplified as:

$$[C]_{\tau=0} = \begin{bmatrix} \sigma_\zeta^2 & \sigma_\zeta^2 & 0 & 0 \\ \sigma_\zeta^2 & \sigma_\zeta^2 & 0 & 0 \\ 0 & 0 & \sigma_\gamma^2 & \sigma_\gamma^2 \\ 0 & 0 & \sigma_\gamma^2 & \sigma_\gamma^2 \end{bmatrix}. \tag{1.22}$$

It is notable that $[C]_{\tau=0}$ is not invertible. As a result, the height and slope of the same point are usually assumed to be uncorrelated.

1.2 Definition of emissivity and reflectivity

The intrinsic thermal radiation of a body is characterized by two quantities: its emissivity and the spectral radiance of a blackbody. Emissivity is a measurement of a material's ability to radiate absorbed energy. For any material, its radiation intensity $L(\lambda,T,\theta)$ is equal to that of a blackbody $B(\lambda,T)$, which would radiate at the same temperature, multiplied by a coefficient named emissivity $\varepsilon(\lambda,T,\theta)$, given by:

$$L(\lambda,T,\theta) = \varepsilon(\lambda,T,\theta)B(\lambda,T). \tag{1.23}$$

Then, emissivity of a sea surface depends on the wavelength, on the sea state (temperature T, roughness), and on the radiation angle θ. Since it ranges from 0 to 1, the radiation of the real body is always inferior to that of a blackbody at the same temperature.

For an incident wave propagating toward another medium, its power E_i is divided into three parts: reflection E_r, absorption E_a and transmission E_t. The conservation of the energy implies:

$$E_i = E_r + E_a + E_t. \tag{1.24}$$

The reflectivity (ρ), absorptivity (α), and transmissivity (t) are defined as the portion of energy reflected, absorbed and transmitted by the medium, respectively, given by:

$$\rho = \frac{E_r}{E_i}, \qquad \alpha = \frac{E_a}{E_i}, \qquad t = \frac{E_t}{E_i}. \tag{1.25}$$

Accordingly, we obtain:

$$\rho + \alpha + t = 1.$$

The blackbody is defined by $\alpha = 1$, which means all the received energy is absorbed.

Under thermal equilibrium condition, the emissivity of a body is equal to its absorptivity (Kirchoff's law):

$$\varepsilon = \alpha. \tag{1.26}$$

Consequently, the emissivity of an opaque body (no energy can be transmitted through the medium, $t = 0$) is:

$$\varepsilon = 1 - \rho. \tag{1.27}$$

Under GO, specular reflections are considered and no diffusion (that is, reflection rays spread out to a angular region around the specular direction) occurs. Fig. 1.5 shows a specular reflection on a flat surface. The medium is assumed to be opaque, thus all the energy of the refracted ray are absorbed.

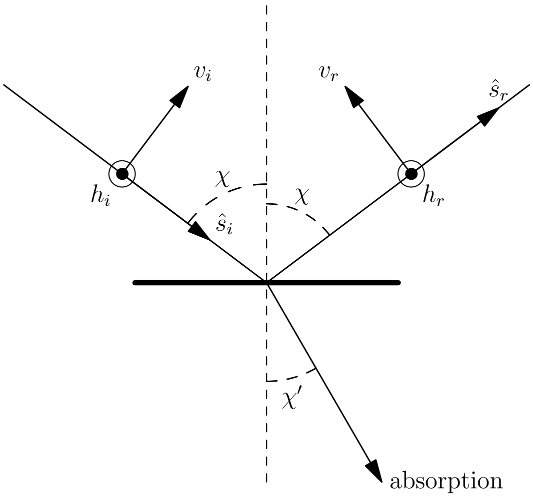

Figure 1.5: Specular reflection on a flat surface.

The intensity of the reflected ray L_r is related to the intensity of the incident ray L_i by:

$$L_r = |r_{H,V}(\chi)|^2 L_i, \tag{1.28}$$

where χ is the local angle of incidence, and $r_{H,V}$ are the Fresnel reflection coefficients in horizontal (H, the electric vector is perpendicular to the plane of incidence) and vertical (V, the electric vector is parallel to the plane of incidence) polarizations, given by:

$$\begin{aligned} r_H(\chi) &= \frac{\cos\chi - \widetilde{n}\cos\chi'}{\cos\chi + \widetilde{n}\cos\chi'}, \\ r_V(\chi) &= \frac{\widetilde{n}\cos\chi - \cos\chi'}{\widetilde{n}\cos\chi + \cos\chi'}, \end{aligned} \tag{1.29}$$

where $\widetilde{n}$ is the complex index of refraction of the sea water, and χ' is the local angle of refraction given by Snell's law:

$$\sin(\chi') = \frac{\sin(\chi)}{\widetilde{n}}. \tag{1.30}$$

According to Eqs. (1.27) and (1.28), the directional infrared reflectivity ρ and emissivity ε of a flat opaque surface is given by [23, 10, 9, 6]:

$$\begin{aligned} \rho(\chi) &= |r_{H,V}(\chi)|^2 \\ \varepsilon(\chi) &= 1 - |r_{H,V}(\chi)|^2 \end{aligned} \tag{1.31}$$

Eq. (1.31) is the emissivity ε and reflectivity ρ of a flat surface. The models of ε and ρ for rough surfaces are developed based on Eq. (1.31), which is reviewed in the next section.

1.3 Models of sea surface emissivity

Sea surface infrared emissivity in the atmospheric transmission windows is an important parameter in oceanic remote sensing. Except for the usage in predicting the surface-leaving radiance, sea surface infrared emissivity plays an important role in various fields of environment studies, such as earth temperature measurement, weather forecasting and pollution study. As a passive infrared receiver simply receives the natural radiation of the target and does not send out any signal, it is highly stealth and has military use.

The development of the oceanic infrared remote sensing requires that the sea surface infrared emissivity is calculated with high accuracy. Many researches have been devoted to determining the sea surface infrared emissivity.

Sea surface infrared emissivity is nearly constant for observation directions θ near zenith, but it varies significantly for grazing angles (that is, the receiver near the horizon, or θ is close to $90°$). In these observation directions, shadowing and surface reflections become significant, increasing the difficulty in predicting the sea surface emissivity with accuracy.

1.3.1 Emissivity with shadowing effect

Early models of sea surface infrared emissivity derived the emissivity without considering sea surface reflections (named direct emissivity, or zero-order emissivity contribution). By contrast, the shadowing effect was usually considered.

As the sea surface varies in time and in space, it is of limited predictability. As a result, sea surfaces are usually modeled as ergodic random processes. Under geometric optics approximation, the average emissivity of the surface point of interest is usually estimated by the average emissivity of the whole surface, given by [23, 24, 10, 6]:

$$\varepsilon_0(\theta) = \left\langle [1 - |r|^2] g_0 \right\rangle , \tag{1.32}$$

where the symbol $\langle \cdots \rangle$ stands for the statistical average over the random variables. The term $1 - |r|^2$ is the local emissivity of the point of interest, and the term g_0 results from projecting the area around this point onto the orthogonal direction of the direction of observation. Eq. (1.32) is the basic idea of the sea surface infrared emissivity modeling.

However, the main problem of Eq. (1.32) is that the shadowing effect (see Fig. 1.2 (a)) is not considered. Without considering the shadowing effect, the sea surface emissivity ε_0 obtained by Eq. (1.32) exceeds 1 and tends to infinity for large zenith angles θ (see Fig. (3.2)) [10], which is not physical. This is because the radiance of the points in shadow are included in Eq. (1.32), which do not actually contribute to the radiation field.

Much effort has been devoted to developing an illumination function (or call shadowing function [1]) to take into account the shadowing effect. The illumination function which takes shadowing effect into account is called monostatic zero-order illumination function [26], denoted as S^0_{M}, where the subscript "M" stands for the monostatic configuration (only one receiver is used), and the superscript "0" stands for that no surface reflection is considered. It gives the probability that an arbitrary point of the surface is seen by the receiver. With the monostatic illumination function, the direct emissivity of the sea surface is calculated by:

$$\varepsilon_0(\theta) = \left\langle [1 - |r|^2] g_0 S^0_{\mathrm{M}} \right\rangle . \tag{1.33}$$

Some properties of the illumination function can be predicted. For normal observation direction, that is, the receiver is located in the zenith direction $\theta = 0°$, all points of the surface are seen by the receiver, meaning that the monostatic zero-order illumination function $S^0_{\mathrm{M}} = 1$. On the other hand, if the receiver is located at the horizon, $S^0_{\mathrm{M}} = 0$ because all the surface are in the shadow of the receiver.

The shadowing effect has been studied from early 1960s. Several models of statistical illumination functions can be found in the literature, which are summarized in the following of this section.

1.3.1.1 Ray-tracing model

The most straight forward method is the one of Brockelman & Hagfors [27], which is a numerical Monte Carlo ray-tracing method. In this method, a lot of random rough surfaces was generated, over which ray-tracing was performed. Incident rays were sent along a given observation direction (θ) and were traced to find out the surface points in shadow and the ones seen by the receiver (see Fig. 2.7 for example). The monostatic illumination function S^0_{M} was given by (the definition of symbols are modified):

$$S^0_{\mathrm{M}}(\theta) = \frac{N_j}{N_s}, \tag{1.34}$$

---

[1] The illumination function was originally called "shadowing" function ([3, 25]). But as the word "shadowing" leads to confusion when surface reflections are considered, more recent models named it "illumination" function ([15, 22]).

where N_j was the number of points seen by the receiver, and N_s was that of the total surface. Here, S_{M}^0 did not give the probability that an arbitrary point was seen by the receiver. Instead, it gave the proportion of the surface seen by the receiver.

This idea was adopted and developed by Bourlier *et al.* [20, 26]. Bourlier *et al.* used the same ray-tracing algorithm to find the points seen by the receiver, but instead of simply calculating the proportion of the surface seen by the receiver, Bourlier *et al.* also calculated the histograms of the heights and the slopes of the points seen by the receiver.

The methods of Brockelman & Hagfors [27] is usually used as a reference to check the accuracy of other analytical methods [25, 3, 28].

1.3.1.2 Statistical models

The model of Beckmann [29] is one of the earliest model of statistical illumination function. The illumination function S_{M}^0 was solved by a differential equation (see Eq. (2.11) in Chap. 2), which gives the probability that the point of interest is seen by the receiver.

Ricciardi & Sato [30, 31] showed that the shadowing function was rigorously defined by the Rice's infinite series, in which integrations were involved. For an uncorrelated Gaussian process, a closed-form expression of the series can be obtained, but the results were unphysical for grazing angles because the correlation was neglected [26]. Taking into account the correlation may overcome this problem, but it was impossible to obtain a closed-form of the series (requires numerical integration).

The model of Wagner [3] equaled the first term of the series of Ricciardi & Sato [30, 31], which was physical for grazing angles. The model of Smith [25] was developed based on that of Wagner [3], but was stricter in mathematics and physics. As the models of Wagner and Smith are widely used, they are reviewed in detail in Sec. 2.1.3.

Bourlier *et al.* [26] compared the models of Ricciardi & Sato [30, 31] , Wagner [3] and Smith [25]. They concluded that, the model of Ricciardi & Sato is the less accurate, as it was not physical for grazing observation angles. The model of Smith was the most accurate, because the results of the Smith illumination function agreed with the Monte Carlo ray-tracing result the best.

Many models of sea surface emissivity are developed with the above analytical S_{M}^0 models. The model of Yoshimori *et al.* [6, 7] calculated the sea surface infrared emissivity, where shadowing was taken into account by using the Smith illumination function [25]. In the model of Bourlier *et al.* [32], the Smith illumination function [25] was used. They took a step forward by considering a non-Gaussian surface slope distribution introduced by Cox & Munk [17], which takes the skewness and kurtosis effects into account. Caillault *et al.* [33] and Fauqueux *et al.* [24] both developed multi-resolution models of sea infrared emissivity, in which the Smith illumination function was used.

1.3.1.3 Models with normalization factor

Instead of using a statistical illumination function, Saunders [34] and Masuda *et al.* [10] introduced normalization factors to take into account the shadowing effect. These two normalization factors are almost the same and are also widely used because of their simplicity. They are reviewed in detail in Sec. 2.1.4 and compared with the Smith illumination function [25].

Masuda *et al.* [10] calculated the unpolarized sea surface infrared emissivity by modeling the sea as a two-dimensional (2D surface, 3D problem) surface with Gaussian surface slope distribution. Because ignoring the shadowing effect, Eq. (1.32) leads to infinity as θ closes $90°$, Masuda *et al.* calculated the sea surface emissivity by dividing Eq. (1.32) by a normalization factor:

$$\varepsilon_0(\theta) = \frac{\langle [1 - |r|^2] g_0 \rangle}{\langle g_0 \rangle}. \tag{1.35}$$

The normalization factor $\langle g_0 \rangle$ was used to estimate the shadowing effect, and

$$p(\theta) = \frac{1}{\langle g_0 \rangle} \tag{1.36}$$

played the role of an illumination function.

The normalization factor of Masuda *et al.* [10] is widely adopted. Freund *et al.* [35] followed the same idea as Masuda *et al.* [10] and used a similar normalization factor to estimate the influence of shadowing. After that the sea surface emissivity was calculated by an hemispherical ensemble average. Shaw and Marston [36] calculated the polarized sea surface infrared emissivity following the model of Masuda *et al.* [10].

In practice, the accuracy of sea surface emissivity is important. It is report that a difference of of 3×10^{-3} in surface emissivity could result in a difference of 0.5 K when estimating the surface temperature [1]. However, this accuracy is not achieved by direct emissivity models. Indeed, compared with experimental data obtained by Smith *et al.* [37] and Niclòs *et al.* [38], the direct emissivity model of Masuda *et al.* [10] shows a difference of about $2 - 3 \times 10^{-2}$ at large observation angles ($\theta \gtrsim 60°$). As a result, it is necessary to take the emissivity with surface reflections into account.

1.3.2 Emissivity with surface reflections

It is also possible that the emission ray from an arbitrary surface point intersects the surface and is then reflected toward the receiver, as shown in Fig. 1.2 (b). This is known as the surface reflections, and the corresponding emissivity is called surface-emitted surface-reflected (SESR) emissivity.

To calculate the sea surface infrared emissivity with higher accuracy, several authors tried to include surface reflections in their emissivity models. The main difficulty in taking this effect into account lies in the derivation of the probability of observing surface reflections. In what follows, the major models are summarized.

1.3.2.1 Ray-tracing model

The most straightforward model is the numerical model of Henderson *et al.* [13]. In this model, a ray-tracing Monte Carlo algorithm was used to calculate the sea surface emissivity with up to 10 surface reflections. Many random rough surfaces were generated, over which ray-tracing were performed. The surface points leading to surface reflections were then found (see Fig. 2.15 for example). The surface emissivity with reflections was calculated accordingly.

This method is very similar to that of Brockelman & Hagfors [27], except that surface reflections are considered. This method gives reliable results and is an important reference of other analytical models [15, 11]. The drawback is that the computation time is long (usually, hours for one observation direction for an ordinary office PC).

1.3.2.2 Empirical models with cut-off angles

Watts *et al.* [39] and Wu & Smith [1] both defined the probability of observing surface reflections empirically, by defining an ambiguous cut-off angle measured from zenith, illustrated in Fig. 1.6.

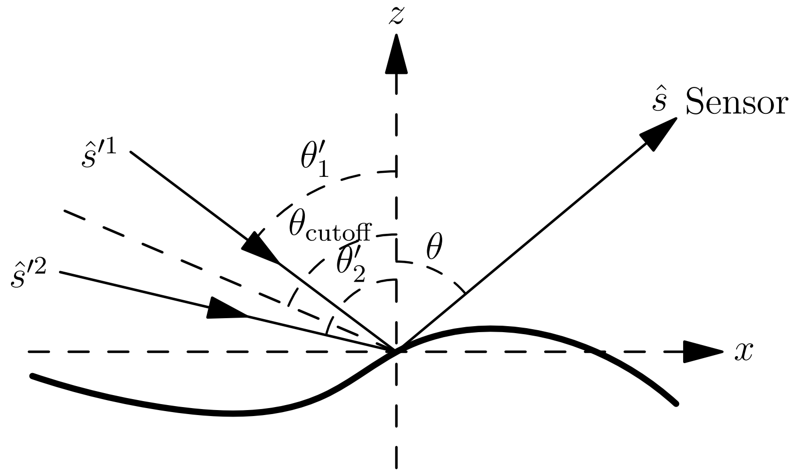

Figure 1.6: Surface reflection and cut-off angle.

Fig. 1.6 shows two incident rays, noted as $\hat{s}'^1$ and $\hat{s}'^2$, reflected by some surface point to the receiver direction. If the incident ray is emitted by another point of the surface, the reflected ray $\hat{s}$ contributes to the surface-emitted surface-reflected (SESR) emissivity. The main task is the determination of the probability P that the incident ray originates from the sea surface.

To do so, Watts *et al.* [39] defined a cut-off angle θ_{cutoff} (Eq. (2.8) of [39]) to calculate the probability P. For angle of incidence less than θ_{cutoff}, Watts *et al.* defined that the incident ray originated from the sky (sun light, atmosphere emission, etc), e.g. the incident ray $\hat{s}'^1$ in Fig. 1.6. Otherwise the incident ray was assumed to originate from the surface, e.g. the incident ray $\hat{s}'^2$ in Fig. 1.6. The mathematical expression of P was then given by:

$$P = \begin{cases} 1, & \text{if} \quad \theta' > \theta_{\text{cutoff}} \\ 0, & \text{if} \quad \theta' < \theta_{\text{cutoff}} \end{cases} . \tag{1.37}$$

Watts *et al.* calculated the cut-off angle as a function of the surface wave height and the surface wavelength. They pointed out that θ_{cutoff} is between $79°$ and $89.9°$.

Wu & Smith [1] used nearly the same method. The only difference was that two cut-off angles were defined, with one being $90°$ and the other being $85°$. They defined that the rays with $\theta' < 85°$ originate from the sky, and the rays with $\theta' > 90°$ originate from the surface. For rays with $85° \leq \theta' \leq 90°$, the probability that they originate from the surface was given empirically. The mathematical expression of

P was then given by (Eq. (23) of [1]):

$$P = \begin{cases} 1, & \text{if} \quad \theta' > 90^\circ \\ 1 - (\theta' - 85^\circ)^2/25, & \text{if} \quad 85^\circ \leq \theta' \leq 90^\circ \\ 0, & \text{if} \quad \theta' < 85^\circ \end{cases} . \tag{1.38}$$

It is difficult to define properly the cut-off angles, and the obtained emissivity heavily depends on the definition of the cut-off angles. Watts *et al.* showed that the sea surface emissivity with one surface reflection with $\theta_{\text{cutoff}} = 85^\circ$ and 90° differed from each other by about 2.5×10^{-3} for moderate surface wind speed u_{12}. This difference increased with the increase of the surface wind speed u_{12} (see Fig. 5 of [39]).

1.3.2.3 Models with weighting function

To avoid defining an exact cut-off angle, Masuda [11] calculated the first-order emissivity (SESR, one reflection) by using a weighting function. This weighting function weighted the probability that an incident ray $\hat{s}'$ with an angle of incidence θ' originated from the sea surface. It was developed based on the normalization factor of Masuda *et al.* [10], given by [2] [11]:

$$P = \begin{cases} 1, & \text{if} \quad \theta' \geq 90^\circ \\ 1 - p(\theta'), & \text{if} \quad \theta' < 90^\circ \end{cases} , \tag{1.39}$$

where $p(\theta')$ is the Masuda illumination function given by Eq. (1.36) [10].

In the region where $\theta' < 90^\circ$, the Masuda illumination function $p(\theta')$ represented approximately the probability that one point of the surface was viewed by the receiver. Thus, the weighting function gave approximately the probability that the ray $\hat{s}'$ originated from the surface.

However, as the Masuda illumination function did not represent the true statistical probability, besides, $p(\theta')$ did not hold for $\theta' > 90^\circ$, the performance of the weighting function is in doubt. It was shown that the first-order emissivity calculated by Masuda *et al.* [11] with this weighting function did not agree well with the result of a Monte Carlo ray-tracing method [22]. Li *et al.* [22] calculated the first-order sea surface emissivity with a Monte Carlo ray-tracing algorithm, and found that the first-order emissivity tended to zero when the zenith observation θ tended to 90°. The result of Masuda *et al.* at $\theta = 90^\circ$ was about 0.02, which is far larger than the precision requisition (0.3×10^{-3}).

Nalli *et al.* [9] shared the idea of Masuda [11] and developed a new weighting function to calculate the first-order emissivity contribution, by replacing the shadowing term used in [11] by that of Saunders *et al.* [34].

1.3.2.4 Statistical models

More rigorously, Bourlier *et al.* [15, 26] evaluated the first-order emissivity contribution by developing a statistical first-order illumination function S^1_{M} (with one reflection), which estimated the probability that a surface-emitted ray was reflected once by another surface point into the observation direction.

---

[2] The definition of symbols is modified to agree with that in this thesis.

However, this model [15] did not agree well with the result of Henderson *et al.* [13] (Monte Carlo ray-tracing method), neither in form nor in level. Bourlier *et al.* [15] pointed out that it was because S_{M}^1 was not well determined.

To calculate the emissivity with higher accuracy, a refined illumination function with surface reflection S_{M}^1 must be developed, which is one of the main tasks of this thesis and is addressed in Chap. 2.

1.4 Models of sea surface reflectivity

Sea surface reflectivity ρ corresponds to the radiance of the atmosphere reflected by the surface to the observation direction θ, as shown in Fig. 1.2 (c) with one reflection and in Fig. 1.2 (d) with two reflections.

Sea surface reflectivity ρ is usually calculated when deriving the sun glitter on the sea surface, or the sea surface Bidirectional Reflectance Distribution Function (BRDF). The surface reflectivity ρ is usually a directional property that depends on the incident direction $\hat{s}_i(\theta_i, \phi_i)$ and the reflected direction $\hat{s}(\theta, \phi)$. However it is also commonly averaged the incident or the reflected direction over the hemisphere to give the hemispherical reflectivity [12, 6], expressed as:

$$\rho^{\mathrm{hemi}}(\theta, \rho) = \int_0^{2\pi} \int_0^{\pi/2} \rho(\theta, \rho, \theta_i, \rho_i) \, \mathrm{d}\theta_i \, \mathrm{d}\phi_i. \tag{1.40}$$

In the infrared domain, geometrical optics approximation is assumed to be valid, meaning that only specular reflections are considered. In most of the models, one surface reflection is considered. More surface reflections are usually ignored because of the complexity of the problem.

1.4.1 Reflectivity with one surface reflection

Under geometrical optics approximation and by assuming that the sea surface is an ergodic random process, the surface reflectivity of a given surface point can be obtained by the average reflectivity of the whole surface, given by:

$$\rho_1 = \left\langle |r|^2 g_0 \right\rangle, \tag{1.41}$$

where the symbol $\langle \cdots \rangle$ stands for the statistical average over the random variables. The term $|r|^2$ is the local reflectivity of the point of interest, and g_0 results from projecting the area around this point onto the orthogonal direction of the observation direction. Eq. (1.41) is the basic idea of the sea surface infrared reflectivity modeling.

As shown in Fig. 1.2 (c), some parts of the surface are shadowed either from the transmitter (atmosphere here) or from the receiver, especially for large zenith incident θ_i or observation θ angles. As a result, a bistatic first-order illumination function S_{B}^1 is required to take into account this phenomenon. The subscript "B" stands for bistatic configuration (the transmitter and the receiver are in different locations), and the superscript "1" stands for the fact that one surface reflection is considered.

In the model of Wagner [3], the monostatic Wagner's illumination function S_{M}^0 is extended to the bistatic configuration. Bourlier *et al.* [4] extended the Smith illumination function [25] to a bistatic case to obtain the bistatic Smith illumination function in the same way as the model of Wagner. These bistatic first-order illumination functions are widely used in sea surface reflectivity models [6, 40, 23, 42, 33, 8]. The bistatic Smith illumination function is reviewed in Sec. 4.1, and is employed to calculate the surface reflectivity with one surface reflection in Sec. 5.1.

1.4.2 Reflectivity with multiple surface reflections

It is also possible that the incident ray is reflected several times by the surface before it arrives at the receiver, as shown in Fig. 1.2 (d) for two reflections. Thus, to be more accurate, multiple surface reflections must be considered. However, as it requires deriving a nth-order bistatic illumination function, where n denotes the number of reflections, this is a difficult problem and is not widely addressed.

Lynch & Wagner [12] built a bistatic illumination function with two surface reflections. It was assumed that the rough surface was a perfect reflector. The unpolarized reflectivity of the rough surface was then calculated and they pointed out that the energy conservation condition was better satisfied better after the second reflection was considered.

Bourlier *et al.* [41] developed a bistatic illumination function with multiple surface reflections, which is the product of a successive monostatic zero-order illumination functions. This result has not been compared with any numerical result or with measurements.

In the model of Schott *et al.* [42], a Monte Carlo ray-tracing method was developed to calculate the reflectivity with multiple reflections of an one-dimensional rough dielectric surface. They arrived at the same conclusion that the energy conservation test was improved when the second surface reflection was considered.

The model of Lynch & Wagner [12] is reviewed in detail in Sec. 4.2.2. Based on the model of Lynch & Wagner, a refined model is developed, and is used to calculate the surface reflectivity with two reflections in Sec. 5.2.

1.5 Conclusion

In this chapter, the sea surface emissivity and reflectivity are introduced. Because of the sea wave, the sea surface is unpredictable. As a result, it is usually modeled as a random process. The researches about the sea surface height and slope probability density functions (PDF), and about sea surface height autocorrelation function are reviewed. Then, the main models of sea surface emissivity and reflectivity in the literature are reviewed. The shadowing effect and the surface reflections are the most important phenomena that must be taken into account. Among the sea surface emissivity models, polarization is usually not studied. Shadowing effect is usually considered. Some models took into account surface reflections, with the results needing justify. The models of surface reflectivity usually consider one surface reflection, with shadowing form the receiver and from the transmitter being considered. Multiple surface reflection is seldom studied.

This thesis is aimed to model the sea surface emissivity and reflectivity accurately, which means that both shadowing effect and surface reflections must be taken into account. In Chap. 2, the monostatic illumination function is studied. Shadowing effect and one surface reflection are considered. With the monostatic illumination function, sea surface emissivity is calculated in Chap. 3. In Chap. 4 the bistatic illumination function is studied. Single and double surface reflections are considered. The sea surface reflectivity is then calculated with the bistatic illumination function in Chap. 5.

2

Monostatic illumination function

When solving the infrared emissivity of rough sea surfaces, shadowing effect (see Fig. 1.2 (a)) and surface reflections (see Fig. 1.2 (b)) have to be taken into account. These two phenomena are the most important aspects in the calculation of sea surface emissivity, which makes it very different from that of a flat surface away from normal incidence $\theta = 0°$. The difficulty of the prediction of the sea surface infrared emissivity is increased because of the appearance of these two phenomena.

In this chapter, the monostatic illumination functions without surface reflections S_{M}^{0} and the one with n reflections S_{M}^{n} are studied, which evaluate the shadowing effect and the surface reflection effect, respectively. The superscripts "0" and "n" denote the number of reflections. The subscript "M" stands for the monostatic configuration, which means that the transmitter and the receiver (sensor) are at the same location, or only a receiver appears (for passive systems). These monostatic illumination functions are used to calculate the surface emissivity in the next chapter.

In section 2.1, the monostatic illumination function without surface reflections S_{M}^{0} is studied, and some classical models are summarized. In section 2.2, the models of monostatic illumination function with surface reflections S_{M}^{n} are reviewed, and a new model of monostatic illumination function with one surface reflection S_{M}^{1} is developed. The monostatic illumination function with one reflection S_{M}^{1} is the first contribution of this thesis. A Monte Carlo ray-tracing method is used to evaluate the accuracy of the present model.

2.1 Illumination function without reflection

2.1.1 Shadowing effect

Fig. 2.1 shows a receiver which is measuring the radiance of a rough sea surface. The receiver is situated in the $\hat{s}(\theta, \phi)$ direction [1]. The observation direction $\hat{s}$ forms an angle $\theta \in [0°, 90°]$ with the zenith $\hat{z}$, which is named the zenith angle. The azimuth angle $\phi \in [0°, 360°]$ is the one between the up-wind direction and the

---

[1] In this thesis, the symbol ˆ represents unitary vectors.

horizontal projection of $\hat{s}$ (named the X direction). Fig. 2.1 shows the profile containing the (X, z) plane, where ϕ is not shown.

Because of the surface roughness, not all parts of the surface can be "seen" by the receiver. Some parts of the surface may lie in the shadow of the receiver, shown as the dashed lines, as the emission rays toward the receiver along the observation direction $\hat{s}$ are blocked by the surface itself. This phenomenon is called the shadowing effect.

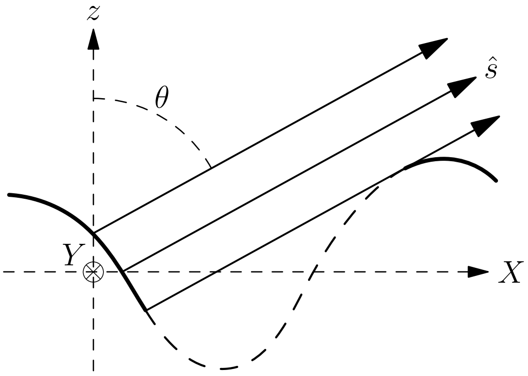

Figure 2.1: Shadowing effect of rough surfaces. The observation direction forms an angle θ with the zenith. The X direction corresponds to the horizontal direction of the receiver. The dashed part of the surface lies in the shadow of the receiver, whereas the solid part of the surface can be seen by the receiver.

Obviously, the shadowing effect depends on the observation direction $\hat{s}$ and the surface roughness (in particular, surface slopes), e.g. a flat surface is always fully illuminated in all observation directions $0° \leq \theta < 90°$. The following physical characteristics can be predicted:

1. In the case where $\theta = 0°$, which means that the emission ray is propagating vertically upward, no emission ray is blocked (see Fig. 2.2(a)).
2. In the case where $\theta = 90°$, which means the emission ray is propagating horizontally toward the receiver located at the level of the horizon, nearly all emission rays are blocked, except for the few ones at the edge of the surface (see Fig. 2.2(b)).
3. The higher the point is, the more likely it is illuminated. The highest point of the surface is illuminated, as no other points can shadow it (see Fig. 2.2(c), the point H). Indeed, if a surface point is in the shadow of the receiver, this implies that its emission ray along $\hat{s}$ reaches the surface at some other point.
4. The surface points with slopes γ_{X_0} in the X direction (corresponds to the horizontal direction of the receiver) being larger than the slope $\mu = \cot\theta$ of the emission ray lie in the shadow of the receiver, as the local angle of incidence[2] (the one between the normal to the facet $\hat{n}$ and the emission ray, see Fig. 2.2(d)) $|\chi| > 90°$, which is not physical.

As predicted by the characteristics 1 and 2 in the above list, shadowing becomes more and more significant as the zenith observation angles θ increases. For large θ,

---

[2] This thesis uses the terms "angle of incidence" and later "plane of incidence" even though there is not a real incident ray. The emission ray is treated as if it was generated by a specular reflection of an incident ray, where the angle of incidence and the plane of incidence are defined.

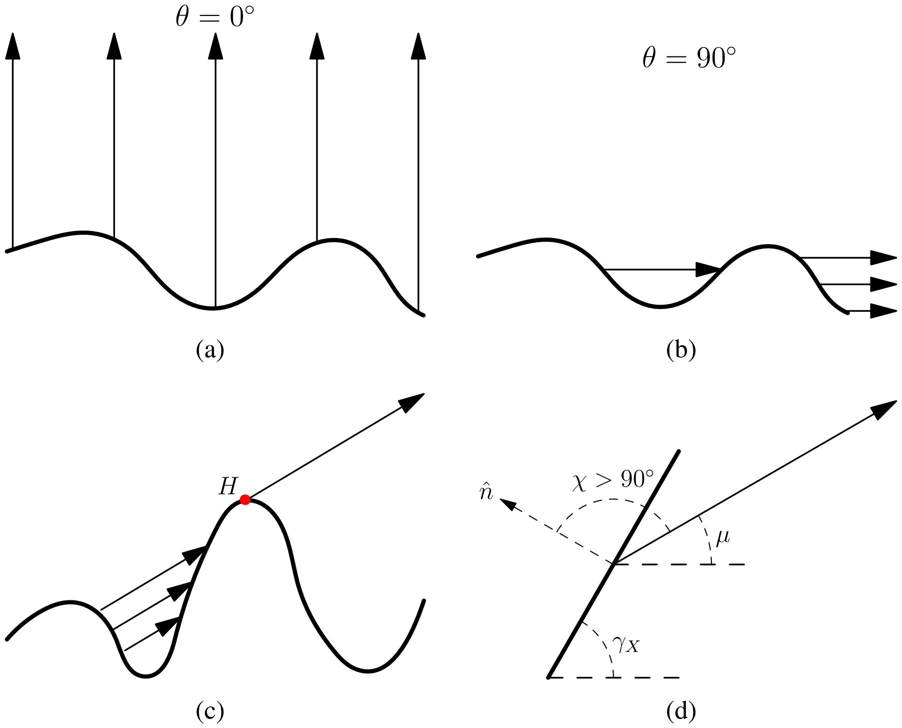

(a) (b) (c) (d)

Figure 2.2: The 4 physical characteristics of the shadowing effect.

shadowing is too significant to be neglected. In measurements of sea surface radiation, the receivers located near the sea surface (e.g. on a ship or an airplane) work in these observation angles. This phenomenon is reinforced by the increase of the wind speed above the sea surface, as it implies that the surface Root Mean Square (RMS) slope increases (characteristics 4 of the above list). As a result, an accurate estimation of the shadowing effect, named shadowing function or illumination function, has to be developed to estimate the sea surface emissivity with accuracy.

Many researches were devoted to evaluate the shadowing effect. Conventional illumination functions, for example Wagner's model [3] and Smith's model [25], can be dated back to the 1960s, and are widely used in the models of scattering and emissivity. Saunder [34] and Masuda *et al.* [10] took the shadowing effect into account by employing normalization factors, which is also widely used as it is simple to understand. Bourlier *et al.* [26] compared the models of Wagner, Smith and Ricciardi–Sato [31, 30], and concluded that Smith's illumination function is the most accurate. Besides, they extended Smith's model by introducing the length of the surface to obtain the illumination function of a surface with finite length. These models, as they do not consider surface reflections, are called zero-order illumination functions. In the following subsections, the main models of zero-order monostatic illumination functions are reviewed in detail.

2.1.2 Geometrical calculation

Before reviewing the models in the literature, some symbols and parameters are introduced and calculated in advance. Fig. 2.3 shows a receiver located in the direction $\hat{s}(\theta, \phi)$, where θ is the zenith angle measured from the zenith and ϕ is the azimuth angle measured from the up-wind direction x. The vector $\hat{n}_0$ is the unitary normal vector to an arbitrary surface point named M_0.

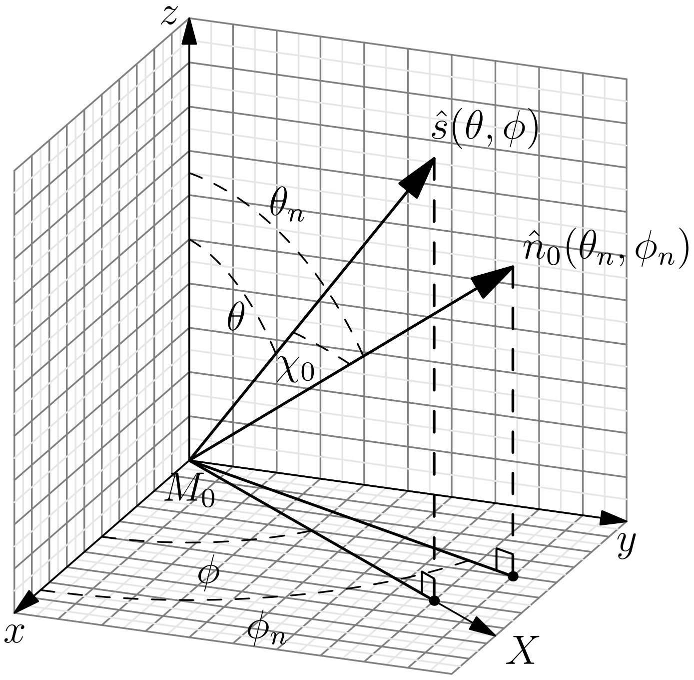

Figure 2.3: The receiver is located in the direction $\hat{s}(\theta,\phi)$. The vector $\hat{n}_0$ is the unitary normal vector to an arbitrary point named M_0.

The system of coordinates (x, y, z) is defined in the directions of the up-wind direction, the cross-wind direction and the zenith direction, respectively. The slope of the point M_0 is noted as $\gamma_0 \equiv (\gamma_{x0}, \gamma_{y0})$, where γ_{x0} and γ_{y0} are its components along the x and y directions, respectively. The unitary normal vector is then given by:

$$\hat{n}_0 = \frac{1}{\sqrt{1+\gamma_{x0}^2+\gamma_{y0}^2}} \begin{bmatrix} -\gamma_{x0} \\ -\gamma_{y0} \\ 1 \end{bmatrix}. \tag{2.1}$$

The receiver is located in the direction $\hat{s}(\theta,\phi)$, with its unitary vector $\hat{s}$ being given by:

$$\hat{s} = \begin{bmatrix} \sin\theta\cos\phi \\ \sin\theta\sin\phi \\ \cos\theta \end{bmatrix}. \tag{2.2}$$

The local angle of incidence χ_0 between $\hat{s}$ and $\hat{n}_0$, is then given by:

$$\begin{aligned} \cos\chi_0 &= \hat{s}\cdot\hat{n}_0 \\ &= \frac{1}{\sqrt{1+\gamma_{x0}^2+\gamma_{y0}^2}} \begin{bmatrix} -\gamma_{x0} \\ -\gamma_{y0} \\ 1 \end{bmatrix} \cdot \begin{bmatrix} \sin\theta\cos\phi \\ \sin\theta\sin\phi \\ \cos\theta \end{bmatrix} \\ &= \frac{\cos\theta - (\gamma_{x0}\cos\phi + \gamma_{y0}\sin\phi)\sin\theta}{\sqrt{1+\gamma_{x0}^2+\gamma_{y0}^2}}. \end{aligned} \tag{2.3}$$

As pointed out in Sec. 2.1.1, the local angle of incidence $|\chi_0|$ should not exceed 90°, otherwise the emission ray $M_0(\hat{s})$ (ray starting from M_0 along the $\hat{s}$ direction) would go into the surface and the point M_0 would be blocked from the receiver. As a result, according to Eq. (2.3), the following condition is obtained:

$$\begin{aligned} \frac{\cos\theta - (\gamma_{x0}\cos\phi + \gamma_{y0}\sin\phi)\sin\theta}{\sqrt{1+\gamma_{x0}^2+\gamma_{y0}^2}} &> 0, \\ \Rightarrow \qquad \gamma_{x0}\cos\phi + \gamma_{y0}\sin\phi &< \mu, \end{aligned} \tag{2.4}$$

where $\mu = \cot\theta$ is the slope of the emission ray with respect to the X direction.

For better convenience in the calculation, a new system of coordinates (X, Y, z) is defined by rotating the basis (x, y) anticlockwise through an angle ϕ about the z axis, so that the receiver lies in the (X, z) plane. For short, (x, y, z) is the coordinate system related to the wind direction, and (X, Y, z) is the one associated to the receiver direction. The slope of M_0 in the (x, y, z) and (X, Y, z) systems of coordinates are related to each other by:

$$\begin{array}{rcl} \gamma_{x0} & = & \gamma_{X_0}\cos\phi - \gamma_{Y_0}\sin\phi \\ \gamma_{y0} & = & \gamma_{X_0}\sin\phi + \gamma_{Y_0}\cos\phi \end{array}, \tag{2.5}$$

or inversely by:

$$\begin{array}{rcl} \gamma_{X_0} & = & \gamma_{x0}\cos\phi + \gamma_{y0}\sin\phi \\ \gamma_{Y_0} & = & -\gamma_{x0}\sin\phi + \gamma_{y0}\cos\phi \end{array}, \tag{2.6}$$

where γ_{X_0} and γ_{Y_0} are the slopes of the point M_0 with respect to the X and Y directions, respectively.

With Eq. (2.6), the condition shown in Eq. (2.4) becomes:

$$\gamma_{X_0} < \mu, \tag{2.7}$$

which means that the $|\chi_0| < 90°$ condition requires that the slope of M_0 in the X direction cannot exceed the slope μ of the emission ray, otherwise the emission ray would go into the surface. Thus this point would lie in the shadow of the receiver. Notably, no restriction is put to the slope of M_0 in the Y direction, allowing us to study the shadowing effect in the X direction or in the (X, z) plane, which simplifies the problem.

2.1.3 Wagner & Smith illumination functions

This section reviews Wagner's [3] and Smith's models [25] for calculating the illumination function without surface reflections S^0_{M} (zero-order), which gives the probability that an arbitrary point of the sea surface can be seen by the receiver along an observation direction $\hat{s}(\theta, \phi)$.

Fig. 2.4 shows a profile of the surface along the X direction. Wagner and Smith derived their illumination functions without surface reflections in very similar ways. The illumination function is developed by introducing a ray emitted from an arbitrary surface point M_0 along the observation direction $\hat{s}(\theta, \phi)$. The probability that this ray leaves the surface without intersecting the surface again is studied, which equals the probability that M_0 is seen by the receiver.

It is defined that the probability that the ray $M_0(\hat{s})$ does not intersect the surface in the interval $X \in [0, \tau]$ equals $S^0_{\mathrm{M}}(\mu, \gamma_{x0}, \gamma_{y0}, \zeta_0, \tau)$. The statistical illumination function is defined by the limit

$$S^0_{\mathrm{M}}(\mu, \gamma_{x0}, \gamma_{y0}, \zeta_0, L_0) = \lim_{\tau \to L_0} S^0_{\mathrm{M}}(\mu, \gamma_{x0}, \gamma_{y0}, \zeta_0, \tau), \tag{2.8}$$

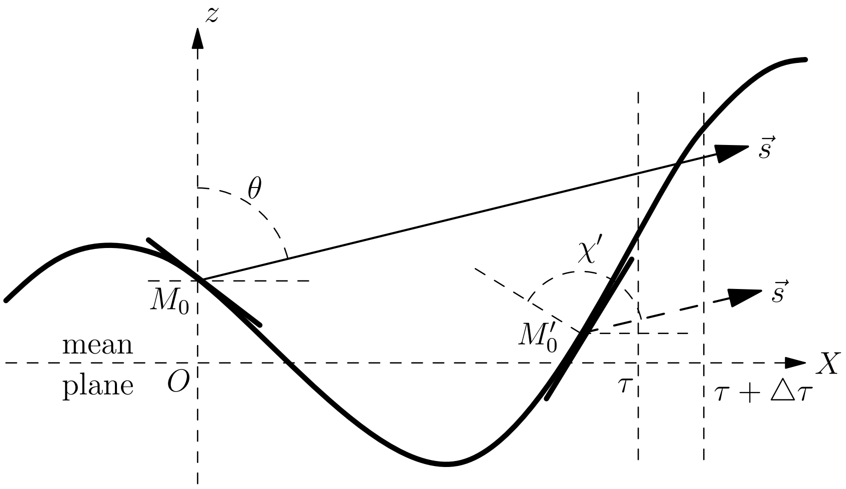

Figure 2.4: Emission rays from the surface propagate to the receiver along the observation direction $\hat{s}$. The emission ray from M_0 is blocked by the surface in the region $X \in (\tau, \tau + \triangle\tau)$. The emission ray from M_0' has a local angle of incidence $|\chi'| > 90°$, which is not physical; thus, this emission ray does not exist.

where L_0 is the surface length introduced by Bourlier *et al.* [26].

The probability that the ray $M_0(\hat{s})$ does not cross the surface in the interval $X \in [0, \tau + \triangle\tau]$ equals [3, 25]:

$$S_{\mathrm{M}}^0(\mu, \gamma_{x0}, \gamma_{y0}, \zeta_0, \tau + \triangle\tau) = S_{\mathrm{M}}^0(\mu, \gamma_{x0}, \gamma_{y0}, \zeta_0, \tau) Q(\triangle\tau|\mu, \gamma_{x0}, \gamma_{y0}, \zeta_0, \tau), \quad (2.9)$$

where $Q(\triangle\tau|\mu, \gamma_{x0}, \gamma_{y0}, \zeta_0, \tau)$ is the conditional probability that the ray does not intersect the surface in the range $X \in [\tau, \tau + \triangle\tau]$, given that it neither does in the interval $X \in [0, \tau]$. Expressing this term by its complementary probability [3, 25]:

$$Q(\triangle\tau|\mu, \gamma_{x0}, \gamma_{y0}, \zeta_0, \tau) = 1 - g(\mu|\gamma_{x0}, \gamma_{y0}, \zeta_0; \tau)\triangle\tau, \quad (2.10)$$

where $g(\mu|\gamma_{x0}, \gamma_{y0}, \zeta_0; \tau)\triangle\tau$ is the conditional probability that the ray does intersect the surface in the range $X \in (\tau, \tau + \triangle\tau)$ (symbolically denoted by β) given that it does not in the interval $X \in (0, \tau)$ (symbolically denoted by α).

When $\triangle\tau$ is sufficiently small, expanding $S_{\mathrm{M}}^0(\mu, \gamma_{x0}, \gamma_{y0}, \zeta_0, \tau + \triangle\tau)$ leads to the following differential equation [3, 25]:

$$\frac{\mathrm{d}S(\mu, \gamma_{x0}, \gamma_{y0}, \zeta_0, \tau)}{\mathrm{d}\tau} = -g(\mu|\gamma_{x0}, \gamma_{y0}, \zeta_0; \tau) S(\mu, \gamma_{x0}, \gamma_{y0}, \zeta_0, \tau), \quad (2.11)$$

which can be integrated over $\tau \in [0, L_0]$ to yield:

$$S_{\mathrm{M}}^0(\mu, \gamma_{x0}, \gamma_{y0}, \zeta_0, L_0) = A \exp\left[-\int_0^{L_0} g(\mu|\gamma_{x0}, \gamma_{y0}, \zeta_0; \tau)\mathrm{d}\tau\right]. \quad (2.12)$$

There leaves two tasks to fully derive Eq. (2.12): the determination of the constant A and the conditional probability $g(\mu|\gamma_{x0}, \gamma_{y0}, \zeta_0; \tau)$. In the following of this subsection, these two parameters are derived.

2.1.3.1 Derivation of the constant A

Mathematically, the factor A can be any arbitrary constant. However, in a physical problem, the choice of A affects the solution heavily, especially when this model is extended to deal with surface reflections, which is the aim of the next section of this chapter. First of all, $S^0_{\mathrm{M}}(\mu, \gamma_{x_0}, \gamma_{y_0}, \zeta_0, L_0)$ should be unity when $\theta = 0°$, because no shadow is produced by such vertical emission rays (characteristic 1), as the surface is assumed to be single-valued. Secondly, as M_0 is chosen randomly, it is obvious that the slope of M_0 must obey the $|\chi_0| < 90°$ condition (characteristic 4, or see Eq. (2.7)), otherwise the emission ray would go into the surface (see the ray $\hat{s}$ from M_0' in Fig. 2.4). In that case, M_0 lies in the shadow of the receiver and the deduction above is neither valid nor necessary.

In the choice of A, Wagner and Smith agreed with each other, and A is chosen as the unit step function such that:

$$A = \Upsilon(\mu - \gamma_{X_0}) = \begin{cases} 0, & \gamma_{X_0} > \mu \\ 1, & \gamma_{X_0} < \mu \end{cases} . \tag{2.13}$$

However, when deriving the conditional probability $g(\mu|\gamma_{x_0}, \gamma_{y_0}, \zeta_0; \tau)\triangle\tau$, Wagner and Smith had different expressions, which are shown below.

2.1.3.2 Wagner's formulation of g_{W}

To derive the illumination function, Wagner simplified the derivation of the conditional probability $g(\mu|\gamma_{x_0}, \gamma_{y_0}\zeta_0; \tau)\triangle\tau$. He neglected the dependence between the two events α and β (see below Eq. (2.10) for the definition of α and β), and approximately expressed it as the probability that the ray does intersect the surface in the range $X \in [\tau, \tau + \triangle\tau]$ [3]. In other words, this approximation is expressed as:

$$p(\beta \mid \alpha) \approx p(\beta). \tag{2.14}$$

A ray intersecting the facet in the horizontal region $X \in [\tau, \tau + \triangle\tau]$ checks the following conditions:

$$\begin{cases} \zeta(\tau) < \zeta_0 + \mu\tau \\ \zeta(\tau + \triangle\tau) > \zeta_0 + \mu(\tau + \triangle\tau) \\ \gamma_{X_0} > \mu \end{cases} , \tag{2.15}$$

where $\zeta(\tau)$ and $\zeta(\tau+\triangle\tau)$ are the heights of the surface at $X = \tau$ and $X = \tau+\triangle\tau$, respectively. Assuming that the slope γ_{X_0} of the facet in the region $X \in [\tau, \tau+\triangle\tau]$ is constant, the above expression can be rewritten as:

$$\begin{cases} \zeta_0 + \mu\tau > \zeta(\tau) > \zeta_0 + \mu\tau - (\gamma - \mu)\triangle\tau \\ \gamma_{X_0} > \mu \end{cases} . \tag{2.16}$$

Then, $g(\mu|\gamma_{X_0}, \zeta_0; \tau)\triangle\tau$ is calculated as:

$$\begin{aligned} g_{\mathrm{W}}(\mu|\gamma_{X_0}, \zeta_0; \tau)\triangle\tau &= \int_{\mu}^{+\infty} \int_{\zeta_0+\mu\tau-(\gamma-\mu)\triangle\tau}^{\zeta_0+\mu\tau} p(\zeta, \gamma|\zeta_0, \gamma_{X_0}; \tau)\, \mathrm{d}\zeta\, \mathrm{d}\gamma, \\ &\approx \triangle\tau \int_{\mu}^{+\infty} (\gamma - \mu) p(\zeta = \zeta_0 + \mu\tau, \gamma|\zeta_0, \gamma_{X_0}; \tau)\, \mathrm{d}\gamma, \end{aligned} \tag{2.17}$$

thus

$$g_{\mathrm{W}}(\mu|\gamma_{X_0}, \zeta_0; \tau) \approx \int_{\mu}^{+\infty} (\gamma - \mu) p(\zeta = \zeta_0 + \mu\tau, \gamma|\zeta_0, \gamma_{X_0}; \tau)\, \mathrm{d}\gamma. \tag{2.18}$$

Eq. (2.18) is difficult to simplify because of the appearance of the conditional probability $p(\zeta = \zeta_0 + \mu\tau, \gamma|\zeta_0, \gamma_{X_0}; \tau)$, which corresponds to the correlation between the heights and the slopes of two points separated by a horizontal distance τ (see Sec. 1.1.4). To simplify the calculation, the simplest way is to ignore the correlation between the heights and the slopes of these points [3, 25]. The other choice is proposed by Bourlier *et al.* [20], where an analytical result of Eq. (2.18) is given for a Gaussian surface.

Uncorrelated solution of g_{W} Ignoring the correlation in $p(\zeta = \zeta_0+\mu\tau, \gamma|\zeta_0, \gamma_{X_0}; \tau)$ greatly facilitates the calculation of Eq. (2.18):

$$\begin{aligned} g_{\mathrm{W}}^{\mathrm{unco}}(\mu|\gamma_{X_0}, \zeta_0; \tau) &\approx p_\zeta(\zeta = \zeta_0 + \mu\tau) \int_{\mu}^{+\infty} (\gamma - \mu) p_\gamma(\gamma) \mathrm{d}\gamma \\ &= \mu\Lambda(\mu) p_\zeta(\zeta = \zeta_0 + \mu\tau), \end{aligned} \tag{2.19}$$

where Λ is given by:

$$\Lambda(\mu) = \frac{1}{\mu} \int_{\mu}^{+\infty} (\gamma - \mu) p_\gamma(\gamma) \mathrm{d}\gamma. \tag{2.20}$$

For surfaces with Gaussian slope PDF $p_\gamma(\gamma)$ (see Eq. (1.7)), Λ is given by:

$$\begin{cases} \Lambda(\nu) = \dfrac{\exp(-\nu^2) - \nu\sqrt{\pi}\,\mathrm{erfc}(\nu)}{2\nu\sqrt{\pi}} \\ \nu = \dfrac{\mu}{\sigma_\gamma\sqrt{2}} \end{cases}, \tag{2.21}$$

where σ_γ is the surface RMS slope in the studied direction (here the X direction). For non Gaussian slope PDF $p_\gamma(\gamma)$ (see Eq. (1.9)), the calculation of Λ is shown in Appendix (A).

The uncorrelated monostatic illumination function without surface reflection is given by substituting the constant A (Eq. (2.13)) and the $g_{\mathrm{W}}^{\mathrm{unco}}$ (Eq. (2.19)) into Eq. (2.12) [3]:

$$S_{\mathrm{M}}^{0,\mathrm{W},\mathrm{unco}}(\mu, \gamma_{X_0}, \zeta_0, L_0) = \Upsilon(\mu - \gamma_{X_0}) \exp\left\{-\Lambda[F(\zeta_0 + \mu L_0) - F(\zeta_0)]\right\}, \tag{2.22}$$

where $F(\zeta)$ is the cumulative distribution function of the height PDF, given by:

$$F(\zeta) = \int_{-\infty}^{\zeta} p_\zeta(t) \mathrm{d}t, \tag{2.23}$$

where p_ζ is the PDF of the surface height. For a surface with infinite length $L_0 \to +\infty$, Eq. (2.22) is simplified as:

$$S_{\mathrm{M}}^{0,\mathrm{W},\mathrm{unco}}(\mu, \gamma_{X_0}, \zeta_0) = \Upsilon(\mu - \gamma_{X_0}) \exp\left\{-\Lambda(\mu)[1 - F(\zeta_0)]\right\}. \tag{2.24}$$

In this thesis, the surface is always assumed to be of infinite length.

The height-averaged zero-order monostatic illumination function corresponds to the slopes of the surface contributing to the emission field. It can be obtained by averaging Eq. (2.24) over the height ζ_0 of M_0, given by:

$$\begin{aligned} \overline{S}_{\mathrm{M}}^{0,\mathrm{W},\mathrm{unco}}(\mu, \gamma_{X_0}) &= \int_{-\infty}^{+\infty} S_{\mathrm{M}}^{0,\mathrm{W},\mathrm{unco}}(\mu, \gamma_{X_0}, \zeta_0) p_\zeta(\zeta_0)\, \mathrm{d}\zeta_0 \\ &= \Upsilon(\mu - \gamma_{X_0}) \frac{1 - \exp[-\Lambda(\mu)]}{\Lambda(\mu)} \end{aligned} \tag{2.25}$$

where $p_\zeta(\zeta_0)$ is the PDF of the surface height ζ_0. The integration in Eq. (2.25) holds for any $p_\zeta(\zeta_0)$.

The slope-averaged zero-order monostatic illumination function corresponds to the heights of the surface contributing to the emission field. It can be obtained by averaging Eq. (2.24) over the slope γ_{X_0} of M_0 along the X direction. For surfaces with Gaussian slope PDF, it is given by:

$$\begin{aligned}\overline{S}_{\mathrm{M}}^{0,\mathrm{W,unco}}(\mu,\zeta_0) &= \int_{-\infty}^{+\infty} S_{\mathrm{M}}^{0,\mathrm{W,unco}}(\mu,\gamma_{X_0},\zeta_0)p_\gamma(\gamma_{X_0})\,\mathrm{d}\zeta_X \\ &= \left[1-\frac{1}{2}\,\mathrm{erfc}\left(\frac{\mu}{\sigma_{\gamma_{X_0}}\sqrt{2}}\right)\right]\exp\{-\Lambda[1-F(\zeta_0)]\}\end{aligned} \tag{2.26}$$

where erfc is the complementary error function, given by:

$$\mathrm{erfc}(v) = \frac{2}{\sqrt{\pi}}\int_v^{+\infty} e^{-t^2}\mathrm{d}t. \tag{2.27}$$

The averaged zero-order monostatic illumination function corresponds to the percentage of the surface seen by the receiver along a given observation direction. It is obtained by averaging Eq. (2.25) over the surface slope γ_{X_0}, or by averaging Eq. (2.26) over the surface height ζ_0. For surfaces with Gaussian slope PDF, it is given by:

$$\overline{\overline{S}}_{\mathrm{M}}^{0,\mathrm{W,unco}}(\mu) = \left[1-\frac{1}{2}\mathrm{erfc}(\frac{\mu}{\sigma_{\gamma_{X_0}}\sqrt{2}})\right]\frac{1-\exp[-\Lambda(\mu)]}{\Lambda(\mu)}. \tag{2.28}$$

Correlated solution of g_{W} Bourlier *et al.* [26, 20] gave an analytical solution of Eq. (2.18) for a surface with Gaussian slope PDF and for any height autocorrelation function, noted as $g_{\mathrm{W}}^{\mathrm{co}}$. These results can be found in [26, 20] and are reviewed in appendix (Appendix for short) B.

When calculating the correlated monostatic illumination function, Eq. (2.12) involves integrating $g_{\mathrm{W}}^{\mathrm{co}}$ over the horizontal distance in the X direction from 0 to infinity. Because of the complexity of the correlated $g_{\mathrm{W}}^{\mathrm{co}}$, the integration has to be carried out numerically, which can take a long computation time if not handled properly. Bourlier *et al.* [26, 20] pointed out that the correlation between the slopes and the heights of two points can be neglected if the distance between these two points is larger than 3 times the correlation length L_c (see also Fig. 1.4). Thus, the calculation is separated in two parts, with one for $\tau \in [0, 3L_c]$ with correlation, and the other for $\tau \in [3L_c, +\infty)$ without correlation, shown as [26, 20]:

$$S_{\mathrm{M}}^{0,\mathrm{W,co}}(\mu,\gamma_{X_0},\zeta_0) = \Upsilon(\mu-\gamma_{X_0})\exp\left[-\int_0^{3L_c} g_{\mathrm{W}}^{\mathrm{co}}\,\mathrm{d}\tau + G_{\mathrm{W}}\right] \tag{2.29}$$

where G_{W} is given by:

$$\begin{aligned}G_{\mathrm{W}} &= \int_{3L_c}^{+\infty} g_{\mathrm{W}}^{\mathrm{unco}}(\mu|\gamma_0,\zeta_0;\tau)\mathrm{d}\tau \\ &= \Lambda(\mu)[1-F(\zeta_0+3\mu L_c)].\end{aligned} \tag{2.30}$$

The integration in Eq. (2.29) from 0 to $3L_c$ is carried out numerically. Some details of calculation are also presented in Appendix B. The height or slope averaged $\overline{S}_{\mathrm{M}}^{0,\mathrm{W,co}}$ and the averaged $\overline{\overline{S}}_{\mathrm{M}}^{0,\mathrm{W,co}}$ correlated illumination functions can be obtained in the same way as the uncorrelated ones, shown in Eqs. (2.25), (2.26) and (2.28), with the integrations being carried out numerically.

2.1.3.3 Smith's formulation $g_{\rm S}$

When determining the conditional probability $g(\mu|\gamma_{X_0},\zeta_0;\tau)\triangle\tau$, Smith made an approximation which replaces the condition "the ray $M_0(\theta)$ does not intersect the surface in $l\in[0,\tau]$" with "the ray $M_0(\theta)$ is not shadowed by the point $l=\tau$", which is expressed as

$$\zeta(\tau)<\zeta_0+\mu\tau, \tag{2.31}$$

and symbolically denoted as α'. In other words, this approximation is expressed as (see below Eq. (2.10) for the definition of α and β):

$$p(\beta\mid\alpha)\approx p(\beta\mid\alpha'). \tag{2.32}$$

The conditional probability is then expressed as:

$$\begin{aligned}
g_{\rm S}(\mu|\gamma_{X_0},\zeta_0;\tau)\triangle\tau &= p(\beta|\alpha') = \frac{p(\alpha',\beta)}{p(\alpha')},\\
&= \frac{\displaystyle\int_{\mu}^{+\infty}\int_{\zeta_0+\mu\tau-(\gamma-\mu)\triangle\tau}^{\zeta_0+\mu\tau} p(\zeta,\gamma|\zeta_X,\gamma_{X_0};\tau)\mathrm{d}\gamma\mathrm{d}\zeta}{\displaystyle\int_{-\infty}^{+\infty}\int_{-\infty}^{\zeta_0+\mu\tau} p(\zeta,\gamma|\zeta_0,\gamma_{X_0};\tau)\mathrm{d}\gamma\mathrm{d}\zeta}\\
&\approx \frac{\displaystyle(\gamma-\mu)\triangle\tau\int_{\mu}^{+\infty} p(\zeta=\zeta_0+\mu\tau,\gamma|\zeta_0,\gamma_{X_0};\tau)\mathrm{d}\gamma}{\displaystyle\int_{-\infty}^{+\infty}\int_{-\infty}^{\zeta_0+\mu\tau} p(\zeta,\gamma|\zeta_0,\gamma_{X_0};\tau)\mathrm{d}\gamma\mathrm{d}\zeta}.
\end{aligned} \tag{2.33}$$

Uncorrelated solution of $g_{\rm S}$ Similar to the Wagner formulation, Eq. (2.33) also contains the conditional PDF $p(\zeta,\gamma|\zeta_0,\gamma_{X_0};\tau)$. The correlation between the heights and slopes of two points is ignored, and the uncorrelated solution of Eq. (2.33) is given by:

$$g_{\rm S}^{\rm unco}(\mu|\gamma_{X_0},\zeta_0;\tau)=\mu\Lambda(\mu)\frac{p_\zeta(\zeta=\zeta_0+\mu\tau)}{F(\zeta_0+\mu\tau)}, \tag{2.34}$$

where $\Lambda(\mu)$ is given by Eq. (2.20).

For surfaces of infinite length, the uncorrelated zero-order monostatic illumination function is given by substituting the constant A (Eq. (2.13)) and the uncorrelated $g_{\rm S}^{\rm unco}$ (Eq. (2.34)) into Eq. (2.12), given by [25]:

$$S_{\rm M}^{0,\rm S,unco}(\mu,\gamma_{X_0},\zeta_0)=\Upsilon(\mu-\gamma_{X_0})F(\zeta_0)^{\Lambda(\mu)}. \tag{2.35}$$

The height-averaged zero-order monostatic illumination function can be obtained by averaging Eq. (2.35) over the height ζ_0 of M_0, given by:

$$\begin{aligned}
\overline{S}_{\rm M}^{0,\rm S,unco}(\mu,\gamma_{X_0}) &= \Upsilon(\mu-\gamma_{X_0})\int_{-\infty}^{+\infty}F(\zeta_0)^{\Lambda(\mu)}p_\zeta(\zeta_0)\mathrm{d}\zeta_0\\
&= \Upsilon(\mu-\gamma_{X_0})\frac{1}{\Lambda(\mu)+1}.
\end{aligned} \tag{2.36}$$

This result holds for any height PDF p_ζ.

The slope-averaged zero-order monostatic illumination function can be obtained by averaging Eq. (2.35) over the slope γ_{X_0} of M_0 along the X direction. For surfaces with Gaussian slope PDF p_γ, it is given by:

$$\begin{aligned}\overline{S}_{\mathrm{M}}^{0,\mathrm{S},\mathrm{unco}}(\mu,\zeta_0) &= \int_{-\infty}^{+\infty} \Upsilon(\mu-\gamma_{X_0}) F(\zeta_0)^{\Lambda(\mu)} p_\gamma(\gamma_{X_0})\,\mathrm{d}\gamma_{X_0} \\ &= \left[1-\frac{1}{2}\operatorname{erfc}\left(\frac{\mu}{\sigma_{\gamma_{X_0}}\sqrt{2}}\right)\right] F(\zeta_0)^{\Lambda(\mu)}.\end{aligned} \tag{2.37}$$

The average illumination function without reflection is obtained by averaging Eq. (2.36) over the surface slope γ_{X_0} along the X direction, or by averaging Eq. (2.37) over the surface height ζ_0. For surfaces with Gaussian slope PDF p_γ, it is given by:

$$\overline{\overline{S}}_{\mathrm{M}}^{0,\mathrm{S},\mathrm{unco}}(\mu) = \left[1-\frac{1}{2}\operatorname{erfc}\left(\frac{\mu}{\sigma_{\gamma_{X_0}}\sqrt{2}}\right)\right]\frac{1}{\Lambda(\mu)+1}, \tag{2.38}$$

where erfc is the complementary error function given by Eq. (2.27).

Correlated solution of g_{S} The solution of Eq. (2.33) with correlation, noted as $g_{\mathrm{S}}^{\mathrm{co}}$, is also derived by Bourlier *et al.* [26, 20] in the same way as that shown in the Wagner formulation. The calculation details are also reviewed in Appendix B.

When calculating the correlated monostatic illumination function, the integration in Eq. (2.12) over the horizontal distance in the X direction from 0 to infinity is also computed in two parts, with one for $\tau \in [0, 3L_c]$ with correlation, and the other for $\tau \in [3L_c, +\infty)$ without correlation. The result is shown below [26, 20]:

$$S_{\mathrm{M}}^{0,\mathrm{S},\mathrm{co}}(\mu,\gamma_{X_0},\zeta_0) = \Upsilon(v-s_0)\exp\left[-\int_0^{3L_c} g_{\mathrm{S}}^{\mathrm{co}}\,\mathrm{d}\tau + G_{\mathrm{S}}\right] \tag{2.39}$$

where G_{S} is given by:

$$\begin{aligned}G_{\mathrm{S}} &= \int_{3L_c}^{+\infty} g_{\mathrm{S}}^{\mathrm{unco}}(\mu|\gamma_0,\zeta_0;\tau)\mathrm{d}\tau \\ &= -\ln[F(\zeta_0+\mu 3L_c)]^{\Lambda(\mu)}.\end{aligned} \tag{2.40}$$

The height- or slope- averaged $\overline{S}_{\mathrm{M}}^{0,\mathrm{S},\mathrm{co}}$ and the average $\overline{\overline{S}}_{\mathrm{M}}^{0,\mathrm{S},\mathrm{co}}$ correlated illumination functions can be obtained in the same way as the uncorrelated ones, shown in Eqs. (2.36), (2.37) and (2.38), with the integrations being carried out numerically.

2.1.3.4 $S_{\mathrm{M}}^{0,\mathrm{W},\mathrm{S}}$ for 1D surfaces and discussion

The above Wagner and Smith illumination functions are deduced for 2D surfaces (3D problem). For computational ease, sometimes it is assumed that the surfaces are 1D (2D problem). The 1D expressions of Wagner's and Smith's illumination function can be obtained by setting $\gamma_0 = \gamma_{x_0}$ while suppressing γ_{y_0} or setting $\gamma_{y_0} = 0$. The surface RMS slope σ_γ is set to the one of the studied direction. Then, the 1D illumination function is obtained with the same equations. In fact, the same forms will be obtained by replacing $\gamma_0 = \gamma_X$ and $\sigma_\gamma = \sigma_{\gamma_{X_0}}$. The physical reason is that, under the geometrical optics approximation (GO), a ray propagates in one plain thus shadowing can studied in one profile of the surface.

From the construction of g_{W} (Eq. (2.18)) and g_{S} (Eq. (2.33)), it is notable that g_{S} is built by deviding g_{W} by a denominator ranging from 0 to 1 (which corresponds to the probability $p(\alpha')$). As a result, $g_{\mathrm{S}} \geq g_{\mathrm{W}}$ always holds, thus $S_{\mathrm{M}}^{0,\mathrm{S}} \leq S_{\mathrm{M}}^{0,\mathrm{W}}$.

2.1.4 Saunders & Masuda shadowing factor

Saunders and Masuda used the same shadowing factor to evaluate the shadowing effect, although their mathematical expressions are a little different (see Eqs. (6) - (9) in [34] and Eqs. (13), (21) in [10]).

When deriving the sea surface infrared emissivity, Saunders and Masuda both indicated that without considering the shadowing effect, the resulting emissivity would exceed 1 and tend to infinity as θ approaches 90° [34, 10]. This is unphysical. As a result, they calculated the surface emissivity as [3]:

$$\varepsilon_{\text{global}} = \frac{\displaystyle\int_{-\infty}^{\infty}\int_{-\infty}^{\infty} \varepsilon_{\text{local}} \frac{\cos\chi_0}{\cos\theta\cos\theta_n} p(\gamma_x,\gamma_y)\,\mathrm{d}\gamma_x\,\mathrm{d}\gamma_y}{\displaystyle\int_{-\infty}^{\infty}\int_{-\infty}^{\infty} \frac{\cos\chi_0}{\cos\theta\cos\theta_n} p(\gamma_x,\gamma_y)\,\mathrm{d}\gamma_x\,\mathrm{d}\gamma_y} \qquad \text{for} \quad |\chi_0| < 90^\circ. \tag{2.41}$$

The numerator is the same as the right-hand side of Eq. (1.32), which is the basic model of sea surface infrared emissivity. Masuda called the denominator, together with the $|\chi| < 90^\circ$ restriction, a normalization factor. As this normalization factor results from the shadowing effect, we name this normalization factor a shadowing factor. It is given by [10]:

$$p(\theta) = \frac{1}{\displaystyle\int_{-\infty}^{\infty}\int_{-\infty}^{\infty} \frac{\cos\chi_0}{\cos\theta\cos\theta_n} p(\gamma_x,\gamma_y)\,\mathrm{d}\gamma_x\,\mathrm{d}\gamma_y} \qquad \text{for} \quad |\chi_0| < 90^\circ. \tag{2.42}$$

In what follows, the above shadowing factor is simplified, so as to compare it with other models. The angle θ_n can be expressed by the slope of the studied point M_0, given by:

$$\cos\theta_n = \frac{1}{\sqrt{1+\gamma_{x0}^2+\gamma_{y0}^2}}. \tag{2.43}$$

The substitution of Eqs. (2.43) and (2.3) into Eq. (2.42) leads to:

$$\begin{aligned} p(\theta) &= \frac{1}{\displaystyle\int_{-\infty}^{+\infty} \Upsilon(\mu-\gamma_{X_0}) \frac{\cos\theta - \gamma_{X_0}\sin\theta}{\cos\theta} p(\gamma_{X_0})\,\mathrm{d}\gamma_{X_0}}, \\ &= \frac{1}{\displaystyle\int_{-\infty}^{\mu} \left(1-\frac{\gamma_{X_0}}{\mu}\right) p(\gamma_{X_0})\,\mathrm{d}\gamma_{X_0}}, \\ &= \frac{1}{1-\displaystyle\int_{\mu}^{+\infty} p(\gamma_{X_0})\mathrm{d}\gamma_{X_0} - \frac{1}{\mu}\int_{-\infty}^{\mu} \gamma_{X_0} p(\gamma_{X_0})\mathrm{d}\gamma_{X_0}}, \end{aligned} \tag{2.44}$$

---

[3] The mathematical expression is slightly modified here to agree with the definition of the symbols used in this thesis.

where the change of variables of Eq. (2.5) is performed, and the condition $|\chi_0| < 90°$ is replaced by $\Upsilon(\mu - \gamma_{X_0})$ (see Eq. (2.7)).

For an even slope PDF $p(\gamma_{X_0})$, we have

$$\int_{-\infty}^{+\infty} \gamma_{X_0} p(\gamma_{X_0}) \mathrm{d}\gamma_{X_0} = 0, \tag{2.45}$$

which implies

$$\int_{-\infty}^{\mu} \gamma_{X_0} p(\gamma_{X_0}) \mathrm{d}\gamma_{X_0} = -\int_{\mu}^{+\infty} \gamma_{X_0} p(\gamma_{X_0}) \mathrm{d}\gamma_{X_0}. \tag{2.46}$$

The substitution of Eqs. (2.45) and (2.46) into Eq. (2.44) leads to:

$$\begin{aligned} p(\theta) &= \frac{1}{1 + \dfrac{1}{\mu} \displaystyle\int_{\mu}^{+\infty} (\gamma_{X_0} - \mu) p(\gamma_{X_0}) \mathrm{d}\gamma_{X_0}} \\ &= \frac{1}{1 + \Lambda(\mu)}. \end{aligned} \tag{2.47}$$

When Masuda calculated the emissivity, the $|\chi| < 90°$ condition was also applied to the numerator of Eq. (2.41). As a result, the unit step function $\Upsilon(\mu - \gamma_{X_0})$ is multiplied to the numerator of Eq. (2.47), which is called Masuda illumination function, given by:

$$S_{\mathrm{M}}^{0,\mathrm{M}}(\theta, \gamma_{X_0}) = \frac{\Upsilon(\mu - \gamma_{X_0})}{1 + \Lambda(\mu)}. \tag{2.48}$$

It is notable that Eq. (2.48) is the same as the height-averaged uncorrelated Smith illumination function (see Eq. (2.36)). It can be concluded that for a surface with even surface slope PDF, the Masuda shadowing factor is equal to the uncorrelated Smith illumination function.

2.1.5 Monte Carlo ray-tracing method

The above subsections presented the analytical models of the monostatic illuminations functions without surface reflections. This subsection reviews the Monte Carlo ray-tracing method given by Bourlier *et al.* [26], which is a numerical method and is used as a reference to evaluate the performance of the above analytical models.

In the Monte Carlo ray-tracing method, a large number of rough surfaces are generated, over which incident rays along a given observation direction $\hat{s}$ are put. The incident rays are traced to find out the surface points seen by the receiver and the ones in the shadow of the receiver. As the points illuminated are found, the distribution of the illuminated slopes (height-averaged illumination function $\overline{S}_{\mathrm{M}}^{0}$) and the percentage of the illuminated surface (average illumination function $\overline{\overline{S}}_{\mathrm{M}}^{0}$) can be calculated. The results of each surface are then averaged to obtain a final result. Because of the long computation time, one-dimensional (1D) surfaces are considered, which are profiles of the sea surface along the X direction. This method is the same as that of Henderson *et al.* [13], except for that Henderson *et al.* considered two-dimensional (2D) surfaces and the surface height autocorrelation is ignored (the surfaces are modeled as 2D white Gaussian noise).

2.1.5.1 Generation of rough surfaces

First of all, a 1D random rough surface is generated, which is used later in the ray-tracing algorithm. It is assumed that the sea surface is a stationary Gaussian process, which requires that: firstly, the surface height PDF is Gaussian given by Eq. (1.5); secondly, the surface slope PDF is Gaussian given by Eq. (1.7); thirdly, the surface height autocorrelation function is also Gaussian given by Eq. (1.14).

Bourlier *et al.* introduced a filter to generate a signal which meets the above requirements, shown as [20]:

$$h(x_i) = \sigma_\zeta \sqrt{\frac{2}{L_c\sqrt{\pi}}} \exp\left(\frac{-2x_i^2}{L_c^2}\right), \tag{2.49}$$

where σ_ζ is the surface RMS height and L_c is the surface correlation length, and i is the index of the surface point. As the height autocorrelation function is assumed to be Gaussian, the RMS slope is related to the RMS height by $\sigma_\gamma = \sqrt{2}\sigma_\zeta / L_c$ (see Eq. (1.21)).

The random surface is given by the convolution product of a Gaussian white noise $n(x_i)$ and the above filter coefficient:

$$\zeta(x_i) = n(x_i) \otimes h(x_i), \tag{2.50}$$

where the symbol $\otimes$ stands for the convolution product.

Fig. 2.5 shows the results of the generated surfaces. In this calculation, 500 surfaces are generated, each of which has a length of 100 times of the correlation length L_c. During the calculation, the up-wind direction is chosen ($\sigma_\gamma = \sigma_{\gamma_x}$), as 1D surfaces are generated. To be more general, the height ζ and the slope γ of the surface are normalized as follows:

$$h = \frac{\zeta}{\sigma_\zeta\sqrt{2}}, \qquad s = \frac{\gamma}{\sigma_\gamma\sqrt{2}}. \tag{2.51}$$

The results are shown with respect to the normalized height h and slope s.

Fig. 2.5(a) shows one sample of the generated surfaces. It is shown that the generated surface is rather "smooth". In the model of Henderson *et al.*, a Monte Carlo ray-tracing algorithm is also performed. However, Henderson *et al.* described the surface as a white Gaussian noise. It is less similar to a real sea surface.

The surface height autocorrelation is also calculated, given by

$$R(\tau) = \langle \zeta(x_i)\zeta(x_i + \tau) \rangle, \tag{2.52}$$

where $\langle \cdots \rangle$ stands for the ensemble average. This process is repeated for each surface. The final result is shown in Fig. 2.5(b) and compared with the Gaussian height autocorrelation function (Eq. (1.14)), where a good agreement is obtained.

Figs. 2.5(c) and 2.5(d) show the histogram of the surface heights and slopes, respectively, and compared with Gaussian height and slope PDF. As can be predicted theoretically, the surface height and slope distributions agree very well with the Gaussian distribution.

In conclusion, the generated surfaces meet all the requirements mentioned at the beginning of this subsection. In what follows, these surfaces are used in the ray-tracing algorithm, so as to evaluate the shadowing effect numerically.

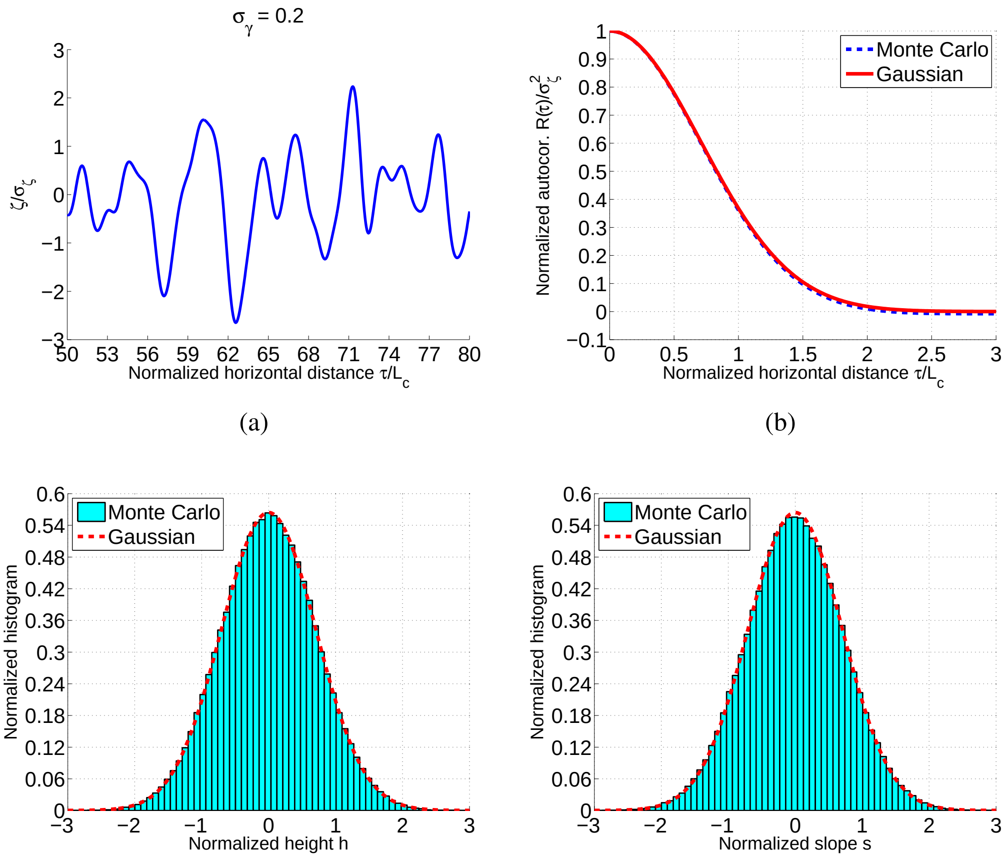

(a) (b)

(c) (d)

Figure 2.5: Results related to generated surface. (a) one sample of the generated rough surfaces, (b) surface autocorrelation, (c) histogram of the surface heights, (d) histogram of the surface slopes.

2.1.5.2 Ray-tracing algorithm

After the rough surfaces are generated, incident rays are introduced, which propagate from the receiver to the rough surface along a given observation direction $\hat{s}(\theta)$. According to the definition of the direction X, the receiver is located at the positive end of the rough surface. Every surface point x_i is studied from largest index x_{end} to smallest one x_0, and marked whether it is illuminated.

The heart of the task lies in finding the points tangent to the incident ray, beginning from which the shadowing line is drawn. The points under the shadowing lines are in the shadow of the receiver. The criterion for these points is

$$(\gamma_i - \mu)(\gamma_{i+1} - \mu) < 0, \tag{2.53}$$

where μ is the slope of the incident ray and γ_i is the slope of the ith point on the surface.

The algorithm is shown in Fig. 2.6, which is taken from Bourlier *et al.* [26]. Note that in their algorithm, the incident ray comes from the negative end of the surface.

Fig. 2.7 shows the result of this algorithm, for a RMS slope $\sigma_\gamma = 0.2$ (for sea surface, Beaufort scale ≈ 5) and observation zenith angle $\theta = 85°$. The illuminated surface is marked as solid lines and the points in shadow are marked as dashed lines. The shadowing line is clearly shown.

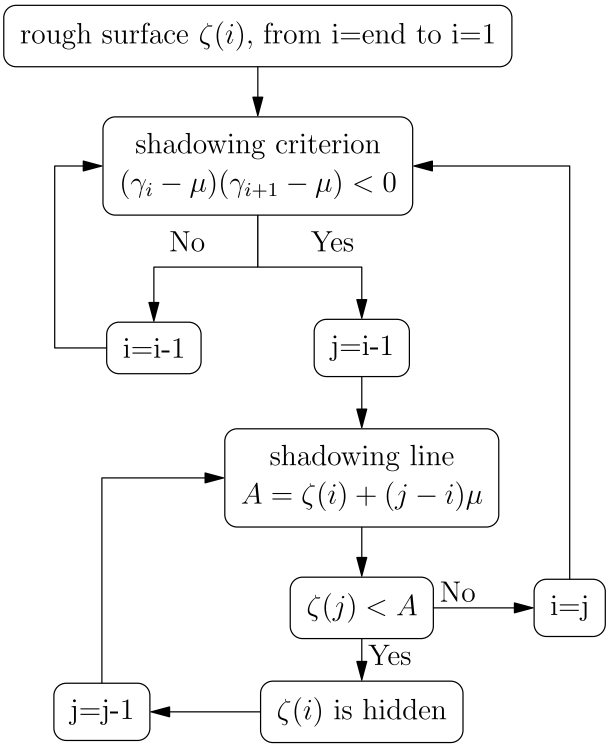

Figure 2.6: Ray-tracing algorithm without considering surface reflections.

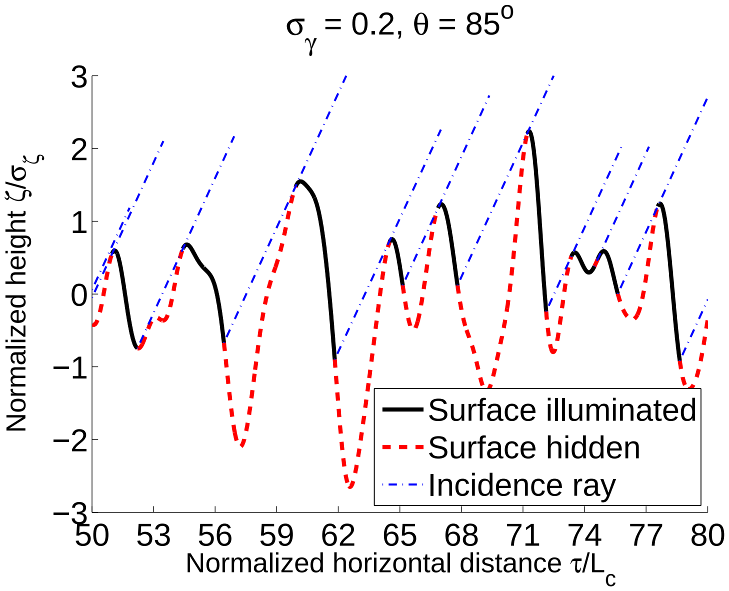

Figure 2.7: One sample of the output of the ray-tracing algorithm, for a RMS slope $\sigma_\gamma = 0.2$ and observation zenith angle $\theta = 85°$. The illuminated surface is marked as solid lines and the parts in shadow are marked as dashed lines.

In the algorithm, every surface point $\zeta(x_i)$ is marked as "illuminated" or "hidden", after which the height and slope histograms of the illuminated points are calculated. The percentage of the illuminated part over the whole surface can also be obtained. The algorithm is repeated for all the generated surfaces to obtain the statistical moments of the illumination function.

2.1.6 Numerical results

In this section, numerical results of the zero-order illumination functions of the above models are shown and compared between one another. For the calculation, 1D surfaces are considered to be consistent with the Monte Carlo ray-tracing method. The up-wind direction is studied, which means the X direction is parallel to the x direction ($\gamma_0 = \gamma_x = \gamma_{X_0}$, $\sigma_\gamma = \sigma_{\gamma_x} = \sigma_{\gamma_{X_0}}$, see Fig. 2.3) and the (x, z) plane is considered. The surface height and slope PDFs are assumed to be Gaussian. To be more general, the surface height ζ and slope γ, and the slope of the emission ray μ are normalized as follows:

$$s_0 = \frac{\gamma_0}{\sigma_\gamma\sqrt{2}}, \qquad h_0 = \frac{\zeta_0}{\sigma_\zeta\sqrt{2}}, \qquad \nu = \frac{\mu}{\sigma_\gamma\sqrt{2}}. \tag{2.54}$$

The corresponding Gaussian distributions of normalized slope and height, s_0 and h_0, respectively, become:

$$p_s(s_0) = \frac{1}{\sqrt{\pi}} \exp\left(-s_0^2\right) \qquad p_h(h_0) = \frac{1}{\sqrt{\pi}} \exp\left(-h_0^2\right). \tag{2.55}$$

By doing so, the RMS height σ_ζ and the RMS slope σ_γ are suppressed, which reduces the number of degrees of freedom.

2.1.6.1 Marginal histograms $\widetilde{p}^0_{s,h}$

Marginal histograms of the illuminated slope and height are useful parameters to evaluate the performance of the corresponding illumination function. The marginal histogram of the illuminated slopes and heights without surface reflections are defined respectively as:

$$\begin{aligned} \widetilde{p}^0_s(\nu, s_0) &= \overline{S}^0_{\mathrm{M}}(\nu, s_0) p_s(s_0), \\ \widetilde{p}^0_h(\nu, h_0) &= \overline{S}^0_{\mathrm{M}}(\nu, h_0) p_h(h_0), \end{aligned} \tag{2.56}$$

where $\overline{S}^0_{\mathrm{M}}(\nu, s_0)$ and $\overline{S}^0_{\mathrm{M}}(\nu, h_0)$ are the height- and the slope-averaged illumination functions, respectively.

Fig. 2.8 compares the zero-order marginal histograms of slopes and heights of the illuminated points, given by the zero-order illumination functions with and without correlation and by the Monte Carlo method, for a normalized emission ray slope $\nu = 0.31$ (corresponding to $\sigma_\gamma = 0.2$, $\theta = 85°$). The y scale is changed for each sub-figure, so as to show the result clearly. The Wagner model is compared with the Monte Carlo model and shown in the upper row, whereas the results of the Smith model are shown in the lower row. The left column are the slope marginal histograms $\widetilde{p}^0_s$, and the right column are the height marginal histograms $\widetilde{p}^0_h$.

The correlated Smith illumination function agrees better with the results of the Monte Carlo algorithm than the Wagner one does. For both Wagner's and Smith's models, the uncorrelated illumination functions overestimate the illumination effect as the normalized slope s_0 approaches ν (Fig. 2.8 (a) and (c)). After taking into account the correlation, the Smith model agrees much better with the Monte Carlo ray-tracing result. Larger difference can be found in the marginal height histograms shown in Fig. 2.8 (b). The Smith illumination agrees generally quite well with

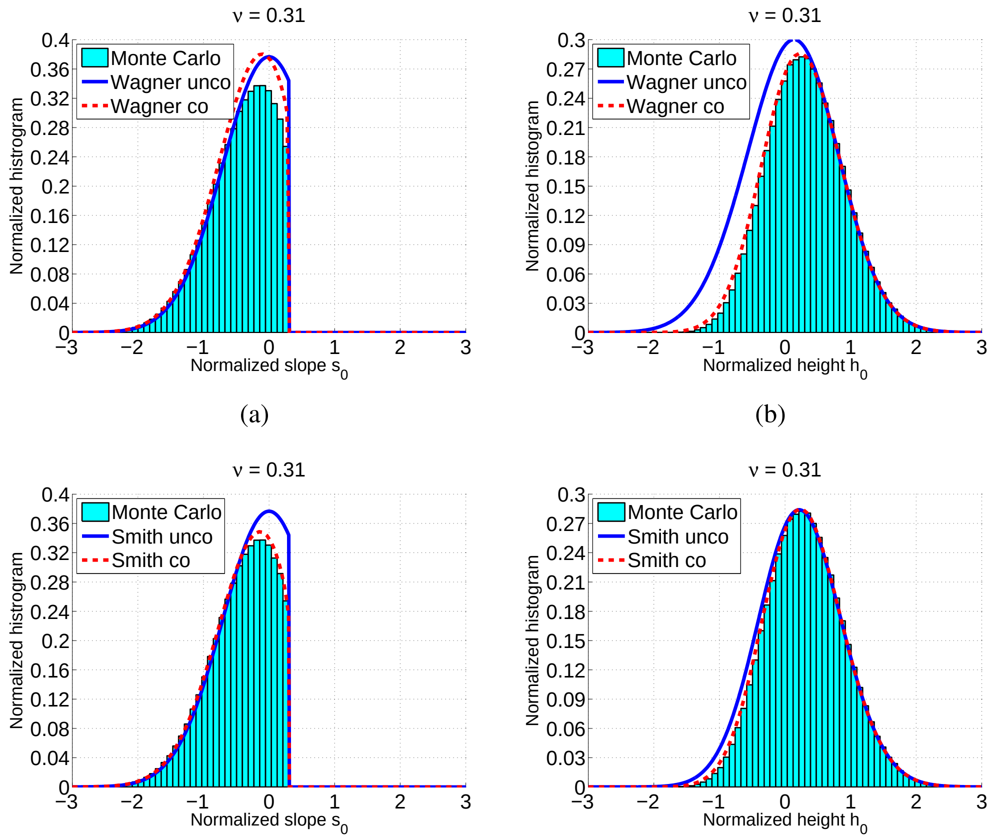

(a) (b)

(c) (d)

Figure 2.8: Marginal histogram of the illuminated slopes (left column) and heights (right column) versus normalized slope s_0 and height h_0, respectively, for the Wagner model (upper row) and the Smith model (lower row).

the Monte Carlo method (d), whereas a large difference is found between the Wagner's model and the Monte Carlo method (b). It can be concluded that the Smith illumination function has a better performance.

The result of Masuda's illumination function is not shown. Firstly, it is not a function of ζ_0, thus it cannot present the marginal illuminated height histogram. Secondly, it has the same behavior as the height illuminated Smith illumination function for surfaces with a Gaussian slope PDF. As a result, it would give the same result as the uncorrelated Smith marginal illuminated slope histogram.

The correlation between two points of the surface is negligible only when the horizontal distance between two points $\triangle x$ is large in comparison to the correlation length of the surface. However, as the height of the emission ray from M_0 at a distance $\triangle x = \tau$ equals $\zeta_0 + \tau\mu$ (see Fig. 2.4), the larger $\triangle x$ is, the higher is the ray at that point, the weaker is the probability of having one point on the surface with that height. As a result, given that a ray $M_0(\theta)$ is blocked by the surface, it is more likely that it is blocked by some facet which is close to M_0. In such a case, $\triangle x$ is of the order of the correlation length, which means that the correlation between these points should be considered. Ignoring this correlation leads to a difference between the uncorrelated model and the Monte Carlo result, as shown in Fig. 2.8.

2.1.6.2 Angular illumination behavior

Eqs. (2.25) and (2.36) suggest that, for both Wagner's and Smith's models, all points with slopes $\gamma_0 < \mu$ are shadowed equally. However, this is true only when the correlation between the heights and the slopes of the surface is neglected. It is interesting to have a close look at the angular illumination behavior of Wagner's and Smith's illumination functions, which equals the height-averaged illumination function. It is recalled that the uncorrelated height-averaged illumination functions are given analytically by Eqs. (2.25) and (2.36) for the Wagner and the Smith formulations, respectively, whereas the correlated ones are obtained from numerical integrations.

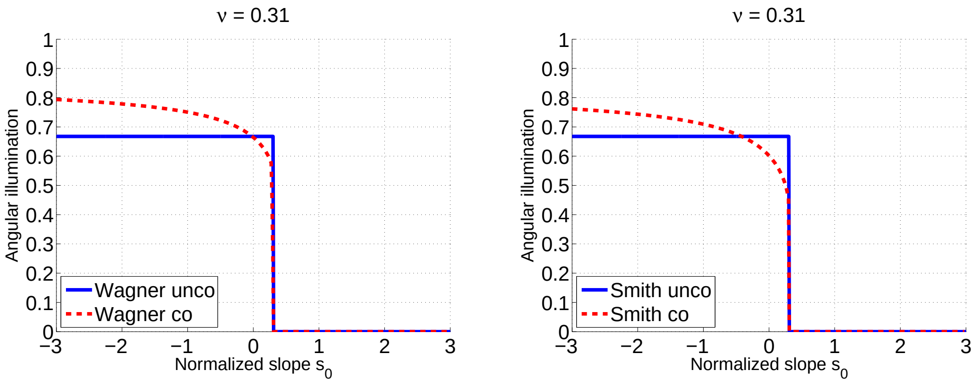

(a) (b)

Figure 2.9: Angular illumination behavior of the illumination functions with correlation (dashed curve) and without correlation (full curve) versus the normalized slope s_0 for the Wagner (left) and the Smith (right) models, for a normalized emission ray slope $\nu = 0.31$.

It is notable that the angular illumination curve of both Wagner's and Smith's models with correlation bend down significantly as s_0 approaches ν (for increasing s_0), or equally as γ_0 approaches μ, whereas the uncorrelated ones remains constant for $s_0 < \nu$ and jump to 0 at $s_0 > \nu$. In fact, in the deduction of the Wagner or the Smith illumination functions, it is never assumed that all points with slope $\gamma_0 < \mu$ should be equally shadowed. Instead, throughout the deductions, the two models neglect the correlation of the heights and slopes for computational ease. This is the main difference between the correlated and the uncorrelated models.

2.1.6.3 Average illumination function $\overline{\overline{S}}_{\mathrm{M}}^{0}$

The zero-order average illumination function $\overline{\overline{S}}_{\mathrm{M}}^{0}$ gives the percentage of the surface seen by the receiver. The uncorrelated average illumination functions of Wagner and of Smith are given by Eqs. (2.26) and (2.38), respectively. The correlated ones are calculated from numerical integrations. The results of the models of Saunders and Masuda are not shown, as they equal the uncorrelated Smith model.

Fig. 2.10 shows the results of the correlated and uncorrelated average illumination functions without reflections with respect to the parameter ν, which is given by Eq. (2.54).

It is shown that shadowing effect is significant when ν is small. When $\nu = 0$, which corresponds to $\theta = 90°$, the averaged illumination functions equal zero,

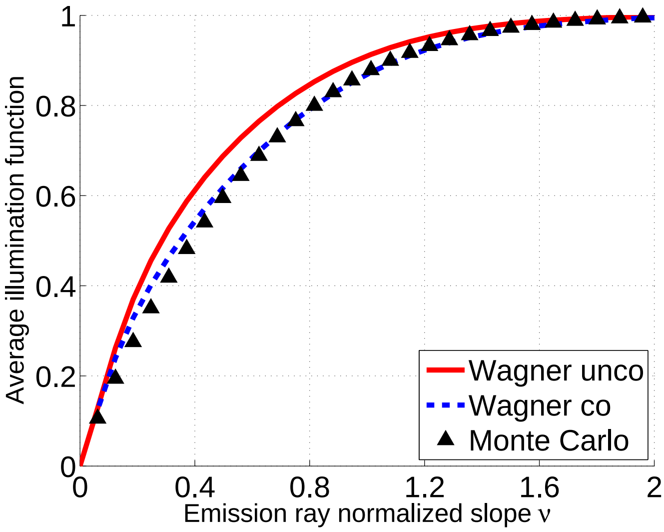

(a)

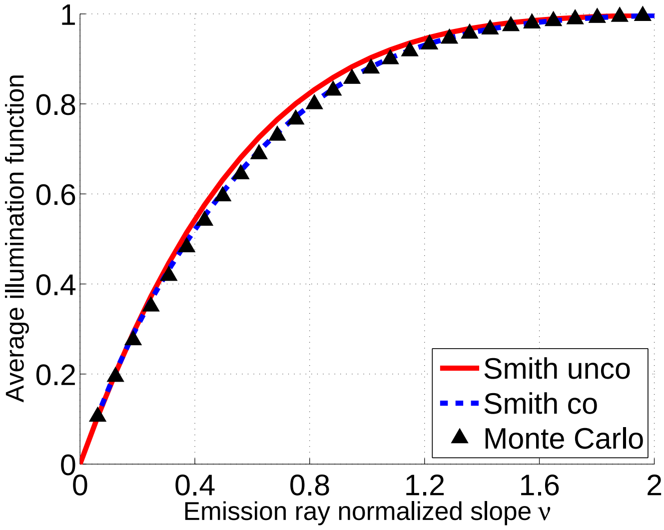

(b)

Figure 2.10: Average illumination function of Wagner (a) and Smith (b) versus ν. The correlated (dashed curve) and uncorrelated (full curve) results are compared with the Monte Carlo result (triangles).

meaning that all the surface is shadowed. When $\nu > 2$, the average illumination function tends to 1, which means that all the surface is illuminated. Compared with the Monte Carlo ray-tracing results, both uncorrelated models of Wagner and Smith overestimate the percentage of the illuminated surface. After taking into account the correlation, better agreements are obtained. In any case, the Wagner and Smith models agree well with the Monte Carlo result. In addition, it can be seen that the Smith model shows generally better agreements than the Wagner one with the Monte Carlo result.

Fig. 2.11 shows the results of the correlated and uncorrelated average illumination functions without reflections versus the zenith angle θ, for surfaces with RMS slope $\sigma_\gamma = 0.2$ (relatively calm sea surface, Beaufort scale $\approx$ 5).

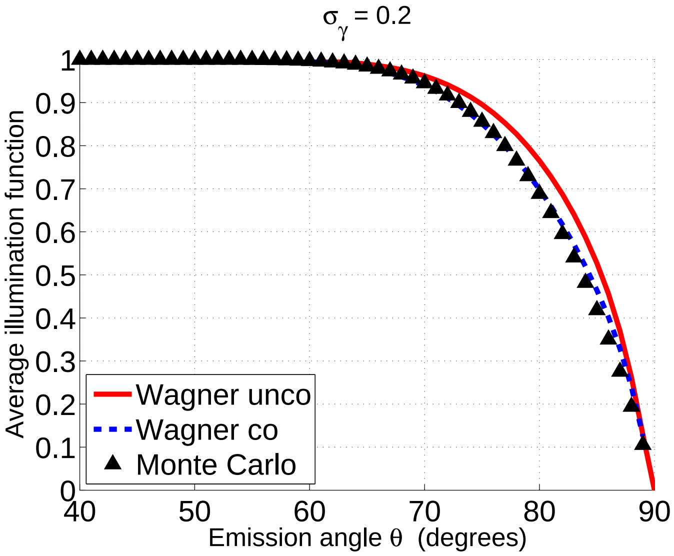

(a)

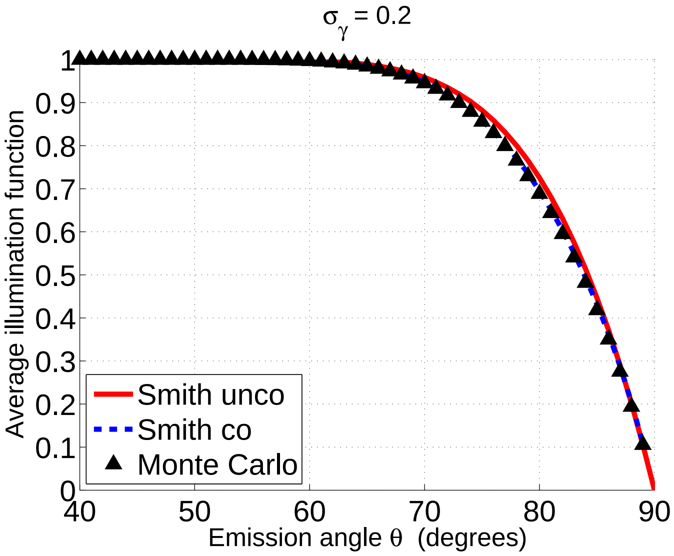

(b)

Figure 2.11: Average illumination function of Wagner (a) and Smith (b) versus the zenith angle θ. The correlated (dashed curve) and uncorrelated (full curve) results are compared with the Monte Carlo result (triangles). The surface RMS slope $\sigma_\gamma = 0.2$.

A similar conclusion as Fig. 2.10 is obtained. Shadowing is negligible for the small zenith observation angles, e.g. $\theta < 60°$. For larger θ, the shadowing effect shows up and increases rapidly. At $\theta = 90°$, the average illumination function equals zero, meaning that all the surface is in the shadow of the receiver.

It is shown in Figs. 2.8, 2.10 and 2.11, that the Smith model works better than the one of Wagner. In the following of thesis, the Smith model is used to evaluate the shadowing effect.

2.1.6.4 Averaged illumination function $\overline{\overline{S}}^0_{\mathrm{M}}$: 2D surface

To study the influence of the wind direction, the average illumination function of Smith is also calculated for 2D surfaces. The ray-tracing Monte Carlo method is not performed, because the time of computation is too long.

Fig. 2.12 shows the average Smith illumination of 2D surface with respect to the azimuth angle ϕ (corresponds to the wind direction). The zenith angle is $\theta = 85°$. The wind speed is $u_{12} = 5$ m/s (a) and 10 m/s (b) (corresponding to Beaufort scale $\approx$ 3 and 5, respectively). The surface slope PDF is firstly assumed to be Gaussian (noted as G), then skewness (noted as S) and kurtosis (noted as K) effects are considered.

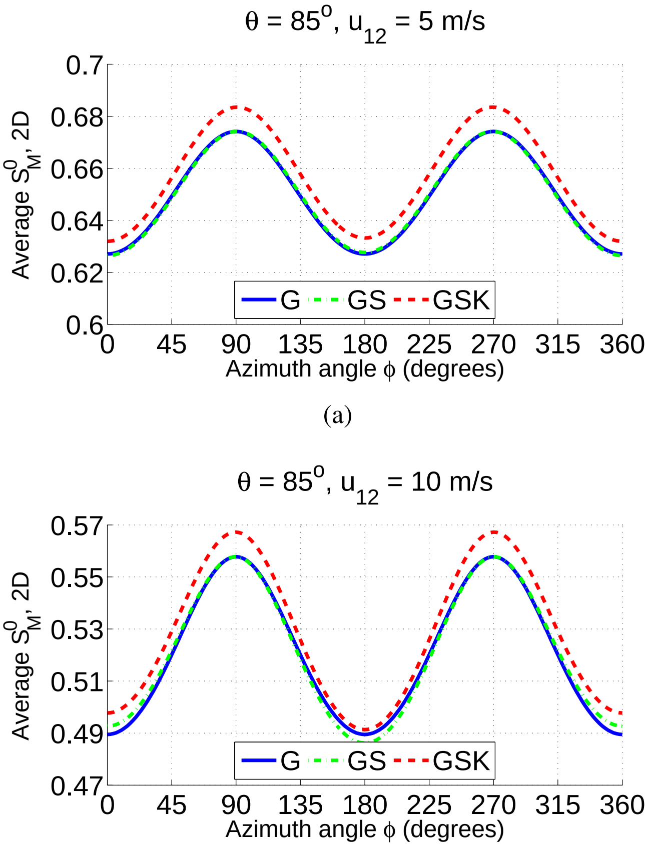

(a)

(b)

Figure 2.12: Average Smith illumination function of 2D surface with respect to the azimuth angle ϕ. The wind speed is $u_{12} = 5$ m/s (a) and 10 m/s (b).

It is shown in Fig. 2.12 that the shadowing effect depends on the wind direction. In general, under the same condition, more points are seen by the receiver at the cross-wind directions ($\phi = 90°$, $270°$). For the same θ and ϕ, more points are seen if the wind speed u_{12} is smaller.

The averaged Smith illumination function $\overline{\overline{S}}^0_{\mathrm{M}}$ is symmetry about the up-wind and cross-wind directions ($\phi = \{0°,\ 90°,\ 180°,\ 270°\}$) for Gaussian slope PDF. After the skewness effect is considered, $\overline{\overline{S}}^0_{\mathrm{M}}$ is symmetry only about the up-wind and down-wind directions ($\phi = \{0°,\ 180°\}$), which checks the conclusion obtained in Sec. 1.1.3.2. In general, the averaged Smith illumination function is increased for $\theta = 85°$ after considering the skewness and kurtosis effects.

To conclude, this section reviews and compares the existing illumination functions without surface reflections (zero-order). It is shown that shadowing is significant when the zenith observation angle θ is large, which corresponds to the case that the receiver is located near the sea surface. When θ is small, shadowing can be negligible. In the following section, one surface reflection is considered, and the illumination function with one reflection is derived basing on the Smith model.

2.2 Illumination function with one reflection

It is reported that models of sea surface emissivity which do not consider surface reflections underestimate the surface emissivity [1, 13, 11]. For higher accuracy, surface reflections should be taken into account. The key to the problem lies in deriving the illumination function with surface reflections.

In this section, a statistical illumination function with one surface reflection (called first-order) is derived. It is recalled that the geometrical optics approximation (GO) is employed, under which specular reflections are considered. In the infrared domain, the sea surface is smooth enough in terms of the surface radius curvature versus the studied wavelength, so that the geometrical optics approximation is assumed to be valid.

To take into account surface reflections, the main task lies in the calculation of the probability that an emission ray from an arbitrary point of the surface arrives at the receiver after it is reflected once or several times by some other points of the surface (surface-emitted surface-reflected). Fig. 2.13 shows one surface reflection as an example.

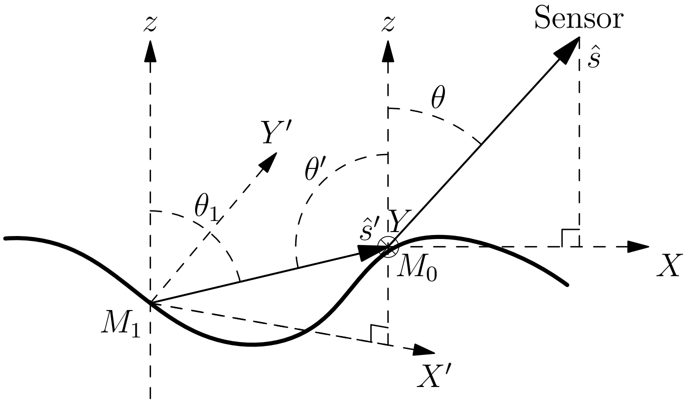

Figure 2.13: The emission ray form the source point M_1 propagates along the $\hat{s}'$ direction. It intersects the surface at M_0, and is then reflected specularly to the receiver along the $\hat{s}$ direction.

An emission ray starts from the source point M_1 and propagates along the $\hat{s}'(\theta_1, \phi_1)$ direction. It intersects the surface at point M_0, where it is reflected to the observation direction $\hat{s}(\theta, \phi)$, where $\theta_1 \in [0°, 180°]$ and $\phi_1 \in [0°, 360°]$ are zenith and azimuth angle of $\hat{s}'$. Note that $\hat{s}'$, $\hat{s}$ and $\hat{z}$ are not necessarily in the same plane.

The zenith angle $\theta' \in [0°, 180°]$ of $-\hat{s}'$ is an important parameter which affect heavily the fact that the incident ray $\hat{s}'$ originates from the sky or the surface.

Several authors tried to take into account surface reflections in their emissivity models. For example, the models of Watts *et al.* [39] and of Wu & Smith [1] are empirical models which introduced cut-off angles to extimate the probability of having single surface reflection. The model of Masuda [11] is an analytical model, but the results were not in good agreement with numerical results [22]. To calculate the emissivity with surface reflections with accuracy, a more accurate illumination function with surface reflections has to be developed.

2.2.1 Improved statistical model

In this thesis, one surface reflection is considered for the emissivity calculation. A monostatic statistical illumination function with one surface reflection is developed in this section, which gives the probability that the emission ray from an arbitrary point M_1 of the surface arrives at the receiver after it is reflected once by some other surface point M_0.

2.2.1.1 Geometric calculation of the reflection

In this thesis, the GO approximation is assumed to be valid, which means that local specular reflections are considered. The observation direction $\hat{s}$ is given by the zenith angle θ and the azimuth angle ϕ in Eq. (2.2). The unitary normal vector $\hat{n}_0$ is given by the slope of M_0 in Eq. (2.1).

With the knowledge of $\hat{s}$ and $\hat{n}_0$, the unitary vector of the reflected ray $-\hat{s}'$ can be obtained by the laws of reflection, given by:

$$\begin{aligned} -\hat{s}' &= 2\hat{n}_0(\hat{n}_0 \cdot \hat{s}) - \hat{s}, \\ &= 2\cos\chi_0 \hat{n}_0 - \hat{s}, \end{aligned} \tag{2.57}$$

where $\cos\chi_0$ is given by Eq. (2.3), with χ_0 being the local angle of incidence. According to Eq. (2.2), the vector $\hat{s}'$ can also be expressed by its zenith angle $\theta_1 \in [0°, 180°]$ and its azimuth angle $\phi_1 \in [0°, 360°]$, given by:

$$\begin{aligned} \theta_1 &= \operatorname{acos}(\hat{s}'_z), \\ \cos\phi_1 &= \hat{s}'_x / \sin\theta_1, \\ \sin\phi_1 &= \hat{s}'_y / \sin\theta_1, \end{aligned} \tag{2.58}$$

with $\hat{s}'_{x,y,z}$ being the x, y and z component of vector $\hat{s}'$. The slope of the ray $M_0(-\hat{s}')$ (or the ray $M_1(\hat{s}')$) is given by:

$$\mu_1 = \cot\theta_1. \tag{2.59}$$

The local angle of incidence of the point M_1 is given in the same way as Eq. (2.3) by:

$$\cos\chi_1 = \frac{\cos\theta_1 - (\gamma_{x_1}\cos\phi_1 + \gamma_{y_1}\sin\phi_1)\sin\theta_1}{\sqrt{1 + \gamma_{x_1}^2 + \gamma_{y_1}^2}}, \tag{2.60}$$

where γ_{x_1} and γ_{y_1} are the slopes of the point M_1 with respect to the x and y directions, respectively.

For better convenience in the calculation, a new system of coordinates (X', Y', z) is defined by rotating anticlockwise the basis (x, y) through an angle ϕ_1 about the z axis, so that the ray $M_1(\hat{s}')$ lies in the (X', z) plane. The slope of M_1 in the (x, y, z) and (X', Y', z) systems of coordinates are related to each other by:

$$\begin{array}{lcl} \gamma_{x_1} & = & \gamma_{X_1'} \cos\phi_1 - \gamma_{Y_1'} \sin\phi_1 \\ \gamma_{y_1} & = & \gamma_{X_1'} \sin\phi_1 + \gamma_{Y_1'} \cos\phi_1 \end{array}, \tag{2.61}$$

or inversely by:

$$\begin{array}{lcl} \gamma_{X_1'} & = & \gamma_{x_1} \cos\phi_1 + \gamma_{y_1} \sin\phi_1 \\ \gamma_{Y_1'} & = & -\gamma_{x_1} \sin\phi_1 + \gamma_{y_1} \cos\phi_1 \end{array}, \tag{2.62}$$

where $\gamma_{X_1'}$ and $\gamma_{Y_1'}$ are the slopes of the point M_1 with respect to the X' and Y' directions, respectively. Note that the directions X' and X are not necessarily colinear with each other.

2.2.1.2 Statistical determination of the problem

The problem can be expressed equally as determining the probability that the ray from M_0 to the receiver (denoted as $M_0(\hat{s})$) does not intersect the surface while the ray from M_0 to M_1 (denoted as $M_0(-\hat{s}')$) intersects the surface, which can be written mathematically as:

$$\begin{array}{rcl} S_{\mathrm{M}}^1 & = & p(M_0(\hat{s}) \text{ does not intersect } \cap M_0(-\hat{s}') \text{ intersects}), \\ & = & p(M_0(\hat{s}) \text{ does not intersect}) \\ & & \times p(M_0(-\hat{s}')\text{intersects}|\ M_0(\hat{s}) \text{ does not intersect}), \\ & = & p(M_0(\hat{s}) \text{ does not intersect}) \\ & & \times\left[1 - p(M_0(-\hat{s}') \text{ does not intersect} \mid M_0(\hat{s}) \text{ does not intersect})\right] \\ & = & p(a)[1 - p(b|a)], \end{array} \tag{2.63}$$

where "$M_0(\hat{s})$ *does not intersect the surface*" is denoted symbolically as "a" and "$M_0(-\hat{s}')$ *does not intersect the surface*" as "b".

The probability $p(a)$ corresponds to the statistical illumination function without surface reflections. The probability $p(b)$ is obtained similarly by:

$$p(b) = A \exp\left[-\int_{-\infty}^{0} g^{-}(\mu_1|\gamma_{x_0}, \gamma_{y_0}, \zeta_0; \tau)\, \mathrm{d}\tau\right], \tag{2.64}$$

Here, the integration range is changed from $\tau \in (0, +\infty)$ to $\tau \in (-\infty, 0)$, because the ray $M_0(-\hat{s}')$ propagates toward the negative direction of X'. The superscript of g^{-} stands for rays propagating toward the negative direction of X'. The full expression of g^{-} is given in Appendix C. The conditional probability $p(b|a)$ can be obtained by modifying $p(b)$ with the correlation between the events a and b.

There is a strong correlation between the events a and b. The event "$M_0(\hat{s})$ *does not cross the surface*" is the prerequisite for the existence of $M_0(-\hat{s}')$: $M_0(-\hat{s}')$ is the reflected ray of $M_0(\hat{s})$. It makes θ' different from θ: θ' is the reflection angle which depends on θ and on the slope of M_0 according to the law of reflection, whereas θ is an arbitrary angle ranging from 0 to $\pi/2$. The constant A for $p(b)$ must check that $M_0(-\hat{s}')$ does not go into the surface at the very beginning. For example, A might be another unit step function $\Upsilon(\gamma_{X_0'} - \mu_1)$. However, knowing that $M_0(-\hat{s}')$ is the reflected ray of $M_0(\theta)$ gives information on both the slopes of M_0 and $M_0(-\hat{s}')$. According to the law of reflection, it is obvious that the reflected ray does not go into the surface. In other words, $\gamma_{X_0'} > \mu_1$ is always satisfied, which means that A must be set to $A \equiv 1$. As a result, $p(b|a)$ is obtained approximately by modifying $p(b)$ as:

$$p(b|a) \approx \exp\left[-\int_{-\infty}^{0} g^-(\mu_1|\gamma_{x0},\gamma_{y0}\zeta_0;\tau)\mathrm{d}\tau\right]. \tag{2.65}$$

The statistical illumination function with one surface reflection is then derived:

$$S_1 = S_0\left\{1 - \exp\left[\int_{-\infty}^{0} g^-(\mu_1|\gamma_{x0},\gamma_{y0},\zeta_0;\tau)\,\mathrm{d}\tau\right]\right\}. \tag{2.66}$$

2.2.1.3 Expression for any uncorrelated process

Fig. 2.14 illustrates 2 configurations in which surface reflections happen. Note that $\hat{s}'$, $\hat{s}$ and $\hat{z}$ are not necessarily in the same plane. In case 1, the ray $M_0(-\hat{s}')$ propagates downward ($\theta' > 90°$), whereas in case 2 it propagates upward ($\theta' < 90°$). Eq. (2.66) can be greatly simplified according to each configuration.

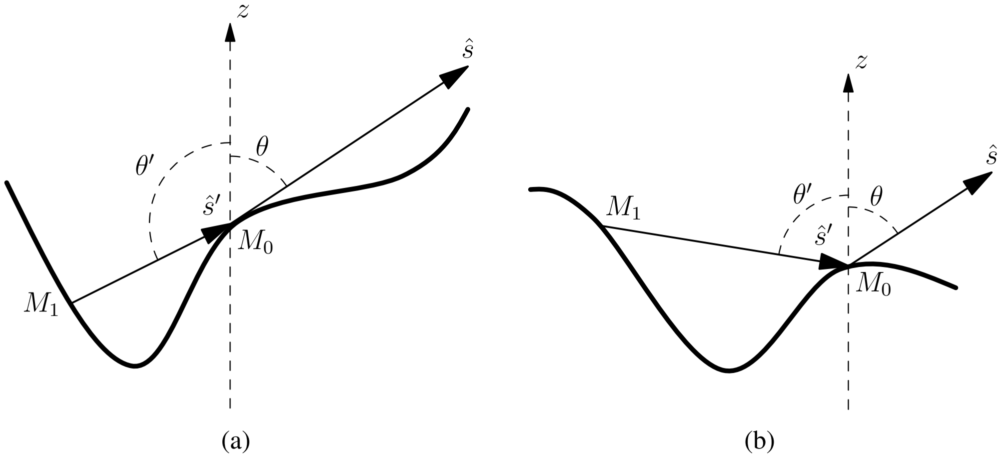

Figure 2.14: Two configurations of surface reflections. (a) case 1, $\theta' > 90°$; (b) case 2, $\theta' < 90°$. Note that $\hat{s}'$, $\hat{s}$ and $\hat{z}$ are not necessarily in the same plane (M_1 may not in the (X, z) plane).

The probability $p(a)$ corresponds to the statistical illumination function without surface reflections. In this thesis, surfaces with infinite length are considered. As shown in the previous section, the Smith illumination function agrees better with the Monte Carlo ray-tracing method than the model of Wagner. As a result, it is employed to evaluate $p(a)$. To simplify the problem, the correlation between the heights and the slopes of different points is ignored here. The uncorrelated $p(a)$ is given by:

$$p(a) = S_{\mathrm{M}}^0 = \Upsilon(\mu - \gamma_{X_0})F(\zeta_0)^{\Lambda(\mu)}. \tag{2.67}$$

In case 1, where the ray $M_0(-\hat{s}')$ propagates downward ($\theta' > 90°$), the conditional probability $p(b|a) = 0$. It can be calculated strictly as shown in Appendix C, or more physically, it can be explained as: a ray propagating downward certainly intersects the surface. Thus its complementary probability equals 0.

In case 2, where the ray $M_0(-\hat{s}')$ propagates upward ($\theta' < 90°$), the conditional probability $p(b|a)$ is given by (see Appendix C for calculation details):

$$p(b|a) = F(\zeta_0)^{\Lambda^-(\mu_1)}, \qquad \text{for} \qquad \theta' < 90°, \tag{2.68}$$

where $\Lambda^-(\mu_1)$ is given by:

$$\Lambda^-(\mu_1) = \frac{1}{\mu_1}\int_{-\infty}^{\mu_1} (\gamma - \mu_1) p_\gamma(\gamma)\, \mathrm{d}\gamma. \tag{2.69}$$

For a Gaussian slope PDF $p_\gamma(\gamma)$ (see Eq. (1.7)), Λ^- is given by:

$$\begin{cases} \Lambda^-(\nu_1) = -1 - \dfrac{\exp(-\nu_1^2) - \nu_1\sqrt{\pi}\,\mathrm{erfc}(\nu_1)}{2\nu_1\sqrt{\pi}} \\ \nu_1 = \dfrac{\mu_1}{\sigma_\gamma\sqrt{2}} \end{cases} \tag{2.70}$$

For non Gaussian slope PDF $p_\gamma(\gamma)$ (see Eq. (1.9)), the calculation of Λ^- is shown in Appendix (A).

To sum up, the statistical illumination function with one surface reflection (first-order) is given by:

$$\begin{aligned} S_{\mathrm{M}}^{1,\mathrm{unco}}(\theta, \gamma_{x_0}, \gamma_{y_0}, \zeta_0) &= \Upsilon(\mu - \gamma_{X_0}) F(\zeta_0)^{\Lambda(\mu)} \\ &\quad \times \begin{cases} 1 & \text{if} \quad \theta' > 90° \\ 1 - F(\zeta_0)^{\Lambda^-(\mu_1)} & \text{if} \quad \theta' < 90° \end{cases}. \end{aligned} \tag{2.71}$$

It is recalled that the illumination function without reflections (zero-order) involves the slope of M_0 by the Heaviside function $\Upsilon(\mu - \gamma_{X_0})$, which gives only two alternatives: the facet is either possible ($\Upsilon = 1$) or impossible ($\Upsilon = 0$) to be illuminated. However, the illumination function is more complicated to consider one reflection, as it involves an incident ray and a reflected ray. The slope of the reflected ray heavily affects the illumination function. As a result, the points with slope fulfilling the $\Upsilon = 1$ condition is redivided in two parts. The first part corresponds to case 1, where the reflected ray goes downward and surely intersects the surface. Thus, the first-order monostatic illumination function requires only calculating the probability that the point M_0 is viewed by the receiver, which equals $F(\zeta_0)^{\Lambda(\mu)}$. The other part corresponds to case 2, where the reflected ray goes upward. The first-order illumination function requires considering additionally the probability that the reflected ray $M_0(-\hat{s}')$ intersects the surface during propagation. As a result, an additional term $1 - F(\zeta_0)^{\Lambda(\mu_1)}$ shows up.

2.2.1.4 Expression for a correlated Gaussian process

For a correlated Gaussian surface, the illumination function with one reflection is given by equation (2.66), where g and g^- are obtained with considering the correlation between heights and slopes. The conditional PDF of the heights and slopes of two points of the surface (Eq. (1.17)) is thus used to include the correlation. The integration over τ is performed numerically. The calculation is similar to that of the correlated zero-order illumination function.

2.2.1.5 Discussion on first-order illumination function

It is notable that this statistical illumination function with one reflection S_{M}^{1} depends on the angle of incidence θ (or equally on the slope of the incident ray $\mu = \cot\theta$), the height and the slope of M_0, while surprisingly, the height and the slope of M_1 have no influence on S_{M}^{1}. Bourlier *et al.* [41] developed a statistical illumination function with multiple surface reflections, where the statistical first-order illumination function[4] is expressed in terms of the slopes and the heights of both M_0 and M_1. The difference comes from the different expression of M_1. In the model developed here, M_1 is an uncertain point, which exists but whose exact position is unknown and of no importance. Bourlier *et al.* defined the position of M_1 to be the end of an observation length $\tau = l_1$. However, l_1 is in fact the length of the sub-surface $\tau \in (0, l_1)$, and $S_{\mathrm{M}}^{0}(\mu, \gamma_0, \zeta_0, l_1)$ only gives the probability that the ray $M_0(\theta)$ crosses this sub-surface, which does not ensure that M_1 is at the point $\tau = l_1$. Bourlier developed another similar model [15] to calculate the surface emissivity . The result shows that his model underestimates greatly the surface reflection effect.

Although the monostatic illumination function with one reflection does not depend on M_1, it does restrict the height and the slope of M_1. As discussed in section 2.2.1.3, the event "*ray* $M_0(-\hat{s}')$ *intersects the surface*" does not give restriction to M_0. However, as $M_0(-\hat{s}')$ intersects the surface at the point M_1, it gives restrictions to the height and the slope of M_1 as:

$$\begin{cases} \zeta_1 \in (\zeta_0, +\infty) & \text{if} \quad \theta' < 90^\circ \\ \zeta_1 \in (-\infty, \zeta_0) & \text{if} \quad \theta' > 90^\circ \end{cases} . \tag{2.72}$$

and

$$\gamma_{X_1'} < \mu_1. \tag{2.73}$$

The above restriction should be taken into account when determining some parameters which depend on the height and the slope of M_1 and on this illumination function, for example the monostatic illumination function with more reflections and the surface reflectance.

2.2.1.6 Expression for 1D surfaces

The above expressions of the monostatic illumination function with one reflection are developed for 2D surfaces (3D problem). Sometimes, it is assumed that the surfaces is 1D (2D problem) to reduce the complexity of the problem.

For 1D surfaces, the zenith angle of a vector is usually oriented to better defined the direction of the vector. It is convenient to define the horizontal direction of the receiver as the positive x direction, and the direction of the receiver's zenith angle θ as the positive direction for the zenith angles.

The 1D monostatic illumination function with one reflection S_{M}^{1} can be obtained in the same way as the one for 2D surface. Here, S_{M}^{0} for 1D surfaces is given directly, by:

$$\begin{aligned} S_{\mathrm{M}}^{1,\mathrm{unco}}(\theta, \gamma_0, \zeta_0) &= \Upsilon(\mu - \gamma_0) F(\zeta_0)^{\Lambda(\mu)} \\ &\times \begin{cases} 1 & \text{if} \quad |\theta'| > 90^\circ \\ 1 - F(\zeta_0)^{\Lambda^-(\mu_1)} & \text{if} \quad 0 < \theta' < 90^\circ \\ 1 - F(\zeta_0)^{\Lambda(\mu_1)} & \text{if} \quad -90^\circ < \theta' < 0^\circ \end{cases} . \end{aligned} \tag{2.74}$$

---

[4] Bourlier *et al.* denoted the first-order defined here as second-order. M_0 and M_1 are also inversely denoted.

It is notable that for 2D surfaces, the third case corresponding to $-90^\circ < \theta' < 0^\circ$ does not exist. For 2D surface, this situation is considered in the case where $\phi = \phi_1 + 180^\circ$, which means that X' and X are in opposite directions. Note that for 1D surfaces, the reflected ray $-\hat{s}$ propagates toward the possitive end of x under this situation, thus $\Lambda(\mu_1)$ is used.

2.2.2 Numerical results

In this section, the numerical results of the first-order monostatic illumination function are presented. The marginal histograms of the first-order illuminated slopes and heights are shown, which describe the distributions of the slopes and the heights which may lead to single surface reflection. The average monostatic illumination function with one reflection is also calculated, which equals the proportion of the surface where surface reflections occur.

To evaluate the performance of the method presented, a Monte Carlo ray-tracing method is employed. For computational ease, 1D surfaces are considered ($\gamma_0 = \gamma_{x0} = \gamma_{X0}$, γ_{y0} and γ_Y are suppressed). The upwind direction is studied ($\sigma_\gamma = \sigma_{\gamma_x}$). It is assumed that the surface is a Gaussian process with Gaussian slope and height PDFs. The results with and without correlation (Gaussian height autocorrelation) are simulated and compared.

2.2.2.1 Monte Carlo ray-tracing method

To evaluate the model, a Monte Carlo ray-tracing algorithm is used, shown in Fig. 2.15. In the ray-tracing algorithm, a large number of 1D rough surfaces are generated, with Gaussian height and slope distributions. Moreover, the surface points are assumed to be correlated with a Gaussian height autocorrelation function, instead of being uncorrelated as in the model of Henderson *et al.* [13]. In this subsection, the surfaces generated have surface lengths $L = 100L_c$, where L_c is the surface correlation length. The Monte Carlo results are the average result of $N = 2000$ surfaces.

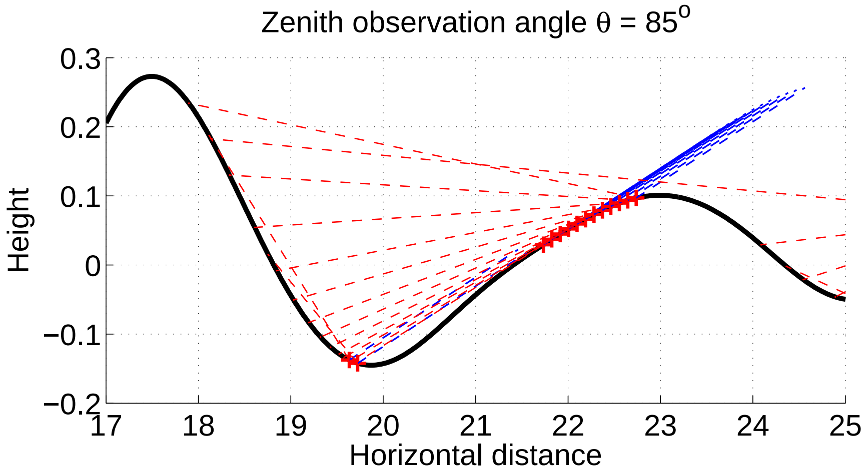

Figure 2.15: One sample of the ray-tracing method with one surface reflection for $\theta = 85^\circ$.

After the generation of the rough surfaces, the same ray-tracing algorithm shown in Sec. 2.1.5.2 is performed. The inverse ray path is used, which means that a ray is emitted by the receiver, which propagates along a given zenith observation angle θ to the surface (blue rays in Fig. 2.15). These rays are traced to find out the illuminated surface points. The illuminated points are noted as red "+", and the corresponding reflected rays (red rays) at these points are traced. For the reflected rays which intersect the surface again, the intersections, which correspond to point M_1, are noted. The corresponding reflection point is noted as M_0. Each surface point M_1 and its corresponding point M_0 are called one pair. The histogram of the slope of point M_0 is calculated to obtain the slope distribution, which corresponds to the marginal slope distribution of the first-order illumination. The percentage of the surface where single reflection occurs is given by $S_{\mathrm{M}}^{1,\mathrm{MC}} = N_i/N_s$, where N_s is the number of points of the generated surface, and N_i is the number of pairs of M_0 and M_1.

2.2.2.2 Marginal histograms $\widetilde{p}^1_{\gamma,\zeta}$

The first-order marginal histograms of the illuminated slopes and heights provide different aspects to examine the performance of the models. They are defined in a way very similar to that of the zero-order:

$$\begin{aligned} \widetilde{p}^1_{\gamma}(\mu,\gamma_0) &= p_\gamma(\gamma_0)\int_{-\infty}^{+\infty} S^1_{\mathrm{M}}(\mu,\gamma_0,\zeta_0)p_\zeta(\zeta_0)\mathrm{d}\zeta_0, \\ \widetilde{p}^1_{\zeta}(\mu,\zeta_0) &= p_\zeta(\zeta_0)\int_{-\infty}^{+\infty} S^1_{\mathrm{M}}(\mu,\gamma_0,\zeta_0)p_\gamma(\gamma_0)\mathrm{d}\gamma_0. \end{aligned} \tag{2.75}$$

For an uncorrelated first-order illumination function, Eq. (2.71) is applied to Eq. (2.75). For any height PDF, the integrations over ζ_0 are shown below.

For case 1, the integration is given by:

$$\begin{aligned} \widetilde{p}^{1,\mathrm{unco}}_{\gamma}(\mu,\gamma_0) &= p_\gamma(\gamma_0)\int_{-\infty}^{+\infty} F(\zeta_0)^{\Lambda(\mu)}p_\zeta(\zeta_0)\,\mathrm{d}\zeta_0 \\ &= \frac{1}{\Lambda(\mu)+1}p_\gamma(\gamma_0). \end{aligned} \tag{2.76}$$

For case 2, the integration is given by:

$$\begin{aligned} \widetilde{p}^{1,\mathrm{unco}}_{\gamma}(\mu,\gamma_0) &= p_\gamma(\gamma_0)\int_{-\infty}^{+\infty} F(\zeta_0)^{\Lambda(\mu)}[1-F(\zeta_0)^{\Lambda(\mu_1)}]p_\zeta(\zeta_0)\mathrm{d}\zeta_0 \\ &= \frac{\Lambda^-(\mu_1)}{[\Lambda(\mu)+1][\Lambda^-(\mu_1)+\Lambda(\mu)+1]}p_\gamma(\gamma_0). \end{aligned} \tag{2.77}$$

Unfortunately, as μ_1 is a function of γ_0, the integration over the slope γ_0 has to be calculated numerically. Moreover, it depends on the slope PDF. The slope PDF is assumed to be Gaussian for simplification here. The marginal histogram of illuminated heights is expressed as:

$$\begin{aligned} \widetilde{p}^1_{\zeta,\mathrm{unco}}(\mu,\zeta_0) &= F(\zeta_0)^{\Lambda(\mu)}p_\zeta(\zeta_0) \\ &\quad \left\{\int_{\gamma_0\in \text{ case 1}} p_\gamma(\gamma_0)\,\mathrm{d}\gamma_0 \right. \\ &\quad \left. + \int_{\gamma_0\in \text{ case 2}} \left[1-F(\zeta_0)^{\Lambda^-(\mu_1)}\right]p_\gamma(\gamma_0)\,\mathrm{d}\gamma_0\right\}. \end{aligned} \tag{2.78}$$

For a correlated process, the correlated first-order illumination function is used to replace $S_{\mathrm{M}}^{1}(\mu,\gamma_0,\zeta_0)$ in equation (2.75). The calculation of the first-order correlated illumination function is explained previously in Sec 2.2.1.4. The variable transformations given in equation (2.54) are also performed during the calculation. However, it is impossible to suppress σ_γ here, as μ_1 is a function of θ and γ_0 (see Eqs. (2.58) and (2.59)).

The result is shown in Fig. 2.16. To show the result clearly, the y scales of each sub-figure are different. Fig. 2.16 (a) and (b) show the histograms of the slopes and the heights of M_0 of a surface with RMS slope $\sigma_\gamma = 0.2$ (relatively calm sea surface, Beaufort scale ≈ 5) for an observation zenith angle $\theta = 80°$. This observation angle usually corresponds to receivers located near the sea surface, e.g. on a ship. Fig. 2.16 (c) and (d) shows the same simulation but for a surface with $\sigma_\gamma = 0.2$ (unlikely to be a sea surface). Fig. 2.16 (e) and (f) show the same histograms as (c) and (d) but for a much smaller observation zenith angle $\theta = 5°$. This observation angle typically corresponds to receivers located near the zenith.

In general, the uncorrelated histograms overestimate the surface reflections. The correlated first-order marginal histograms agree very well with the Monte Carlo results.

By comparing Fig. 2.16 (a) (b) and (c) (d), it is shown that for $\theta = 80°$, surface reflections are more significant for a surface with smaller RMS slope. In fact, the θ corresponding to the peak of the rate of occurrence of single surface reflection differs with the surface RMS slope, which is shown later.

It is interesting to have a closer look at Fig. 2.16 (a) and Fig. 2.16 (e). In Fig. 2.16 (e), two lobes show up, rather than one in 2.16 (a). A smaller lobe shows up in the region where the slope of M_0 has large absolute but negative values. In this region, the incident ray is reflected backward, which means the reflected ray propagates toward the receiver. In the lobe where the slope of M_0 is positive, the incident ray is reflected forward, which means the reflected ray propagates away from the receiver. Fig. 2.17 illustrates the geometric configurations corresponding to each segment of the slope histogram in Fig. 2.16 (e). The negative slope lobe does not show up in Fig. 2.16 (a) as θ is too large. To produce a backward reflection, the slope of M_0 should have a very large absolute but negative value (for $\theta = 80°$, $\gamma_0 \approx -5.67$, for the case in Fig. 2.16 (a) $s_0 \approx 28.35$), whose probability density is too low.

2.2.2.3 Average illumination function $\overline{\overline{S}}_{\mathrm{M}}^{1}$

To see the performance of the presented model, the average monostatic illumination function with one reflection is studied. It is obtained by integrating S_{M}^{1} over the heights and the slopes of M_0, given by:

$$\overline{\overline{S}}_{\mathrm{M}}^{1}(\theta) = \int_{-\infty}^{+\infty}\int_{-\infty}^{+\infty} S_{\mathrm{M}}^{1}(\theta,\gamma_0,\zeta_0)p(\gamma_0,\zeta_0)\,\mathrm{d}\zeta_0\,\mathrm{d}\gamma_0. \tag{2.79}$$

The integration over ζ_0 is given in the same way as in Eqs. (2.76) and (2.77), whose result is shown directly as:

$$\overline{S}_{\mathrm{M}}^{1}(\theta,\gamma_0) = \begin{cases} \dfrac{1}{\Lambda(\mu)+1}, & \text{case 1} \\ \dfrac{\Lambda^{-}(\mu_1)}{[\Lambda(\mu)+1][\Lambda^{-}(\mu_1)+\Lambda(\mu)+1]}, & \text{case 2} \end{cases}. \tag{2.80}$$

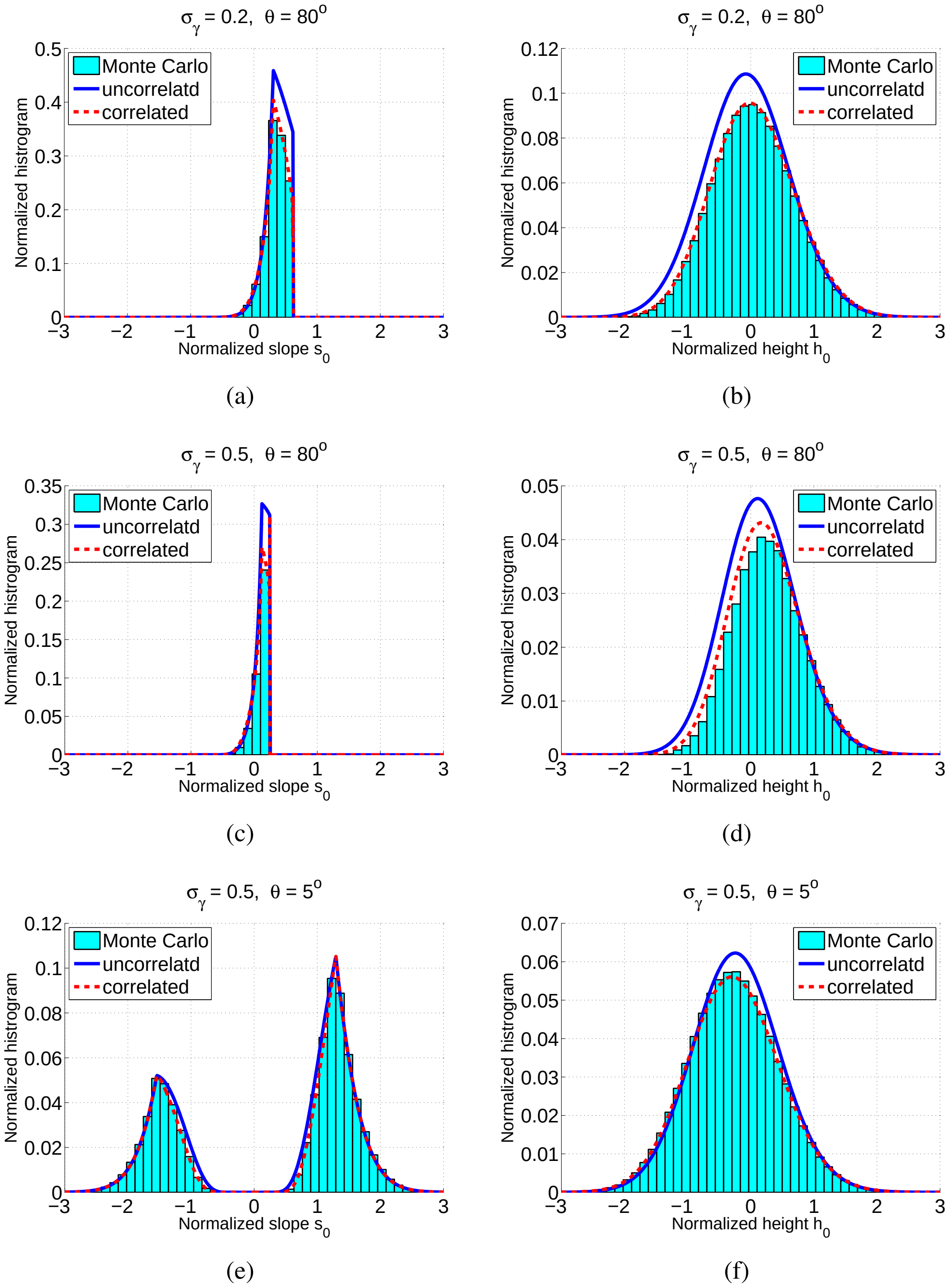

(a) (b)

(c) (d)

(e) (f)

Figure 2.16: First-order marginal histogram of slopes (left) and heights (right) versus the normalized slopes s_0 and heights h_0.

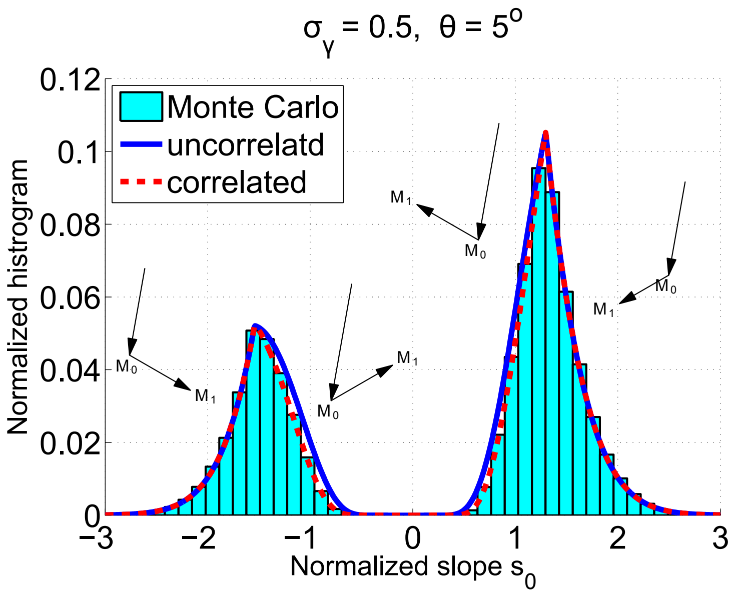

Figure 2.17: Configurations corresponding to each segment of the slope histogram.

However, the integration over γ_0 is more difficult to derive, as θ_1 is a function of γ_0 and θ. Besides, the slope PDF of the surface should be given precisely. As a result, it is calculated numerically, with the slope PDF assumed to be Gaussian.

The average monostatic illumination function with one reflection, with and without correlation, is shown in Fig. 2.18 and compared with the Monte Carlo ray-tracing method. Fig. 2.18 (a) shows the results for surfaces with RMS slope $\sigma_\gamma = 0.2$, whereas the results for surfaces with $\sigma_\gamma = 0.5$ is shown in Fig. 2.18 (b).

As predicted by Fig. 2.16, the present model without correlation agrees quite well with the Monte Carlo ray-tracing result. Overestimation is significant for large zenith observation angles, e.g. $\theta > 60^\circ$ for surfaces with RMS slope $\sigma_\gamma = 0.2$. With correlation, the agreement is greatly improved. Unfortunately, the model with correlation is too complex in formulation and takes considerably long computation time.

It is notable that the first-order illumination function is quite large for large zenith observation angles θ, with a maximum over 0.2 occurring at about $\theta \approx 75^\circ$ for surfaces with $\sigma_\gamma = 0.2$ and about $\theta \approx 50^\circ$ for surfaces with $\sigma_\gamma = 0.5$, which means that surface reflections are found at 20% area of the surface for these observation angles. In several papers about surface infrared emissivity [1, 13], it is said that the models without considering surface reflections underestimate the surface emissivity at large zenith observation angles by comparison with measurements. It is shown here that considering one surface reflection can be very promising to reduce the discrepancy between the analytical models and the measurements. This conclusion is proved in the next chapter.

2.2.2.4 Averaged illumination function $\overline{\overline{S}}^1_{\mathrm{M}}$: 2D

The average illumination function with one surface reflection $\overline{\overline{S}}^1_{\mathrm{M}}$ is also calculated for 2D surfaces. The ray-tracing Monte Carlo method is not performed, because the time of computation is too long.

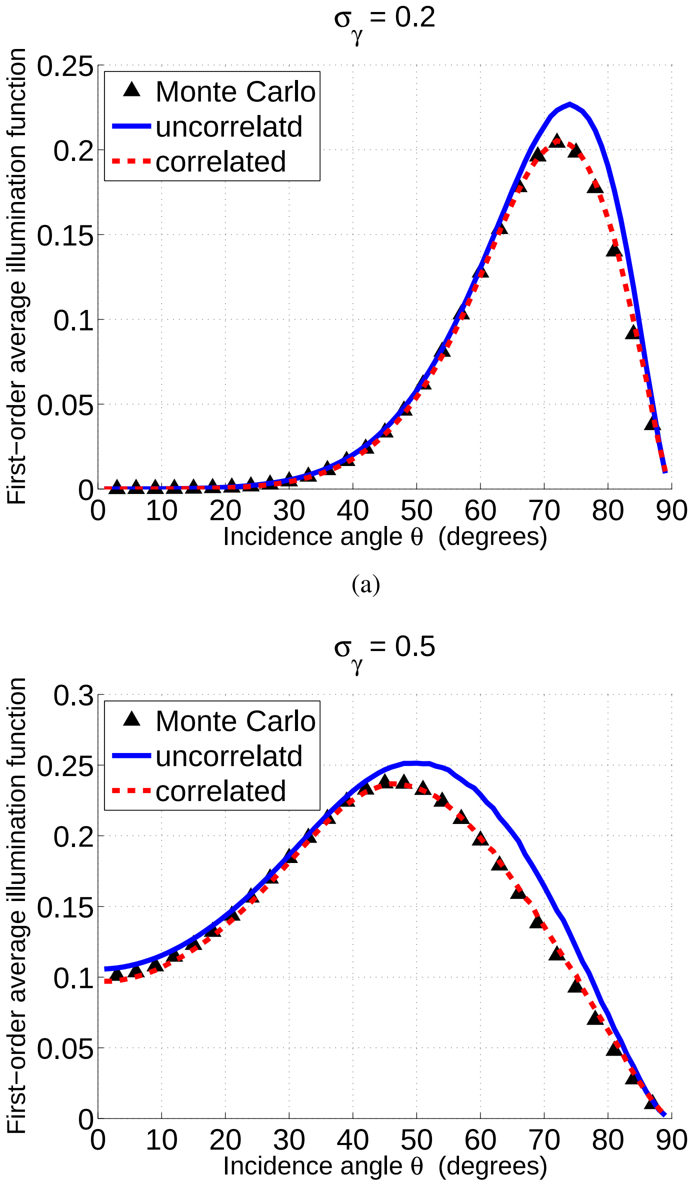

(a)

(b)

Figure 2.18: Correlated and uncorrelated average monostatic illumination functions with one surface reflection compared with Monte Carlo ray-tracing method for RMS slope $\sigma_\gamma = 0.2$ (a) and $\sigma_\gamma = 0.5$ (b).

Fig. 2.19 shows the average average illumination function with one surface reflection of 2D surface with respect to the azimuth angle ϕ (corresponds to the wind direction). The zenith angle is $\theta = 85°$. The wind speed is $u_{12} = 5$ m/s (a) and 10 m/s (b) (corresponding to Beaufort scale ≈ 3 and 5, respectively). The surface slope PDF is firstly assumed to be Gaussian (noted as G), then skewness (noted as S) and kurtosis (noted as K) effects are considered.

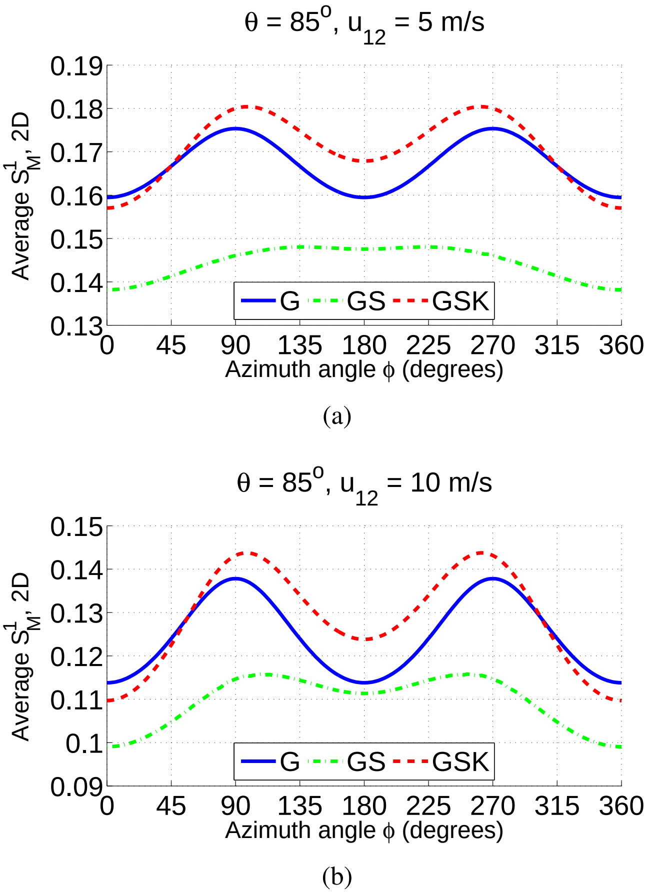

Figure 2.19: Average illumination function with one surface reflection of 2D surface with respect to the azimuth angle ϕ. The wind speed is $u_{12} = 5$ m/s (a) and 10 m/s (b).

It is shown in Fig. 2.19 that $\overline{\overline{S}}_{\mathrm{M}}^{1}$ depends on the wind direction. it is symmetry about the up-wind and cross-wind directions ($\phi = \{0°, 90°, 180°, 270°\}$) for Gaussian slope PDF. After the skewness effect is considered, $\overline{\overline{S}}_{\mathrm{M}}^{0}$ is symmetry only about the up-wind and down-wind directions ($\phi = \{0°, 180°\}$), which checks the conclusion obtained in Sec. 1.1.3.2.

2.2.3 Empirical approach

The performance of the first-order correlated illumination function is high, while the uncorrelated one takes less computation time and better meets the practical application requirements. For example, to compute one single point of the curve of the average first-order illumination function for a surface with $\sigma_\gamma = 0.2$ (Fig. 2.18 (a)), the correlated model takes 4.5 s on average, while the uncorrelated model takes

5.5×10^{-4} s only[5]. In this section, we aim at deriving an empirical method which could improve the performance of the uncorrelated illumination function while no significant extra computation time is added.

2.2.3.1 Determination of the empirical factor

As the illumination function with one reflection is developed based on the one without reflection, the goal here is to determine an empirical factor f, which is then multiplied with the uncorrelated monostatic illumination function without reflection to obtain an empirical one:

$$S_{\mathrm{M}}^{0,\mathrm{emp}} = f S_{\mathrm{M}}^{0,\mathrm{unco}}. \tag{2.81}$$

This empirical illumination function without reflection should agree well with the Monte Carlo result. The monostatic first-order illumination function would be improved automatically after the zero-order one is corrected.

The first task is to determine the form of the empirical factor. As we discussed in Sec. 2.1.6, the drawback of the uncorrelated illumination function without reflection is that neglecting the correlation between heights and slopes results in an equal probability of illumination for the points with $\gamma_0 < \mu$ (see the solid curves in Fig. 2.9). In fact, the illumination probability should decrease as s approaches ν (see the dashed curves in Fig. 2.9). Thus, the empirical factor should generate a curve similar to the angular illumination factor given by the monostatic zero-order illumination function with correlation. We assume that the empirical factor has the following form:

$$f = (B-1)\exp\left[-C(\nu - s_0)\right] + 1 \qquad \text{for} \qquad s_0 < \nu, \tag{2.82}$$

where B and C are constants for any given v. B ranges from 0 to 1, which describes the magnitude of the damping. C controls the rate of decreasing. Thus, the empirical factor decreases from 1 to B as s_0 approaches ν, which meets our requirement.

The next task is to obtain the parameters B and C. To do so, a series of samples are studied. For a given ν, the numerical sample of f is obtained by:

$$f_{\mathrm{num}} = \frac{\overline{S}_{\mathrm{M}}^{0,\mathrm{MC}}}{\overline{S}_{\mathrm{M}}^{0,\mathrm{unco}}}, \tag{2.83}$$

where $\overline{S}_{\mathrm{M}}^{0,\mathrm{MC}}$ is the Monte Carlo result of zero-order angular illumination factor, given by dividing the illuminated slope histogram by the Gaussian slope PDF. $\overline{S}_{\mathrm{M}}^{0,\mathrm{unco}}$ is the uncorrelated height-averaged monostatic zero-order illumination function. B is the fraction given by:

$$B = \frac{\overline{S}_{\mathrm{M}}^{0,\mathrm{MC}}(s_0 = \nu)}{\overline{S}_{\mathrm{M}}^{0,\mathrm{unco}}(s_0 = \nu)}. \tag{2.84}$$

With the least square method, C can be obtained without difficulty. The least square method for the calculation of C can be found in Appendix D. Substituting B and C back into Eq. (2.82), the empirical factor for a given ν is obtained. Take $\nu = 0.31$ (corresponding to $\sigma_\gamma = 0.2$, $\theta = 85°$) for example, B and C are given by:

$$B = 0.6382 \qquad C = 3.6619. \tag{2.85}$$

---

[5] For an office PC, with CPU 3 GHz and 4.0 GB memory, 32bit system.

Table 2.1: Parameters for B and C

n	0	1	2	3	4	5
b_n	0.8660	1.2388	2.2895	-2.0372	0.8845	-0.1476
c_n	6.1608	-18.0344	39.3244	-36.2345	16.2922	-2.7097

The empirical factor f (dashed curve) and the numerical samples f_{num} (scattered points) are shown for $\nu = 0.62$ in Fig. 2.20 (a). The least square method is performed to fit only the points where $f_{\mathrm{num}} < 1$. In the region where $f_{\mathrm{num}} \geq 1$, $\overline{S}_{\mathrm{M}}^{0,\mathrm{MC}}$ and $\overline{S}_{\mathrm{M}}^{0,\mathrm{unco}}$ are very similarly to each other, thus it does not need any correction (See Fig. 2.8 (c)). Multiplying the empirical factor and the angular illumination factor of the uncorrelated zero-order illumination function leads to the zero-order empirical angular illumination factor, which is then compared with the correlated one. It is shown in Fig. 2.20 (b) that the empirical angular illumination factor is no longer constant but decreases as s_0 approaches ν, which is the same case in the correlated angular illumination factor. In the region where $f < 1$, the empirical angular illumination factor fits that of the correlated illumination function so great that the empirical illumination function seems to match the performance of the correlated illumination function.

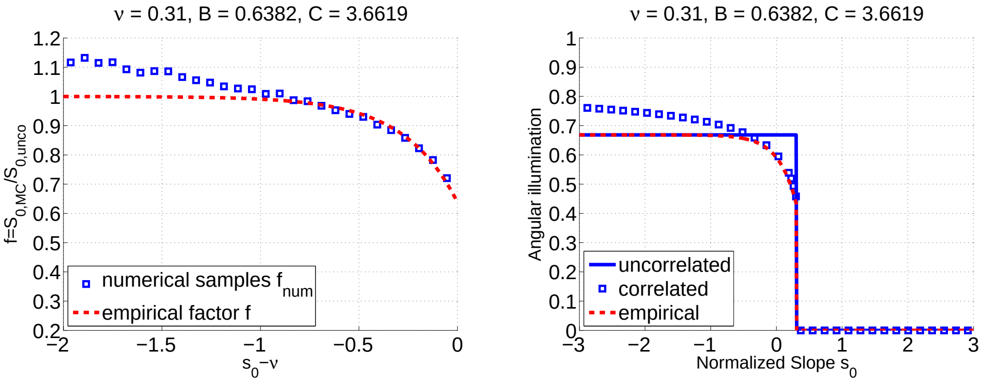

(a) (b)

Figure 2.20: Empirical factor together with the numerical samples (a), and the comparison of angular illumination factor of the correlated, uncorrelated and empirical zero-order illumination functions (b).

For any ν, the previous step is repeated and $B(\nu)$ and $C(\nu)$ are obtained. As indicated by Bourlier *et al.* [26], shadowing can be neglected for $\nu > 2$. In this paper, all $\nu \in [0.05, 2]$ are investigated, with a step equals 0.05. The range $\nu \in [0, 0.05)$ is not included because the surface generated in the Monte Carlo algorithm is not of infinite length which heavily affects the result. Unfortunately, B and C are not constants but vary with ν, as shown by the scattered points in Fig. 2.21. As a result, a power 5 polynomial is used to fit the data, which is shown:

$$B = \sum_{i=0}^{i=5} b_i \nu^i, \qquad C = \sum_{i=0}^{i=5} c_i \nu^i. \tag{2.86}$$

Another least square method is performed and the parameters b_n and c_n are reported in Tab. 2.1. B and C in equation (2.86) are shown as solid curves in Fig. 2.21.

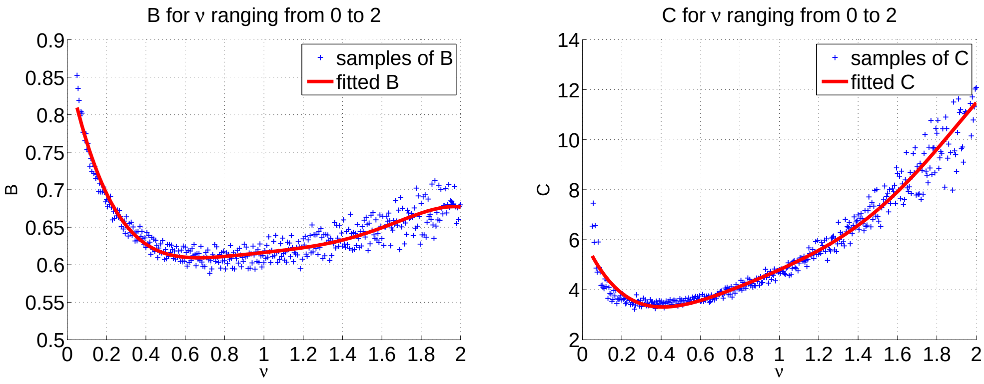

(a) (b)

Figure 2.21: B (left) and C (right) for $v \in [0.05, 2]$.

Although it is time consuming to obtain all the Monte Carlo results needed to compute b_n and c_n, it is very easy to compute the empirical factor once b_n and c_n are obtained. The data in Tab. 2.1 can be used for the whole region $\nu \in [0, 2]$ (that is, including $[0, 0.005]$), beyond which shadowing is negligible. f is set to 1 for $\nu > 2$. The empirical factor is then modified as follows to fit all situations:

$$f(\nu, s_0) = \begin{cases} (B-1)\exp\left(-C(\nu - s_0)\right) + 1 & \text{for} \quad \nu \in [0,2] \\ 1 & \text{for} \quad \text{otherwise} \end{cases}. \tag{2.87}$$

2.2.3.2 Simulation of the empirical S_{M}^{0}

The zero-order empirical illumination function $S_{\mathrm{M}}^{0,\mathrm{emp}}$ is obtained by multiplying zero-order uncorrelated illumination function with the empirical factor. Recall that the Smith illumination function (Eq. (2.35)) is used in this thesis, the result is given by:

$$S_{\mathrm{M}}^{0,\mathrm{emp}}(\mu, \gamma_0, \zeta_0) = S_{\mathrm{M}}^{0,\mathrm{S,unco}}(\mu, \gamma_0, \zeta_0) \times f. \tag{2.88}$$

As the empirical factor does not depend on the height, it does not affect the integration over ζ_0. Thus the empirical zero-order marginal histogram of illuminated slopes is given by:

$$\widetilde{p}_{\gamma}^{0,\mathrm{emp}}(\mu, \gamma_0) = \frac{\Upsilon(\mu - \gamma_0)}{\Lambda(\mu) + 1} p_{\gamma}(\gamma_0) \times f. \tag{2.89}$$

Fig. 2.22 shows the results for $\nu = 0.31$ (corresponding to $\sigma_\gamma = 0.2$, $\theta = 85°$) and $\nu = 0.62$ (corresponding to $\sigma_\gamma = 0.2$, $\theta = 80°$). It is shown that the empirical factor improves the performance of the zero-order uncorrelated illumination function effectively.

The first-order empirical monostatic illumination function is given by:

$$S_{\mathrm{M}}^{1,\mathrm{emp}}(\mu, \gamma_0, \zeta_0) = \begin{cases} f(\nu, s_0) F(\zeta_0)^{\Lambda(\mu)}, & \text{case 1} \\ f(\nu, s_0) F(\zeta_0)^{\Lambda(\mu)} [1 - f(\nu_1, s_0) F(\zeta_0)^{\Lambda(\mu_1)}], & \text{case 2} \end{cases}, \tag{2.90}$$

where $\nu_1 = \mu_1 / (\sigma_\gamma \sqrt{2})$. To obtain the average empirical first-order shadowing function, equation (2.90) is averaged over γ_0 and ζ_0:

$$\overline{\overline{S}}_{\mathrm{M}}^{1,\mathrm{emp}}(\mu) = \int_{-\infty}^{+\infty} \int_{-\infty}^{+\infty} S_{\mathrm{M}}^{1,\mathrm{emp}}(\mu, \gamma_0, \zeta_0) p_{\zeta}(\zeta_0) p_{\gamma}(\gamma_0) \mathrm{d}\zeta_0 \mathrm{d}\gamma_0. \tag{2.91}$$

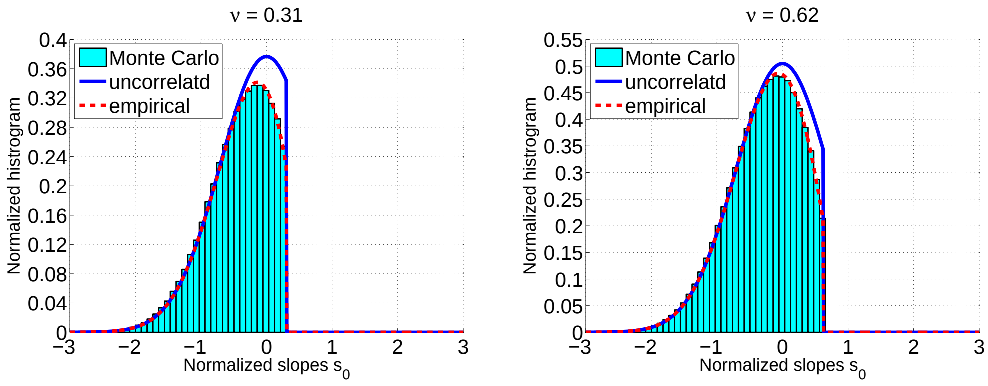

(a) (b)

Figure 2.22: Zero-order empirical marginal histogram of illuminated slopes for $\nu = 0.31$ (a) (corresponding to $\sigma_\gamma = 0.2$, $\theta = 85°$) and $\nu = 0.62$ (b) (corresponding to $\sigma_\gamma = 0.2$, $\theta = 80°$).

The integration over the heights ζ_0 can still be done analytically, which is given by:

$$\overline{S}_{1,\mathrm{e}}(\mu,\gamma_0)=\begin{cases}\dfrac{1}{\Lambda(\mu)+1}f(\nu,s_0), & \text{case 1}\\ \dfrac{[1-f(\nu_1,s_0)][\Lambda(\mu)+1]+\Lambda(\mu_1)}{[\Lambda(\mu)+1][\Lambda(\mu_1)+\Lambda(\mu)+1]}f(\nu,s_0), & \text{case 2}\end{cases}. \qquad (2.92)$$

Thus, the marginal histogram of the illuminated slopes given by the first-order empirical illumination function is expressed analytically by:

$$\tilde{p}^{1}_{\gamma_0,\mathrm{emp}}(\mu,\gamma_0)=\overline{S}^{1,\mathrm{emp}}_{\mathrm{M}}(\mu,\gamma_0)p_\gamma(\gamma_0). \qquad (2.93)$$

Fig. 2.23 shows the results for $\{\sigma_\gamma = 0.2, \theta = 80°\}$ and for $\{\sigma_\gamma = 0.5, \theta = 5°\}$, which are the same parameters as in Fig. 2.16 (a) and (e). It can be seen that the empirical illumination function agrees greatly with the Monte Carlo result at large angles of incidence (Fig. 2.23 (a)). At small zenith angles θ, there is no significant improvement (Fig. 2.23 (b)). Fortunately, the discrepancy is small in this area.

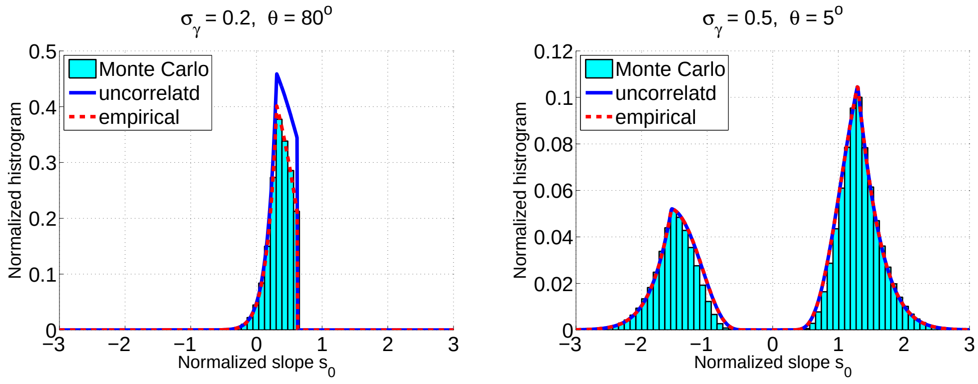

(a) (b)

Figure 2.23: First-order empirical marginal histogram of illuminated slopes.

As μ_1 and $f(\nu_1)$ are functions of γ_0, the integration over γ_0 is performed numerically. The results are shown in Fig. 2.24 for $\sigma_\gamma = 0.2$ and 0.5, where again very good agreements are obtained.

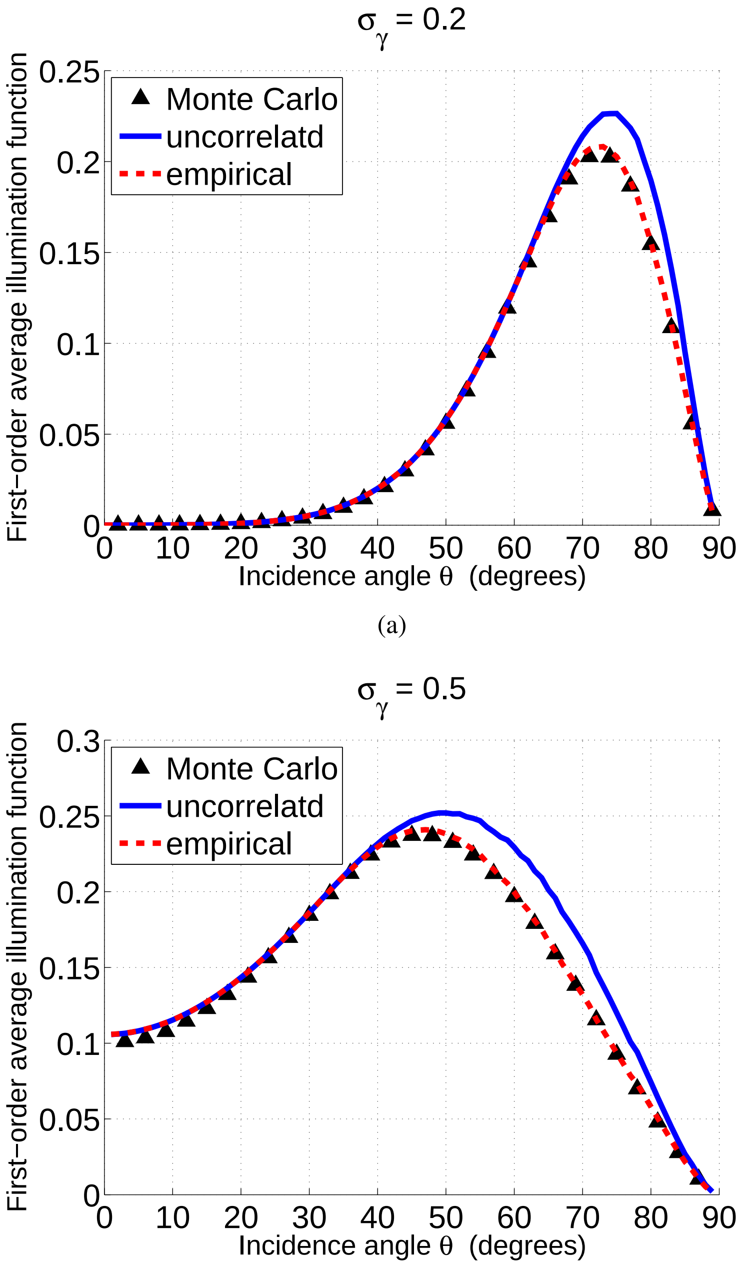

(a)

(b)

Figure 2.24: Empirical average first-order illumination function comparing with the Monte Carlo method.

It is shown that the empirical illumination function works quite well, with nearly the same performances as the correlated illumination function. Besides, it consumes much less computation time. Take the same example as we did at the beginning of this subsection: to compute one single point of the curve of the average first-order illumination function for a surface with $\sigma_\gamma = 0.2$, the empirical model takes 1.1×10^{-3} s only. This empirical factor is a good compromise between accuracy and time consumption for solving the problem.

The first-order monostatic illumination function is an important parameter when calculating the sea surface infrared emissivity, and it is the key work of this thesis. We have published this first-order illumination function in 2011 [28].

2.3 Conclusion

In this chapter, the monostatic illumination function is studied. The main models of the monostatic illumination function without surface reflections (zero-order) are reviewed. It is shown that the Smith illumination function agrees best with the Monte Carlo ray-tracing method. Surface reflections are studied. A statistical illumination function with one surface reflection is developed. It is shown that this first-order illumination function agrees well with the result of the Monte Carlo ray-tracing method.

In what follows, the sea surface infrared emissivity is studied, where shadowing and surface reflections are taken into account. The Smith illumination function is used to evaluate the shadowing effect. The first-order illumination function is the main contribution of this thesis. The model developed here is used in the next chapter to take single surface reflection into account when calculating the surface emissivity.

3

Sea surface infrared emissivity

Sea surface infrared emissivity in the atmospheric transmission windows ($\lambda \in [3, 5]$ and $[8, 13]$ μm) is an important parameter in oceanic remote sensing, e.g. for deriving the sea surface temperature. Sea surface infrared emissivity is nearly constant for observation directions (θ see Fig. 3.1) near zenith, but it varies significantly with the observation angle measured from zenith (named zenith angle). In these observation directions, shadowing and surface reflections become significant, increasing the difficulty in predicting the sea surface emissivity with accuracy.

Early models of sea surface infrared emissivity derived the emissivity without considering sea surface reflections (named direct emissivity, or zero-order emissivity). By contrast, the shadowing effect was usually considered. However, Smith *et al.* [37] reported a difference of about 0.02-0.03 between the measurements and the direct emissivity model of Masuda *et al.* [10] for a zenith angle θ (see Fig. 3.1) of $73.5°$, because surface reflections were ignored.

Several authors tried to include surface reflections in their emissivity models. The main difficulty lies in the derivation of the probability of observing surface reflections at the consider surface point, which is called the nth-order illumination function, where n denotes the number of surface reflections. This part was studied in the previous chapter, and an analytical first-order illumination function was developed.

It is also reported that infrared intrinsic radiation of surfaces is partially polarized at large zenith observation angles ($\theta \rightarrow 90°$) [43, 36]. It is of great interest to study the polarization state of the surface radiation energy.

In this chapter, the sea surface infrared emissivity is determined, by taking both the zero- (direct) and first-order emissivity contributions into account, denoted as ε_0 and ε_1, respectively. The first-order emissivity is also called surface-emitted surface-reflected emissivity, or SESR for short [39]. Polarization is taken into account and carefully dealt with, and the degree of polarization (DOP) is calculated. The sea surface is modeled as one- (1D surface, 2D problem) and two-dimensional (2D surface, 3D problem). Moreover, the skewness and kurtosis effects of the sea surface are considered, following the mathematical development of the sea surface slope probability density function (PDF) given by Cox and Munk [17] and Bourlier *et al.* [32].

This chapter is organized as follows: In section 3.1, the emissivity without surface reflection (ε_0, direct emissivity) is calculated, whereas in section 3.2, the analytical model of the emissivity with one surface reflection (ε_1, first-order or SESR emissivity) is derived. Polarization is taken into account and the degree of polarization (DOP) is calculated. Emissivity with two surface reflections (ε_2, second-order) is also calculated with a Monte Carlo ray-tracing method. The sea surface infrared emissivity calculated by the analytical model is then compared with measurements.

3.1 Direct infrared emissivity ε_0

The sea surface infrared emissivity without reflection, which is shown in Fig. 3.1, corresponds to the intrinsic radiation energy propagating directly toward the receiver situated in the observation direction $\hat{s}(\theta, \phi)$, where $\theta \in [0°, 90°]$ is the zenith angle and $\phi \in [0, 360°]$ is the azimuth angle measured from the up-wind direction. It is also called the zero-order emissivity, as no surface reflection occurs. Models of zero-order sea surface infrared emissivity are well known [10, 32, 6, 7, 35]. A review of these models is given in Sec. 1.3.1. This section follows the work of Bourlier *et al.* [32] to derive the zero-order infrared emissivity of sea surfaces. In addition, polarization is taken into account.

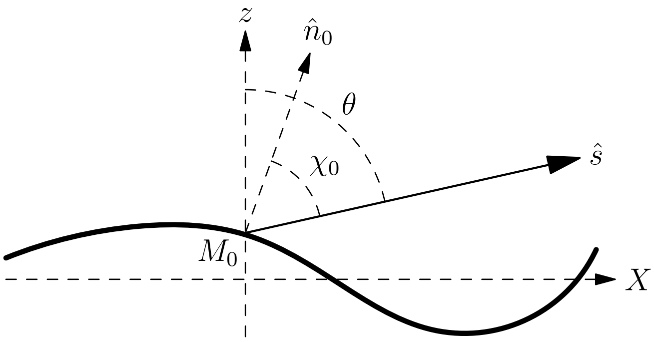

Figure 3.1: Direct surface infrared emissivity. The emission ray propagates directly toward the receiver located in the $\hat{s}(\theta, \phi)$ direction. The figure is presented in the (X, z) plane, with X being the horizontal direction of the receiver, which forms an azimuth angle ϕ with up-wind direction.

The direct emissivity ε_0 is calculated firstly for one-dimensional sea surface (1D surface, 2D problem) in Sec. 3.1.1, as it is simple studied. Then the model is extended to two-dimensional (2D surface, 3D problem) in Sec. 3.1.2 to study the cross-polarization effect. When deriving the direct infrared emissivity, shadowing effect has to be taken into account, as explained in the beginning of Chap. 2.

3.1.1 Model for 1D sea surfaces

3.1.1.1 Derivation of zero-order emissivity

In this subsection, 1D rough surfaces are considered. Thus, the azimuth angle ϕ is suppressed. The unitary vectors $\hat{n}_0$ and $\hat{s}$ are given by:

$$\hat{n}_0 = \frac{1}{\sqrt{1+\gamma_0^2}} \begin{bmatrix} -\gamma_0 \\ 1 \end{bmatrix}, \qquad \hat{s} = \begin{bmatrix} \sin\theta \\ \cos\theta \end{bmatrix}, \tag{3.1}$$

and the local angle of incidence χ_0 is given by:

$$\cos\chi_0 = \hat{n}_0 \cdot \hat{s} = \frac{\cos\theta - \gamma_0 \sin\theta}{\sqrt{1+\gamma_0^2}}. \tag{3.2}$$

It is assumed that the sea is opaque for infrared wavelengths, which means that all the refractive energy of an infrared incident ray is absorbed. It is also assumed that the sea surface is in thermal equilibrium. The local emissivity of an arbitrary surface point M_0 (see Fig. 3.1) is given by [10]:

$$\varepsilon_{0,H,V}^{\text{local}}(\chi_0) = 1 - |r_{H,V}(\chi_0)|^2, \tag{3.3}$$

where $r_{H,V}$ are the Fresnel reflection coefficients in horizontal (H, the electric vector is perpendicular to the plane of incidence) and vertical (V, the electric vector is parallel to the plane of incidence) polarizations, given by Eq. (1.29).

It is notable that, for 1D surfaces, the horizontal and vertical polarization directions of different surface points are identical according to the definition of the polarization directions. As a 1D surface belongs to a plane, e.g. the (X, z) plane here, the observation direction $\hat{s}$ and the local normal to the point $\hat{n}_0$ belong to the same plane containing the surface (the (X, z) plane). The horizontal polarization direction is the one perpendicular to this plane, and the vertical polarization direction is the one parallel to this plane and perpendicular to $\hat{s}$. These two directions do not change from surface point to another. As a result, cross-polarization does not occur.

The direct infrared emissivity ε_0 of a flat surface can be obtained from Eq. (3.3) by setting $\gamma_0 \equiv 0$. The direct infrared emissivity of rough surfaces ε_0 is the average of the local emissivity $\varepsilon_{0,H,V}^{\text{local}}$ of the facets seen by the receiver, given by [32]:

$$\varepsilon_{0,H,V} = \left\langle \left[1 - |r_{H,V}(\chi_0)|^2\right] g_0^{\text{1D}}\, S_{\text{M}}^0 \right\rangle_{0,\text{1D}}, \tag{3.4}$$

where $\langle\cdots\rangle_{0,\text{1D}}$ stands for the statistical average:

$$\langle\cdots\rangle_{0,\text{1D}} = \int_{-\infty}^{+\infty}\int_{-\infty}^{+\infty} \cdots p(\zeta_0, \gamma_0)\, \mathrm{d}\zeta_0\, \mathrm{d}\gamma_0, \tag{3.5}$$

with $p(\zeta, \gamma)$ being the joint probability density function (PDF) of the heights and the slopes of the surface.

The term g_0^{1D} in Eq. (3.4) results from projecting the area of the facet around M_0 onto the orthogonal direction of the observation direction θ. It is given by:

$$g_0^{\text{1D}} = 1 - \gamma_0 \tan\theta. \tag{3.6}$$

S_{M}^0 is the zero-order illumination function, which gives the probability that point M_0 is viewed by the receiver. In this thesis, the illumination function of Smith [25] is adopted, which is reviewed in the Sec. 2.1.3. It is recalled that, when deriving S_{M}^0, the conditional PDF $p(\zeta, \gamma \mid \zeta_0, \gamma_0; \tau)$ of the heights and the slopes of two points of the surface is involved [25]. Considering the correlation between the heights and the slopes of these two points leads to the correlated zero-order illumination function $S_{\text{M}}^{0,\text{co}}$, otherwise the uncorrelated one $S_{\text{M}}^{0,\text{unco}}$ is obtained. In this chapter, both of them are used to calculate the surface emissivity and compared.

3.1.1.2 Degree of polarization

Infrared intrinsic radiation of a rough surface is partially polarized at large zenith observation angles [36, 43]. The degree of polarization (DOP) of the infrared emissivity is given by [43]:

$$DOP = \frac{\varepsilon_H - \varepsilon_V}{\varepsilon_H + \varepsilon_V}, \tag{3.7}$$

where ε_H and ε_V are the emissivities in horizontal and vertical polarizations, respectively.

The magnitude of the DOP describes the fraction of the polarized component power with respect to the total power, whereas its sign relates to the dominant polarized energy. A positive DOP indicates that the horizontally polarized energy (H) is larger than the vertically polarized (V) one, and vice versa.

3.1.1.3 Monte Carlo ray-tracing method

To evaluate the accuracy of the model, a Monte Carlo ray-tracing algorithm is used. In the ray-tracing algorithm, 1D rough surfaces are generated, with Gaussian height and slope distributions (number of surface $N = 2000$, each surface with length $L = 100L_c$ in the chapter). Moreover, the surface points are assumed to be correlated with a Gaussian height autocorrelation function. After the generation of the rough surfaces, the same ray-tracing procedure as shown in Fig. 2.6 is performed to find out all the surface points seen by the receiver.

The local angles of incidence and the Fresnel reflection coefficients of points seen by the receiver are calculated, and the Monte Carlo zero-order emissivity is given by:

$$\varepsilon_{0,H,V}^{\mathrm{MC}} = \frac{1}{N_s} \sum_{i=1}^{N_i} \left[1 - |r_{H,V}(\chi_{0,i})|^2\right] g_{0,i}, \tag{3.8}$$

where N_s is the total number of points of the surface and N_i is the number of surface points seen by the receiver. The parameter $g_{0,i}$ results from projecting each facet onto the direction orthogonal to the observation direction θ, given by

$$g_{0,i} = 1 - \gamma_{0,i} \tan\theta. \tag{3.9}$$

3.1.1.4 Numerical results for 1D surfaces

The zero-order infrared emissivity and its degree of polarization (DOP) are simulated for 1D surfaces. The infrared emissivity is simulated at wavelengths inside the infrared atmospheric windows of 3 to 5 μm and 8 to 13 μm. The sea refraction indexes in these two regions are given by the model of Hale and Querry [49]: for instance, for wavelengths $\lambda = \{4,\ 10\}$ μm, the sea refraction indexes $n = \{1.3510 + 0.0046i,\ 1.2180 + 0.0508i\}$, respectively. The sea refraction indexes used in this thesis can be found in Appendix E. We recall that the model of Hale and Querry does not take into account the sea water salinity. The upwind direction is studied, where the RMS slope relates to the wind speed u_{12} at 12.5 m above the sea surface, which is given by [17] [1]:

$$\sigma_\gamma^2 = 3.16 \times 10^{-3} u_{12}. \tag{3.10}$$

---

[1] The uncertainty of measurement shown in Eq. 1.8 is not considered.

As the local emissivity of a facet $\varepsilon_0^{\text{local}}$ does not depends on the height of the facet (see Eq. (3.3)), and the integration of the monostatic zero-order illumination function S_{M}^0 over the surface heights holds for any form of height PDF, the knowledge of the exact surface height PDF is not required. The surface slope PDF is assumed to be Gaussian (Eq. (1.7)) first, and then the non-Gaussian slope PDF (Eq. (1.11)) is considered to study the skewness and kurtosis effects (see Sec. 1.1.3.2 for introduction of the skewness and kurtosis effects). For the surfaces Gaussian slope PDF, the correlation between the heights and the slopes of different surface points is considered when determining the illumination function S_{M}^0.

Zero-order emissivity ε_0 Fig. 3.2 shows the zero-order emissivity of 1D rough surfaces without considering the shadowing effect (set $S \equiv 1$). The results are compared with the model with shadowing effect. The wind speed u_{12} at 12.5 m above the sea surface 10 m/s and the wavelength is $\lambda = 10$ μm.

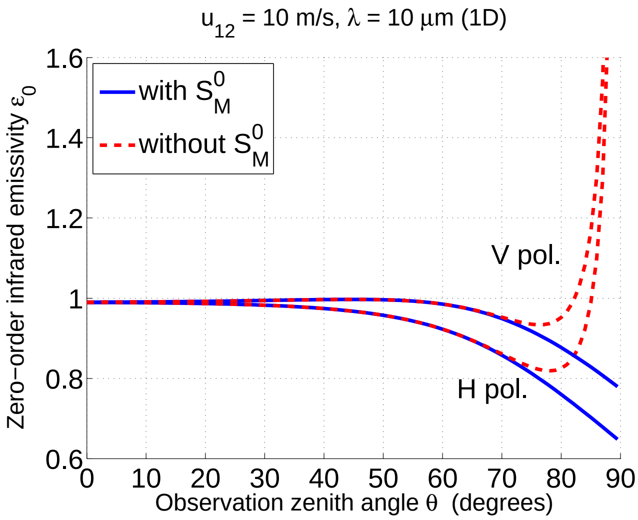

Figure 3.2: 1D zero-order infrared emissivity ε_0 of a surface, with and without considering the shadowing effect. The wind speed is $u_{12} = 10$ m/s and the wavelength $\lambda = 10$ μm.

It is shown that, the zero-order emissivities ε_0 in horizontal (H, lower) or vertical (V, upper) polarizations with and without considering shadowing effect are very similar when the zenith observation angle θ is small, e.g. $\theta < 70°$ for surfaces with wind speed $u_{12} = 10$ m/s. This is because shadowing is not significant for these zenith angles θ. As θ continues to increase, discrepancies show up and increase rapidly. For $\theta > 85°$, the zero-order emissivity ε_0 exceeds 1 and tends to infinity as θ increases to $90°$, which is not physical. The reason is that shadowing is significant for large zenith angles θ. The model without considering the shadowing effect takes all the surface points to calculate the surface emissivity, including the ones in the shadow of the receiver, which does not contribute to the surface radiation. As a result, it is essential to built accurately the monostatic illumination function S_{M}^0, which evaluates the shadowing effect.

Fig. 3.3 shows the 1D zero-order infrared emissivities ε_0 of a flat surface and that of sea surfaces with wind speeds $u_{12} = 5$ and 10 m/s, in H polarization on the left (a) and V polarization on the right (b). The sea surface slope PDF is assumed to be Gaussian and the correlation between the heights and slopes is not considered.

The wavelength λ equals 10 μm. The results for $\lambda = 4$ μm are also calculated, but are not shown as they are very similar and lead to the same conclusion.

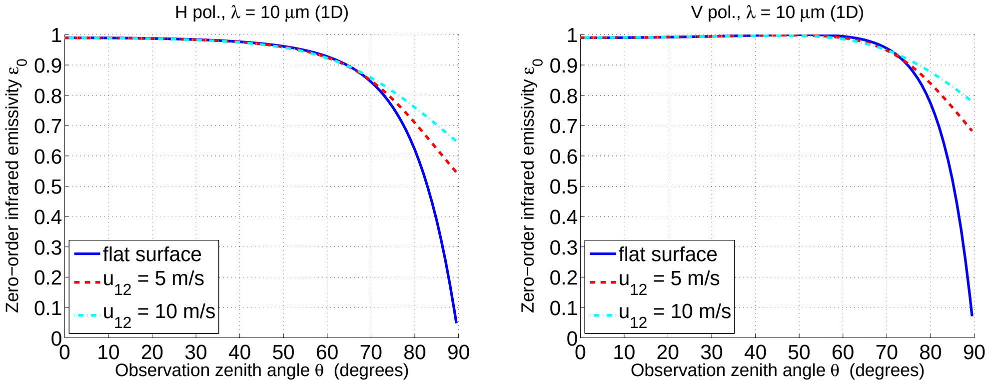

(a) (b)

Figure 3.3: 1D zero-order infrared emissivity ε_0 of a flat surfaces and two wind roughenned surfaces, in H polarization on the left (a) and V polarization on the right (b). The wavelength $\lambda = 10$ μm. The sea surface slope PDF is assumed to be Gaussian.

It is shown that the zero-order infrared emissivity ε_0 is close to 1 when θ is small. The zero-order emissivity of a flat surface equals 0 for $\theta = 90°$, whereas the ones of wind roughened surfaces do not. Moreover, as the wind speed u_{12} increases, the zero-order emissivity slightly decreases at moderate zenith angles (e.g. $50° \lesssim \theta \lesssim 70°$), and significantly increase at large zenith angles (e.g. $\theta \gtrsim 70°$).

Fig. 3.4 shows the results of the zero-order sea surface emissivity with Gaussian slope PDF. The correlation between the heights and the slopes of the surface points are considered. The wavelength λ equals 10 μm. The results are compared with the ones of the Monte Carlo ray-tracing method.

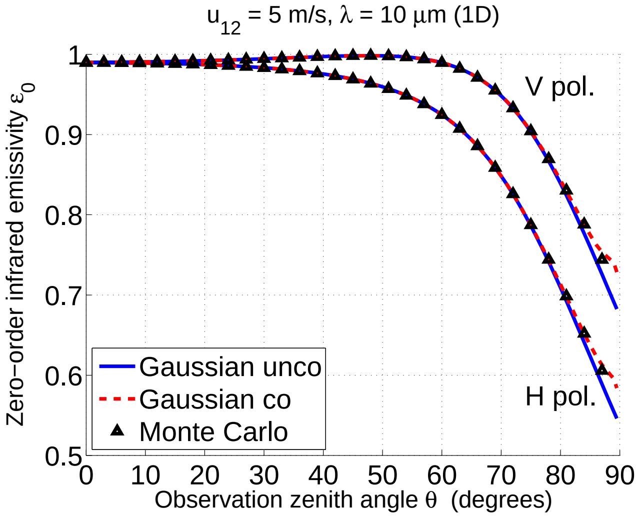

Figure 3.4: 1D zero-order infrared emissivity ε_0 of sea surfaces with wind speed $u_{12} = 5$ m/s, and the wavelength $\lambda = 10$ μm. The sea surface slope PDF is assumed to be Gaussian. The correlation between the heights and the slopes of the surface points is considered.

It is shown that the results agree very well with each other for $\theta \lesssim 85°$. In general, the zero-order emissivity with correlated height and slope PDF agrees with the Monte Carlo result better. Small differences are found for $\theta > 85°$. In this region, the calculation error in the numerical integration of g^{co} over τ (see Eq. (2.39)) and the one of the local emissivity over γ_0 becomes significant, which is the main reason for this discrepancy.

In Fig. 3.4, it is notable that the V polarized emissivity slightly increases to a maximum around $\theta = 55°$ and then decreases, while the H polarized component decreases monotonically with respect to θ. This phenomenon occurs because of the Brewster angle ($\theta_{\mathrm{B}} \approx 50.6°$ for $\lambda = 10$ μm, flat surface).

The skewness and kurtosis effects are then studied. Fig. 3.5 shows the results of 1D zero-order emissivity ε_0 of sea surfaces with Gaussian slope PDF (denoted G), Gaussian PDF plus skewness effect (denoted GS), Gaussian PDF plus kurtosis effect (denoted GK), and Gaussian PDF plus skewness and kurtosis effects (denoted GSK). The correlation between the heights and the slopes of the surface is not considered. The wind speeds $u_{12} = 5$ (left) and 10 (right) m/s are compared, and the wavelength $\lambda = 10$ μm.

When the sea surface is relatively calm, for example $u_{12} = 5$ m/s (Fig. 3.5 (a), Beaufort scale ≈ 3), the zero-order emissivity with Gaussian and non Gaussian slope PDFs are very similar, which means that the skewness and kurtosis effects are not significant. The differences between them are shown in Fig. 3.5 (c) in horizontal polarization and (e) in vertical polarization. For small zenith angles, e.g. $\theta \lesssim 60°$, the differences are negligible. For moderate and large zenith angles, e.g. $60° \lesssim \theta \lesssim 85°$, ε_0 is increased after taking into account the skewness effect (G-GS<0), while it is decreased after taking into account the kurtosis effect (G-GK>0). In total, the skewness and kurtosis effects increases the zero-order emissivity for moderate zenith angles θ. For very large zenith angles, e.g. $\theta \gtrsim 85°$, the skewness and kurtosis effects both reduce the zero-order emissivity (G-GS>0, G-GK>0). In general, the differences are of the order of 10^{-3}. The differences between the emissivities in H polarization (c) and in V polarization (e) have a similar trend and are of the same order.

As the wind speed increases, the skewness and kurtosis effects become more significant. Fig. 3.5 (a) shows the zero-order emissivity of surfaces with wind speed $u_{12} = 10$ m/s (Beaufort scale ≈ 5), with Gaussian and non Gaussian slope PDFs. The differences between them are shown in (d) in horizontal and (f) in vertical polarizations. The same conclusion as in Fig. 3.5 (a), (c) and (e) is found, except that the differences are increased.

In general, the influence of the skewness effect is more significant for higher wind speeds. For example, in Fig. 3.5 (c) where $u_{12} = 5$ m/s, the maximum of the contribution of the skewness effect (G-GS) is about 7.4×10^{-3}, whereas the one of the kurtosis effect (G-GK) is about 2.5×10^{-3}. In Fig. 3.5 (d), the wind speed increases to $u_{12} = 10$ m/s. The maximum of the contribution of the skewness effect is about 1.5×10^{-2}, whereas the one of the kurtosis effect is about 2.7×10^{-3}. It is notable that the contribution of the skewness effect is doubled by the increase of wind speed, but the contribution of the kurtosis effect is hardly changed.

Degree of polarization The polarization state is also studied. Fig. 3.6 shows the degree of polarization (DOP) of sea surface emissivities with wind speed $u_{12} = 5$ and 10 m/s. The wavelength is $\lambda = 10$ μm. The results of Gaussian and non Gaussian surface slope PDFs are compared. The receiver is located in the up-wind

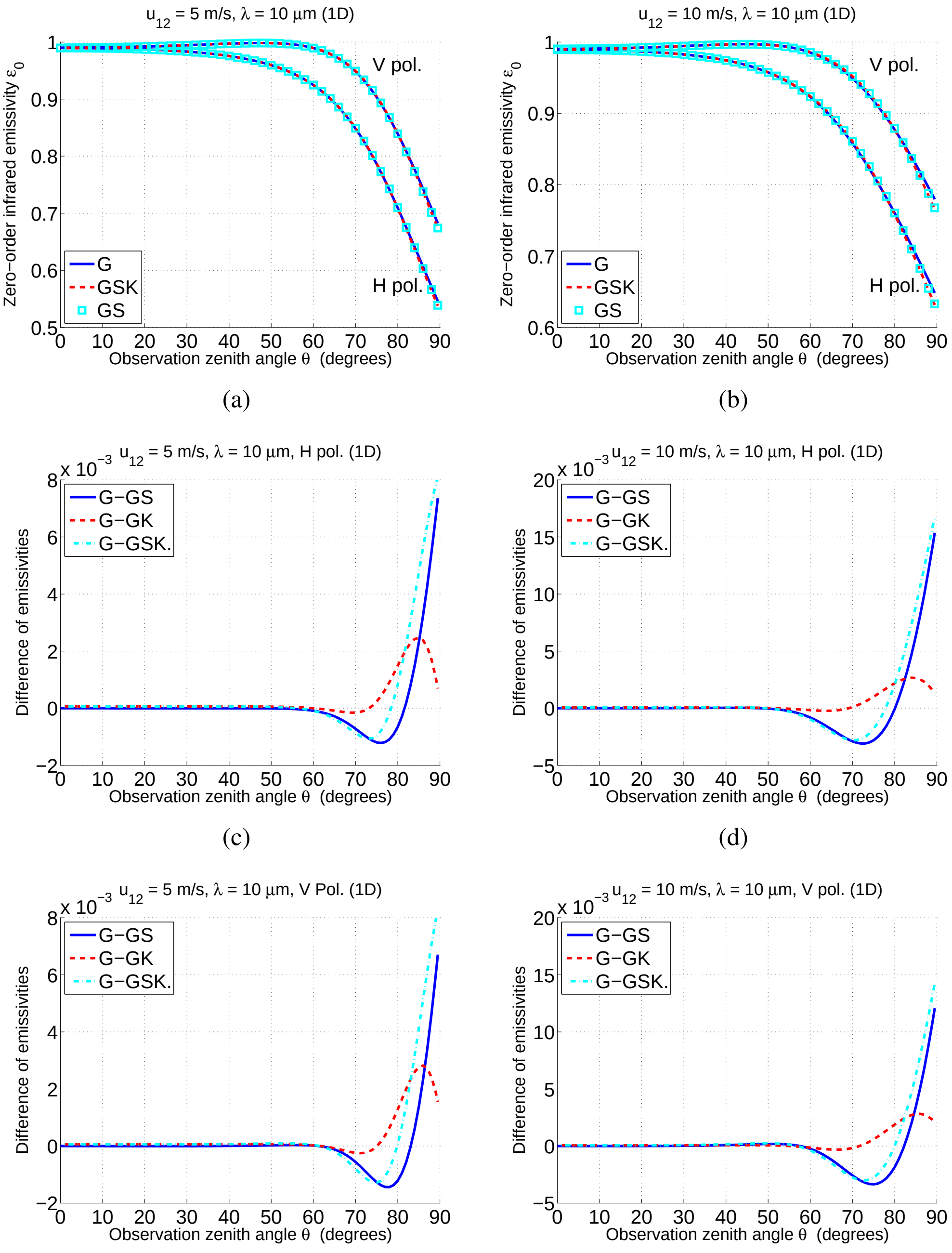

(a) (b)

(c) (d)

(e) (f)

Figure 3.5: 1D zero-order infrared emissivity ε_0 of Gaussian and non-Gaussian sea surfaces and their differences. In the left column, $u_{12} = 5$ m/s, and in the right column, $u_{12} = 10$ m/s.

direction.

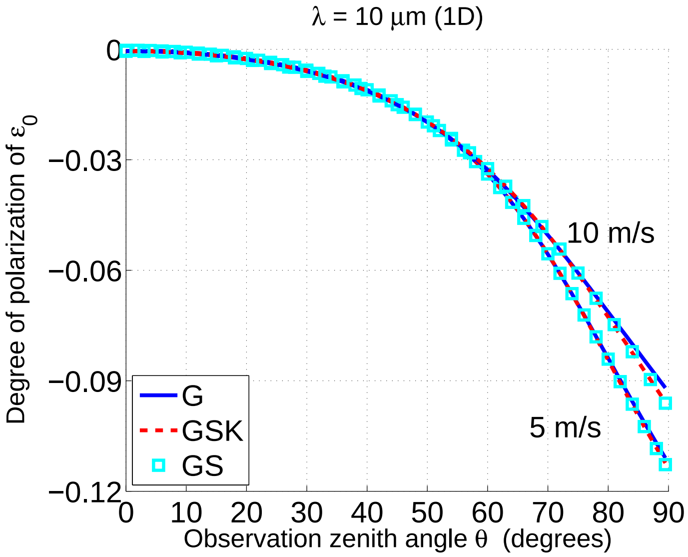

Figure 3.6: Degree of polarization (DOP) of the zero-order emissivity for $\lambda = 10$ μm. The wind speed is 5 (lower group) and 10 (upper group) m/s. The results for Gaussian and non Gaussian slope PDF are compared. The receiver is located in the up-wind direction.

To study the influence of the wind speed on the DOP, the results are shown both for $u_{12} = 5$ m/s and for $u_{12} = 10$ m/s. It is shown that the DOP is always negative, meaning that the H polarized direct emissivity ε_0 is always smaller than the V polarized component (see Eq. (3.7)), which is predictable from Fig. 3.5 (a) and (b). As the wind speed increases, the absolute value of the DOP decreases, which means that the increase in wind speed reduces the polarization characteristics of the direct emissivity. In general, DOP is quite large for large zenith angles θ. For example, for a wind speed $u_{12} = 10$ m/s and $\lambda = 10$ μm, the DOP of the direct emissivity is about -0.1, meaning that about 10% of the surface intrinsic radiation energy at $\lambda = 10$ μm is polarized.

The DOPs of surfaces with Gaussian and non-Gaussian (skewness and kurtosis) slope PDFs are very similar for a wind speed $u_{12} = 5$ m/s. The differences are more obvious for $u_{12} = 10$ m/s at large zenith angles, e.g. $\theta \gtrsim 80°$. It can be concluded that the influence of the skewness and kurtosis effects is more obvious for high wind speeds and for large zenith observation angles θ. The DOP of zero-order emissivity ε_0 with GS slope PDF and that with GSK PDF are very similar, meaning that in the up-wind direction, skewness effect is the main non-Gaussian effect. The contribution of the kurtosis effect is weak.

The 1D surface model is simpler to build and faster to calculate. However, it hides some characteristics of a general 2D surface, for example the cross-polarization effect. In what follows, the model for 2D surfaces is studied.

3.1.2 Model for 2D sea surfaces

3.1.2.1 Rotation angle α

In this subsection, general 2D rough surfaces (3D problem) are considered. The direct emissivity of 2D surfaces is calculated in a very similar way as for the 1D model.

Fig. 3.7 shows the tangent plane of an arbitrary surface point M_0 of the sea surface, with unitary normal vector $\hat{n}_0$. The $\hat{x}$ direction is the up-wind direction, and the $\hat{y}$ direction is the cross-wind direction. The vector $\hat{z}$ points to the zenith. The receiver is located in the direction $\hat{s}(\theta, \phi)$, with θ being the zenith angle and ϕ being the azimuth angle measured from the up-wind direction. For convenience, a new coordinate system (X, Y) is defined by rotating anticlockwise the basis (x, y) through an angle ϕ about the z axis, so that the receiver lies in the (X, z) plane.

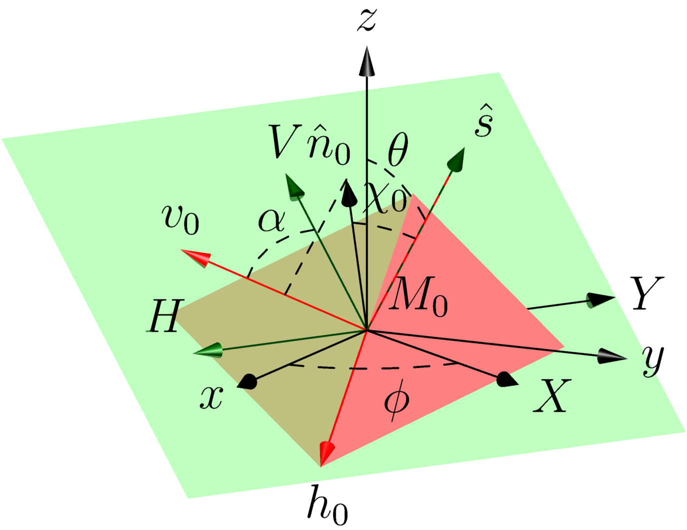

Figure 3.7: Tangent plane of an arbitrary surface point M_0 (red) of the sea surface, with a unitary normal $\hat{n}_0$. The receiver is located in the $\hat{s}(\theta, \phi)$ direction. The light-green plane crosses point M_0 and is perpendicular to $\hat{s}$. The normal to the tangent plane $\hat{n}_0$ and the direction of observation $\hat{s}$ define the local plane of incidence, as well as the local angle of incidence χ_0 and the local horizontal h_0 and vertical v_0 polarizations. The normal to the average surface (horizontal plane) $\hat{z}$ and $\hat{s}$ define the global plane of incidence, as well as the global horizontal H and vertical V polarizations. When $\hat{n}_0$ is different from $\hat{z}$, there is an angle α between the corresponding local and global polarization directions.

The local plane of incidence of M_0 is defined by the local normal to the tangent plane $\hat{n}_0$ and the observation direction $\hat{s}$. The angle χ_0 between $\hat{n}_0$ and $\hat{s}$ is the local angle of incidence. The local horizontal polarization (denoted h_0, the electric vector is perpendicular to the local plane of incidence) and local vertical polarization (denoted v_0, the electric vector is parallel to the local plane of incidence) are defined. The unitary vector $\hat{u}_{v_0}$ of the v_0 polarization direction belongs to the local plane of incidence and is perpendicular to $\hat{s}$, and points upward of the tangent plane. The unitary vector $\hat{u}_{h_0}$ of the h_0 polarization direction is perpendicular to the local plane of incidence and checks the relation:

$$\hat{u}_{v_0} \times \hat{u}_{h_0} = \hat{s}, \tag{3.11}$$

where $\times$ is the cross product. As the slope of M_0 is arbitrary, the direction of the local normal vector $\hat{n}_0$ is arbitrary, as well as the local polarization directions.

To describe the polarization state of the sea surface infrared emissivity, the average sea surface is considered, which is parallel to the horizontal plane ((X, Y) or (x, y)). The normal vector $\hat{z}$ to the average plane and the propagation direction $\hat{s}$

of the emission ray define the global plane of incidence. The global horizontal polarization (denoted H) and global vertical polarization (denoted V), as well as the corresponding unitary vectors $\hat{u}_V$ and $\hat{u}_H$, are defined in the same way as the local ones, by replacing the local normal vector $\hat{n}_0$ with the global one $\hat{z}$. The global polarization directions are fixed by the observation direction $\hat{s}$ and the zenith direction $\hat{z}$.

Generally, the tangent plane at an arbitrary surface point M_0 is not identical to the average sea surface (horizontal plane), which means that the local normal vector $\hat{n}_0$ is not identical to the $\hat{z}$ direction. As a result, the local plane of incidence is generally not identical to the global one. As $\hat{u}_V$, $\hat{u}_H$, $\hat{u}_{v_0}$ and $\hat{u}_{h_0}$ are perpendicular to $\hat{s}$, they belong to the same plane (the light green plane in Fig. 3.7). However, as the tangent plane is "rotated" from the average sea surface, there is an angle α between the local and global planes of incidence, which equals the one between $\hat{u}_V$ and $\hat{u}_{v_0}$, or between $\hat{u}_H$ and $\hat{u}_{h_0}$ (see Fig. 3.7). As the local polarization directions differ from a surface point to another, the intensity of the intrinsic radiation in local v_0 and h_0 polarizations should be projected onto the global V and H polarization directions when deriving the sea surface infrared emissivity. As a result, a part of the locally horizontally (or vertically) polarized energy may pass to vertical (or horizontal) polarization in a global point of view. This effect is named "cross-polarization" for short here. "cross-polarization" never occurs when deriving the zero-order 1D sea surface infrared emissivity in Sec. 3.1, because the local and global planes of incidence are always identical, which means α equals 0.

3.1.2.2 Derivation of ε_0 for 2D surfaces

To derive the polarized zero-order infrared emissivity of sea surfaces, the local emissivity of an arbitrary point M_0 is calculated firstly. The local angle of incidence χ_0 is given by Eq. (2.3). The local emissivity of point M_0 is then given by:

$$\varepsilon^{\text{local}}_{0,h_0,v_0}(\chi_0) = 1 - |r_{h_0,v_0}(\chi_0)|^2, \tag{3.12}$$

where $r_{h_0,v_0}(\chi)$ are the Fresnel reflection coefficients in local horizontal and vertical polarizations, given by Eq. (1.29).

To derive the polarized emissivity of the sea surface, the local emissivity in v_0 and h_0 polarizations is projected onto the V and H polarization directions. The emissivities in v_0V (local v_0 polarization projected to global V polarization), v_0H, h_0V, h_0H polarizations are given by:

$$\begin{array}{rcl} \varepsilon_{0,v_0V} & = & \varepsilon^{\text{local}}_{0,v_0}\cos^2\alpha \\ \varepsilon_{0,v_0H} & = & \varepsilon^{\text{local}}_{0,v_0}\sin^2\alpha \\ \varepsilon_{0,h_0V} & = & \varepsilon^{\text{local}}_{0,h_0}\sin^2\alpha \\ \varepsilon_{0,h_0H} & = & \varepsilon^{\text{local}}_{0,h_0}\cos^2\alpha \end{array}, \tag{3.13}$$

where the squares in $\cos^2\alpha$ and $\sin^2\alpha$ show up because emissivity corresponds to energy intensity, which relates to the square of the wave magnitude. The rotation angle α is derived in detail in Appendix F. The emissivities in global V and H polarizations are given by:

$$\begin{array}{rcl} \varepsilon'_{0,V} & = & \varepsilon_{0,v_0V} + \varepsilon_{0,h_0V} \\ \varepsilon'_{0,H} & = & \varepsilon_{0,v_0H} + \varepsilon_{0,h_0H} \end{array}. \tag{3.14}$$

Following the same method as for 1D surfaces, the zero-order infrared emissivity θ_0 of the 2D surfaces is given by:

$$\begin{aligned} \varepsilon_{0,V} &= \left\langle \varepsilon'_{0,V}\, g_0^{\mathrm{2D}}\, S_{\mathrm{M}}^0 \right\rangle_{0,\mathrm{2D}} \\ \varepsilon_{0,H} &= \left\langle \varepsilon'_{0,H}\, g_0^{\mathrm{2D}}\, S_{\mathrm{M}}^0 \right\rangle_{0,\mathrm{2D}} \end{aligned}, \tag{3.15}$$

where $\langle \cdots \rangle_{0,\mathrm{2D}}$ stands for the statistical average:

$$\langle \cdots \rangle_{0,\mathrm{2D}} = \int_{-\infty}^{+\infty} \int_{-\infty}^{+\infty} \cdots p(\zeta_0, \gamma_{x_0}, \gamma_{y_0})\, \mathrm{d}\zeta_0\, \mathrm{d}\gamma_{x_0}\, \mathrm{d}\gamma_{y_0} \tag{3.16}$$

with $p(\zeta, \gamma_x, \gamma_y)$ being the joint probability density function (PDF) of the heights and the slopes of the surface. The term g_0^{2D} results from projecting the surface area around the point M_0 onto the direction perpendicular to the observation direction (θ, ϕ), given by:

$$g_0^{\mathrm{2D}} = 1 - (\gamma_{x_0} \cos\phi + \gamma_{y_0} \sin\phi) \tan\theta. \tag{3.17}$$

We recall that the Smith illumination function $S_{\mathrm{M}}^{0,\mathrm{S}}$ is used. To agree with the Smith illumination function, the change of variables given in Eq. (2.5) is also performed, which allows us to study the problem in the (X, Y, z) coordinates. The integration variables in Eq. (3.16) become:

$$\mathrm{d}\gamma_{x_0}\, \mathrm{d}\gamma_{y_0} = |J| \mathrm{d}\gamma_X\, \mathrm{d}\gamma_Y, \tag{3.18}$$

where $J = 1$ is the Jacobian of the change of variables.

3.1.2.3 Numerical results for 2D surfaces

Cross-polarization The polarized zero-order infrared emissivity ε_0 with shadowing effect and its DOP are calculated for 2D surfaces. It is recalled that the polarization state of the sea surface infrared emissivity is measured by the global horizontal and vertical polarizations, which are defined referring to the average sea surface.

The most important difference between 1D and 2D surfaces is that, cross-polarizations occur for 2D surfaces. The cross-polarization effect is studied in Fig. 3.8.

Fig. 3.8 (a) and (b) shows the zero-order emissivity ε_0 with shadowing effect in h_0H, h_0V, v_0H and v_0V polarizations (the terms of the right-hand side of Eq. (3.14)) for the wavelength $\lambda = 10$ μm. The receiver is located in the up-wind direction ($\phi = 0°$). The wind speed u_{12} at 12.5 m above the sea surface equals 5 and 10 m/s. The surface slope PDF is assumed to be Gaussian. The results for other ϕ and for a non-Gaussian PDF are also calculated, but are not shown here as they have similar trends and lead to the same conclusions.

It is shown that the cross-polarization terms (h_0V and v_0H) are significant only for small zenith angles θ, e.g. $\theta < 30°$ for $u_{12} = 5$ m/s and $\theta < 35°$ for $u_{12} = 10$ m/s. It can be concluded that the increase of wind speed u_{12} enhances the cross-polarization effect for small zenith angles θ.

These cross-polarization terms decrease rapidly with the increase of the zenith angle θ and are rather small for large zenith angles: for instance, $\varepsilon_{0,h_0V} \approx 0.0068$ and $\varepsilon_{0,v_0H} \approx 0.0093$ for $\theta = 85°$ in Fig. 3.8 (a). On the other hand, the terms ε_{0,h_0H} and ε_{0,v_0V} are always strong.

To find the reason for the rapid decrease of the cross-polarization terms, the average of the rotation angle α, given by $\langle \alpha S_{\mathrm{M}}^0 \rangle_0$, is calculated for both Gaussian

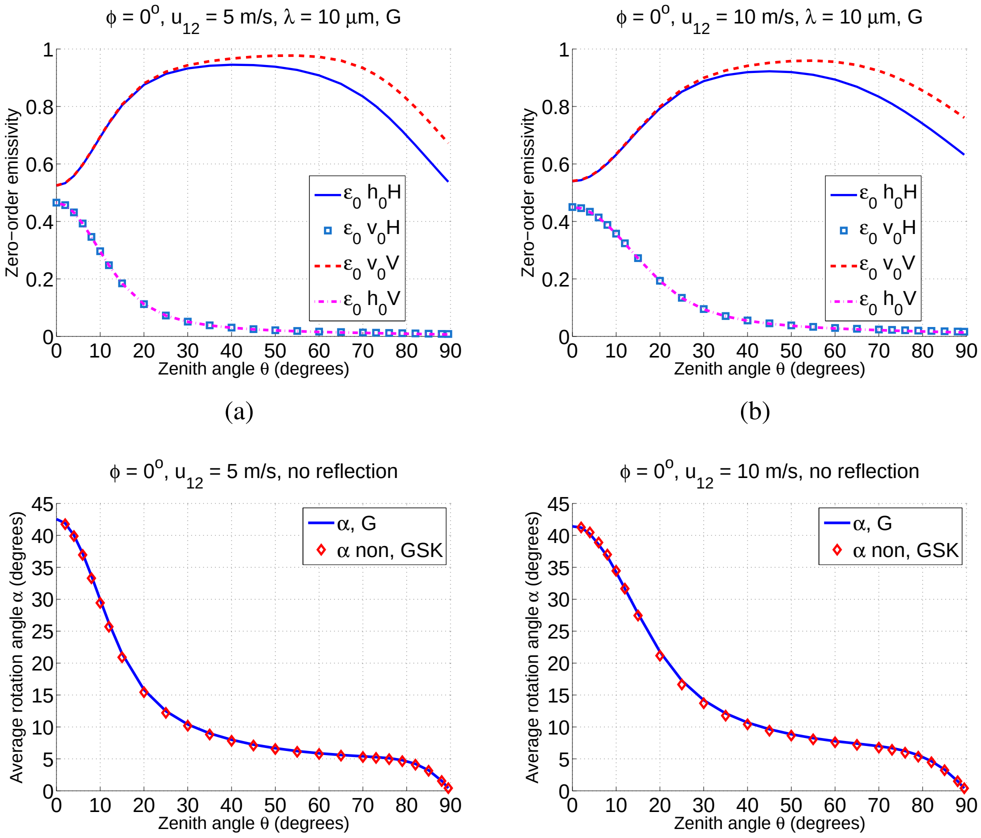

(a) (b)

(c) (d)

Figure 3.8: Sea surface zero-order emissivity in v_0V, h_0V, h_0H and v_0H polarizations for $u_{12} = 5$ m/s (a) and $u_{12} = 10$ m/s (b). The average rotation angle $\langle \alpha S_{\mathrm{M}}^{0} \rangle_0$ is also shown for $u_{12} = 5$ m/s (c) and for $u_{12} = 10$ m/s (d). The receiver is located in the up-wind direction ($\phi = 0°$).

and non-Gaussian surface slope PDFs. The angle α is derived in Appendix F. The illumination function S_{M}^{0} is taken into account to eliminate the influence of the points in shadow, which do not contribute to the observed emissivity. The results are shown in Fig. 3.8 (c) and (d) for $u_{12} = 5$ and 10 m/s, respectively.

It is shown that the average of α is slightly over $40°$ for $\theta = 0°$ for both $u_{12} = 5$ and 10 m/s. This is consistent with Fig. 3.8 (a) and (c), which show that the co- (h_0H, v_0V) and cross-polarization terms are similar for $\theta = 0°$, implying that α is close to $45°$.

The average of α decreases with the increase of θ, from slightly over $40°$ for $\theta = 0°$ to about $0°$ for $\theta = 90°$. As a result, $\sin\alpha$ decreases rapidly as θ increases, and the cross-polarization terms vanish (see Eq. (3.13)). Besides, the average of α decreases more rapidly when the wind speed is small.

Comparison of 1D and 2D ε_0 In Fig. 3.9, the results of zero-order emissivity ε_0 of 1D and 2D surfaces are compared. The receiver is located in the up-wind direction $\phi = 0°$. The wavelength is $\lambda = 10$ μm, and the wind speed is $u_{12} = 5$ and 10 m/s. The surface slope is assumed to be Gaussian, and the correlation between the heights and the slopes of surface points is not considered.

Fig. 3.9 (a) and (b) shows the zero-order emissivity ε_0 for wind speeds $u_{12} = 5$ and 10 m/s, respectively. Although cross-polarization occurs for 2D surfaces, the

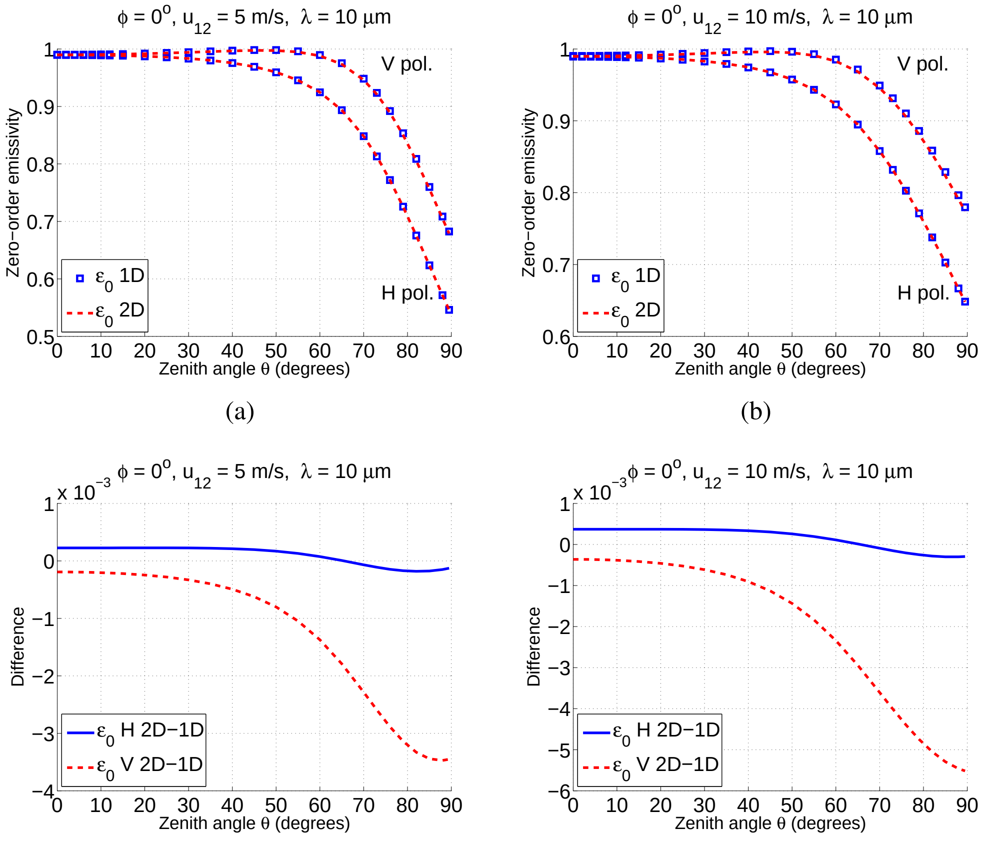

(a) (b) (c) (d)

Figure 3.9: Polarized sea surface zero-order infrared emissivity ε_0 of 1D and 2D surfaces (upper row) and their differences (lower row). The wind speed is $u_{12} = 5$ (left) and 10 m/s (right), and the wavelength is $\lambda = 10\ \mu$m.

zero-order emissivities ε_0 in global H and V polarizations are very similar with the ones of 1D surfaces. The surface emissivity in H polarization continuously decreases with the increase of θ, while the one in V polarization slightly increases to a maximum value and then decreases, because of the Brewster angle ($\theta_B \approx 50.6°$ for $\lambda = 10\ \mu$m, flat surface).

Their differences are shown in Fig. 3.9 (c) and (d) for wind speed $u_{12} = 5$ and 10 m/s, respectively. It is shown that the differences between the 1D and 2D surface models are relatively small and are of the same order for $u_{12} = 5$ and 10 m/s. The differences between the emissivity in horizontal polarization stay nearly constant, with maxima about 2×10^{-4}. The differences in vertical polarization increase with the zenith observation angle θ, with maxima about 3.5×10^{-3} for $u_{12} = 5$ m/s and about 5.5×10^{-3} for $u_{12} = 10$ m/s at $\theta = 90°$. In general, the 1D surface model of sea surface zero-order emissivity ε_0 is a good approximation of the one for 2D surfaces.

Non-Gaussian effect The zero-order infrared emissivity of 2D surfaces in global H and V polarizations are calculated for both Gaussian and non-Gaussian sea surface slope PDFs, with the same parameters as in Fig. 3.9, using Eq. (3.14).

The skewness and the kurtosis effects are studied separately. Very similar results are found as in Fig. 3.5 for 1D surfaces, and the same conclusions are obtained. It is shown in Fig. 3.10 (a) and (b) that the zero-order emissivities ε_0 of 2D surfaces with

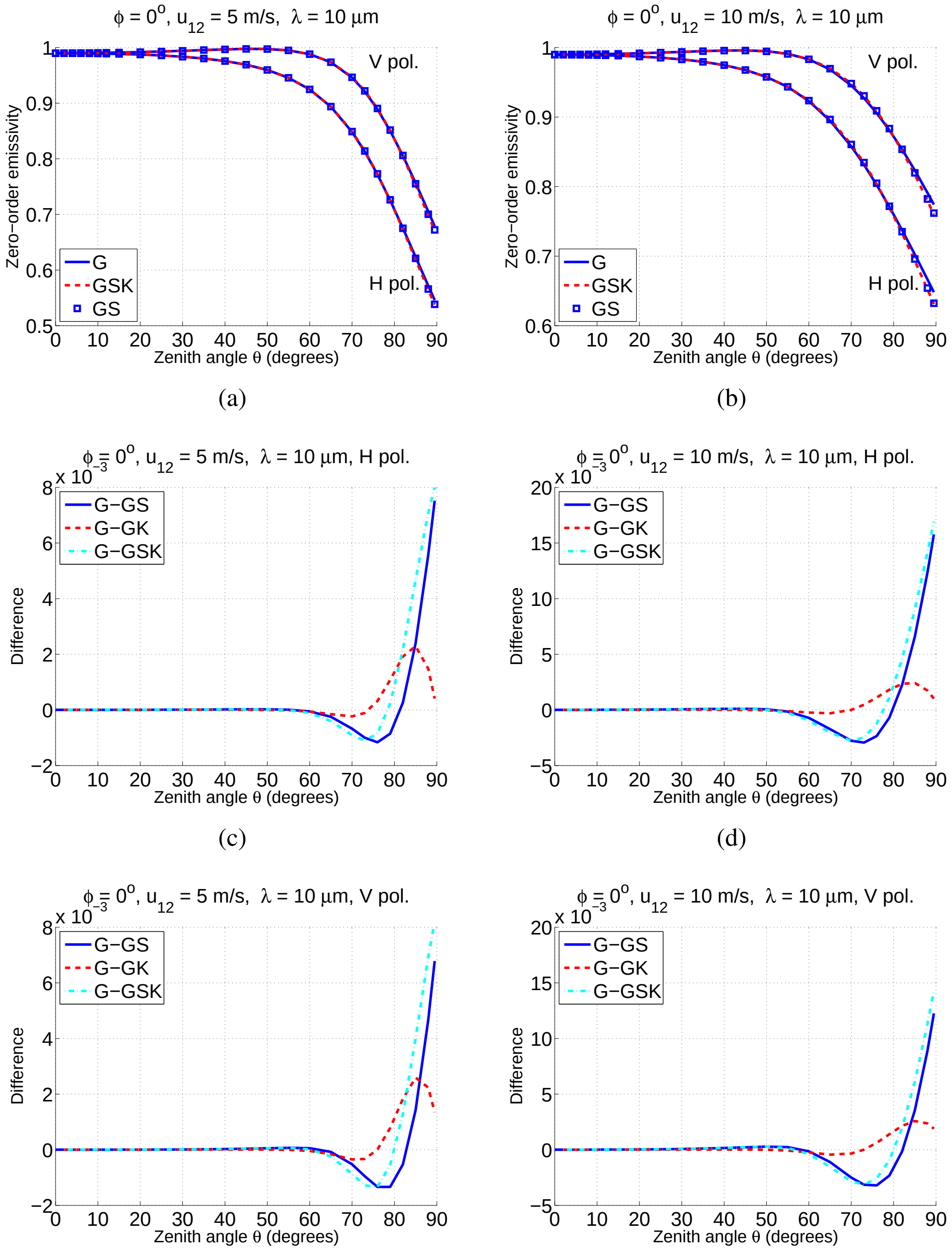

(a) (b)

(c) (d)

(e) (f)

Figure 3.10: Polarized sea surface zero-order infrared emissivity ε_0 of 2D surface with Gaussian and non-Gaussian slope PDFs (a) and (b). Their differences are shown in (c)-(f). The wind speed is $u_{12} = 5$ (left) and $u_{12} = 10$ m/s. The receiver is located in the up-wind direction ($\phi = 0°$).

Gaussian (noted G) or non-Gaussian surface slope PDFs (noted GS for Gaussian plus skewness, GK for Gaussian plus kurtosis, and GSK for Gaussian plus skewness and kurtosis) have similar trends. Their differences are also small, but becomes larger for large zenith angles $\theta > 85°$, meaning that the skewness and kurtosis effects become significant only in this region.

Again, it is shown that the differences between the emissivities with G and GS PDFs for large θ are larger than those between emissivities with G and GK PDFs, meaning that influence of the skewness effect is more significant for the up-wind direction.

By comparing Fig. 3.5 and Fig. 3.10, it can be concluded again that the 1D surface model of zero-order sea surface emissivity ε_0 is a good approximation of that for 2D surfaces.

Fig. 3.11 shows the zero-order emissivity versus the azimuth angle (corresponding to the wind direction) in global H polarization in (a) and in global V polarization in (b). The wind speed is $u_{12} = 10$ m/s and the wavelength is $\lambda = 10$ μm. The zenith angle is $\theta = 85°$.

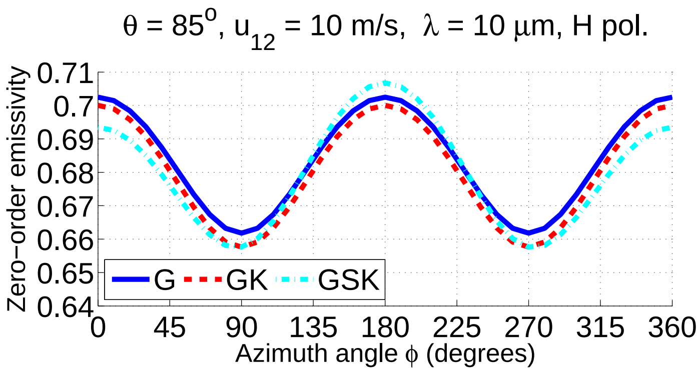

(a)

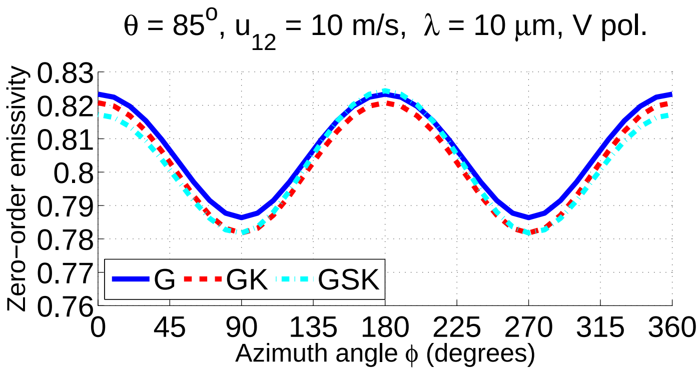

(b)

Figure 3.11: Zero-order emissivity ε_0 versus azimuth angle ϕ in global H polarization in (a) and in global V polarization in (b). The wind speed is $u_{12} = 10$ m/s and the wavelength is $\lambda = 10$ μm. The zenith angle is $\theta = 85°$.

The zero-order emissivity ε_0 with Gaussian PDF (noted G), Gaussian PDF plus kurtosis effect (noted GK) and Gaussian PDF plus skewness and kurtosis effects (noted GSK) are shown. It is shown that ε_0 with G and GK PDFs are symmetrical about the up-wind ($\phi = 0°$), down-wind ($\phi = 180°$) and the cross-wind ($\phi = \{90°, 270°\}$) directions. After taking into account the skewness effect, ε_0

with GSK PDF is not symmetrical about the cross-wind directions, whereas ε_0 is always symmetrical about the up-wind and down-wind directions. This checks the conclusion in 1.1.3.2.

It is difficult to conclude which of the skewness and the kurtosis effects is more significant. It depends on the zenith angle θ and the azimuth angle ϕ. In general, the skewness effect is more significant than the kurtosis effect in the up-wind ($\phi = 0°$) and down-wind ($\phi = 180°$) directions. In the cross-wind directions ($\phi = \{90°, 270°\}$), ε_0 with GK and GSK PDFs are very similar, meaning that the kurtosis effect is the dominant one and the influence of skewness effect is negligible.

Degree of polarization The DOP of the zero-order emissivity of 2D surfaces is also calculated according to Eq. (3.7). Fig. 3.12 shows the DOPs of zero-order emissivity versus the zenith angle θ, for wind speed $u_{12} = 5$ m/s (a) and $u_{12} = 10$ m/s (b), and are compared with the results of 1D surface model. The wavelength is $\lambda = 10$ μm. The sea surface slope PDF is assumed to be Gaussian. The receiver is located in the up-wind direction ($\phi = 0°$).

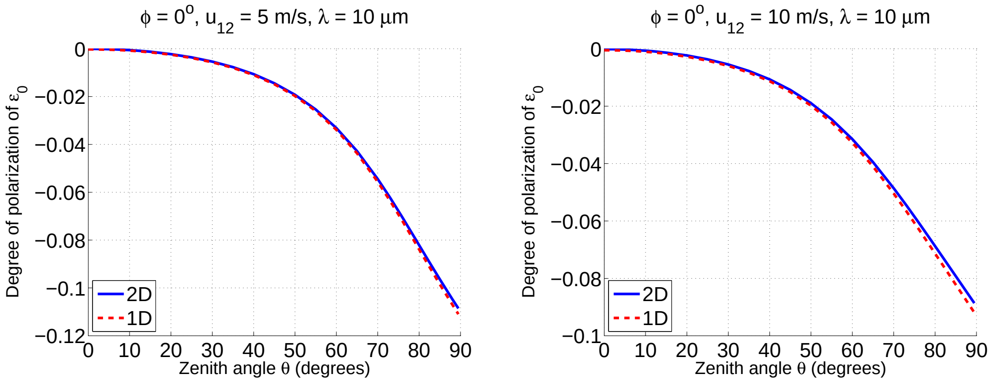

(a) (b)

Figure 3.12: Degree of polarization of 2D sea surfaces with wind speeds $u_{12} = 5$ m/s (a) and $u_{12} = 10$ m/s (b). The sea surface slope PDF is assumed to be Gaussian. The receiver is located in the up-wind direction ($\phi = 0°$).

The same conclusion is obtained as Fig. 3.6 for 1D surface model. Besides, although cross-polarization occurs for 2D surfaces, the DOPs of 1D and 2D surfaces are very similar. Small differences are found for large zenith observation angles θ, which increases with θ. The differences are larger for a wind speed equals 10 m/s.

As the zero-order emissivities ε_0 and their DOPs of 1D and 2D surfaces are very similar, we may conclude that the 1D surface model is a good approximation, which gives reasonably accurate results and takes a short computation time.

Fig. 3.13 shows the DOP of zero-order emissivity of 2D sea surfaces versus the azimuth angle ϕ (corresponding to wind direction). The wind speed is $u_{12} = 10$ m/s and the wavelength is $\lambda = 10$ μm. The zenith angle is $\theta = 80°$ in (a) and $\theta = 85°$ in (b).

It is shown that the DOP of ε_0 depends on the wind direction ϕ. Similar conclusions are obtain as in Fig. 3.11. The DOP with G and GK PDFs are symmetrical about the up-wind ($\phi = 0°$), down-wind ($\phi = 180°$) and the cross-wind ($\phi = \{90°, 270°\}$) directions. After taking into account the skewness effect, the DOP with GSK PDF is not symmetrical about the cross-wind directions, whereas

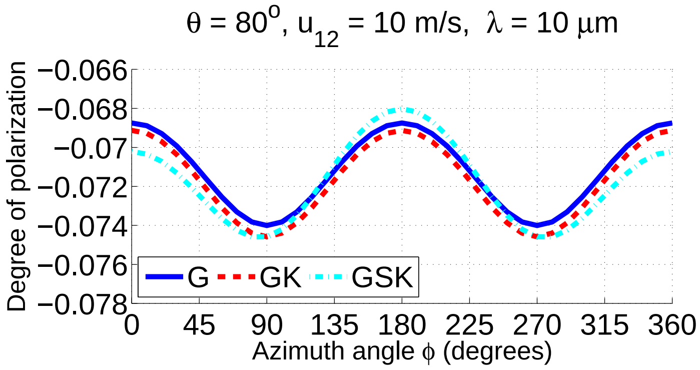

(a)

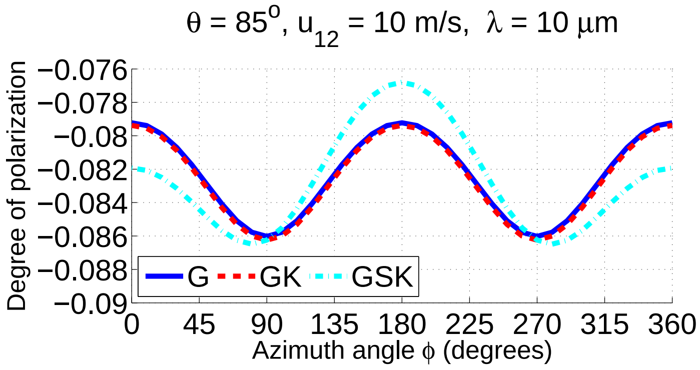

(b)

Figure 3.13: Degree of polarization of zero-order emissivity ε_0. The wind speed is $u_{12} = 10$ m/s and the wavelength is $\lambda = 10$ μm. The zenith angle is $\theta = 80°$ (a) and $\theta = 85°$ (b).

it is always symmetrical about the up-wind and down-wind directions. This checks the conclusion in 1.1.3.2.

The influence of the kurtosis effect is reduced as the zenith angle θ increases from $80°$ to $85°$, whereas the influence of the skewness effect increases significantly, especially in the up-wind and down-wind directions. This conclusion can be predicted by Fig. 3.10. The skewness effect is small in the cross-wind directions.

In General, the skewness and kurtosis effects together increase the absolute value of the DOP in the up-wind direction ($\phi = 0°$), and reduce it in the down-wind direction ($\phi = 180°$). The change of DOP in the cross-wind directions ($\phi = \{90°, 270°\}$) are relatively small.

3.2 Infrared emissivity with one reflection ε_1

The comparisons with measurements showed that the zero-order models underestimate the sea surface infrared emissivity for large zenith angles θ [39, 1, 22]. A reason is that the surface-emitted surface-reflected emissivity (SESR, first-order contribution) is not taken into account, as the surface reflection effect is significant for large zenith angles θ.

In this section, the analytical model of infrared emissivity with one surface reflection is developed. Fig. 3.14 illustrates the geometrical configuration of the first-order emissivity. The first-order illumination function derived in Sec. 2.2.1 is used. In addition, polarization is taken into account. In the end, the sea surface infrared emissivity obtained by the analytical model is compared with measurements.

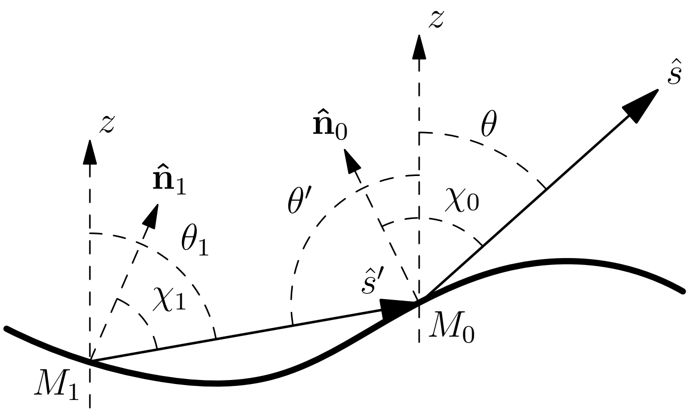

Figure 3.14: First-order infrared emissivity. The emission ray form the source M_1 intersects the surface at M_0, and is then reflected specularly to the receiver along the $\hat{s}(\theta, \phi)$ direction.

The sea surface is firstly modeled as one-dimensional (1D) in Sec. 3.2.1 and then two-dimensional (2D) in Sec. 3.2.2 to study the cross-polarization effect. It is recalled that geometric optics approximation is assumed to be valid, which implies that specular reflections are considered.

3.2.1 Model for 1D sea surfaces

3.2.1.1 Derivation of first-order emissivity ε_1

In this subsection, 1D rough surfaces are considered. Thus, the azimuth angle ϕ is suppressed. The up-wind direction ($\phi = 0°$) is taken, which means that the surface belongs to the (x, z) plane.

The first-order emissivity ε_1 corresponds to the energy emitted from a surface point M_1 which is reflected to the observation direction by the facet at point M_0. The energy emitted at point M_0 is ignored, as it is already included in the zero-order emissivity. As a result, the first-order local emissivity of the facet at point M_0 is given by [15]:

$$\varepsilon_1^{\text{local}} = \left[1 - |r(\chi_1)_{H,V}|^2\right] |r(\chi_0)_{H,V}|^2. \tag{3.19}$$

Attention must be paid to the polarization of the first-order local emissivity. For 1D rough surfaces, the emission and the reflection rays both belong to the (x, z) plane. The polarization state of the emission ray is not changed when it propagates to the facet of reflection. As a result, the cross-polarization terms do not contribute. In other words, the H polarized first-order local emissivity results from the combination of $r_H(\chi_1)$ and $r_H(\chi_0)$ [HH for short, where the first H corresponds to the subscript of $r(\chi_1)$ and the second corresponds to that of $r(\chi_0)$] in Eq. (3.19). The same remark holds for the V polarized first-order local emissivity. The VH and HV combinations never contribute for 1D surfaces. Thus, the first-order local emissivity is given by:

$$\left\{ \begin{array}{lcl} \varepsilon_{1,H}^{\text{local}} & = & [1 - |r_H(\chi_1)|^2]\, |r_H(\chi_0)|^2 \\ \varepsilon_{1,V}^{\text{local}} & = & [1 - |r_V(\chi_1)|^2]\, |r_V(\chi_0)|^2 \end{array} \right. . \tag{3.20}$$

The first-order emissivity is given in the same way as that of the zero-order:

$$\left\{\begin{array}{lcl}\varepsilon_{1,V} & = & \left\langle \varepsilon_{1,V}^{\text{local}} g_{0,1D} S_{\text{M}}^{1} \right\rangle_{1,\text{1D}} \\ \varepsilon_{1,H} & = & \left\langle \varepsilon_{1,H}^{\text{local}} g_{0,1D} S_{\text{M}}^{1} \right\rangle_{1,\text{1D}}\end{array}\right. , \tag{3.21}$$

where $g_{0,1D}$ is given by Eq. (3.9). The symbol $\langle \cdots \rangle_{1,\text{1D}}$ stands for the first-order statistical average:

$$\begin{aligned}\langle \cdots \rangle_{1,\text{1D}} = & \int_{-\infty}^{+\infty} \int_{-\infty}^{+\infty} \int_{-\infty}^{+\infty} \int_{-\infty}^{+\infty} \cdots \\ & \times p(\zeta_1, \gamma_1, \zeta_0, \gamma_0)\, \mathrm{d}\zeta_1\, \mathrm{d}\gamma_1\, \mathrm{d}\zeta_0 \mathrm{d}\gamma_0,\end{aligned} \tag{3.22}$$

with $p(\zeta_1, \gamma_1, \zeta_0, \gamma_0)$ the joint PDF of the heights and the slopes of points M_1 and M_0, respectively.

S_{M}^{1} is the first-order illumination function which gives the probability that single reflection is observed at the studied point. In this thesis, the first-order illumination function developed in Sec. 2.2.1 is used.

3.2.1.2 Estimation of the slope PDF of M_1

The first-order illumination function S_{M}^{1} developed in Sec. 2.2.1 is a function of the height ζ_0 and the slope γ_0 of point M_0. However, it does not depend on the height and the slope of point M_1. In fact, no information about ζ_1 or γ_1 is provided, which makes it difficult to compute the statistical average in Eq. (3.22).

As the first-order local emissivity does not depend on the heights ζ_0 or ζ_1 of the surface points M_0 or M_1, and the average of the first-order illumination function does not depend on the height PDFs of M_1 and M_0, the knowledge of the height PDF of ζ_1 and ζ_0 are unnecessary. However, the first-order local emissivity does depend on the slopes of point M_0 and M_1. As a result, the PDF of γ_1 has to be derived first. As discussed in Sec. 2.2.1.5, to ensure $|\chi_1| < 90°$, the slope γ_1 must satisfy:

$$\gamma_1 \leq \mu_1, \tag{3.23}$$

where $\mu_1 = \cot\theta_1$ is the slope of the ray $\hat{s}'$ (see Fig. 3.14). As no further information about γ_1 is provided, any slope checking Eq. (3.23) is equally considered as the slope of point M_1. The PDF of γ_1 is then given by:

$$p(\gamma_1) = \frac{\Upsilon(\mu_1 - \gamma_1)}{\displaystyle\int_{-\infty}^{\mu_1} p_\gamma(t)\, \mathrm{d}t} p_\gamma(\gamma_1) \tag{3.24}$$

where p_γ is the surface slope PDF.

3.2.1.3 Monte Carlo ray-tracing method

To evaluate the model, the Monte Carlo ray-tracing algorithm shown in Sec. 2.2.2.1 is used again. In the algorithm, all the pairs of M_0 and M_1 are found. Then the Fresnel reflection coefficients at these points are calculated, and the Monte Carlo first-order emissivity is given by:

$$\left\{\begin{array}{l}\varepsilon_{\text{MC},H} = \dfrac{1}{N_s} \displaystyle\sum_{i=1}^{N_i} \left[1 - |r_H(\chi_{1,i})|^2\right] |r_H(\chi_{0,i})|^2 g_0^{\text{1D}} \\ \varepsilon_{\text{MC},V} = \dfrac{1}{N_s} \displaystyle\sum_{i=1}^{N_i} \left[1 - |r_V(\chi_{1,i})|^2\right] |r_V(\chi_{0,i})|^2 g_0^{\text{1D}}\end{array}\right. , \tag{3.25}$$

where N_s is the total number of points of the surface and N_i is the number of pairs of points M_0 and M_1.

3.2.1.4 Numerical results for 1D surfaces

In this subsection, the first-order infrared emissivity and its degree of polarization (DOP) are simulated for 1D surfaces. The up-wind direction is taken, which means that $\phi = 0°$.

As the distance between the surface points M_0 and M_1 is unknown, it is assumed that the heights and the slopes of the surface are uncorrelated (except for the calculation of the correlated illumination function). Under such an assumption, the knowledge of the surface height PDF is not required. The surface slope PDF is assumed to be Gaussian, given by Eq. (1.7). The skewness and kurtosis effects will be included in the 2D surface model in Sec. 3.2.2.

First-order emissivity ε_1 Figs. 3.15 and 3.16 show the results of the polarized first-order infrared emissivity of sea surfaces with wind speeds $u_{12} = 5$ and 10 m/s. The wavelength λ is 4 μm in Fig. 3.15 and 10 μm in Fig. 3.16.

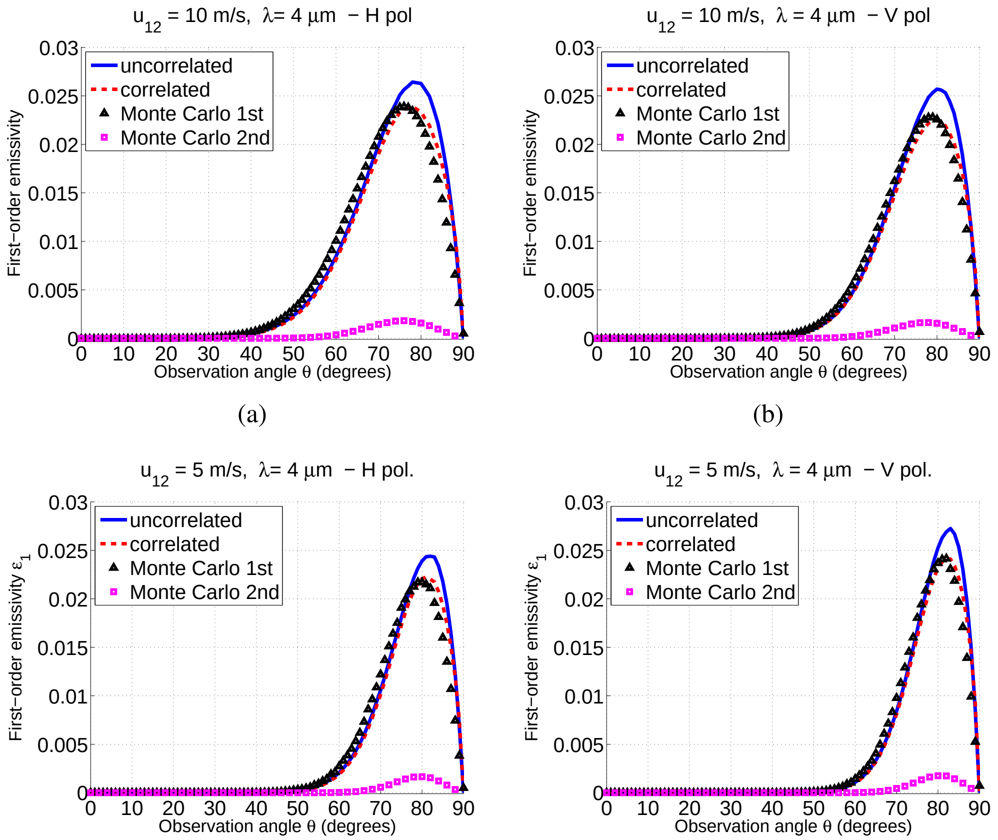

(a) (b)

(c) (d)

Figure 3.15: First-order emissivity for $\lambda = 4$ μm, in H polarization (left column) and in V polarization (right column), and for $u_{12} = 10$ m/s (upper row) and $u_{12} = 5$ m/s (lower row).

It is shown that the first-order infrared emissivity contributes at large observation angles. Employing the uncorrelated first-order illumination function S^1_{M}, the present model predicts the first-order emissivity quite well in both H and V polarizations.

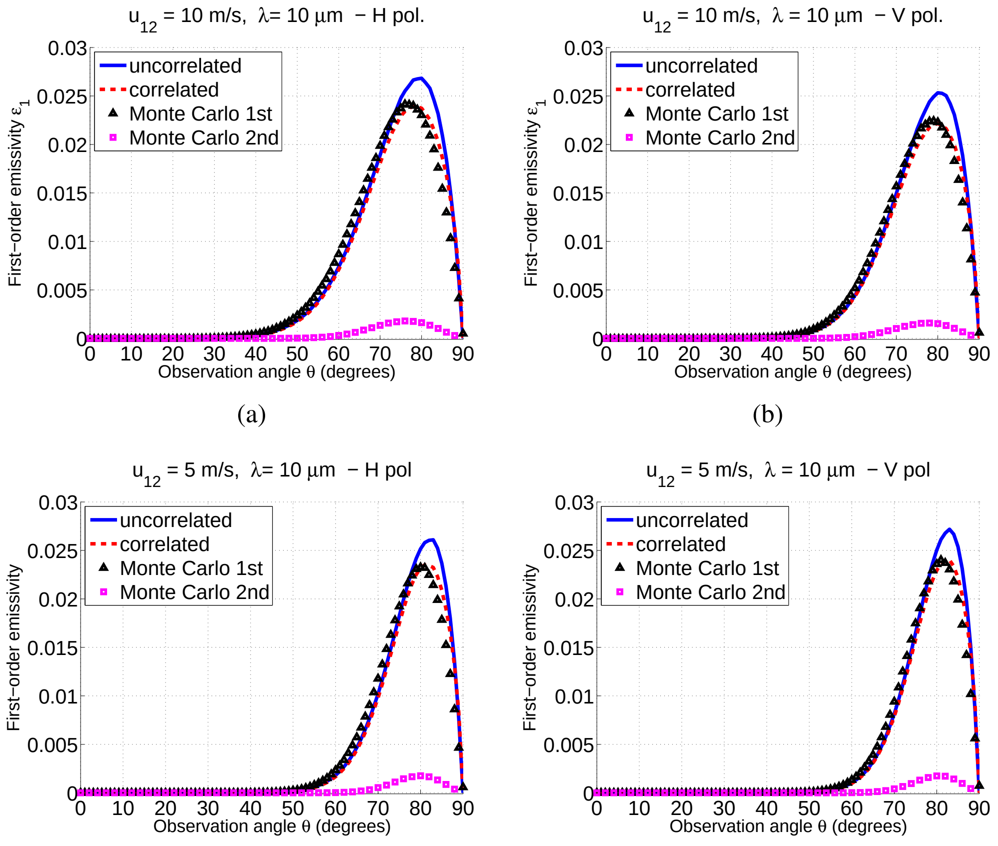

(a) (b)

(c) (d)

Figure 3.16: First-order emissivity for $\lambda = 10$ μm, in H polarization (left column) and in V polarization (right column), and for $u_{12} = 10$ m/s (upper row) and $u_{12} = 5$ m/s (lower row).

The first-order emissivities in H and V polarizations are slightly overestimated at large observation angles. This was predictable, as the adopted uncorrelated first-order illumination function slightly overestimates the surface reflection effect at these angles (see Fig. 2.18).

The agreements are significantly improved when the correlated first-order illumination function is employed. However, the agreements are not as good as that shown for the corresponding surface reflection effect in Fig. 2.18. For both H and V polarizations, the present model using the correlated first-order illumination function slightly overestimates the first-order emissivity at large observation angles ($\theta > 80°$), while slightly underestimates it at smaller observation angles ($\theta < 80°$).

A closer look at Eq. (3.21) helps us explain this deviation. Indeed, the first-order emissivity ε_1 depends on three terms: the first-order local emissivity $\varepsilon_1^{\mathrm{local}}$, the area projection term g_0, and the first-order illumination function S^1_{M}. It has already been observed in Sec. 2.2.2 that the first-order illumination function works very well and that the slope distribution of point M_0 is also well predicted. As g_0 depends only on the slope of point M_0 and on the observation angle θ, it should not be the source of the error. As a result, the discrepancy should come from the first-order local emissivity, which depends on the slopes of points M_0 and M_1. As the distribution of γ_0 is well predicted by the first-order illumination function (see Fig. 2.16 (a) and (c)), the error should mainly come from the fact that the definition of the PDF of γ_1 is not enough accurate.

The PDF of γ_1 is given in Eq. (3.24), which is based on the assumption that all the slopes which fulfill the prerequisite "the local angle of incidence χ_1 is not larger than $90°$ in absolute value" could equally be the slope of point M_1. Until now, no rigorous proof is found to support this assumption. However, as little knowledge about γ_1 is given by the first-order illumination function, this problem is left to future work.

Referring to the Monte Carlo ray-tracing method, the first-order emissivity has a maximum of about 2.5×10^{-2} and tends to zero at $\theta = 90°$. However, the first-order emissivity of Masuda (Fig. 3 of [11], noted $r_1^\star$) reaches a maximum of about 5×10^{-2}, which is nearly twice the maximum of the Monte Carlo result. In addition, it does not equal zero at $\theta = 90°$ while the Monte Carlo result does. There are two possible reasons for the appearance of this discrepancy. Firstly, Masuda used a weighting function to estimate the probability of observing one surface reflection, which is built on a shadowing term. The shadowing term gives the proportion that the surface is illuminated, which does not equal the probability that a certain point is illuminated and which is not suitable for extension to higher orders. The second reason is that Masuda used the direct emissivity of the surface at $\theta > 90°$. In this region, the receiver is below the sea surface, which is not physical.

The Monte Carlo ray-tracing method for calculating the second-order infrared emissivity (with two surface reflections) was also developed, and the corresponding results are shown in Figs. 3.15 and 3.16 (squares). A maximum of about 2.5×10^{-3} at $80°$ is observed for both H and V polarizations, which is less than the sensitivity requirement 5×10^{-3} reported by Wu and Smith in 1997 [1]. The Monte Carlo results for calculating three surface reflections were also computed, which show a maximum of about 4×10^{-4} (not shown here). As a result, the second and higher orders infrared emissivities are negligible for our application.

Total emissivity of the surface ε_{tot} The total infrared emissivity is obtained by summing up the zero- and first-order ones, whereas the higher orders are ignored:

$$\varepsilon_{\text{tot}} = \varepsilon_0 + \varepsilon_1. \tag{3.26}$$

Although the first-order emissivity model using the correlated first-order illumination function better agrees with the Monte Carlo result, the uncorrelated model is considered because of its significantly lower time consumption. Fig. 3.17 shows the uncorrelated zero-order and total emissivities of the surface for a wind speed $u_{12} = 10$ m/s and a wavelength $\lambda = 10$ μm. The results for $u_{12} = 5$ m/s and for $\lambda = 4$ μm are not shown as they lead to the same observations and conclusions.

It is shown that the total emissivity of the sea surface decreases with the observation angle. Compared with the zero-order emissivity, the total emissivity is significantly increased at large observation angles by taking the first-order emissivity into account. The analytical results agree well with the Monte Carlo results, except for gazing angles ($\theta > 80°$).

Degree of polarization To study the polarization state of the sea surface emissivity, the degree of polarization (DOP) of the zero-order, the first-order and the total infrared emissivities are calculated according to equation (3.7) and plotted in Fig. 3.18. The results for $u_{12} = 5$ m/s and for $\lambda = 4$ μm are not shown as they lead to the same conclusions.

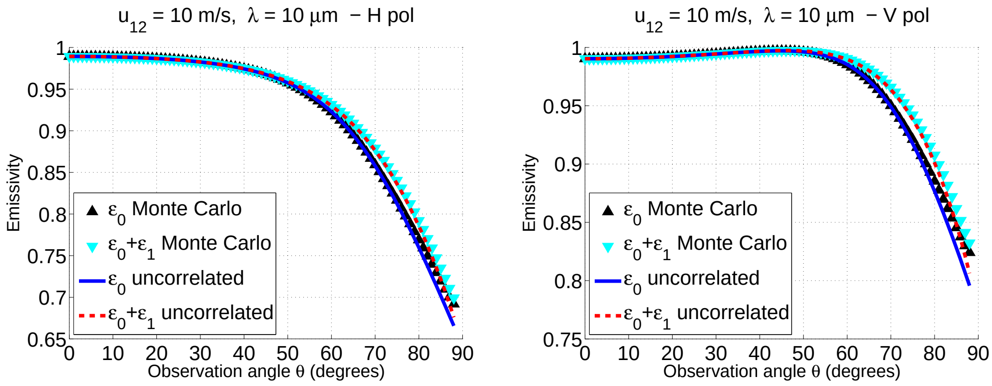

(a) (b)

Figure 3.17: Uncorrelated zero-order emissivity ε_0 of the surface (solid) and the corresponding Monte Carlo result (triangle), and the total emissivity ε_0+ ε_1 of the surface (dashed) and the corresponding Monte Carlo result (wedge) in H polarization (a) and in V polarization (b). The wind speed is $u_{12} = 10$ m/s and the wavelength $\lambda = 10$ μm.

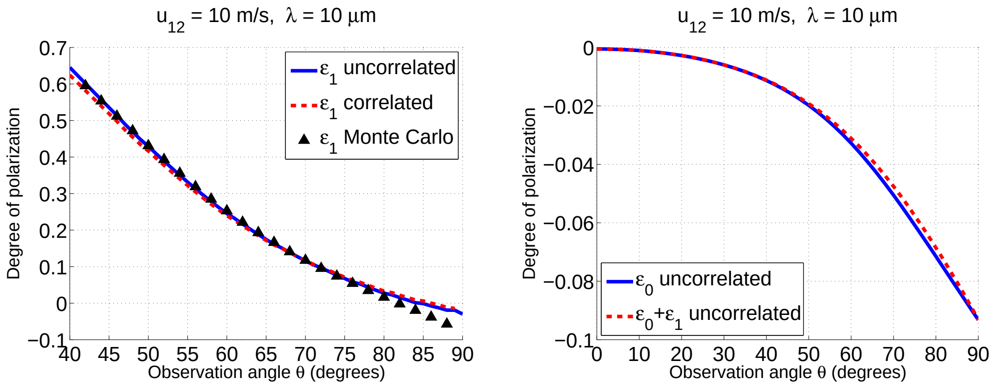

(a) (b)

Figure 3.18: DOP of the first-order infrared emissivity ε_1 of the sea surface (a), and the comparison between the DOPs without surface reflections ε_0 (solid line in (b)) and with one reflection $\varepsilon_0 + \varepsilon_1$(dashed line in (b)).

Fig. 3.18 (a) shows the DOP of the first-order infrared emissivity of the sea surface. It is shown that the first-order infrared emissivity ε_1 can be highly polarized at small to moderate observation angles (up to 65% at $\theta \approx 40°$ in Fig. 3.18 (a)), although the magnitude of ε_1 is close to zero and very small compared to ε_0 (see Fig. 3.15 and 3.16). The DOP of ε_1 decreases to zero at $\theta \approx 85°$, and continuously decreases to about -5% at $\theta = 90°$. In other words, for the polarized component of the first-order infrared emissivity, the globally H polarized energy is the majority for $\theta < 85°$, while the globally V polarized energy is the majority for $\theta > 85°$. At $\theta \approx 85°$, ε_1 is unpolarized.

Fig. 3.18 (b) shows the DOPs of the uncorrelated zero-order and total infrared emissivities of the sea surface. It is shown that the DOP of the total infrared emissivity of the surface is negative and decreases to about -9% as the observation angle increases to $\theta = 90°$, which means that the globally V polarized energy is the majority, and that up to 9% of the energy is polarized at $\theta = 90°$. The DOP of the total surface emissivity is slightly reduced in magnitude at large observation angles, which means that surface reflections slightly reduce the polarization feature of the surface radiation.

3.2.2 Model for 2D sea surfaces

3.2.2.1 Rotation angle β

In this subsection, 2D rough surfaces (3D problem) are considered. The first-order emissivity of 2D rough surfaces is calculated in the same way as that for 1D rough surfaces. It is recalled that, to describe the polarization state of the sea surface infrared emissivity, the average sea surface is considered and global horizontal polarization (H) and global vertical polarization (V) are defined (see Sec. 3.1.2 for details).

Fig. 3.19 shows two points M_1 and M_0 of the sea surface and their tangent planes. An emission ray $\hat{s}'$ propagates from M_1 to M_0, where it is then reflected specularly to the receiver. Unlike 1D surfaces, the propagation direction of the emission ray $\hat{s}'$ and the normals to these two points are generally not in the same plane. As a result, the local planes of incidence (defined by $\hat{s}'$, $\hat{s}$ and the local normals $\hat{n}_1$ and $\hat{n}_0$) of these two points are not identical, but differ from a rotation angle β, as shown in Fig. 3.19. The angle β is derived in Appendix F.

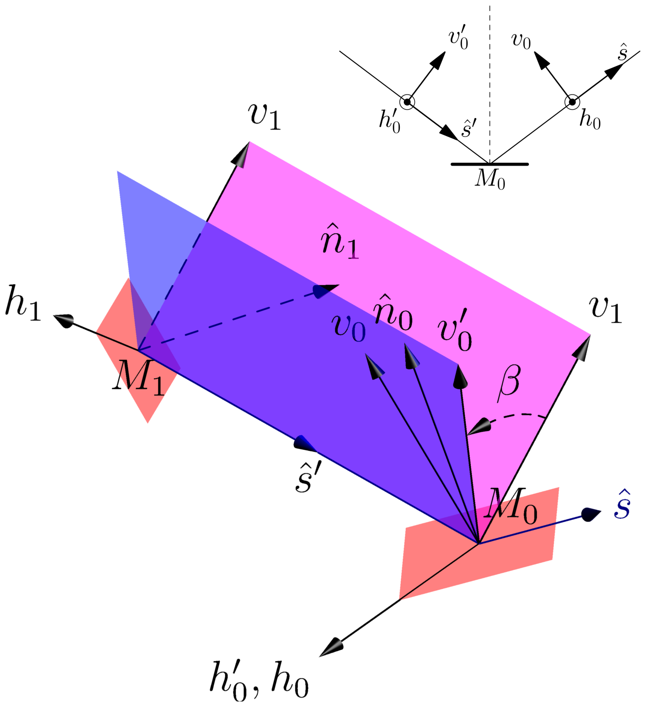

Figure 3.19: The tangent planes (red planes) of points M_0 and M_1, and the local planes of incidence (blue plane for M_0, magenta plane for M_1).

The local vertical and horizontal polarizations (denoted as v_1 and h_1 to avoid confusion) of the emission ray from M_1 are defined in the same way as v_0 and h_0. The v_0' and h_0' directions are the local vertical and horizontal polarization directions of the incident ray $\hat{s}'$ to the point M_0. Before calculating the reflection, the intensity of the intrinsic radiation of v_1 and h_1 polarizations should be projected to the v_0' and h_0' polarizations, which also leads to the cross-polarization effect.

3.2.2.2 Derivation of the first-order emissivity ε_1

In this subsection, the sea surface infrared emissivity with one reflection ε_1 is developed according to the slopes of the points M_0 and M_1 and the observation angle $\hat{s}(\theta, \phi)$.

The calculation of the geometry can be found in Sec. 2.2.1.1. The vector $\hat{s}'$ and the local angle of incidence χ_1 are given by Eqs. (2.57) and (2.60), respectively.

The local emissivity in v_1 and h_1 polarizations referring to the point M_1 is then given by:

$$\varepsilon^{\text{local}}_{1,v_1,h_1} = 1 - |r_{v_1,h_1}(\chi_1)|^2. \tag{3.27}$$

Before reflecting the ray specularly from $\hat{s}'$ to $\hat{s}$, the intensity of the intrinsic radiation in v_1 and h_1 polarizations should be projected to v'_0 and h'_0 polarizations, given by:

$$\begin{aligned}
\varepsilon^{\text{local}}_{1,v_1v'_0} &= \varepsilon^{\text{local}}_{1,v_1} \cos^2\beta = [1 - |r_{v_1}(\chi_1)|^2]\cos^2\beta,\\
\varepsilon^{\text{local}}_{1,v_1h'_0} &= \varepsilon^{\text{local}}_{1,v_1} \sin^2\beta = [1 - |r_{v_1}(\chi_1)|^2]\sin^2\beta,\\
\varepsilon^{\text{local}}_{1,h_1v'_0} &= \varepsilon^{\text{local}}_{1,h_1} \sin^2\beta = [1 - |r_{h_1}(\chi_1)|^2]\sin^2\beta,\\
\varepsilon^{\text{local}}_{1,h_1h'_0} &= \varepsilon^{\text{local}}_{1,h_1} \cos^2\beta = [1 - |r_{h_1}(\chi_1)|^2]\cos^2\beta.
\end{aligned} \tag{3.28}$$

After the reflection, the emissivity in v_0 and h_0 polarizations is given by:

$$\varepsilon^{\text{local}}_{1,p_1q_0} = \varepsilon^{\text{local}}_{1,p_1q'_0} |r_{q_0}(\chi_0)|^2, \tag{3.29}$$

where $p_1 = \{v_1, h_1\}$, $q_0 = \{v_0, h_0\}$.

To derive the polarized emissivity of the sea surface, the local emissivity is projected to the global polarization directions V and H as:

$$\varepsilon_{1,p_1,q_0,C} = \varepsilon^{\text{local}}_{1,p_1,q_0} f(\alpha), \tag{3.30}$$

where $C = \{V, H\}$. The function $f(\alpha) = \cos^2\alpha$ if q_0 and C are both horizontal or vertical polarizations. Otherwise, $f(\alpha) = \sin^2\alpha$. The emissivity in V and H polarizations is given by:

$$\begin{aligned}
\varepsilon'_{1,V} &= \textstyle\sum_{p_1=\{v_1,h_1\},q_0=\{v_0,h_0\}} \varepsilon_{1,p_1,q_0,V},\\
\varepsilon'_{1,H} &= \textstyle\sum_{p_1=\{v_1,h_1\},q_0=\{v_0,h_0\}} \varepsilon_{1,p_1,q_0,H}.
\end{aligned} \tag{3.31}$$

Compared with the emissivity of 1D sea surfaces (see Eq. (3.20)), cross-polarization terms, where p_0, q_0 and C do not represent the same polarization, appear here. For 1D surfaces, these terms never occur, as the angles α and β both equal 0.

Finally, the polarized emissivity of the sea surface is obtained by averaging $\varepsilon'_{1,V}$ and $\varepsilon'_{1,H}$ over the slopes of M_1 and M_0, given by:

$$\begin{aligned}
\varepsilon_{1,V} &= \left\langle \varepsilon'_{1,V} g_0^{\text{2D}} S^1_{\text{M}} \right\rangle_{1,\text{2D}},\\
\varepsilon_{1,H} &= \left\langle \varepsilon'_{1,H} g_0^{\text{2D}} S^1_{\text{M}} \right\rangle_{1,\text{2D}},
\end{aligned} \tag{3.32}$$

where S^1_{M} is the monostatic first-order illumination function developed in Sec. 2.2.1. The symbol $\langle \cdots \rangle_{1,2D}$ stands for the statistical average over the heights and the slopes of M_1 and M_0:

$$\begin{aligned}
\langle \cdots \rangle_{1,\text{2D}} = &\int_{-\infty}^{+\infty}\int_{-\infty}^{+\infty}\int_{-\infty}^{+\infty}\int_{-\infty}^{+\infty}\int_{-\infty}^{+\infty}\int_{-\infty}^{+\infty} \cdots\\
&p(\zeta_1, \gamma_{x_1}, \gamma_{y_1}, \zeta_0, \gamma_{x_0}, \gamma_{y_0})\, \mathrm{d}\zeta_1\, \mathrm{d}\gamma_{x_1}\, \mathrm{d}\gamma_{y_1}\, \mathrm{d}\zeta_0\, \mathrm{d}\gamma_{x_0}\, \mathrm{d}\gamma_{y_0},
\end{aligned} \tag{3.33}$$

where $p(\zeta_1, \gamma_{x_1}, \gamma_{y_1}, \zeta_0, \gamma_{x_0}, \gamma_{y_0})$ is the joint PDF of the heights and the slopes with respect to the x and y directions of the points M_1 and M_0.

To calculate the integration in Eq. (3.33), the changes of variables given by Eqs. (2.5) and (2.61) are performed. The integration variables in Eq. (3.33) become:

$$\mathrm{d}\gamma_{x_1}\,\mathrm{d}\gamma_{y_1}\,\mathrm{d}\gamma_{x_0}\,\mathrm{d}\gamma_{y_0} = |J|\,\mathrm{d}\gamma_{X'}\,\mathrm{d}\gamma_{Y'}\,\mathrm{d}\gamma_{X}\,\mathrm{d}\gamma_{Y}, \tag{3.34}$$

where $J = 1$ is the Jacobian of the changes of variables.

3.2.2.3 Estimation of the slope PDF of M_1

The joint PDF $p(\zeta_0, \gamma_{x_0}, \gamma_{y_0}, \zeta_1, \gamma_{x_1}, \gamma_{y_1})$ of the heights and the slopes of the surface points M_0 and M_1 is involved when calculating the integrations in Eq. (3.33). It is given by:

$$p(\zeta_0, \gamma_{x_0}, \gamma_{y_0}, \zeta_1, \gamma_{x_1}, \gamma_{y_1}) = p_\gamma(\zeta_0, \gamma_{x_0}, \gamma_{y_0}) p(\zeta_1, \gamma_{x_1}, \gamma_{y_1} \mid \zeta_0, \gamma_{x_0}, \gamma_{y_0}). \tag{3.35}$$

The statistical correlation between the heights and slopes of M_0 and M_1 is ignored, as the distance between them is unknown. Thus, only the physical correlation is considered. As the integration of the first-order illumination function over the heights holds for any height PDF, and the first-order local emissivity does not depend on the height PDF, the integrations over ζ_0 and ζ_1 are not shown in detail here.

As we discussed in Sec. 3.2.1.2, the slopes of M_1 must fulfill the condition that $|\chi_1| \leq 90°$, and all the slopes fulfilling this condition are assumed to be the slope of M_1 with the same probability. According to Eq. (2.60), the following condition is then obtained:

$$\cos\theta_1 - (\gamma_{x_1}\cos\phi_1 + \gamma_{y_1}\sin\phi_1)\sin\theta_1 > 0, \tag{3.36}$$

or equally:

$$\gamma_{X'} < \mu_1. \tag{3.37}$$

The slope PDF of the point M_1 is then given by:

$$p(\gamma_{x_1}, \gamma_{y_1} \mid \gamma_{x_0}, \gamma_{y_0}) = \frac{\Upsilon(\mu_1 - \gamma_{X'})}{\displaystyle\int_{-\infty}^{\mu_1} p_\gamma(t)\mathrm{d}t} p_{\gamma_{x'}}(\gamma_{x_1}, \gamma_{y_1}), \tag{3.38}$$

where $p_{\gamma_{x'}}$ is the marginal surface slope PDF along the X' direction.

3.2.2.4 Numerical results for 2D surfaces

First-order emissivity In this section, we present calculations based upon the first-order components of sea surface infrared emissivity. The calculation is performed for wavelengths inside the infrared atmospheric windows of 3 to 5 μm and 8 to 13 μm. The sea refraction index n in these regions is given by Hale and Querry [49]. We recall that Hale and Querry did not take salinity into account.

The first-order sea surface infrared emissivity (SESR) ε_1 is calculated by Eq. (3.32). The calculations are performed for 2D sea surfaces with Gaussian or non-Gaussian slope PDF, and are compared with the 1D surface model. The results for a wind speed $u_{12} = 5$ m/s and the wavelengths 4 and 10 μm are shown in Fig. 3.20,

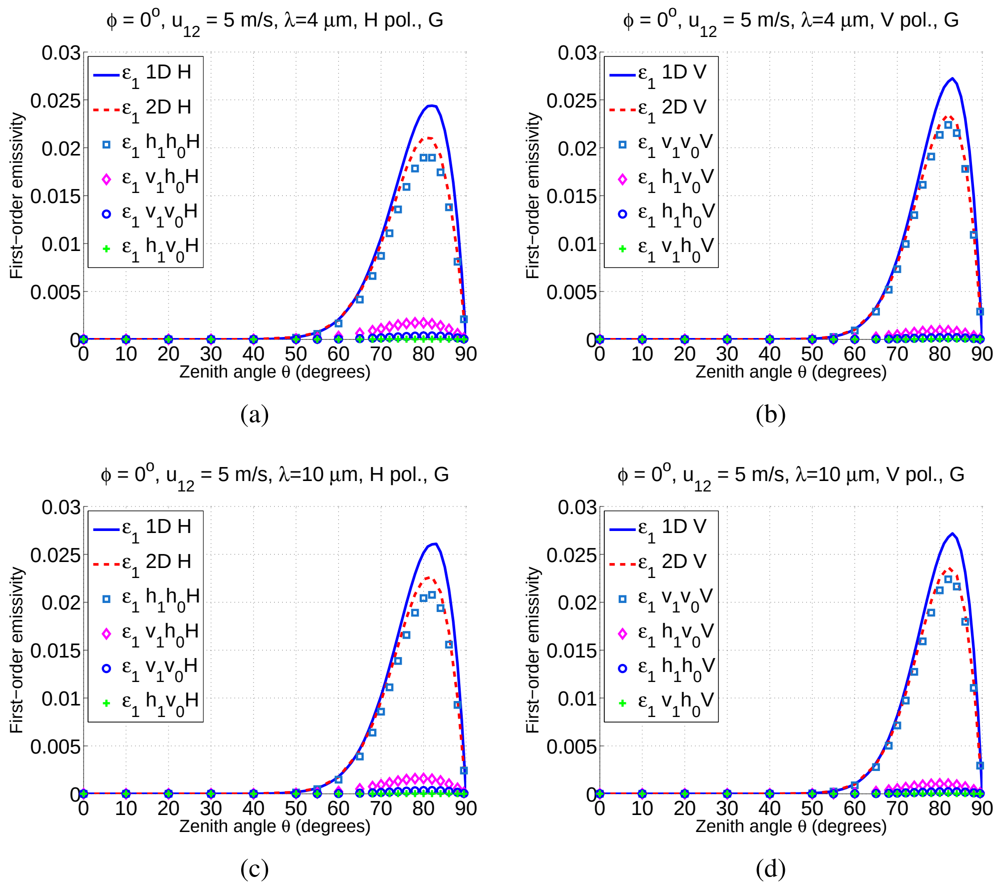

(a) (b)

(c) (d)

Figure 3.20: First-order sea surface infrared emissivity in H polarization (left column) and in V polarization (right column). The wavelength is 4 μm (upper row) and 10 μm (lower row). The receiver is located in the up-wind direction. The wind speed is $u_{12} = 5$ m/s.

and the results for $u_{12} = 10$ m/s are shown in Fig. 3.21. The receiver is located in the up-wind direction ($\phi = 0°$).

For any wind speed, it is shown that the first-order sea surface emissivity ε_1 is significant for large zenith angles, e.g. $\theta > 60°$. This region is enlarged with the increase of the wind speed u_{12}. Maxima about 0.025 are found around $\theta = 80°$. The first-order emissivity of 1D and 2D surfaces (solid and dashed lines in Fig. 3.20 and Fig. 3.21) are similar. The surface emissivity of 2D surfaces in either H or V polarization is slightly smaller than that of 1D surfaces for large zenith angles $\theta > 70°$.

The cross-polarization terms (terms where p_1, q_0 and C do not represent the same polarization) are very weak for both wind speed. It is shown that these terms are weaker for $u_{12} = 5$ m/s. It can be concluded that the increase of wind speed enhances the cross-polarization effect.

The averages of the angles α and β are calculated, which are given by $\langle \alpha \bar{S}^1_{\mathrm{M}} \rangle_1$ and $\langle \beta \bar{S}^1_{\mathrm{M}} \rangle_1$. The first-order illumination function is taken into account so as to weight each α and β according to the corresponding probability of observing surface reflections. The result is shown in Fig. 3.22, with the same parameters as in Fig. 3.20 and Fig. 3.21.

It is shown that the average values of α and β are very small, with maxima about $3°$ for β and $1°$ for α ($\sin^2(3°) \approx 2.7 \times 10^{-3}$, $\sin^2(1°) \approx 3 \times 10^{-4}$) for $u_{12} = 5$ m/s,

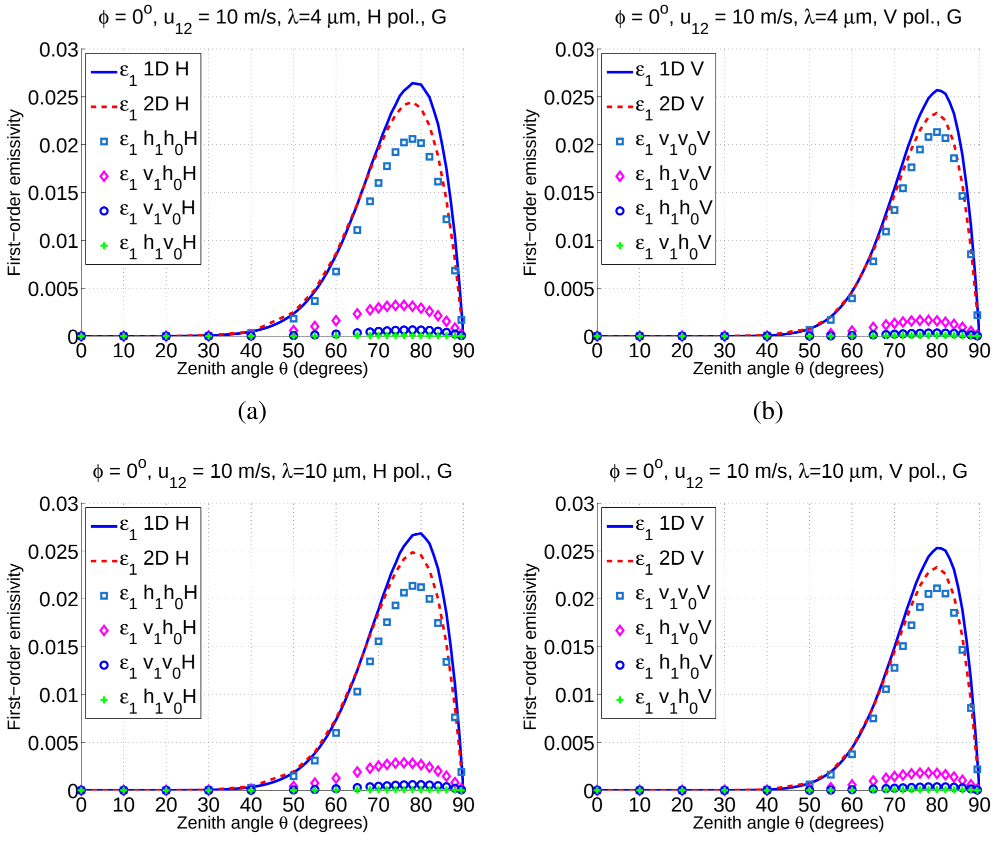

(a) (b)

(c) (d)

Figure 3.21: First-order sea surface infrared emissivity in H polarization (left column) and in V polarization (right column). The wavelength is 4 μm (upper row) and 10 μm (lower row). The receiver is located in the up-wind direction. The wind speed is $u_{12} = 10$ m/s.

and with maxima about 4° for β and 1.5° for α ($\sin^2(4^\circ) \approx 4.9 \times 10^{-3}$, $\sin^2(1.5^\circ) \approx 6.8 \times 10^{-4}$) for $u_{12} = 10$ m/s. In other words, the local and global polarization directions are almost the same, thus the cross-polarization terms are weak. This also proved that the increase of wind speed enhance the cross-polarization effect.

In addition, as α and β are small, the local planes of incidence at the source point (M_0) and the reflection point (M_1), and the global plane of incidence are almost parallel with each other. As a result, only a narrow angular area of the sea surface around its intersection with the global plane of incidence participates in producing the first-order emissivity.

Although a receiver can neither measure the emissivity of $p_1 q_0 C$ polarization separately, nor measure the value of the rotation angles α and β, it is relevant to study the cross-polarization effect. First of all, it helps us better understand the physical process. Secondly, when the surface reflectivity is calculated, cross-polarization can be measured.

Fig. 3.23 compares the polarized first-order emissivity ε_1 with Gaussian and non-Gaussian sea surface slope PDFs versus the zenith angle θ, in global H polarization on the left (a) and V polarization on the right. The wind speed is $u_{12} = 10$ m/s and the wavelength is $\lambda = 10$ μm. The receiver is located in the up-wind direction ($\phi = 0^\circ$).

It is shown that in the up-wind direction ($\phi = 0^\circ$), the first order emissivities ε_1

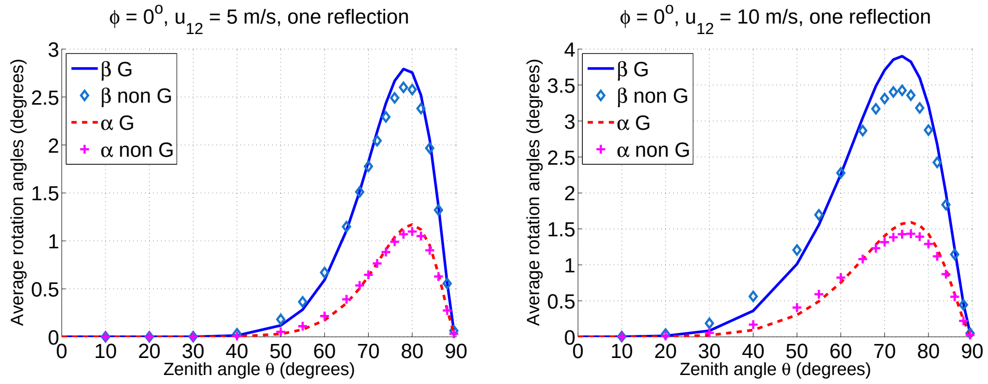

(a) (b)

Figure 3.22: Averaged α and β. The wind speed $u_{12} = 5$ m/s on the left (a) and $u_{12} = 10$ m/s on the right. The receiver is located in the up-wind direction.

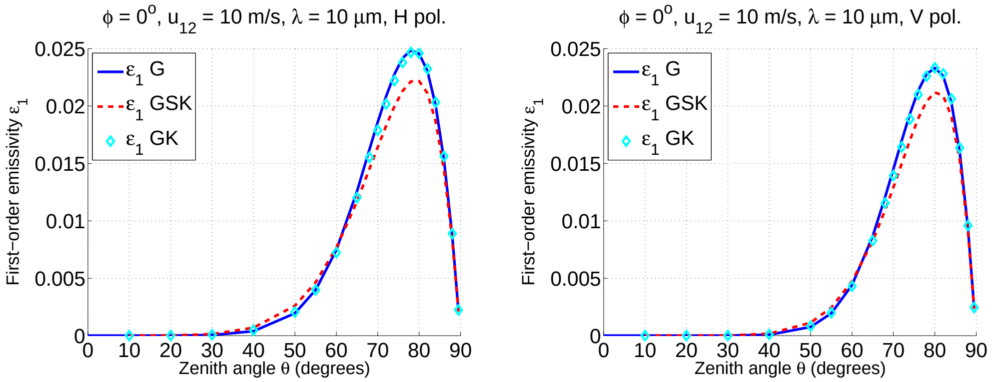

(a) (b)

Figure 3.23: Comparison of the first-order sea surface infrared emissivity with Gaussian and non-Gaussian slope PDF versus the zenith angle θ, in global H polarization on the left (a) and V polarization on the right (b). The wind speed is $u_{12} = 10$ m/s and the wavelength is $\lambda = 10$ μm. The receiver is located in the up-wind direction ($\phi = 0°$).

with G and GK PDFs are very similar in both H and V polarizations, meaning that kurtosis effect is very weak. Skewness effect is dominant for $\phi = 0°$. In general, taking into account the skewness and kurtosis effects (GSK), ε_1 is slightly larger for moderate zenith angles (e.g. $20° < \theta < 60°$) and smaller for larger zenith angles (e.g. $\theta > 60°$). The largest differences caused by the skewness and kurtosis effects are about 2.5×10^{-3}, which occurs around $\theta = 80°$.

Fig. 3.24 shows the first-order surface emissivity ε_1 versus the azimuth angle ϕ, with the H polarized component shown in (a) and the V polarized one in (b). The zenith angle is $\theta = 85°$. The other parameters are the same as in Fig. 3.23.

The first-order emissivity ε_1, in H or V polarization, varies with the azimuth angle. It is shown that ε_1 with Gaussian slope PDF if symmetrical about the up-wind, down-wind and cross-wind directions. The same conclusion is found when the kurtosis effect is taken into account (GK). The first-order emissivity is slightly increased for all ϕ, with the most significant increase occurring in the cross-wind directions ($\phi = \{90°, 270°\}$).

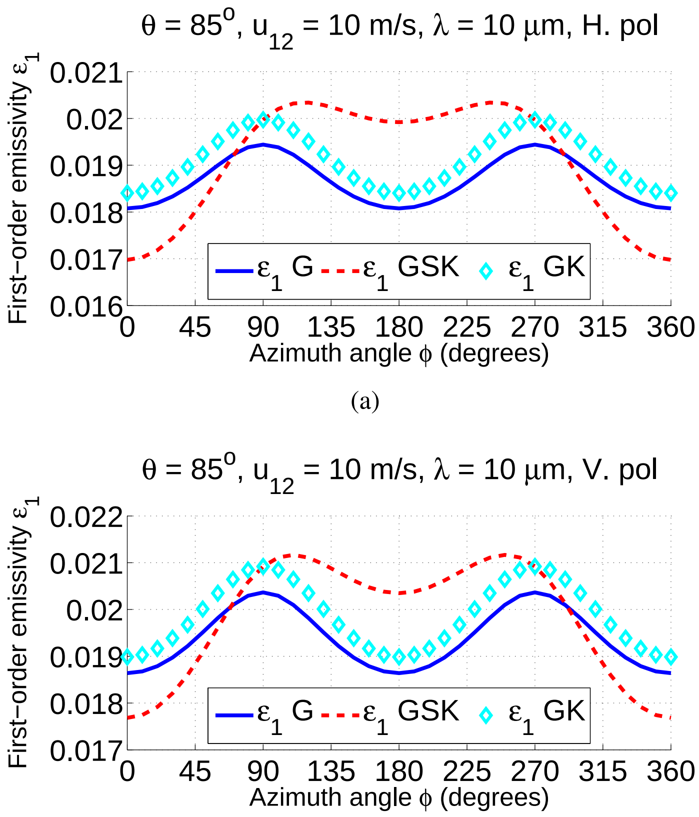

(a)

(b)

Figure 3.24: Comparison of the first-order sea surface infrared emissivity with Gaussian and non-Gaussian slope PDF versus the zenith angle θ, in global H polarization at the top (a) and V polarization at the bottom (b). The wind speed is $u_{12} = 10$ m/s and the wavelength is $\lambda = 10$ μm. The receiver is located in the up-wind direction ($\phi = 0°$).

After taking into account the skewness effect in additional, the first-order emissivity ε_1 is not symmetrical about the cross-wind directions, whereas it is always symmetrical about the up- and down-wind directions. The skewness effect is more significant for the up- and down-wind directions, whereas it is very weak in the cross-wind directions (the curves of GK and GSK PDFs overlap).

In general, the emissivity with one surface reflection ε_1 is more sensitive to the wind direction after taking the skewness and kurtosis effects into account. The first-order emissivity ε_1 reaches minimum in the up- and down-wind direction, and has maximum in the cross-wind directions. The largest difference for ε_1 with Gaussian slope is about 0.0015, in both H and V polarizations. After taking into account the skewness and the kurtosis effects, ε_1 has smaller value for $\phi = 0°$ and has larger value for $\phi = 90°$, with the difference increasing to about 0.0035.

Total emissivity of the sea surface ε_{tot} As we showed in the 1D model that emissivities with two and more reflections (second and higher order , or SESRSR, $\cdots$) are negligible, the total emissivity ε_{tot} of the sea surface can be estimated by the sum of the zero- and first-order contributions, ε_0 and ε_1 respectively.

Fig. 3.25 shows the zero-order emissivity and the total emissivity of the sea surface (a) and their DOPs (b), versus the zenith angle θ. The other parameters are the same as in Fig. 3.23.

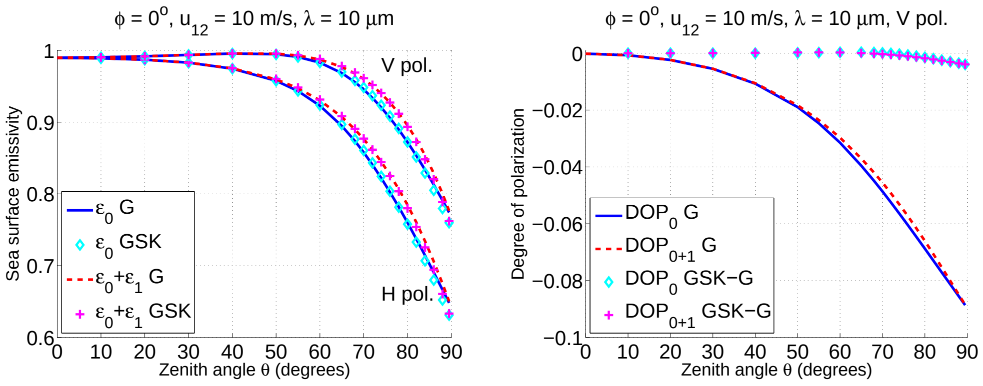

(a) (b)

Figure 3.25: Sea surface infrared emissivity (a) and the degree of polarization (DOP) (b) with Gaussian and non-Gaussian slope PDFs versus the zenith angle θ. The differences of DOPs with Gaussian and non-Gaussian slope PDFs are shown in (b) as diamonds and pluses.

It is shown that the total sea surface infrared emissivity ($\varepsilon_{\text{tot}} = \varepsilon_0 + \varepsilon_1$) is significantly increased after taking into account one surface reflection for large zenith angles, e.g. $\theta > 60^\circ$ (see Fig. 3.25 (a)), in both H and V polarizations. The influence of the skewness and kurtosis effects is not obvious for $\theta < 70^\circ$. Beyond this angle, the skewness and kurtosis effects effects contribute. The zero-order emissivity ε_0 and the total emissivity ε_{tot} are both reduced in the up-wind direction ($\phi = 0^\circ$), which can be predicted by Fig. 3.11 and Fig. 3.24, in which ε_0 and ε_1 are reduced by the skewness effect in the up-wind direction.

The DOP of the sea surface emissivity is also calculated and shown in 3.25 (b) versus the zenith angle θ. It is notable that the DOP is negative, which means that surface radiance in V polarization is larger (which can be verified in 3.25 (a)). The absolute value of the DOP can be relatively large for large θ, e.g. it is larger than 6% for $\theta > 60^\circ$, meaning that the sea surface infrared intrinsic radiance is partially polarized, with over 6% energy emitted being polarized. The absolute value of the DOP is reduced after taking one reflection into account. In other words, surface reflection reduces the polarization property of the sea surface intrinsic radiation.

As the DOPs of ε_0 and ε_{tot} with G and GSK PDFs are very similar, the difference of their DOPs are shown in 3.25 (b) (diamonds and pluses). The DOPs with Gaussian and non-Gaussian PDFs are very similar for $\theta < 70^\circ$ (difference ≈ 0), meaning that skewness and kurtosis effects are weak. Beyond this angle, the skewness and kurtosis effects contribute. The absolute value of the DOPs are increased, meaning that skewness and kurtosis effects enhance the polarization characteristics of the surface intrinsic radiation.

Fig. 3.26 shows the zero-order emissivity and the total emissivity of the sea surface (a) and their DOPs (b), versus the azimuth angle ϕ. The other parameters are the same as in Fig. 3.24.

It is shown that the total sea surface infrared emissivity is significantly increased after taking into account one surface reflection for any ϕ when $\theta = 85^\circ$, in both H and V polarization. The zero-order emissivity ε_0 and the total emissivity ε_{tot} both have larger values in the up- and down-wind directions $\phi = \{0^\circ, 180^\circ\}$ than in the

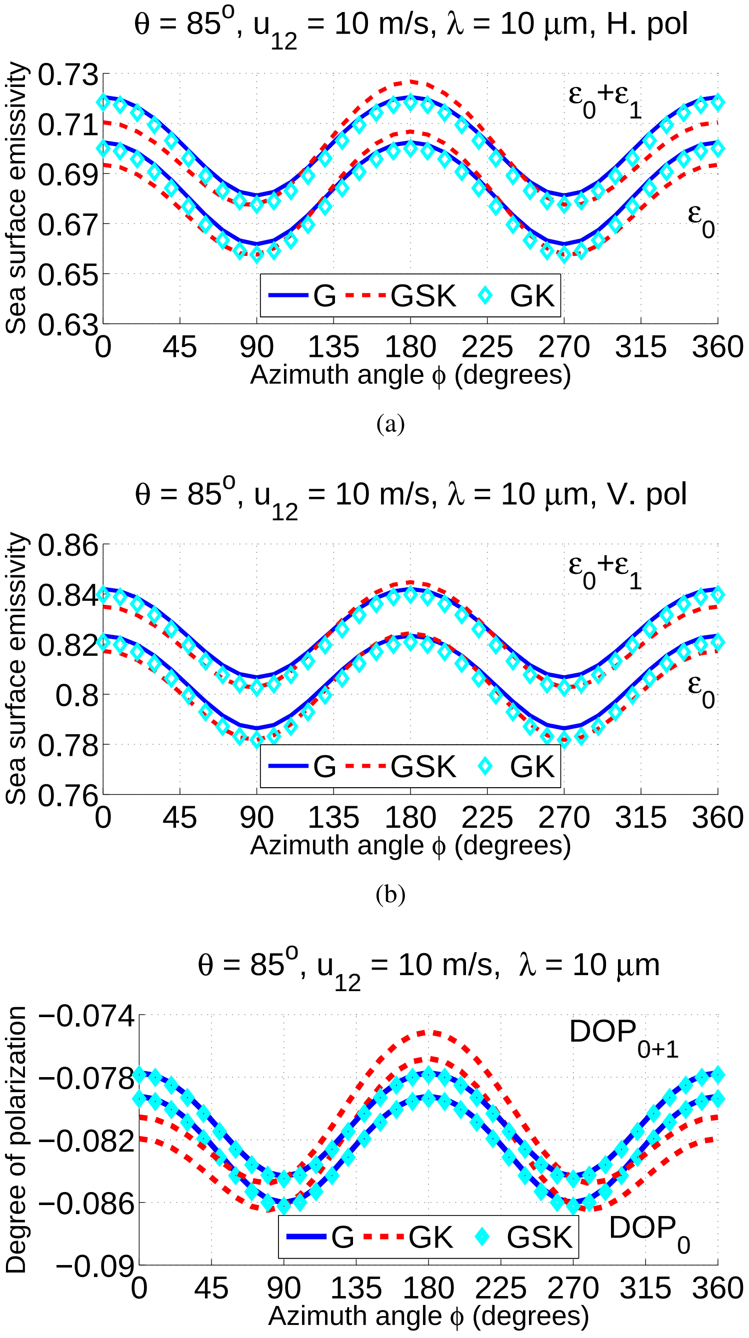

(a)

(b)

(c)

Figure 3.26: Sea surface infrared emissivity in H (a) and V (b) polarizations, and the degree of polarization (DOP) (c), with Gaussian and non-Gaussian slope PDFs, versus the azimuth angle ϕ.

cross-wind directions $\phi = \{90°, 270\}$, as the sea surface has a larger RMS slope in the up- and down-wind directions.

The total emissivity of the surface is symmetrical about the up- cross- and down-wind directions when Gaussian PDF is considered. The same properties of symmetry is obtained when the kurtosis effect is considered. After the skewness effect is taken into account, it is not symmetrical about the cross-wind directions, but it is always symmetrical about the up- and down-wind directions. This conclusion can be predicted by Fig. 3.11 and Fig. 3.24, in which the zero-order emissivity ε_0 and the first-order emissivity ε_1 has the same properties of symmetry.

The degree of polarization (DOP) of the total emissivity ε_{tot} is also calculated and compared with that of the zero-order emissivity ε_0. The results are shown in 3.26 (c). The DOP of the total emissivity also depends on the wind direction. Generally, for Gaussian and non-Gaussian PDFs, the surface infrared intrinsic radiation is less polarized in the cross-wind directions than in the up-wind and down-wind directions (minima in absolute value).

The DOP of surfaces with Gaussian and non-Gaussian slope PDFs are compared. It is shown that the DOPs of ε_0 and ε_{tot} have the same properties of symmetry. After taking into account the skewness and kurtosis effect, ε_0 and ε_{tot} are more polarized in the region $\phi \in [0°, 90°] \cup [270°, 360°]$ (absolute values of DOPs increased), and are less polarized in the region $\phi \in [90°, 270°]$ (absolute values of DOPs reduced).

3.2.2.5 Comparison with measurements

Comparison with Smith *et al.* Smith *et al.* [37] derived the sea surface infrared emissivity in the Gulf of Mexico by measurements. The measurements were carried out in January 1995. The sea surface emissivity was obtained for zenith angles $\theta = 36.5°$, $56.5°$ and $73.5°$, whereas the azimuth angle ϕ was not specified. During the measurements, the wind speed was ranging from 2 to 8 m/s. The unpolarized emissivity was then obtained for wavelengths $\lambda \in [8, 12]$ μm ($1/\lambda \in [830, 1250]$ cm^{-1}) and compared with the analytical model of Masuda *et al.* [10], in which no surface reflection was considered. It was shown that the measurements and the analytical result agreed well with each other for $\theta = 36.5°$ and $56.5°$, but a difference of over 0.02 appeared for $\theta = 73.5°$.

In this subsection, the 2D sea surface emissivity is calculated under similar conditions. The non-Gaussian surface slope PDF is used rather than the Gaussian one, as it better represents real sea surfaces. Besides, the results with Gaussian and non-Gaussian PDFs are quite similar for $\theta = 73.5°$. The unpolarized sea surface emissivity is obtained by averaging the emissivities in H and V polarizations. As the azimuth angle is not specified in the measurement, an error-bar is obtained corresponding the uncertainty of the wind directions $\phi =\in [0°, 180°]$ during the calculation. The wind speed is set to $u_{12} = 5$ m/s, which is the average wind speed during the measurement. The results are shown in Fig. 3.27.

It is shown in Fig. 3.27 that the analytical results and the measurements have a similar form. The error-bars in the measurement corresponds to the error of measurement. For $\theta = 36.5°$, no difference is obtained after taking the first-order emissivity ε_1 into account, as ε_1 is really small for this zenith angle. For $\theta = 56.5°$, a small improvement in the agreement is obtained after taking ε_1 into account. For $\theta = 73.5°$, the zero-order emissivity ε_0 underestimates the sea surface emissivity

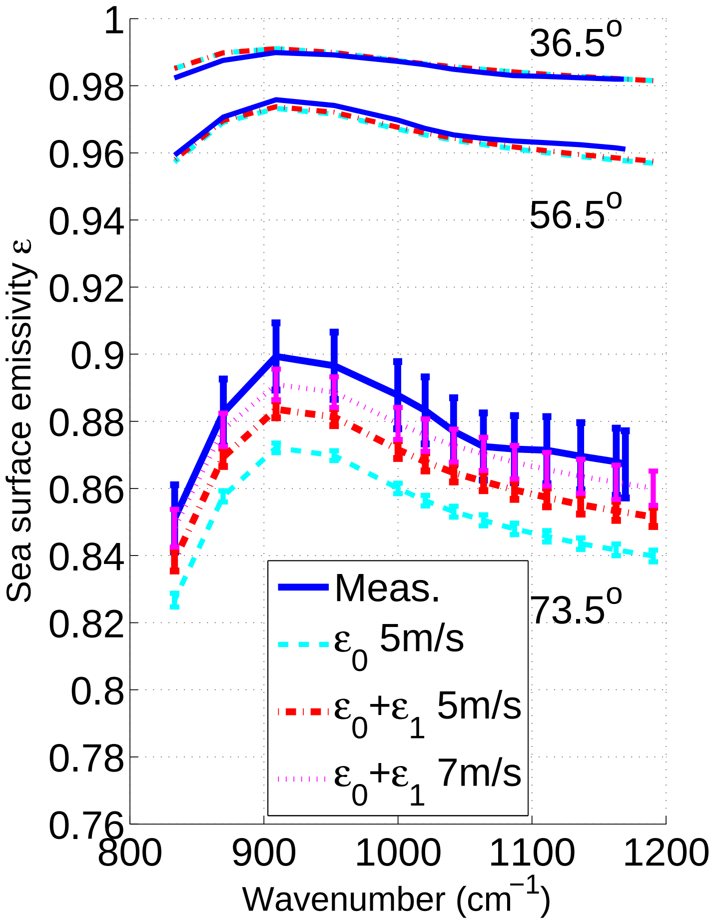

Figure 3.27: Comparison of the sea surface infrared emissivity with the measurement of Smith *et al.* for $\theta = 73.5°$.

by at least 0.02. A much better agreement is obtained after taking the first-order emissivity ε_1 into account. However, the analytical results still underestimate the measurements, although their error-bars overlap for some wavenumbers (around $1/\lambda \approx 1060\,\mathrm{cm}^{-1}$).

This underestimation can be attributed to several reasons. As surface emissivities with two and more surface reflections are very weak (emissivity with two reflection (SESRSR) $\varepsilon_2 \approx 0.001$ for $u_{12} = 5$ m/s, $\theta = 73.5°$, see Figs. 3.15 and 3.16 for 1D surfaces), taking into account higher orders surface reflected emissivities should not reduce significantly the underestimation. One reason is that we do not take the salinity and the temperature of sea water into account (the refraction index we used is derived for fresh water at 25°C). Another reason might be that the wind speed was not measured precisely enough. In Fig. 3.27, we also show the calculation result for a wind speed $u_{12} = 7$ m/s and $\theta = 73.5°$, where a much better agreement is obtained.

Comparison with Niclòs *et al.* Niclòs *et al.* [38] derived the sea surface infrared emissivity of the Mediterranean sea from an oil rig above the sea surface. The measurement data are obtained for four channels of wavelengths: 8-14, 8.2-9.2, 10.5-11.5, and 11.5-12.5 μm. Measurements were carried out under two different wind speeds u_{12}, which were approximately 4.5 and 10.3 m/s. The wind direction was not specified.

To make a comparison, calculations are carried out for similar conditions. For the channel 8.2-9.2 μm, the sea surface emissivity is calculated with a step of 0.2 μm and is then averaged. For the channels 10.5-11.5 and 11.5-12.5 μm, a step of 0.5 μm is taken. These wavelengths are chosen because the corresponding sea surface refraction indices are provided by Hale and Querry [49]. An error-bar is obtained corresponding to the uncertainty of the wind direction $\phi \in [0°, 180°]$ during the calculation. The results with non-Gaussian slope PDF are compared with measurements in Fig. 3.28.

Generally, the analytical result better agrees with measurements for large zenith angles ($\theta = 55°$ and $65°$) after taking into account the first-order emissivity ε_1. In most of the cases, considering one reflection brings the analytical results into the uncertainty of measurements for $\theta = 65°$ (at least error-bars overlap), except for the cases of Figs. 3.28 (e). Even though in case of Figs. 3.28 (e), considering one surface reflection still reduces the difference between the analytical result and the measurements.

3.3 Conclusion

This chapter calculates the polarized infrared emissivity of the sea surface with an analytical model, where one surface reflection is considered. A 1D surface analytical model is firstly derived, which gives a good agreement with the results of a Monte Carlo ray-tracing method. This model was published in 2011 in [22]. Further, a 2D surface model is developed, thereby allowing consideration of the "cross-polarization" effect. The skewness and kurtosis effects are also studied. It is shown that the agreement between the model and the measurement is greatly improved for large zenith angles θ by considering one surface reflection. The cross-polarization effect in the zero-order sea surface infrared emissivity ε_0 is significant for small zenith angles, but it vanishes rapidly as the zenith angle increases. Cross-polarization is always weak when studying the first-order emissivity. The skewness and kurtosis effects are significant for grazing zenith angles ($\theta > 80°$). Sea surface infrared emissivity is sensitive to the wind direction, with $\phi = 180°$ being the axis of symmetry. It is also symmetrical about $\phi = 90°$ for Gaussian surfaces, whereas it is not after taking into account the skewness effects. For Gaussian surfaces, surface emissivities for grazing zenith angles reache maxima in the up-wind ($\phi = 0°$) and down-wind ($180°$) directions, whereas minima are found in the cross-wind ($\phi = 90°,\ 270°$) directions. After taking into account the skewness and kurtosis effects, the surface emissivity has larger value in the down-wind direction ($\phi = 180°$) than in the up-wind direction ($\phi = 0°$). The 2D surface model was published in 2012 in [44].

As discussed in Chap. 1, to predict the signal received by the receiver which is measuring the surface radiance, the surface emissivity ε and the surface reflectivity ρ must be derived. As the sea surface emissivity is derived by now, in what follows, the surface reflectivity is derived. The bistatic illumination function is studied in Chap. 4, and then the surface reflectivity is derived in Chap. 5.

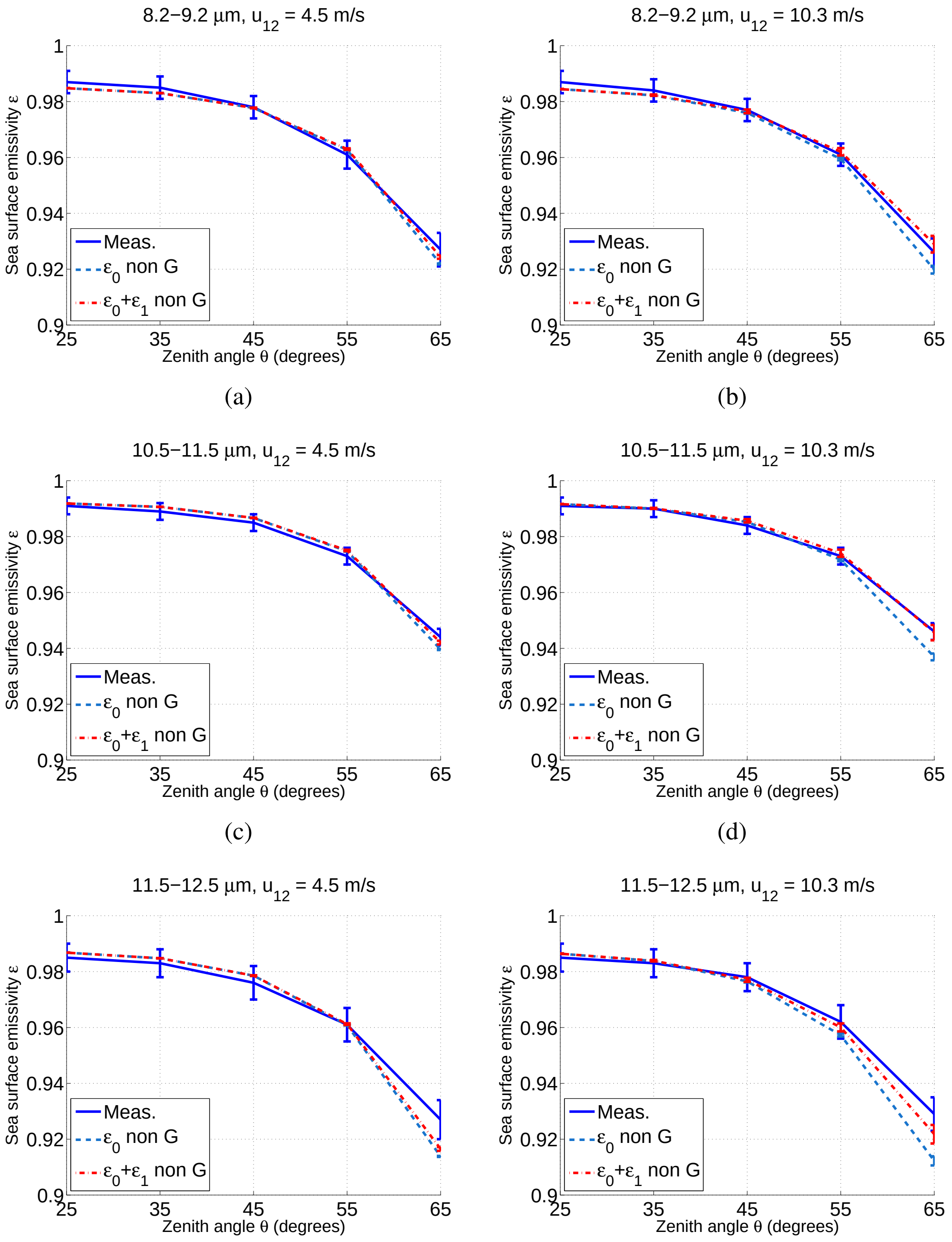

(a) (b)

(c) (d)

(e) (f)

Figure 3.28: Comparison of the sea surface infrared emissivity with the measurements of Niclòs *et al.*, for channels 8.2-9.2 μm ((a) (d)), 10.5-11.5 μm ((b) (e)), 11.5-12.5 μm ((c) (f)), and for wind speed $u_{12} = 4.5$ m/s ((a)-(c)) and $u_{12} = 10.3$ m/s ((d)-(f)).

4

Bistatic illumination function

When solving rough/sea surface reflectivity ρ, shadowing from the transmitter and the receiver (shadowing from the transmitter is also called "hiding", and shadowing from the receiver is also called "masking" [50]) must be studied, especially when the transmitter and the receiver are close to the horizon (θ_i and θ are large, see Fig. 1.2 (c)). On the other hand, the incident ray may undergo multiple surface reflections before it is reflected into the receiver direction (see Fig. 1.2 (d) for two surface reflections).

To deal with the phenomena of shadowing and multiple surface reflections, a bistatic illumination function S_{B}^n must be employed, where $n = 1, 2, 3, \ldots$ denotes the number of reflections. The subscript "B" stands for the bistatic configuration, which means that the transmitter and the receiver are at different locations.

In this chapter, the bistatic illumination function S_{B}^n is studied. Geometric optics approximation is assumed to be valid, thus only specular reflections are considered. In Sec. 4.1, the bistatic illumination function with one surface reflection S_{B}^1 is studied. The Smith bistatic illumination function [37, 4] is adopted and reviewed. In Sec. 4.2, an improved bistatic illumination function with two surface reflections S_{B}^2 is developed and compared with a Monte Carlo ray-tracing method. These bistatic illumination functions $S_{\mathrm{B}}^{1,2}$ are then used in Chap. 5 to calculate the surface reflectivity with accuracy.

4.1 Illumination function with one reflection

4.1.1 Hiding and masking

Fig. 4.1 shows an incident ray $\hat{s}_i$ reflected by a rough surface into the observation direction $\hat{s}$. The receiver is located in the direction $\hat{s}(\theta, \phi)$, where $\theta \in [0°, 90°]$ is the zenith angle and $\phi \in [0°, 360°]$ is the azimuth angle. The transmitter is located in the direction $\hat{s}_i^-(\theta_i, \phi_i) = -\hat{s}_i$, with the zenith angle being $\theta_i \in [0°, 90°]$ and the azimuth angle being $\phi_i \in [0°, 360°]$. The superscript "$^-$" stands for the inversion of direction. The direction of the incident ray $\hat{s}_i$ can also be denoted by the zenith angle $\theta_1 \in [90°, 180°]$ and the azimuth angle $\phi_1 \in [0°, 360°]$. Note that the incident ray $\hat{s}_i$, the reflection ray $\hat{s}$ and the zenith direction $\hat{z}$ usually do not belong to the same plane. The definition of these angles are illustrated in Fig. 4.2.

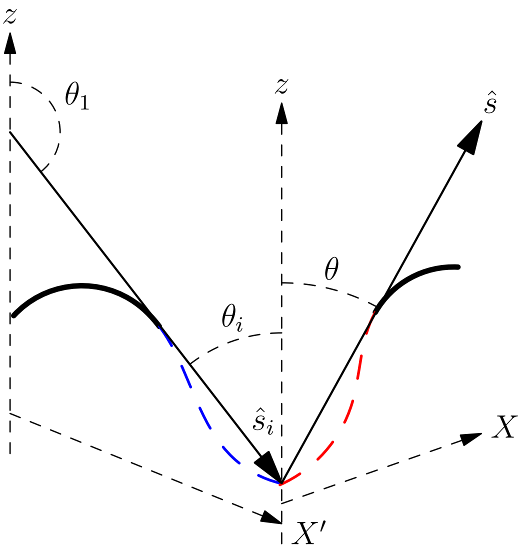

Figure 4.1: Bistatic shadowing: Hiding from the transmitter and masking from the receiver. For 2D surfaces, zenith angles are not oriented.

Because of the roughness of the surface, some part of the surface lies in the shadow of the transmitter, denoted as the blue dashed lines in Fig. 4.1. Similarly, some part of the surface lies in the shadow of the receiver, denoted as the red dashed lines in Fig. 4.1. If the incident ray $\hat{s}_i$ intersects the rough surface in the red dashed region, the reflected ray would be blocked by the surface. This phenomenon is also called masking [50].

The shadowing effect from the transmitter is studied in the $(X'z)$ plane, whereas the masking effect from the receiver is studied in the (X, z) plane. Note that the $(X'z)$ plane and the (X, z) plane are not necessarily parallel. Hiding and masking cannot be ignored for large angles of incidence θ_i and for large observation angles θ.

For better convenience in the calculation, two new systems of coordinates are defined. The first One (X, Y, z) is defined by rotating the basis (x, y) anticlockwise through an angle ϕ about the z axis, so that the receiver lies in the (X, z) plane. The system of coordinates (X, Y, z) is related to the receiver's direction, with X being the horizontal direction of the receiver. This system of coordinates is also used when defining the monostatic illumination function S_{M}^0 in Sec. 2.1.2. The other system of coordinates (X', Y', z) is defined by rotating the basis (x, y) anticlockwise through an angle ϕ_1 about the z axis, so that the ray $\hat{s}_i$ lies in the (X', z) plane. The system of coordinates (X', Y', z) is related to the transmitter direction, with X' being the horizontal direction of the transmitter. This system of coordinates is also used when defining the monostatic illumination function S_{M}^1 in Sec. 2.2.1 by replacing the transmitter with another surface point M_1. The definition of these systems of coordinates is illustrated in Fig. 4.2.

The rays $\hat{s}$ and $\hat{s}_i$ may be seen as two independent rays. Otherwise $\hat{s}$ is treated as the reflected ray of $\hat{s}_i$. For the second case, the inverse path is used when deriving the bistatic illumination function, which assumes that a ray is emitted from the receiver, so as to be consistent with the configuration of the emissivity problem.

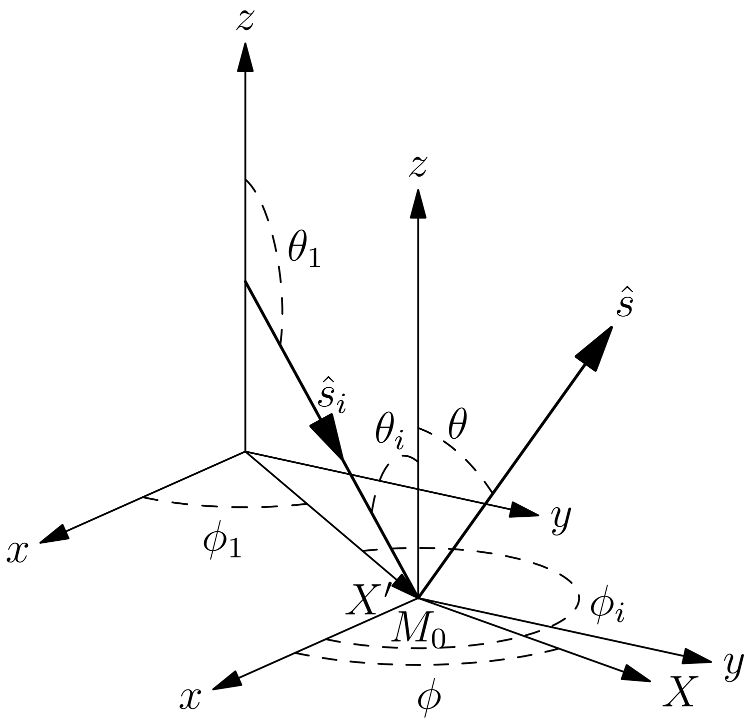

Figure 4.2: Bistatic shadowing: Hiding from the transmitter and masking from the receiver - 3D representation with the different systems of coordinates. Zenith angles are not oriented.

For a given observation direction $\hat{s}$ and a given surface point M_0, the direction of the incidence ray $\hat{s}_i$, under geometrical optics approximation, is given by:

$$\hat{s}_i = \hat{s} - 2\hat{n}_0(\hat{n}_0 \cdot \hat{s}), \tag{4.1}$$

where $\hat{n}_0$ is the unitary normal to the surface point M_0. The vector $\hat{s}_i^- = -\hat{s}_i$ can also be obtained. Using Eq. (2.58), the angles θ_i, ϕ_i are obtained by applying $\hat{s}_i^-$, whereas θ_1, ϕ_1 are obtained by applying $\hat{s}_i$.

4.1.2 Smith bistatic illumination function S_{B}^1

4.1.2.1 S_{B}^1 for 1D surfaces

To solve the hiding and masking effect, a bistatic illumination function with one surface reflection S_{B}^1 must be employed. Wagner defined S_{B}^1 from his monostatic illumination function S_{M}^0 [3]. He defined the bistatic illumination function by two joint monostatic shadowing problems. Bourlier *et al.* [4] followed the same idea as Wagner [3] to extend the monostatic illumination function S_{M}^0 of Smith [25] to a bistatic configuration. This bistatic illumination function gives the probability that an arbitrary point of the surface is seen by both the transmitter and the receiver. As it was shown in Sec. 2.1.6 that the Smith illumination function was more accurate than the Wagner one, the Smith model is adopted here to deal with the bistatic configuration and briefly reviewed.

Here, the profile of a 2D surface in the (X, z) plane is chosen as a 1D surface, and the (X, z) coordinates are used (see Fig. 4.2 for the definition of X). For 1D surfaces, the azimuth angle is reduced to $\{0°, 180°\}$. Thus, it is more convenience to define the zenith angles as oriented to better define the direction of a vector. As the (X, z) coordinates are used, the direction of the zenith angle θ is defined as the positive direction.

Fig. 4.3 shows 3 cases of single reflection of 1D surfaces. The event "the ray $M_0(\hat{s})$ does not intersects the surface" is denoted as a and that "the ray $M_0(\hat{s}_i^-)$ does not intersects the surface" is denoted as b. M_0 is an arbitrary point of the surface with height ζ_0 and slope γ_0. The bistatic illumination function with one surface reflection S_{B}^1 is given by [3, 2, 4]:

$$S_{\mathrm{B}}^1 = p(a)p(b|a). \tag{4.2}$$

The probability $p(a)$ equals the monostatic illumination function without surface reflection S_{M}^0. Note that a similar conditional probability $p(b|a)$ is calculated in Sec. 2.2.1 when deriving the monostatic illumination function with one surface reflection. The difference is that, here, the probability that the point is seen in both directions is calculated, which means $M_0(\hat{s})$ and $M_0(\hat{s}_i^-)$ are two independent rays, instead of being an incident ray and a reflected ray, which is the case in Sec. 2.2.1. The fact that $M_0(\hat{s})$ and $M_0(\hat{s}_i^-)$ are an incident ray and a reflected ray will be taken into account later.

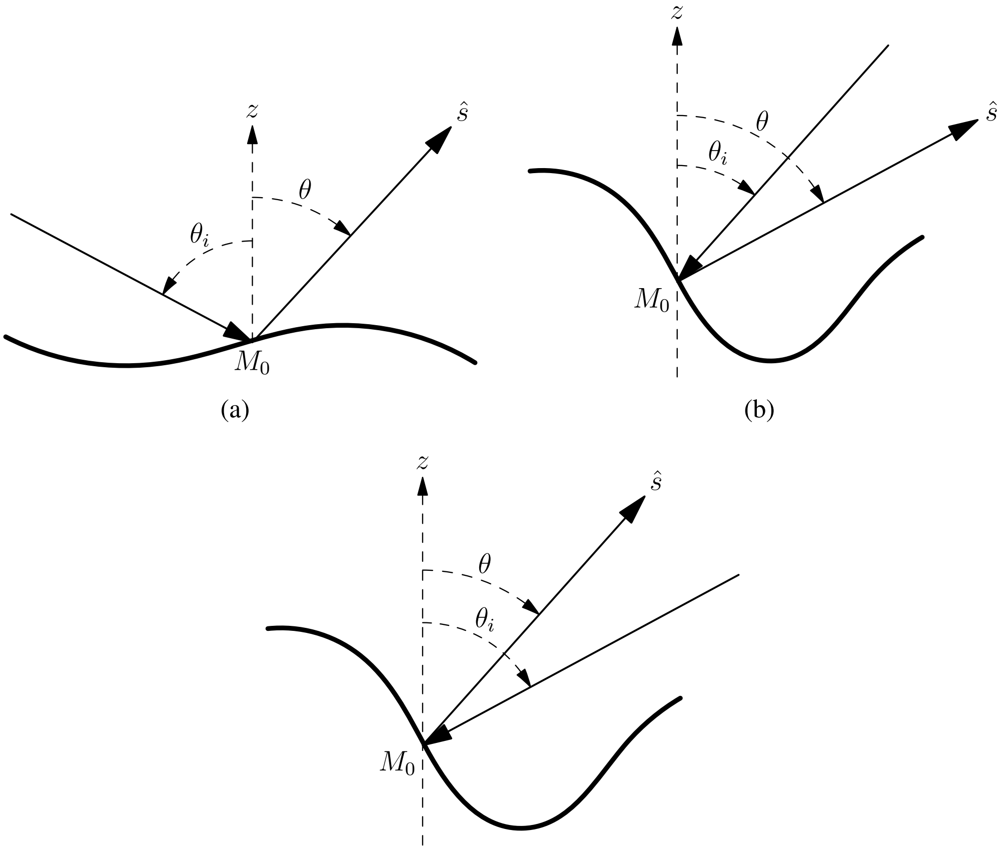

(a) (b)

(c)

Figure 4.3: Three cases of single surface reflection for 1D surfaces. (a) the transmitter and the receiver are on different sides of M_0; (b) the transmitter and the receiver are on the same side with θ_i smaller; (c) the transmitter and the receiver are on the same side with θ smaller. Zenith angles are oriented, with the direction of θ being the positive direction.

In Fig. 4.3 (a), the transmitter and the receiver are on different sides (with respect to the zenith direction) of the point of interest (denoted as point M_0). This case corresponds to $\phi_1 = \phi$ in the 2D surface model (X and X' in the same direction), denoted as case 1 (note that θ_i is negative here as it is in the opposite direction of θ). As no obvious correlation between the events a and b is found, it is assumed that they are uncorrelated for this configuration. Then, the bistatic illumination function is given for the first case by [3, 2, 4]:

$$\begin{aligned} S^1_{\mathrm{B}}(\theta,\theta_i,\gamma_0,\zeta_0) &= p(a)p(b|a), \\ &= p(a)p(b), \\ &= S^0_{\mathrm{M}}(\theta,\gamma_0,\zeta_0)S^0_{\mathrm{M}}(\theta_i,\gamma_0,\zeta_0). \end{aligned} \tag{4.3}$$

In Fig. 4.3 (b), the transmitter and the receiver are on the same side of M_0 with respect to the zenith direction. This case corresponds to $\phi_1 = \phi + 180^\circ$ in the 2D surface model (X and X' in the opposite directions), denoted as case 2. Obvious correlation between the events a and b can be found. As $\theta > \theta_i > 0$, the receiver is lower than the transmitter. Given that M_0 is seen by the receiver, it is sure that it would be also seen by the transmitter. Thus, $p(b|a) = 1$. The bistatic illumination function is given for case 2 by [3, 2, 4]:

$$\begin{aligned} S^1_{\mathrm{B}}(\theta,\theta_i,\gamma_0,\zeta_0) &= p(a)p(b|a), \\ &= p(a) \times 1, \\ &= S^0_{\mathrm{M}}(\theta,\gamma_0,\zeta_0). \end{aligned} \tag{4.4}$$

The case 3 shown in Fig. 4.3 (c) is very similar to case 2, but with $0 < \theta < \theta_i$. Therefore, given that M_0 is seen by the transmitter, it is sure that it would be also seen by the receiver. Thus, $p(a|b) = 1$. The bistatic illumination function is given for case 3 by [3, 2, 4]:

$$\begin{aligned} S^1_{\mathrm{B}}(\theta,\theta_i,\gamma_0,\zeta_0) &= p(b)p(a|b), \\ &= p(b) \times 1, \\ &= S^0_{\mathrm{M}}(\theta_i,\gamma_0,\zeta_0). \end{aligned} \tag{4.5}$$

To sum up and applying the uncorrelated Smith illumination function [25], the uncorrelated first-order bistatic illumination function is given by:

$$S^1_{\mathrm{B}}(\theta,\theta_i,\gamma_0,\zeta_0) = \begin{cases} \Upsilon(\mu-\gamma_0)\Upsilon(\gamma_0-\mu_i)F(\zeta_0)^{\Lambda(\mu)+\Lambda^-(\mu_i)} & \text{for} \quad \text{case } 1 \\ \Upsilon(\mu-\gamma_0)F(\zeta_0)^{\Lambda(\mu)} & \text{for} \quad \text{case } 2 \\ \Upsilon(\mu_i-\gamma_0)F(\zeta_0)^{\Lambda(\mu_i)} & \text{for} \quad \text{case } 3 \end{cases}, \tag{4.6}$$

where $\mu = \cot\theta$ and $\mu_i = \cot\theta_i$ are the slopes of the observation and incident rays $M_0(\hat{s})$ and $M_0(\hat{s}_i^-)$, respectively. Λ and Λ^- are defined in Eqs. (2.20) and (2.69), respectively.

The model S^1_{B} considering the correlation between the heights and the slopes of different surface points can be obtained by applying the correlated monostatic Smith illumination function, which is given by Eq. (2.39).

As stated before, S^1_{B} gives the probability that M_0 is seen by both the transmitter and the receiver, which means that $M_0(\hat{s})$ and $M_0(\hat{s}_i^-)$ are two independent rays. Recall that geometric optics approximation is employed, and only specular reflections are considered. To take into account the fact that $\hat{s}$ is the reflected ray of $\hat{s}_i$, a Dirac delta function is multiplied by S^1_{B} to define another version of bistatic illumination function:

$$S^{1,\mathrm{spe}}_{\mathrm{B}}(\theta,\theta_i,\gamma_0,\zeta_0) = S^1_{\mathrm{B}}(\theta,\theta_i,\gamma_0,\zeta_0)\delta(\gamma_0^{\mathrm{spe}}-\gamma_0), \tag{4.7}$$

where the superscript “spe” stands for that the specular reflection is considered. γ_0^{spe} is the slope of the surface point corresponding to the specular reflection, given by:

$$\gamma_0^{\mathrm{spe}} = -\tan\left(\frac{\theta_i + \theta}{2}\right), \tag{4.8}$$

where θ_i and θ are oriented global incidence and reflection angles.

4.1.2.2 Extension of S_{B}^{1} to 2D surfaces

For 2D surfaces, the bistatic Smith illumination function with one surface reflection S_{B}^{1} is given by:

$$S_{\mathrm{B}}^{1}(\theta, \phi, \theta_i, \phi_i, \gamma_{x0}, \gamma_{y0}, \zeta_0) = \Upsilon(\mu - \gamma_X)\Upsilon(\gamma_{X'} - \mu_i)F(\zeta_0)^{\Lambda(\mu)+\Lambda^{-}(\mu_i)}, \tag{4.9}$$

where γ_{x0}, γ_{y0}, γ_{X_0} and $\gamma_{X_0'}$ are the slope of the point M_0 with respect to the x, y, X and X' directions, respectively. $\mu = \cot\theta$ is the slope of the reflected ray with respect to the X direction and $\mu_i = \cot\theta_1 = -\cot\theta_i$ (note that θ_1 and θ_i are not oriented for 2D surfaces) is the slope of the incident ray with respect to the X' direction.

As shown in Eq. (4.6) for 1D surfaces, for the cases where the transmitter and the receiver belongs to the same plane and are on the same side of M_0 with respect to the zenith, strong dependence is found between the events “$M_0(\hat{s})$ does not intersect the surface” and “$M_0(\hat{s}_i^{-})$ does not intersect the surface” (cases 2 and 3 as shown in Fig. 4.3). This configuration corresponds to $\phi_1 = \phi$ for 2D surfaces. In addition, this strong dependence is also hold when the transmitter and the receiver are close in azimuth angle ($|\phi - \phi_1|$ is small). However, this dependence is difficult to study. Thus, it is left for future research.

To take into account the fact that $\hat{s}$ is the reflected ray of $\hat{s}_i$, S_{B}^{1} in Eq. (4.9) is multiplied by two Dirac delta functions, given by:

$$\begin{aligned} S_{\mathrm{B}}^{1,\mathrm{spe}}(\theta, \phi, \theta_i, \phi_i, \gamma_{x0}, \gamma_{y0}, \zeta_0) \;=\; & S_{\mathrm{B}}^{1}(\theta, \phi, \theta_i, \phi_i, \gamma_{x0}, \gamma_{y0}, \zeta_0) \\ & \times\delta(\gamma_{x0}^{\mathrm{spe}} - \gamma_{x0})\delta(\gamma_{y0}^{\mathrm{spe}} - \gamma_{y0}), \end{aligned} \tag{4.10}$$

where γ_x^{spe} and γ_y^{spe} are the slopes, with respect to the x and y directions, of M_0 corresponding to the specular reflection.

For given incidence direction $\hat{s}_i$ (thus $\hat{s}_i^{-} = -\hat{s}_i$ is also given) and observation direction $\hat{s}$, the unitary normal to the point M_0 corresponding to the specular reflection is given by:

$$\hat{n}_0^{\mathrm{spe}} = \frac{\hat{s} + \hat{s}_i^{-}}{||\hat{s} + \hat{s}_i^{-}||}. \tag{4.11}$$

According to Eq. (2.1), the slopes $\gamma_{x0}^{\mathrm{spe}}$ and $\gamma_{y0}^{\mathrm{spe}}$ can be given by:

$$\gamma_{x0}^{\mathrm{spe}} = -\frac{n_{0,x}^{\mathrm{spe}}}{n_{0,z}^{\mathrm{spe}}}, \qquad \gamma_{y0}^{\mathrm{spe}} = -\frac{n_{0,y}^{\mathrm{spe}}}{n_{0,z}^{\mathrm{spe}}}, \tag{4.12}$$

where $n_{0,x}^{\mathrm{spe}}$, $n_{0,y}^{\mathrm{spe}}$ and $n_{0,z}^{\mathrm{spe}}$ are the components of $\hat{n}_0^{\mathrm{spe}}$ in the x, y and z directions, respectively.

4.1.3 Monte Carlo ray-tracing method

To evaluate the model, a Monte Carlo ray-tracing method is employed. In this section, 1D surfaces are considered to simplify the problem. Ray tracing is performed for both the transmitter and the receiver directions. The points viewed by both the transmitter and the receiver are marked. The slope histogram of these points are calculated, as well as the proportion of these points over the whole surface. This method corresponds to the bistatic illumination function shown in Eq. (4.6), which treats the rays $M_0(\hat{s}_i^-)$ and $M_0(\hat{s})$ independently.

For the bistatic illumination function which takes into account the fact that $\hat{s}$ is the reflected ray of $\hat{s}_i$ (Eq. (4.7)), another method of ray-tracing is performed. The inverse ray-path is used. For a given observation direction $\hat{s}(\theta)$, an incident ray is put along the $-\hat{s}$ direction (inverse path) to find out all the points seen by the receiver. Then, the reflected rays at these points are traced. For the points whose reflected ray does not intersect the surface, the slope of these points and the slope of the reflected rays are recorded.

4.1.4 Numerical results

In this section, the numerical results of the bistatic illumination function S_{B}^1 and $S_{\text{B}}^{1,\text{spe}}$ are calculated. The results are compared with the Monte Carlo ray-tracing method (number of generated surfaces $N = 2000$, surface length $L = 100L_c$). 1D surfaces (2D problem) are considered to be consistent with the Monte Carlo method. The surface height and slope PDFs are assumed to be Gaussian (Eqs. (1.5) and (1.6)), and the Gaussian height auto-correlation function (Eq. (1.14)) is employed. For simplicity, only the case where the transmitter and the receiver are on different sides of the point of interest with respect to the zenith (the case shown in Fig. 4.3 (a)) is considered.

4.1.4.1 Marginal histogram of S_{B}^1

The marginal histograms of the heights and the slopes of the points seen by both the transmitter and the receiver are defined by:

$$\begin{aligned} \widetilde{p}_{\text{B},\gamma}^1 &= p_\gamma(\gamma_0)\int_{-\infty}^{+\infty} S_{\text{B}}^1(\theta,\theta_i,\gamma_0,\zeta_0)p_\zeta(\zeta_0)\,\text{d}\zeta_0, \\ \widetilde{p}_{\text{B},\zeta}^1 &= p_\zeta(\zeta_0)\int_{-\infty}^{+\infty} S_{\text{B}}^1(\theta,\theta_i,\gamma_0,\zeta_0)p_\gamma(\gamma_0)\,\text{d}\gamma_0, \end{aligned} \tag{4.13}$$

where p_γ, p_ζ are the surface slope and height PDFs, respectively.

Applying the uncorrelated Smith illumination function and the Gaussian height and slope PDFs, Eq. (4.13) becomes:

$$\begin{aligned} \widetilde{p}_{\text{B},\gamma}^1 &= p_\gamma(\gamma_0)\frac{\Upsilon(\mu-\gamma_0)\Upsilon(\gamma_0-\mu_i)}{1+\Lambda(\mu)+\Lambda^-(\mu_i)}, \\ \widetilde{p}_{\text{B},\zeta}^1 &= p_\zeta(\zeta_0)\frac{1}{2}[\text{erfc}(\nu_i)-\text{erfc}(\nu)]F(\zeta_0)^{\Lambda(\mu)+\Lambda^-(\mu_i)}, \end{aligned} \tag{4.14}$$

with

$$\nu_i = \frac{\cot\theta_i}{\sigma_\gamma\sqrt{2}}, \qquad \nu = \frac{\cot\theta}{\sigma_\gamma\sqrt{2}}, \tag{4.15}$$

where ν_i and ν are the normalized slopes of the incident and the observation direction. Note that $\theta_i < 0$ here as it is in the opposite direction of θ ($\theta > 0$).

The correlated marginal histograms can be obtained in the same way by applying the correlated Smith illumination function, which requires numerical integrations. The results of the correlated $\widetilde{p}^1_{\mathrm{B},\gamma}$ and $\widetilde{p}^1_{\mathrm{B},\zeta}$ are also shown, without presenting their complex mathematical expressions.

Fig. 4.4 and Fig. 4.5 shows the marginal histograms of the slopes and the heights of the points seen by both the transmitter and the receiver. The results are shown versus the normalized slope $s_0 = \gamma_0/(\sigma_\gamma\sqrt{2})$ and the normalized height $h_0 = \zeta_0/(\sigma_\zeta\sqrt{2})$. The surface RMS slope is $\sigma_\gamma = 0.2$ in Fig. 4.4 and is $\sigma_\gamma = 0.5$ in Fig. 4.5. The directions of the transmitter and the receiver are $\theta_i = -80°$, $\theta = 80°$ (top) and $\theta_i = -85°$, $\theta = 80°$ (bottom).

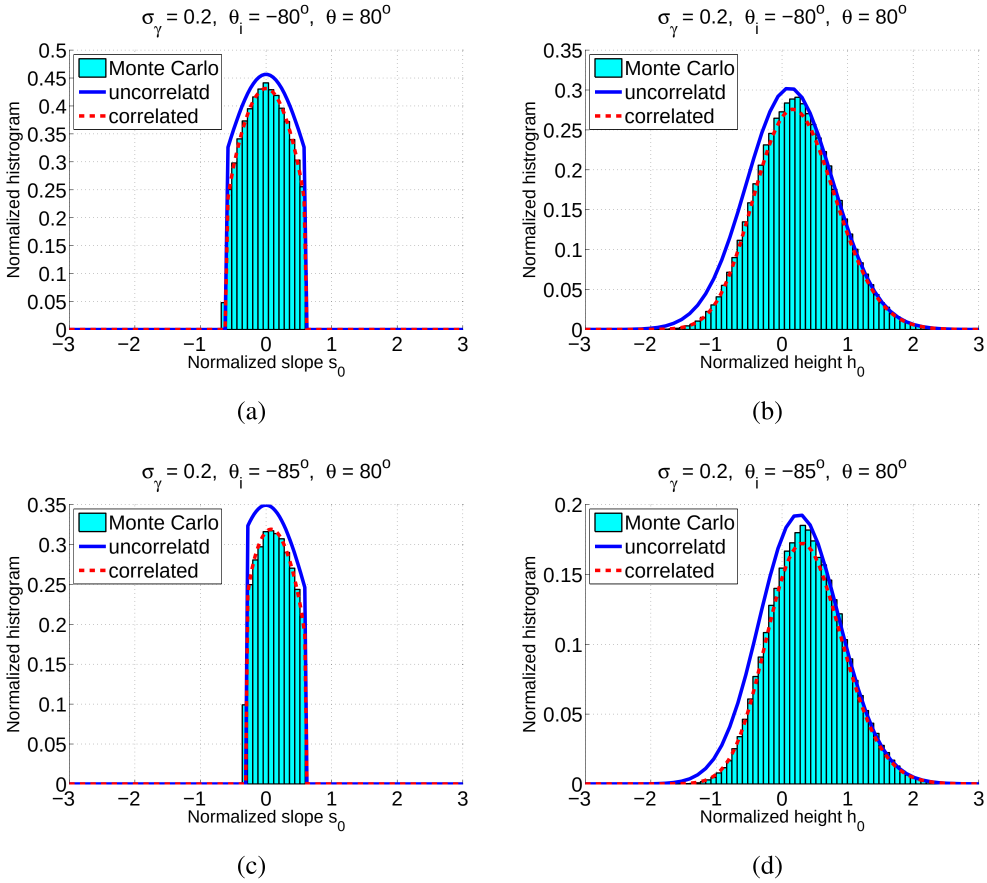

(a)

(b)

(c)

(d)

Figure 4.4: Marginal histogram of the slopes (left) and the heights (right) versus normalized slope s_0 and height h_0. The directions of the transmitter and the receiver are $\theta_i = -80°$, $\theta = 80°$ (top) and $\theta_i = -85°$, $\theta = 80°$ (bottom). The surface RMS slope is $\sigma_\gamma = 0.2$.

As this bistatic illumination function with one surface reflection S^1_{B} is the combination of two Smith monostatic illumination functions S^0_{M}, it can be predicted that S^1_{B} would agree well with the Monte Carlo ray-tracing method, which is proved in Fig. 4.4 and Fig. 4.5. General good agreements are obtained, for both the height and the slope histograms. As expected, the uncorrelated model slightly overestimates the result as s_0 approaches ν and ν_i (see Fig. 4.4 and Fig. 4.5 (a) and (c)), which also occurs for the monostatic illumination function S^0_{M} (see Fig. 2.8 (a) and (c)). The reason is that the uncorrelated Smith illumination function S^0_{M} assumes that

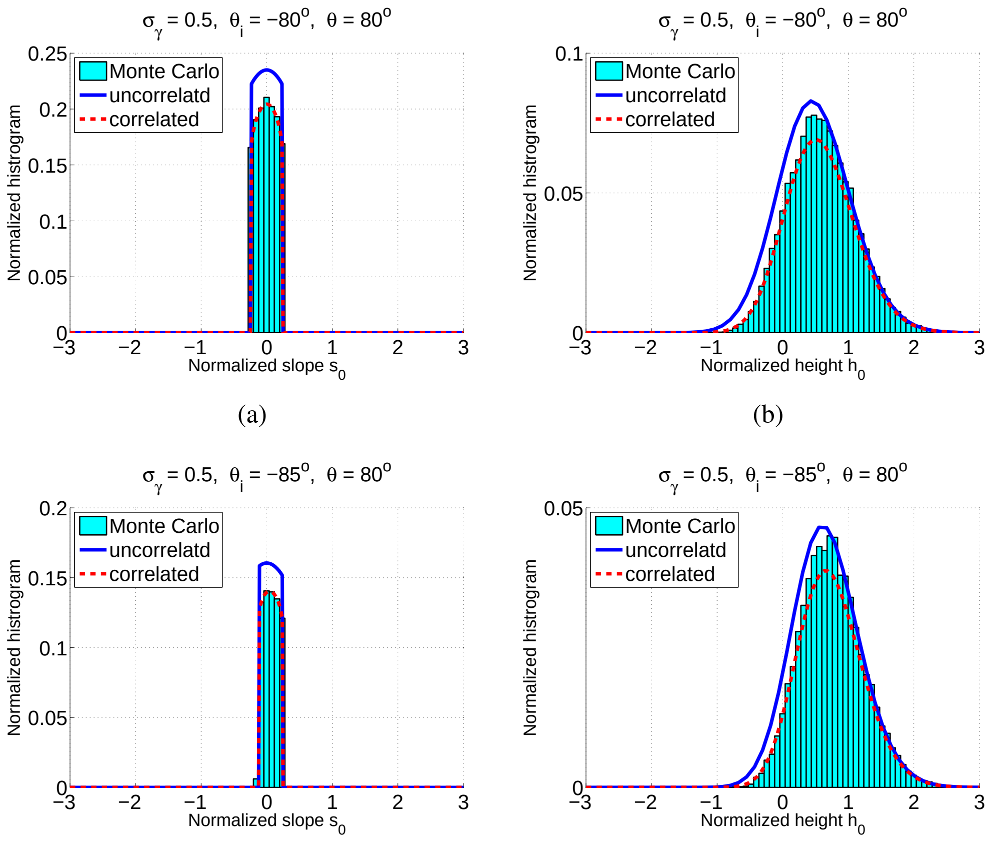

(a) (b)

(c) (d)

Figure 4.5: Marginal histogram of the slopes (left) and the heights (right) versus normalized slope s_0 and height h_0. The directions of the transmitter and the receiver are $\theta_i = -80°$, $\theta = 80°$ (top) and $\theta_i = -85°$, $\theta = 80°$ (bottom). The surface RMS slope is $\sigma_\gamma = 0.5$.

all points with $|\chi_0| < 90°$ are equally illuminated. Slight overestimations are also found in the marginal height histograms (see Fig. 4.4 Fig. 4.5 (b) and (d)) when the surface points are low. After taking into account the correlation, the above discrepancies are largely reduced. The correlated model agrees very well with the Monte Carlo ray-tracing method. The reason is that, if a surface point is shadowed, it is very likely that it is shadowed by some point nearby, which is so close that the correlation between the heights and the slopes cannot be neglected.

4.1.4.2 Average bistatic illumination function $\overline{\overline{S}}{}_{\mathrm{B}}^{1}$

The average bistatic illumination function with one reflection $\overline{\overline{S}}{}_{\mathrm{B}}^{1}$ gives the proportion of the surface seen by both the transmitter and the receiver. It is obtained by averaging S_{B}^{1} over the heights and the slopes of M_0, given by:

$$\overline{\overline{S}}{}_{\mathrm{B}}^{1}(\theta_i, \theta) = \int_{-\infty}^{+\infty} \int_{-\infty}^{+\infty} S_{\mathrm{B}}^{1}(\theta, \theta_i, \gamma_0, \zeta_0) p_\zeta(\zeta_0) p_\gamma(\gamma_0) \, \mathrm{d}\gamma_0 \, \mathrm{d}\zeta_0, \tag{4.16}$$

where p_γ, p_ζ are the surface slope and height PDFs, respectively.

Applying the uncorrelated Smith illumination function and the Gaussian slope

PDFs, Eq. (4.16) becomes:

$$\overline{\overline{S}}^{1}_{\mathrm{B}}(\theta_i, \theta) = \frac{1}{2}[\mathrm{erfc}(\nu_i) - \mathrm{erfc}(\nu)]\frac{1}{1 + \Lambda(\mu) + \Lambda^{-}(\mu_i)}. \tag{4.17}$$

The correlated average bistatic illumination function with one surface reflection can be obtained in the same way by applying the correlated Smith illumination function. The result of the correlated $\overline{\overline{S}}^{1}_{\mathrm{B}}$ will be shown directly.

Fig. 4.6 shows the average first-order bistatic illumination function S^1_{B}, which gives the proportion of the surface seen by both the transmitter and the receiver. The surface RMS slope is $\sigma_\gamma = 0.2$ (top) and $\sigma_\gamma = 0.5$ (bottom). The receiver direction is $\theta = 80°$ (left) and then $\theta = 85°$ (right). The results are shown versus the incident angle θ_i.

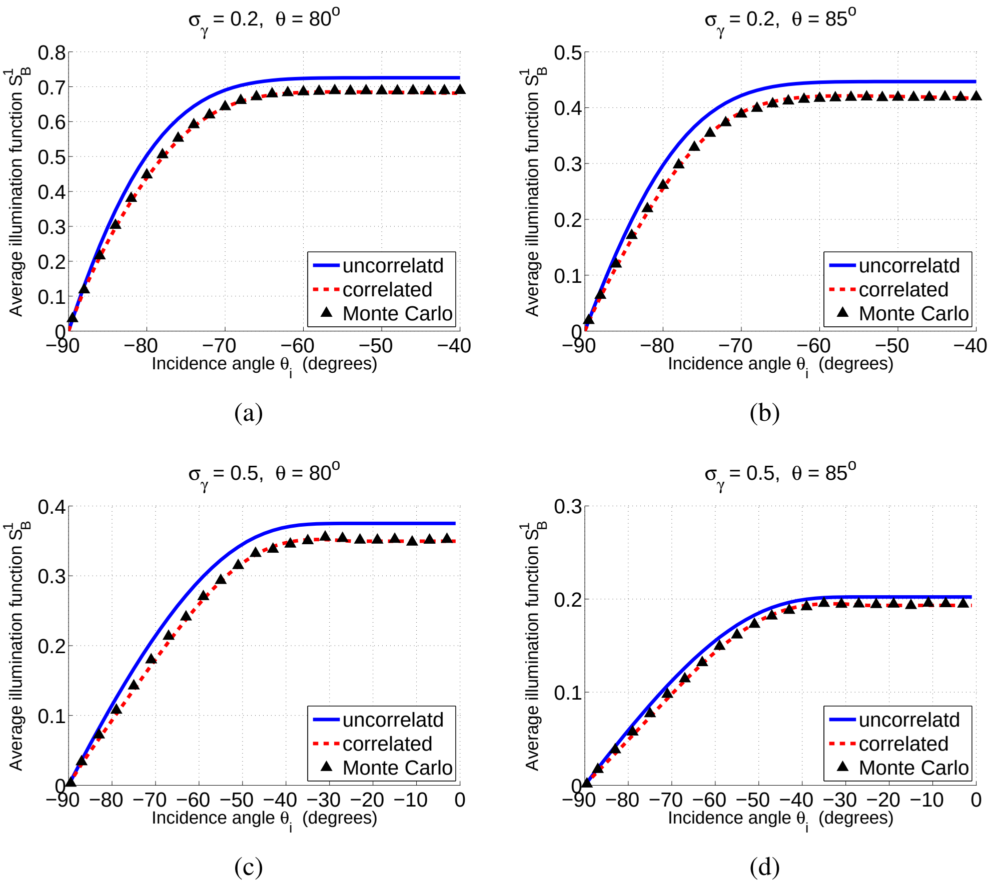

(a) (b)

(c) (d)

Figure 4.6: Average first-order bistatic illumination function S^1_{B} versus θ_i. The receiver is located at $\theta = 80°$ (left) and then at $\theta = 85°$ (right).

As can be predicted by Fig. 4.4 and Fig. 4.5, the uncorrelated model agrees generally well with the Monte Carlo method, and the correlated model gives an even better agreement. The average first-order bistatic illumination function $\overline{\overline{S}}^{1}_{\mathrm{B}}$ is affected by the directions of both the transmitter θ_i and the receiver θ. When θ_i tends to $-90°$, $\overline{\overline{S}}^{1}_{\mathrm{B}} = 0$, as all the surface is in the shadow of the transmitter. As the transmitter elevates ($|\theta_i|$ becomes smaller), $\overline{\overline{S}}^{1}_{\mathrm{B}}$ increases because more area of the surface can be seen by the transmitter. When the transmitter is sufficiently high, e.g. $\theta_i > -60°$ for surfaces with $\sigma_\gamma = 0.2$ and receiver direction $\theta = 80°$ (Fig. 4.6 (a)),

$\overline{\overline{S}}{}_{\mathrm{B}}^{1}$ stays constant because all the surface is seen by the transmitter. In this region, only the direction of the receiver affects $\overline{\overline{S}}{}_{\mathrm{B}}^{1}$. $\overline{\overline{S}}{}_{\mathrm{B}}^{1} \approx 0.7$ for surfaces with $\sigma_\gamma = 0.2$ when the receiver is in the direction $\theta = 80°$ (Fig. 4.6 (a)), meaning that about 70% of the surface is seen by the receiver under this condition. Similar conclusions can be found for Fig. 4.6 (b) (c) and (d). The constant value reduces for surfaces with larger σ_s and more grazing zenith angles θ.

4.1.4.3 Average bistatic illumination function $\overline{\overline{S}}{}_{\mathrm{B}}^{1,\mathrm{spe}}$

In this subsection, the ray $\hat{s}$ is considered as the reflection ray of $\hat{s}_i$. The configuration that the receiver and the transmitter are at different sides of the surface with respect to the zenith is considered.

For given receiver θ and transmitter θ_i directions, the average bistatic illumination function with one reflection $\overline{\overline{S}}{}_{\mathrm{B}}^{1,\mathrm{spe}}$ is given by integrating $S_{\mathrm{B}}^{1,\mathrm{spe}}$ over the slopes and heights of M_0. It gives the bidirectional distribution of S_{B}^{1}, which equals the probability density that M_0 is seen by both the transmitter and the receiver, and the incident ray $\hat{s}_i$ is reflected specularly into the $\hat{s}$ direction. $\overline{\overline{S}}{}_{\mathrm{B}}^{1,\mathrm{spe}}$ is given by:

$$\begin{aligned}\overline{\overline{S}}{}_{\mathrm{B}}^{1,\mathrm{spe}}(\theta_i,\theta) &= \int_{-\infty}^{+\infty}\int_{-\infty}^{+\infty} S_{\mathrm{B}}^{1,\mathrm{spe}}(\theta,\theta_i,\gamma_0,\zeta_0)p_\zeta(\zeta_0)p_\gamma(\gamma_0)\,\mathrm{d}\gamma_0\,\mathrm{d}\zeta_0 \\ &\int_{-\infty}^{+\infty}\int_{-\infty}^{+\infty} S_{\mathrm{B}}^{1}(\theta,\theta_i,\gamma_0,\zeta_0)\delta(\gamma_0-\gamma_0^{\mathrm{spe}})p_\zeta(\zeta_0)p_\gamma(\gamma_0)\,\mathrm{d}\gamma_0\,\mathrm{d}\zeta_0\end{aligned} \tag{4.18}$$

Applying the uncorrelated Smith S_{B}^{1}, Eq. (4.18) becomes:

$$\overline{\overline{S}}{}_{\mathrm{B}}^{1,\mathrm{spe}}(\theta_i,\theta) = \overline{S}{}_{\mathrm{B}}^{1}p_\gamma(\gamma_0^{\mathrm{spe}}), \tag{4.19}$$

where $\overline{S}{}_{\mathrm{B}}^{1}$ is the height-averaged S_{B}^{1}, given by

$$\overline{S}{}_{\mathrm{B}}^{1} = \begin{cases} \dfrac{1}{\Lambda(\mu)+\Lambda^{-}(\mu_i)+1} & \text{for} \quad -90° < \theta_i < 0 \text{ and } 0 < \theta < 90° \\ \dfrac{1}{\Lambda(\mu)+1} & \text{for} \quad 0 < \theta_i < \theta < 90° \\ \dfrac{1}{\Lambda^{-}(\mu_i)+1} & \text{for} \quad 0 < \theta < \theta_i < 90° \end{cases}, \tag{4.20}$$

The correlated one can be obtained by applying the correlated S_{B}^{1}. The result of the correlated $\overline{\overline{S}}{}_{\mathrm{B}}^{1,\mathrm{spe}}$ will also be shown.

For a given θ, Eq. (4.18) or (4.19) gives the distribution density of θ_i. As it is difficult to compare the distribution density of θ_i with the histogram of θ_i obtained with the Monte Carlo method (problem of normalization), the Dirac delta function used in Eq. (4.18) is replaced by a window function W, which is defined as:

$$W = \begin{cases} 1 & \text{for} \qquad \theta_i - \triangle\theta_i < \vartheta_i < \theta_i + \triangle\theta_i \\ 0 & \text{otherwise} \end{cases}, \tag{4.21}$$

where $\triangle\theta_i > 0$ is a small number ($\triangle\theta_i = 0.1°$ is used in this thesis). For a given θ, $\overline{\overline{S}}{}_{\mathrm{B}}^{1}(\theta_i,\theta,W)$ gives the probability that M_0 is seen by the receiver and the reflected ray of $-\hat{s}_i$ leaves the surface in the region $\theta_i \pm \triangle\theta_i$ (inverse path).

Figs. 4.7 and 4.8 show the average bistatic illumination function $\overline{\overline{S}}_{\text{B}}^{1,\text{spe}}$, with $\triangle\theta_i = 0.1°$. The surface RMS slope is $\sigma_\gamma = 0.2$ in Fig. 4.7 and is $\sigma_\gamma = 0.5$ in Fig. 4.8. The direction of the receiver is given (with small zenith angle $\theta = 30°$ (top), moderate $\theta = 60°$ (middle) and large $\theta = 80°$ (bottom)), and the distribution of θ_i is shown. In the inverse path, $\overline{\overline{S}}_{\text{B}}^{1,\text{spe}}$ shown in Fig. 4.7 and Fig. 4.8 equals the distribution of the directions of the reflected rays leaving the surface. The corresponding result of the Monte Carlo method is given by:

$$\overline{\overline{S}}_{\text{B,MC}}^{1,\text{spe}}(\theta_i, \theta, W) = \frac{N_i}{N_s}, \tag{4.22}$$

where N_i is the number of points where the angle of reflection belongs to the $\theta_i \pm \triangle\theta_i$ region.

It is shown that the uncorrelated and the correlated models both agree very well with the Monte Carlo ray-tracing model. For all the three directions $\theta = \{30°, 60°, 80°\}$ studied here, the average bistatic illumination function has maxima around the global specular reflection directions $\theta_i = \{-30°, -60°, -80°\}$, meaning that it is most likely that the reflected ray would leave the surface in the global specular reflection direction of the incident ray.

It is notable that the width of the lobes become narrower as the zenith angle θ of the receiver direction increases, which means that the reflection energy is more concentrated angularly.

4.1.4.4 Hemispherical average bistatic illumination function $\overline{\overline{S}}_{\text{B}}^{1,\text{hemi}}$

The hemispherical average bistatic illumination function with one reflection gives the proportion of the surface which is seen by the receiver (θ), and whose reflected ray leaves the surface after one surface reflection (inverse path). The hemispherical average bistatic illumination function with one surface reflection $\overline{\overline{S}}_{\text{B}}^{1,\text{hemi}}$ can be obtained in a similar way as $\overline{\overline{S}}_{\text{B}}^{1,\text{spe}}(\theta_i, \theta)$ by enlarging the width of the window function in Eq. (4.21) to:

$$W = \left\{ \begin{array}{ll} 1, & \text{for} \quad -90° < \theta_i < 90° \\ 0, & \text{otherwise} \end{array} \right. . \tag{4.23}$$

The angle θ_i is expressed with respect to θ and the slope γ_0 of M_0 as:

$$\theta_i = -2\text{arctan}(\gamma_0) - \theta. \tag{4.24}$$

The hemispherical average bistatic illumination function $\overline{\overline{S}}_{\text{B}}^{1,\text{hemi}}$ is then given by:

$$\begin{aligned} \overline{\overline{S}}_{\text{B}}^{1,\text{hemi}}(\theta) &= \int_{-\infty}^{\infty} \overline{S}_{\text{B}}^{1} W p_\gamma(\gamma_0)\,\text{d}\gamma_0, \\ &= \int_{\gamma_0^{\text{spe},1}}^{\gamma_0^{\text{spe},2}} \frac{1}{\Lambda^-(\mu_i) + 1} p_\gamma(\gamma_0)\,\text{d}\gamma_0 \\ &+ \int_{\gamma_0^{\text{spe},2}}^{\gamma_0^{\text{spe},3}} \frac{1}{\Lambda(\mu) + 1} p_\gamma(\gamma_0)\,\text{d}\gamma_0 \\ &+ \int_{\gamma_0^{\text{spe},3}}^{\gamma_0^{\text{spe},4}} \frac{1}{\Lambda^-(\mu) + \Lambda(\mu) + 1} p_\gamma(\gamma_0)\,\text{d}\gamma_0, \end{aligned} \tag{4.25}$$

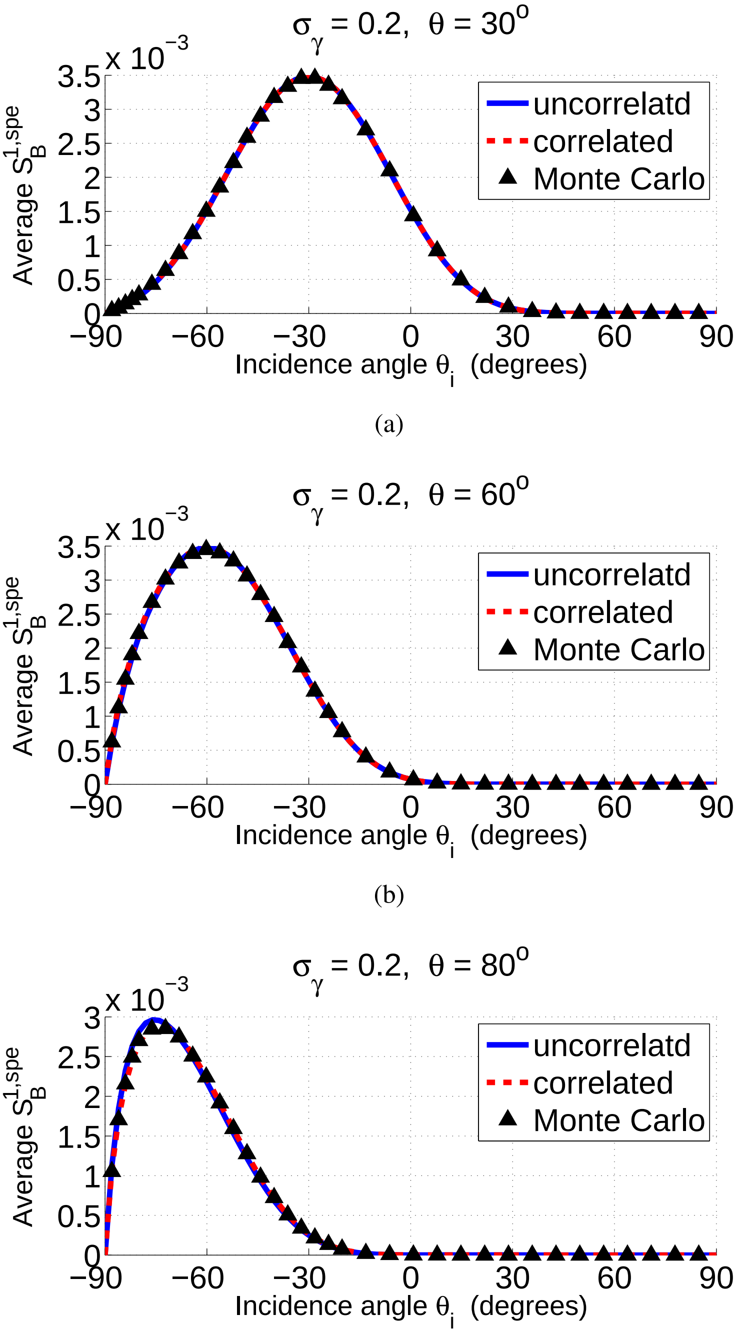

(a)

(b)

(c)

Figure 4.7: Average bistatic illumination function $S_{\mathrm{B}}^{1,\mathrm{spe}}$, which corresponds to the distribution of the reflect (or incidence) angle given the incidence (or reflection) direction. The receiver direction is $\theta = 30^{\circ}$ (a), $\theta = 60^{\circ}$ and $\theta = 80^{\circ}$ (d). The surface RMS slope is $\sigma_{\gamma} = 0.2$.

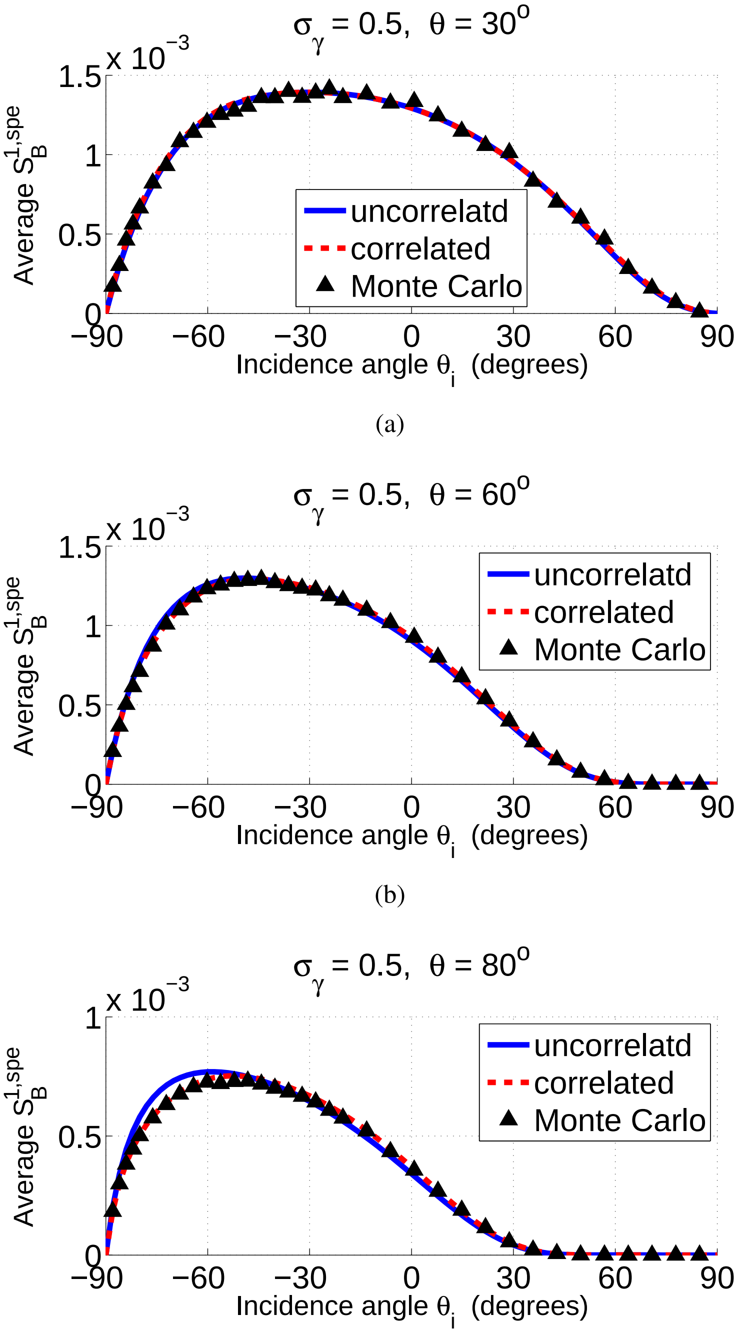

(a)

(b)

(c)

Figure 4.8: Average bistatic illumination function $S_{\mathrm{B}}^{1,\mathrm{spe}}$, which corresponds to the distribution of the reflected (or incident) angle given the incidence (or reflection) direction. The receiver direction is $\theta = 30°$ (a), $\theta = 60°$ and $\theta = 80°$ (d). The surface RMS slope is $\sigma_\gamma = 0.5$.

where $\gamma_0^{\mathrm{spe},1,2,3,4}$ is the slope of M_0 corresponding to $\theta_i = \{90°, \theta, 0°, -90°\}$, respectively, given by:

$$\begin{aligned} \gamma_0^{\mathrm{spe},1} &= -\tan\left(\frac{\theta + 90°}{2}\right), & \gamma_0^{\mathrm{spe},2} &= -\tan\theta, \\ \gamma_0^{\mathrm{spe},3} &= -\tan\left(\frac{\theta}{2}\right), & \gamma_0^{\mathrm{spe},4} &= -\tan\left(\frac{\theta - 90°}{2}\right). \end{aligned} \tag{4.26}$$

Fig. 4.9 shows the hemispherical average bistatic illumination function $\overline{\overline{S}}_{\mathrm{B}}^{1,\mathrm{hemi}}$. The surface RMS slope is $\sigma_\gamma = 0.2$ in Fig. 4.9 (a) and $\sigma_\gamma = 0.5$ in Fig. 4.9 (b).

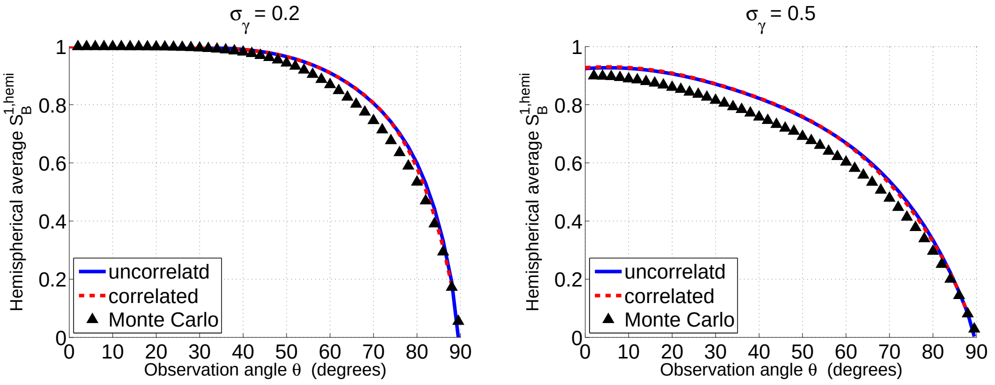

(a) (b)

Figure 4.9: Hemispherical average bistatic illumination function with one surface reflection $\overline{\overline{S}}_{\mathrm{B}}^{1,\mathrm{hemi}}$. The surface RMS slope is $\sigma_\gamma = 0.2$ in (a) and $\sigma_\gamma = 0.5$ in (b).

It is shown that the hemispherical average bistatic illumination function $\overline{\overline{S}}_{\mathrm{B}}^{1,\mathrm{hemi}}$ decreases monotonously with the observation angle θ. The results of the model agree very well with the Monte Carlo ray-tracing results. Considering the correlation between the heights and the slopes of the surface points does not lead to a significant improvement in the agreement.

For surfaces with RMS slope $\sigma_\gamma = 0.2$, the hemispherical average bistatic illumination function $S_{\mathrm{B}}^{1,\mathrm{hemi}}$ is close to 1 when $\theta < 40°$, which means that all the surface is seen by the receiver, and all the reflected rays $-\hat{s}'$ leave the surface without intersecting the surface again. This conclusion can be predicted by Fig. 2.18 (a), where the average monostatic illumination function with one surface reflection $\overline{\overline{S}}_{\mathrm{M}}^{1}$ is shown. It is shown that $\overline{\overline{S}}_{\mathrm{M}}^{1} \approx 1$ for $\theta < 40°$, meaning that no reflected ray intersects the surface.

For surfaces with RMS slope $\sigma_\gamma = 0.5$, $\overline{\overline{S}}_{\mathrm{B}}^{1,\mathrm{hemi}} \approx 0.9$ for $\theta = 0°$, meaning that about 90% of the surface points fulfill both the conditions that "it is seen by the receiver" and "the reflected ray leaves the surface". This result is also consistent with the average monostatic illumination function $\overline{\overline{S}}_{\mathrm{M}}^{1}$. In Fig. 2.18 (b), it is shown that for surfaces with $\sigma_\gamma = 0.5$, $\overline{\overline{S}}_{\mathrm{M}}^{1} \approx 0.1$, meaning that about 10% of the surface points fulfill that "it is seen by the receiver" and "the reflected ray intersects the surface".

The bistatic illumination function with one surface reflection $S_{\mathrm{B}}^{1,\mathrm{spe}}$ is used to calculate the sea surface reflectivity with one reflection. To improve the accuracy of the reflectivity model, more reflections should be considered. As a consequence, in what follows, the illumination function with two reflections is derived.

4.2 Illumination function with two reflections

4.2.1 Surface reflections

It is possible that the incident ray undergoes multiple reflections before it is reflected to the receiver. This section considers two reflections. Fig. 4.10 illustrates the geometry configuration of this problem for 1D surfaces.

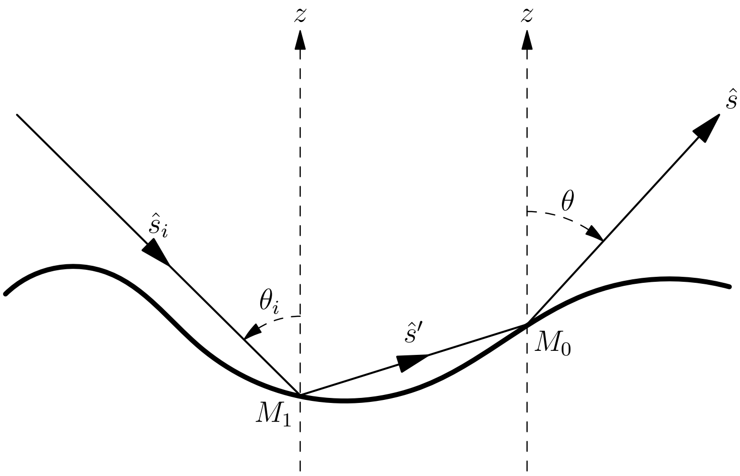

Figure 4.10: The incident ray $\hat{s}_i$ is reflected twice by the surface before it is reflected to the observation direction $\hat{s}$. For 1D surfaces, zenith angles are oriented, with the direction of θ being the positive direction.

An incident ray $\hat{s}_i$ intersects the surface at M_1, where it is reflected into a direction $\hat{s}'$. Then, the ray $\hat{s}'$ intersects the surface again, where it is reflected to the observation direction $\hat{s}$. Note that the transmitter, $\hat{s}_i$, $\hat{s}'$ and $\hat{s}$ are not necessarily in the same plane.

The receiver is located in the direction $\hat{s}(\theta, \phi)$, where $\theta \in [0°, 90°]$ is the zenith angle and $\phi \in [0°, 360°]$ is the azimuth angle. The transmitter is located at the direction $\hat{s}_i^-(\theta_i, \phi_i) = -\hat{s}_i$, with the zenith angle being $\theta_i \in [0°, 90°]$ and the azimuth angle being $\phi_i \in [0°, 360°]$. The superscript "$-$" stands for the inversion of direction. The direction of the incident ray $\hat{s}_i$ can also be denoted by the zenith angle $\theta_2 \in [90°, 180°]$ and the azimuth angle $\phi_2 \in [0°, 360°]$. The direction of the reflected ray $\hat{s}'$ can be obtained according to the direction of the incident ray $\hat{s}^-$ and the unitary normal $\hat{n}_0$ to point M_0, given by Eq. (2.57). The vector $\hat{s}'$ is expressed by the zenith angle $\theta_1 \in [0°, 180°]$ and the azimuth angle $\phi_1 \in [0°, 360°]$, whereas $-\hat{s}'$ is expressed by the zenith angle $\theta' \in [0°, 180°]$ and the azimuth angle $\phi' \in [0°, 360°]$. The definitions of these angles are illustrated in Fig. 4.11.

For computational ease, several new systems of coordinates are defined. The first one (X, Y, z) is defined according to the receiver direction. It is obtained by rotating the basis (x, y) anticlockwise through an angle ϕ about the z axis. This system of coordinates is frequently used in this thesis. The second one (X', Y', z) is defined relating to the points M_1 and M_0. It is defined by rotating anticlockwise the basis (x, y) through an angle ϕ_1 about the z axis, so that the ray $\hat{s}'$ lies in the (X', z) plane, and M_0 is at the positive side of M_1 along the X axis. This system of coordinates is used when defining the monostatic illumination function with one surface reflection S_{M}^1. The third one (X'', Y'', z) is defined according to the transmitter direction. It is defined by rotating anticlockwise the basis (x, y) through an angle ϕ_2 about the z axis, so that the ray $\hat{s}_i$ lies in the (X'', z) plane. The definitions of these system of coordinates are illustrated in Fig. 4.11.

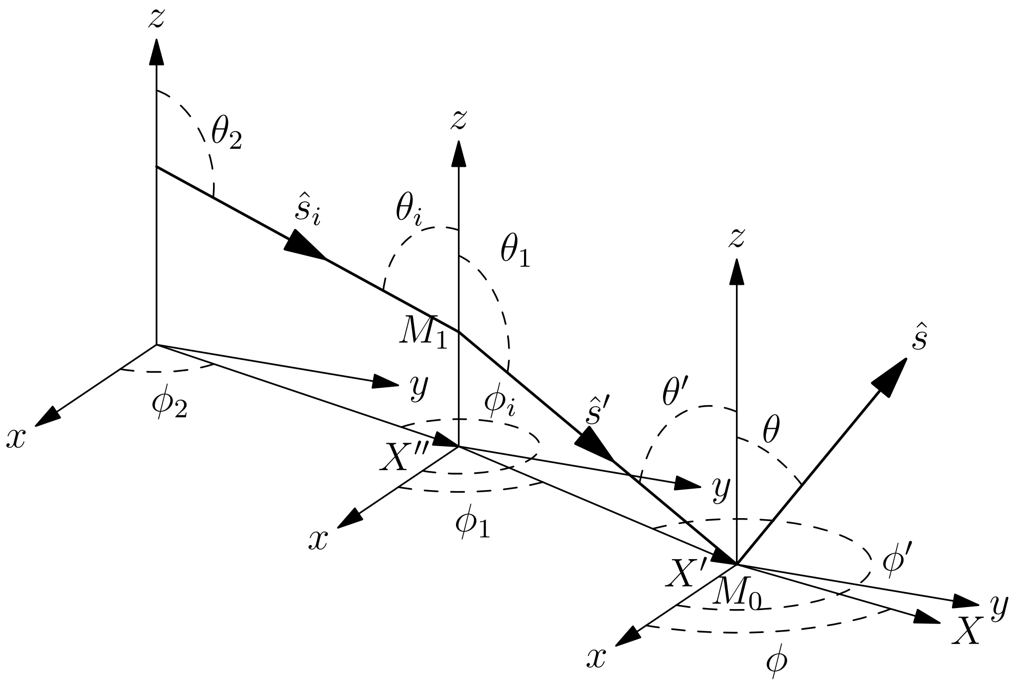

Figure 4.11: Definition of the new systems of coordinates and the angles. The incident ray $\hat{s}_i$ intersects the surface at M_1 where it is specularly reflected into $\hat{s}'$. $\hat{s}'$ intersects the surface again at M_0, where it is specularly reflected to the direction $\hat{s}$. For 2D surfaces, zenith angles are not oriented.

As mentioned in Sec. 4.1.1, the inverse path is used. For a given direction of the receiver $\hat{s}$, the direction of the ray $\hat{s}'$ is given by:

$$\hat{s}' = \hat{s} - 2\hat{n}_0(\hat{n}_0 \cdot \hat{s}), \tag{4.27}$$

where $\hat{n}_0$ is the unitary normal of the surface point M_0. The angles θ', ϕ' and θ_1, ϕ_1 are obtained by applying $-\hat{s}'$ and $\hat{s}'$ to Eq. (2.58), respectively.

The direction $\hat{s}_i$ can be obtained in the same way. Given $\hat{s}'$, $\hat{s}_i$ is given by:

$$\hat{s}_i = \hat{s}' - 2\hat{n}_1(\hat{n}_1 \cdot \hat{s}'), \tag{4.28}$$

where $\hat{n}_1$ is the unitary normal to the surface point M_1. The angles θ_i, ϕ_i and θ_2, ϕ_2 are obtained by applying $-\hat{s}_i$ and $\hat{s}_i$ to Eq. (2.58), respectively.

4.2.2 Model of Lynch & Wagner

Lynch & Wagner [12] developed a bistatic illumination function with two surface reflections for 1D surfaces (see Fig. 4.10), from the height-averaged Smith monostatic illumination function $\overline{S}^0_{\mathrm{M}}$. The surface slope PDF is assumed to be Gaussian. This subsection summarizes the model of Lynch & Wagner for the case where the transmitter and the receiver are at different sides of the surface with respect to the zenith ($\theta > 0$, $\theta_i < 0$).

In the model of Lynch & Wagner [12], the inverse path is also used. To express the bistatic illumination function with two reflections S^2_{B}, 4 events are defined[1]:

---

[1] The definition of symbols is modified to agree with that in this thesis.

- "the ray $\hat{s}$ does not intersect the surface" is denoted as a;
- "the ray $\hat{s}'^{-}$ intersects the surface at M_1" is denoted as b;
- "M_0 has a slope which specularly reflects $\hat{s}'^{-}$ to the given direction $\hat{s}_i^{-}$" is denoted as c;
- "the ray $\hat{s}_i^{-}$ does not intersect the surface" is denoted as d.

The bistatic illumination function S_{B}^2 is then given by:

$$S_{\mathrm{B}}^2 = p(abcd) = p(a)p(b|a)p(c|ab)p(d|abc) \tag{4.29}$$

Lynch & Wagner [12] defined the first part $p(a)$ as the uncorrelated height-averaged Smith illumination function, given by:

$$p(a) = \Upsilon(\mu - \gamma_0)\frac{1}{1+\Lambda(\mu)}, \tag{4.30}$$

where $\mu = \cot\theta$ is the slope of ray $\hat{s}$.

The second part $p(b|a)$ is given by [12]:

$$\begin{aligned} p(b|a) &= 1 - p(\bar{b}|a) = 1 - \frac{p(\bar{b}a)}{p(a)} \\ &= \begin{cases} \dfrac{\Lambda(|\mu|)}{1+\Lambda(\mu)+\Lambda(|\mu_1|)} & \text{for} \quad |\theta'| \leq 90^\circ, \\ 1 & \text{for} \quad |\theta'| > 90^\circ, \end{cases} \end{aligned} \tag{4.31}$$

where $\mu_1 = \cot\theta_1 = \cot\theta'$ is the slope of the ray $\hat{s}'$. Note that for 1D surfaces, the zenith angles are oriented, with the direction of θ being the positive direction. The angles θ' and θ_1 can be positive or negative, depending on the θ and on slope γ_0 of the point M_0.

The third part $p(c|ab)$ corresponds to the probability density of the slope of the point M_1. Considering the dependence on the events a and b, Lynch & Wagner [12] stated that the slope of M_1 should check the condition that the local angle of incidence at M_1 should fulfill $|\chi_1| < 90^\circ$. Inversely, they assumed that any slope checking this condition can equally be the slope of M_1. This assumption is also used in Sec. 3.2.1 when calculating the sea surface emissivity. Thus, $p(c|ab)$ is defined as:

$$p(c|ab) = \frac{p_\gamma(\gamma_1^{\mathrm{spe}})}{1 - \dfrac{1}{2}\operatorname{erfc}\left(\dfrac{|\mu_1|}{\sqrt{2}\sigma_\gamma}\right)}, \tag{4.32}$$

where p_γ is the surface slope PDF.

When calculating the fourth term $p(d|abc)$, which is the probability that M_1 is viewed by the transmitter along the $\hat{s}_i^{-}$ direction, given that $\hat{s}$ does not intersect the surface and $\hat{s}'^{-}$ intersects the surface at M_1 and is reflected into $\hat{s}_i^{-}$, Lynch & Wagner [12] pointed out that it is difficult to take into account the influence of a, b and c on d. Thus, their dependence is ignored, and $p(d|abc)$ is approximated by:

$$p(d|abc) \approx p(d) = \begin{cases} \dfrac{1}{1+\Lambda(|\mu_i|)}, & \text{for} \quad \theta_1 < \theta_i < 0 \\ 0, & \text{for} \quad \theta_i < \theta_1 < 0 \\ \dfrac{1}{1+\Lambda(|\mu_i|)}, & \text{for} \quad \theta_1 > \theta_i > 0 \\ 0, & \text{for} \quad \theta_i > \theta_1 > 0 \end{cases} \tag{4.33}$$

where $\mu_i = \cot\theta_i$ is the slope of the ray $\hat{s}_i$.

The bistatic illumination function with two reflections S_{B}^2 is then obtained by substituting Eqs. (4.30), (4.31), (4.32) and (4.33) into Eq. (4.29). Lynch & Wagner [12] indicated that after taking into the second reflection of the surface, the energy conservation condition was better met. As the model of Lynch *et al.* [12] was developed from the height-averaged illumination function $\overline{S}_{\mathrm{M}}^0$, it is not possible to take into account the correlation between the surface heights and slopes.

4.2.3 Development of a statistical model

In this section, a statistical model of a bistatic illumination function with two surface reflections S_{B}^2 is developed, based on the statistical monostatic illumination function without reflection S_{M}^0 and that with one reflection S_{M}^1.

4.2.3.1 Mathematical expression for 2D surfaces

The bistatic illumination function with two reflections is developed in a similar way as that of Lynch & Wagner [12]. The same 4 events a, b, c and d in the list in Sec. 4.2.2 are used.

Determination of $p(a)p(b|a)$ Note that the two terms $p(a)p(b|a)$ equals the monostatic illumination function with one surface reflection S_{M}^1 developed in Sec. 2.2.1, which is given by:

$$p(a)p(b|a) = \Upsilon(\mu - \gamma_{X_0}) F(\zeta_0)^{\Lambda(\mu)} \times \begin{cases} 1 & \text{if} \quad \theta' > 90^\circ, \\ 1 - F(\zeta_0)^{\Lambda^-(\mu_1)} & \text{if} \quad \theta' < 90^\circ, \end{cases} \tag{4.34}$$

where γ_{X_0}, $\mu = \cot\theta$ is the slope of M_0 and the slope of the ray $\hat{s}$ with respect to the X direction, and $\mu_1 = \cot\theta_1$ (see Fig. 4.11 for the definition of θ_1) is the slope of the ray $\hat{s}'$ with respect to the X' direction. Note that for 2D surfaces, the vectors $\hat{s}$, $\hat{s}'$ are defined by their zenith and azimuth angles, and zenith angles are not oriented.

Determination of $p(c|ab)$ The conditional probability $p(c|ab)$ equals the slope probability density of the point M_1 given that the ray $\hat{s}$ does not intersects the surface whereas $\hat{s}'^-$ intersect the surface at M_1.

To calculate the slope PDF of M_1, the approximation used in Sec. 3.2.1.2 when calculating the sea surface emissivity is also employed, which assumes that any slope checking the condition $|\chi_1| < 90^\circ$ can equally be the slope of the point M_1. The PDF of M_1 is then given by:

$$p(\gamma_{X_1'}) = \frac{\Upsilon(\mu_1 - \gamma_{X_1'})}{\displaystyle\int_{-\infty}^{\mu_1} p_{\gamma_{X'}}(t)\,\mathrm{d}t} p_{\gamma_{X'}}(\gamma_1), \tag{4.35}$$

where $p_{\gamma_{X'}}$ is the surface marginal slope PDF in the X' direction. The model of Lynch & Wagner [12] also uses this approximation.

The conditional probability $p(c|ab)$ is then given by multiplying Eq. (3.24) with two Dirac delta functions:

$$p(c|ab) = p(\gamma_{X_1'}) \delta(\gamma_{x_1} - \gamma_{x_1}^{\mathrm{spe}}) \delta(\gamma_{y_1} - \gamma_{y_1}^{\mathrm{spe}}), \tag{4.36}$$

where $(\gamma_{x1}^{\text{spe}}, \gamma_{y1}^{\text{spe}})$ is the slope the point M_1 which reflects $\hat{s}'^{-}$ specularly into the direction $\hat{s}_i^{-}$, which is given by:

$$\hat{n}_1^{\text{spe}} = \frac{\hat{s} + \hat{s}_i^{-}}{\|\hat{s} + \hat{s}_i^{-}\|}. \tag{4.37}$$

$$\gamma_{x1}^{\text{spe}} = -\frac{\hat{n}_{1,x}^{\text{spe}}}{\hat{n}_{1,z}^{\text{spe}}}, \qquad \gamma_{y1}^{\text{spe}} = -\frac{\hat{n}_{1,y}^{\text{spe}}}{\hat{n}_{1,z}^{\text{spe}}}, \tag{4.38}$$

Determination of $p(d|abc)$ The conditional probability $p(d|abc)$ is the conditional probability that M_1 is viewed by the transmitter along the $\hat{s}_i^{-}$ direction, given that $\hat{s}$ does not intersect the surface and $\hat{s}'^{-}$ intersects the surface at M_1 and is specularly reflected into $\hat{s}_i^{-}$. As no obvious correlation is found, these correlations are ignored, allowing to simply $p(d|abc)$ as:

$$p(d|abc) \approx p(d) = F(\zeta_1)^{\Lambda^{-}(\mu_2)}, \tag{4.39}$$

where $\mu_2 = \cot\theta_2$ is the slope of $\hat{s}_i$ with respect to the X'' direction.

The bistatic illumination function with two surface reflections S_{B}^2 for 2D surfaces is then obtained by substituting Eqs. (4.34), (4.36) and (4.39) into Eq. (4.29).

4.2.3.2 Discussion about the height PDF of M_1

Unlike the monostatic illumination function with one reflection S_{M}^1 or the surface emissivity, the height ζ_1 of M_1 is involved in Eq. (4.39). As discussed in Sec. 2.2.1.5, M_1 is lower than M_0 ($\zeta_1 < \zeta_0$) for $\theta' > 90°$, and M_1 is higher than M_0 ($\zeta_1 > \zeta_0$) for $\theta' < 90°$. The height PDF might be defined accordingly.

However, as the integration of Eq. (4.39) over ζ_1 does not require the knowledge of the PDF of ζ_1, and as the surface reflectivity (subject of the next chapter) does not depend on ζ_1, the height PDF of M_1 is not calculated in this thesis.

4.2.3.3 Mathematical expression for 1D surfaces

To reduce the complexity of the problem and to save computation time, it is usually more convenient to calculate the bistatic illumination function S_{B}^2 for 1D surfaces (2D problem).

Recall that for 1D surfaces, the zenith angle of a vector is oriented. The horizontal direction of the receiver is defined as the positive x direction, and the direction of the receiver zenith angle θ is defined as the positive direction for the zenith angles. The 1D bistatic illumination function with two reflections S_{B}^2 can be obtained in the same way as the one for 2D surfaces. The result is given directly here.

The first part $p(a)p(b|a)$ equals the monostatic illumination function with one surface reflection S_{M}^1, the 1D expression is given in Sec. 2.2.1.6 by:

$$\begin{aligned} p(a)p(b|a) &= \Upsilon(\mu - \gamma_0) F(\zeta_0)^{\Lambda(\mu)} \\ &\times \begin{cases} 1 & \text{if} \quad |\theta'| > 90° \\ 1 - F(\zeta_0)^{\Lambda(\mu_1)} & \text{if} \quad \theta < \theta' < 90° \\ 1 - F(\zeta_0)^{\Lambda^{-}(\mu_1)} & \text{if} \quad -90° < \theta' < 0° \end{cases}, \end{aligned} \tag{4.40}$$

where $\mu = \cot\theta$ and $\mu_1 = \cot\theta_1 = -\cot\theta'$ are the slopes of the ray $\hat{s}$ and $\hat{s}'$, respectively. The case $\theta' < 0°$ corresponds to the situation where $\phi_1 = \phi + 180°$ for 2D surfaces, which means that X' and X are in opposite directions.

The second part $p(c|ab)$ relates to the slope PDF of point M_1, which is approximated as:

$$p(\gamma_1) = \begin{cases} \dfrac{\Upsilon(\mu_1 - \gamma_1)}{\displaystyle\int_{-\infty}^{\mu_1} p_\gamma(t)\,\mathrm{d}t} p_\gamma(\gamma_1) & \text{if} \quad 0 < \theta' < 90^\circ, \\ \dfrac{\Upsilon(\gamma_1 - \mu_1)}{\displaystyle\int_{\mu_1}^{+\infty} p_\gamma(t)\,\mathrm{d}t} p_\gamma(\gamma_1) & \text{if} \quad -90^\circ < \theta' < 0^\circ. \end{cases} \tag{4.41}$$

The conditional probability $p(c|ab)$ is then given by:

$$p(c|ab) = p(\gamma_1)\delta(\gamma_1 - \gamma_1^{\mathrm{spe}}), \tag{4.42}$$

where γ_1^{spe} is the slope of M_1 which reflects $\hat{s}'^{-}$ specularly into $\hat{s}_i^{-}$, given by:

$$\gamma_1^{\mathrm{spe}} = -\tan\left(\frac{\theta_i + \theta_1}{2}\right). \tag{4.43}$$

The last conditional probability $p(d|abc)$ is given by:

$$p(d|abc) \approx p(d) = \begin{cases} F(\zeta_1)^{\Lambda^-(\mu_2)}, & \text{for} \quad \theta_1 < \theta_i < 0 \\ 0, & \text{for} \quad \theta_i < \theta_1 < 0 \\ F(\zeta_1)^{\Lambda(\mu_2)}, & \text{for} \quad \theta_1 > \theta_i > 0 \\ 0, & \text{for} \quad \theta_i > \theta_1 > 0 \end{cases} \tag{4.44}$$

where $\mu_2 = \cot\theta_2$ is the slope of $\hat{s}_i$. Note that either Λ^- or Λ is used as depending on the sign of θ_i, corresponding to $\hat{s}_i^-$ propagating toward the negative or the positive side of the x axis.

The bistatic illumination function with two surface reflections S_{B}^2 for 1D surfaces is then obtained by substituting Eqs. (4.40), (4.42) and (4.44) into Eq. (4.29).

Surprisingly, the statistical average of $p(a)p(b|a)$ defined here over ζ_0 is mathematically the same as $p(a)p(b|a)$ of Lynch & Wagner [12] when the surface slope PDF is even. The same approximations are used in the definitions of $p(c|ab)$ and $p(d|abc)$. As a result, the uncorrelated model developed here would have the same result as that of Lynch & Wagner. The advantage of the model presented here is that, the correlation between the surface heights and slopes can be taken into account.

4.2.4 Monte Carlo ray-tracing method

To evaluate the model, a Monte Carlo ray-tracing method is employed. In this section, 1D surfaces are considered to save computation time. The inverse ray-path is used. The same ray-tracing algorithm as that used for calculating the monostatic illumination function with one reflection is firstly performed. For a given direction of observation $\hat{s}(\theta)$, an incident ray is put along the $-\hat{s}$ direction (inverse path) to find out all the points seen by the receiver (corresponding to M_0). Then, the specular reflected rays at these points are traced. For the points whose reflected ray intersects the surface (corresponding to point M_1), their reflected rays are traced. Finally, for the points whose reflected ray does not intersect the surface again, the slope of the points M_0 and M_1, and the slope of the reflected rays are recorded.

4.2.5 Numerical results

In this subsection, numerical results of the bistatic illumination function with two surface reflections $S_{\mathrm{B}}^{2,\mathrm{spe}}$ is calculated. For computational ease, 1D surfaces are considered. The surface height and slope PDFs are assumed to be Gaussian (Eqs. (1.5) and (1.6)), and a Gaussian height auto-correlation function (Eq. (1.14)) is considered. The results of the model are then compared with the ones of the Monte Carlo ray-tracing method.

4.2.5.1 Average illumination function $\overline{\overline{S}}_{\mathrm{B}}^{2,\mathrm{spe}}$

The average bistatic illumination function with two reflections gives the bidirectional distribution of $S_{\mathrm{B}}^{2,\mathrm{spe}}$. It is obtained by:

$$\overline{\overline{S}}_{\mathrm{B}}^{2,\mathrm{spe}}(\theta_i,\theta) = \int_{-\infty}^{+\infty}\int_{-\infty}^{+\infty}\int_{-\infty}^{+\infty}\int_{-\infty}^{+\infty} S_{\mathrm{B}}^{2} p(\gamma_0,\zeta_0,\gamma_1,\zeta_1)\,\mathrm{d}\zeta_1\,\mathrm{d}\gamma_1\,\mathrm{d}\zeta_0\,\mathrm{d}\gamma_0, \quad (4.45)$$

where $p(\gamma_0,\zeta_0,\gamma_1,\zeta_1)$ is the joint PDF of the heights and the slopes of points M_0 and M_1. Applying the uncorrelated S_{M}^{0}, the integrations over ζ_1, γ_1 and ζ_0 can be carried out analytically. The result is given by:

$$\begin{aligned}\overline{\overline{S}}_{\mathrm{B}}^{2,\mathrm{spe}}(\theta_i,\theta) &= \int_{-\infty}^{+\infty}\int_{-\infty}^{+\infty} \overline{S}_{\mathrm{B}}^{2}\delta(\gamma_1-\gamma_1^{\mathrm{spe}})p_{\gamma_1}(\gamma_1)\,\mathrm{d}\gamma_1 p_{\gamma}(\gamma_0)\,\mathrm{d}\gamma_0 &\quad (4.46)\\ &= \int_{-\infty}^{+\infty} \overline{S}_{\mathrm{B}}^{2} p(\gamma_1^{\mathrm{spe}})p_{\gamma}(\gamma_0)\,\mathrm{d}\gamma_0 &\quad (4.47)\end{aligned}$$

where $\overline{S}_{\mathrm{B}}^{2}$ is obtained by averaging S_{B}^{2} over the heights of M_1 and M_0, given by:

$$\overline{S}_{\mathrm{B}}^{2}(\theta_i,\theta,\gamma_0) = \begin{cases} \dfrac{1}{(1+\Lambda(\mu_i))(1+\Lambda(\mu))} & \text{if} \quad \theta' > 90^\circ \\ \dfrac{1}{(1+\Lambda^-(\mu_i))(1+\Lambda(\mu))} & \text{if} \quad \theta' < 90^\circ \\ \dfrac{\Lambda(\mu_1)}{(1+\Lambda^-(\mu_i))(1+\Lambda(\mu))(1+\Lambda(\mu)+\Lambda(\mu_1))} & \text{if} \quad \theta < \theta' < 90^\circ \\ \dfrac{\Lambda^-(\mu_1)}{(1+\Lambda(\mu_i))(1+\Lambda(\mu))(1+\Lambda(\mu)+\Lambda^-(\mu_1))} & \text{if} \quad -90^\circ < \theta' < 0^\circ \end{cases} \quad (4.48)$$

As θ', μ_1, γ_1^{spe} are all functions of γ_0, the integration over γ_0 in Eq. (4.47) is performed numerically. Applying the correlated S_{M}^{0}, the correlated $\overline{\overline{S}}_{\mathrm{B}}^{2,\mathrm{spe}}$ can be obtained, with all the integrations being performed numerically. The mathematical expression is not shown here because of its complexity.

As it is difficult to compare the $\overline{\overline{S}}_{\mathrm{B}}^{2,\mathrm{spe}}$ with that obtained by the Monte Carlo ray-tracing method (because of problem of normalization), the same strategy as used in $S_{\mathrm{B}}^{1,\mathrm{spe}}$ is applied again. The Dirac delta function used in Eq. (4.42) is replaced by a narrow window function given by Eq. (4.21), with $\triangle\theta_i = 0.1^\circ$.

Figs. 4.12 and 4.13 shows the average bistatic illumination function with two reflections $\overline{\overline{S}}_{\mathrm{B}}^{2,\mathrm{spe}}$. The surface RMS slope is $\sigma_\gamma = 0.2$ in Fig. 4.12 (sea surface with Beaufort scale ≈ 5) and $\sigma_\gamma = 0.5$ in Fig. 4.13 (not a sea surface). The observation

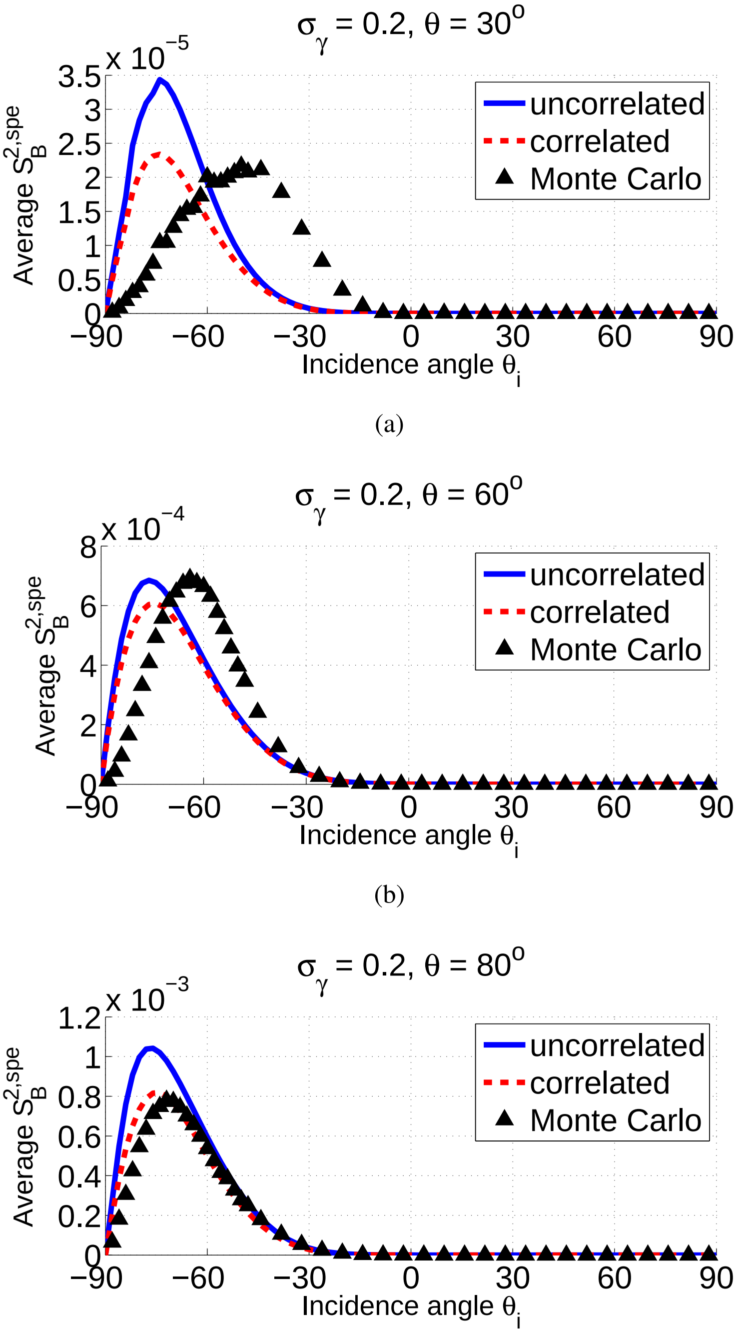

(a)

(b)

(c)

Figure 4.12: Average bistatic illumination function with two reflections $\overline{\overline{S}}_{\mathrm{B}}^{2}$, which corresponds to the bidirectional distribution of S_{B}^{2}. The surface RMS slope is $\sigma_\gamma = 0.2$. The observation direction is $\theta = \{30^\circ, 60^\circ, 80^\circ\}$ in (a), (b) and (c), respectively. The surface RMS slope is $\sigma_\gamma = 0.2$.

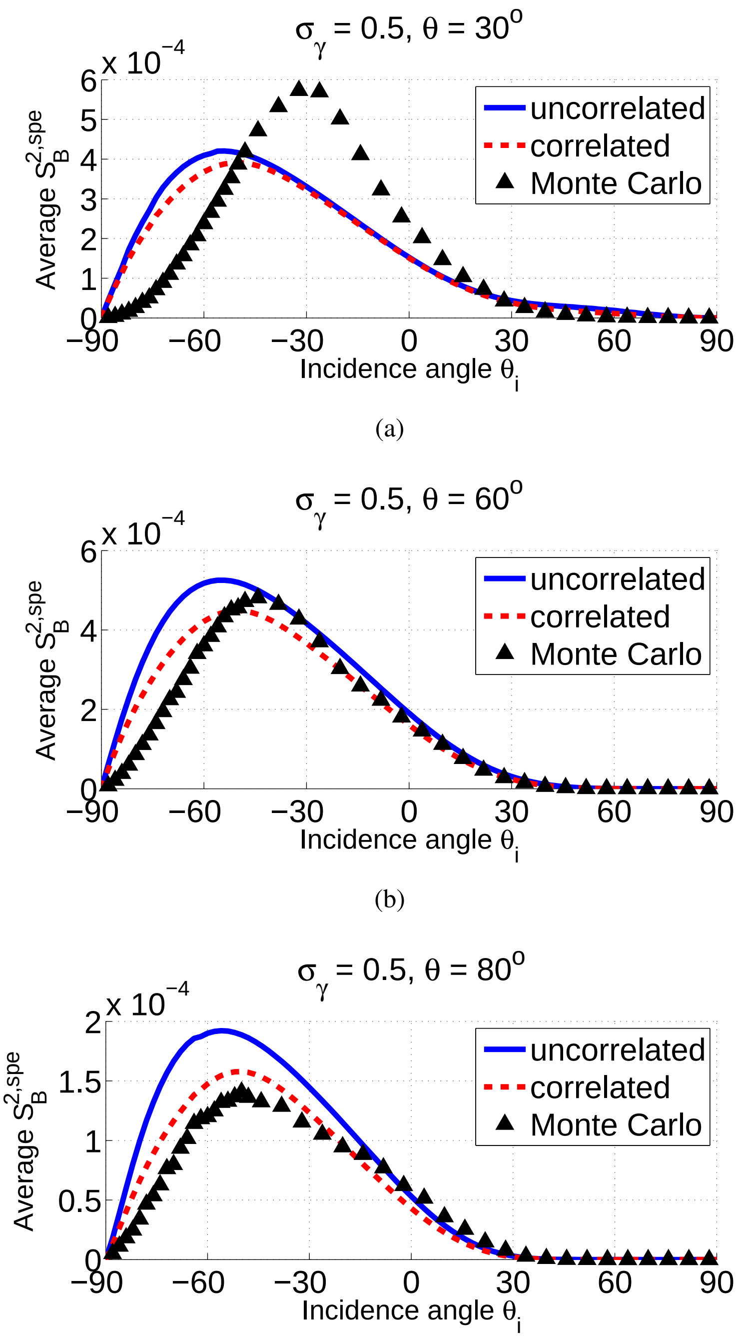

(a)

(b)

(c)

Figure 4.13: Average bistatic illumination function with two reflections $\overline{\overline{S}}^2_{\mathrm{B}}$, which corresponds to the bidirectional distribution of S^2_{B}. The surface RMS slope is $\sigma_\gamma = 0.2$. The observation direction is $\theta = \{30°, 60°, 80°\}$ in (a), (b) and (c), respectively. The surface RMS slope is $\sigma_\gamma = 0.5$.

direction is $\theta = \{30°, 60°, 80°\}$ in (a), (b) and (c), respectively. The results are compared with a Monte Carlo ray-tracing method.

Differences show up between the result of the model and that of the Monte Carlo ray-tracing method, especially for the smaller observation zenith angle $\theta = 30°$. The maxima of the present model, with or without considering the correlation between the surface heights and slopes, occur almost for the same $\theta_i \approx -80°$ for different θ, whereas the Monte Carlo ray-tracing result suggest that its location should significantly depend on the angle θ.

One possible reason for this discrepancy is that the slope PDF of M_1 is not well calculated in the model. In the derivation of the slope PDF of M_1, it is assumed that any slope γ_1 fulfilling $|\chi_1| < 90°$ can equally be the slope of M_1, which depends only on the slope of $\hat{s}'$, but does not take into account the influence of the observation angle θ.

Except for this drawback, the results of the present model are generally in the same level as the ones of the Monte Carlo ray-tracing model. The maxima of $\overline{\overline{S}}_{\mathrm{B}}^{2,\mathrm{spe}}$ for surface with $\sigma_\gamma = 0.2$ are of the order of 10^{-5}, 10^{-4} and 10^{-3} (recalling that $\triangle\theta_i = 0.1°$) for $\theta = 30°, 60°$ and $80°$, respectively, which means that double surface reflections are more probable for large observation angles θ (or incident angles θ_i, for the inverse path). The maxima of $\overline{\overline{S}}_{\mathrm{B}}^{2,\mathrm{spe}}$ for surface with $\sigma_\gamma = 0.5$ are of the same order for $\theta = 30°$, $60°$ and $80°$, meaning that double surface reflections are nearly the same significant for any observation direction.

4.2.5.2 Hemispherical average illumination function $\overline{\overline{S}}_{\mathrm{B}}^{2,\mathrm{hemi}}$

The hemispherical average illumination function with two surface reflections $\overline{\overline{S}}_{\mathrm{B}}^{2,\mathrm{hemi}}$ gives the proportion of the surface which is seen by the receiver (inverse path), and whose reflected rays leave the surface after two surface reflections (see Fig. 4.10).

The hemispherical average bistatic illumination function with two surface reflections can be obtained in a similar way as for $\overline{\overline{S}}_{\mathrm{B}}^{2,\mathrm{spe}}(\theta_i, \theta)$, by enlarging the width of the window function in Eq. 4.21 to:

$$W = \begin{cases} 1, & \text{for} \quad -90° < \theta_i < 90° \\ 0, & \text{otherwise} \end{cases} . \tag{4.49}$$

The angle θ_i is given by θ_1 and the slope γ_1 of M_1 as:

$$\theta_i = 2\arctan(-\gamma_1) - \theta_1. \tag{4.50}$$

The hemispherical average bistatic illumination function with two surface reflections is then given by:

$$\begin{aligned} \overline{\overline{S}}_{\mathrm{B}}^{2,\mathrm{hemi}}(\theta) &= \int_{-\infty}^{+\infty} \int_{-\infty}^{+\infty} \overline{S}_{\mathrm{B}}^{2} W p_{\gamma_1}(\gamma_1)\,\mathrm{d}\gamma_1 p_\gamma(\gamma_0)\,\mathrm{d}\gamma_0, \\ &= \int_{-\infty}^{+\infty} \int_{\gamma_1^{\mathrm{spe},1}}^{\gamma_1^{\mathrm{spe},2}} \overline{S}_{\mathrm{B}}^{2} p_{\gamma_1}(\gamma_1)\,\mathrm{d}\gamma_1 p_\gamma(\gamma_0)\,\mathrm{d}\gamma_0, \end{aligned} \tag{4.51}$$

where

$$\gamma_1^{\mathrm{spe},1} = -\tan\left(\frac{\theta_1 + 90°}{2}\right) \qquad \gamma_1^{\mathrm{spe},2} = -\tan\left(\frac{\theta_1 - 90°}{2}\right) \tag{4.52}$$

The first integration over γ_1 leads to the marginal slope histogram of γ_0, which is seen by the receiver (inverse path) and whose reflected ray leaves the surface after two reflections, given by:

$$\widetilde{p}_{\gamma}^{2,\mathrm{hemi}} = p_{\gamma}(\gamma_0)\int_{\gamma_1^{\mathrm{spe},1}}^{\gamma_1^{\mathrm{spe},2}} \overline{S}_{\mathrm{B}}^{2} p_{\gamma_1}(\gamma_1)\,\mathrm{d}\gamma_1. \tag{4.53}$$

Fig. 4.14 shows the histogram $\widetilde{p}_{\gamma}^{2,\mathrm{hemi}}$ of the slopes of M_0. The surface RMS slope is $\sigma_\gamma = 0.2$ on the left, and $\sigma_\gamma = 0.5$ on the right. The observation angle (or named angle of incidence, in the inverse path) $\theta = 30°$ (top), $60°$ (middle) and $80°$ (bottom). The results are shown versus the normalized slope $s_0 = \gamma_0/(\sigma_\gamma\sqrt{2})$.

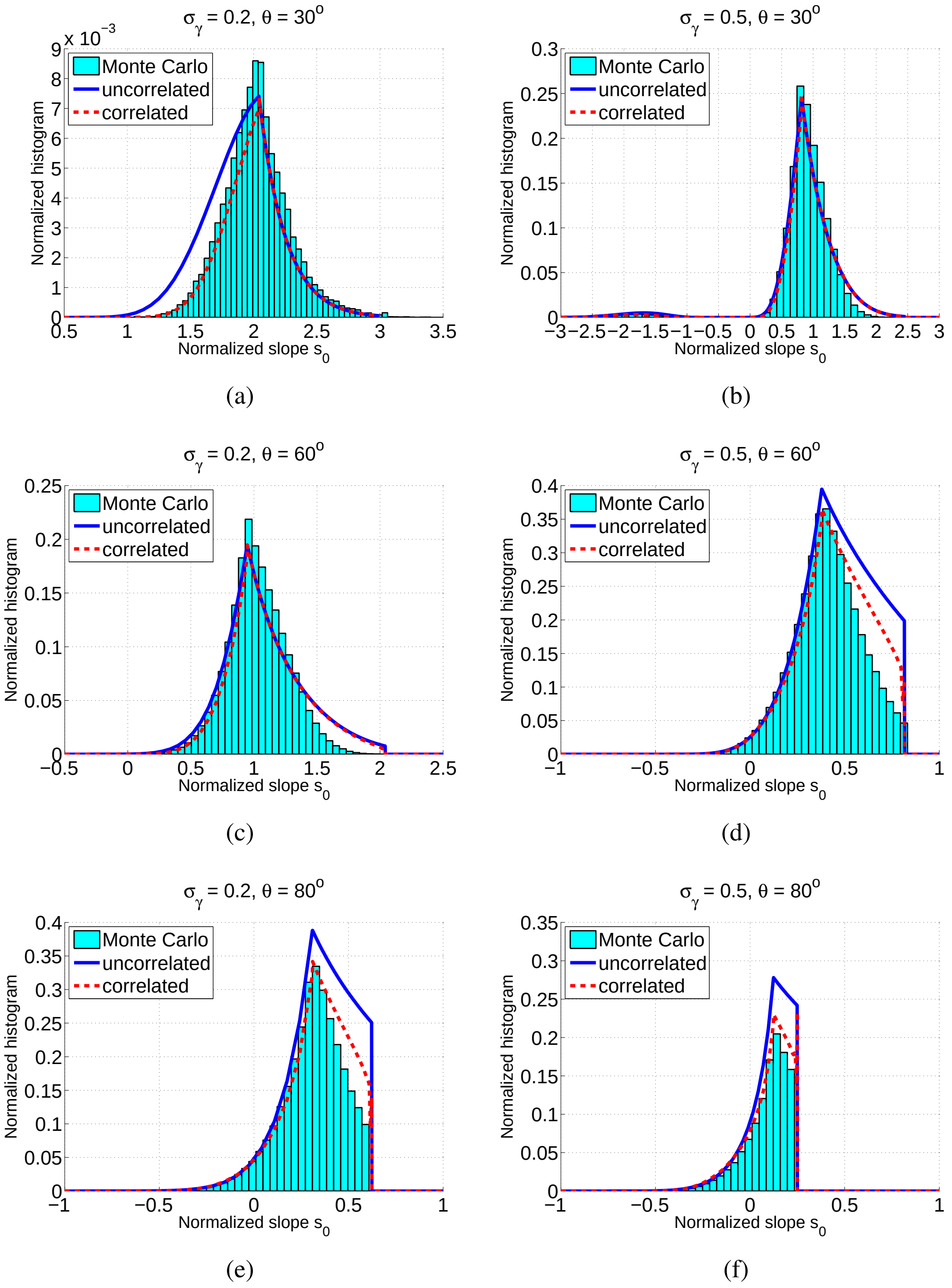

(a) (b)

(c) (d)

(e) (f)

Figure 4.14: Histogram of M_0 leading to double surface reflections.

Although the distribution of θ_i was not well predicted in Fig. 4.12 and Fig. 4.13, the histograms of the slopes of M_0 after averaging over $\theta_i \in [-90°, 90°]$ agree quite well with the results of the Monte Carlo ray-tracing method. In general, the uncorrelated model slightly overestimates the results, while the correlated one gives a better agreement, although the overestimation is not fully overcome. Thus, the present model predicts quite well the slope distribution of M_0, both in shape and in level.

Besides, it is shown that double surface reflections are much more significant for surfaces with $\sigma_\gamma = 0.5$ than that with $\sigma_\gamma = 0.2$ for $\theta = 30°$. For $\theta = 60°$ and $80°$, they are of similar levels.

Fig. 4.15 shows the hemispherical average bistatic illumination function with two reflections. The surface RMS slope is $\sigma_\gamma = 0.2$ (a) and $\sigma_\gamma = 0.5$ (b).

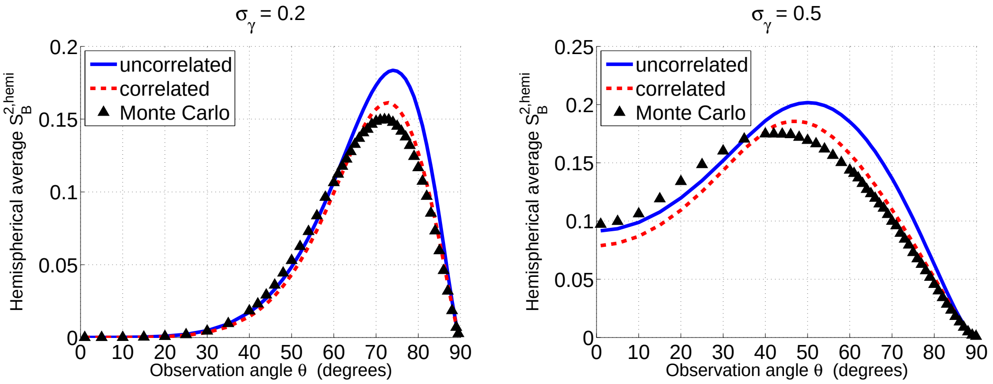

(a) (b)

Figure 4.15: Hemispherical average bistatic illumination function with two surface reflections of surfaces with $\sigma_\gamma = 0.2$ on the left (a) and $\sigma_\gamma = 0.5$ on the right (b).

It is shown that the model agrees quite well with the Monte Carlo ray-tracing method, especially for surfaces with $\sigma_\gamma = 0.2$. The model, either correlated or uncorrelated, slight underestimates the result at small and moderate θ, e.g. $\theta < 65°$ for surfaces with $\sigma_\gamma = 0.2$, and $\theta < 40°$ for surfaces with $\sigma_\gamma = 0.5$. For large θ, the model overestimates the result. In general, a better agreement is obtained by taking into account the correlation between surface heights and slopes.

It is notable that the hemispherical average bistatic illumination function with two reflections $\overline{\overline{S}}_{\mathrm{B}}^{2,\mathrm{hemi}}$ has similar shapes as the average monostatic illumination function with one reflection $\overline{\overline{S}}_{\mathrm{M}}^{1}$ shown in Fig. 2.18, but smaller in level. This is because the bistatic illumination function with two reflections $S_{\mathrm{B}}^{2,\mathrm{spe}}$ is built on the monostatic illumination function with one reflection S_{M}^{1}, by multiplying S_{M}^{1} with two terms smaller than 1.

4.3 Conclusion

Bistatic illumination function is the most important parameter in the calculation of sea surface reflectivity. Usually, one surface reflection is considered. In order to improve the accuracy, more surface reflections have to be taken into account, which implies to calculate the corresponding illumination function. This chapter reviews the bistatic illumination function of Smith, which takes one surface reflection into account. Then, a statistical model of bistatic illumination function with two surface reflections S_{B}^{2} is developed based on the monostatic illumination function with one surface reflection S_{M}^{1} which is shown in Chap. 2. Although the bidirectional distribution of S_{B}^{2} shows a discrepancy with the Monte Carlo ray-tracing, the hemispherical average S_{B}^{2} agrees quite well with the Monte Carlo ray-tracing method. This bistatic illumination function can still be promising for calculating the surface reflectivity.

In the next chapter, sea surface reflectivity is derived with the bistatic illumination functions shown in this chapter. Sea surface reflectivity with one surface reflection is developed by using the bistatic illumination function with one surface reflection $S_{\mathrm{B}}^{1,\mathrm{spe}}$, and the surface reflectivity with two surface reflections is developed by using the one with two reflections $S_{\mathrm{B}}^{2,\mathrm{spe}}$.

5

Sea surface infrared reflectivity

When deriving the sun glitter of the sea surface or the bidirectional reflectance distribution function (BRDF), sea surface infrared reflectivity is calculated. Usually, one surface reflection is considered [23, 8, 45, 6]. To be more accurate, more surface reflections have to be taken into account [9, 12].

In this chapter, the sea surface infrared reflectivity ρ is calculated. We recall that geometric optics approximation is assumed to be valid, so that only specular reflections are considered. The first-order reflectivity ρ_1, which considers single surface reflection, is calculated in Sec. 5.1 using the bistatic illumination function with one reflection $S_{\mathrm{B}}^{1,\mathrm{spe}}$. In Sec. 5.2, the second-order reflectivity ρ_2 is calculated using the bistatic illumination function with two reflections $S_{\mathrm{B}}^{2,\mathrm{spe}}$ which is introduced in Chap. 4.

5.1 Reflectivity with one surface reflection

The first-order sea surface infrared reflectivity corresponds to the radiance from the sky (sun, atmosphere) which is reflected once by the surface into the observation direction. Fig. 5.1 shows an emission ray from the sky which is reflected by the sea surface.

The receiver is in the observation direction $\hat{s}(\theta, \phi)$, and the transmitter is in the direction $\hat{s}'^{-}(\theta_i, \phi_i)$. New systems of coordinates (X, Y, z) and (X', Y', z) are defined according to the receiver and the transmitter directions, respectively. The definitions of the angles and the systems of coordinates are the same as the ones used in Chap. 4 (see Sec. 4.1.1 and Fig. 4.2 for details).

As mentioned in Chap. 4, shadowing from the transmitter (sky) and the receiver have to be both considered. In this section, the Smith bistatic illumination function with one surface reflection [4] is used to evaluate the hiding and masking effects.

5.1.1 Model for 1D surfaces

In this subsection, 1D rough surfaces are considered. For 1D surfaces, the incident and reflected rays and the zenith direction belong to the same plane (named

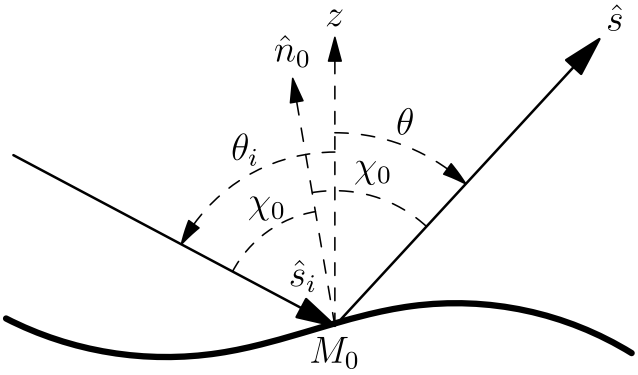

Figure 5.1: An incident ray $\hat{s}_i$ intersects the surface at a point M_0 and is reflected into the observation direction $\hat{s}$. Illustration for 1D surfaces. Zenith angles are oriented with the direction of θ being the positive direction.

(X, z) plane). The local angle of incidence χ_0 is given by Eq. (3.2) and is recalled here:

$$\cos\chi_0 = \hat{n}_0 \cdot \hat{s} = \frac{\cos\theta - \gamma_0 \sin\theta}{\sqrt{1+\gamma_0^2}}, \tag{5.1}$$

where $\hat{n}_0$ is the unitary normal to M_0 and γ_0 is its slope.

The local reflectivity of an arbitrary surface point M_0 (with local angle of incidence χ_0) is given by:

$$\rho^{\mathrm{local}}_{1,H,V}(\chi_0) = |r_{H,V}(\chi_0)|^2, \tag{5.2}$$

where $r_{H,V}$ are the Fresnel reflection coefficients in horizontal and vertical polarizations, respectively, given by Eq. (1.29).

It is notable that, for 1D surfaces, the horizontal and vertical polarization directions of different surface points are identical for given incident $\hat{s}'$ and observation $\hat{s}$ directions. As a 1D surface belongs to a plane (the (X, z) plane), the observation direction $\hat{s}$ and the local normal $\hat{n}_0$ to the point belong to the same plane containing the surface (the (X, z) plane). The horizontal polarization direction H is the one perpendicular to this plane, and the vertical polarization direction V is the one parallel to this plane and perpendicular to $\hat{s}$. These two directions do not change from one surface point to another. The same holds for the incident direction $\hat{s}'$. As a result, cross-polarization does not occur.

The first-order reflectivity of sea surfaces is the average of the local reflectivity of the surface facets seen by both the transmitter and the receiver, given by [23]:

$$\rho_{0,H,V} = \left\langle |r_{H,V}(\chi_0)|^2 g_0^{1\mathrm{D}}\, S_{\mathrm{B}}^{1,\mathrm{spe}} \right\rangle_{0,1\mathrm{D}}, \tag{5.3}$$

where $\langle\cdots\rangle_{0,1\mathrm{D}}$ stands for the statistical average over the heights ζ_0 and the slopes γ_0 of M_0, given by Eq. (3.5). The term $g_0^{1\mathrm{D}}$ results from projecting the area of the facet around M_0 onto the orthogonal direction of the observation direction θ, given by Eq. (3.9). $S_{\mathrm{B}}^{1,\mathrm{spe}}$ is the first-order bistatic illumination function given by Eq. (4.7), which gives the probability density that M_0 is seen by both the receiver and the transmitter, with the slope $\gamma_1 = \gamma_1^{\mathrm{spe}}$ corresponding to the specular reflection from the incident ray $\hat{s}_i$ into the direction of the reflected ray $\hat{s}$.

5.1.2 Model for 2D surfaces

For 2D surfaces, the incident and reflected rays and the zenith direction usually do not belong to the same plane. Thus, new systems of coordinates (X, Y, z) and (X', Y', z) are defined according to the directions of the transmitter and the receiver (see Sec. 4.1.1), so that the receiver belongs to the (X, z) plane, and the transmitter belongs to the (X', z) plane. The local angle of incidence χ_0 is given by Eq. (2.3), and is recall here:

$$\cos\chi_0 = \frac{\cos\theta - (\gamma_{x_0}\cos\phi + \gamma_{y_0}\sin\phi)\sin\theta}{\sqrt{1+\gamma_{x_0}^2+\gamma_{y_0}^2}}. \tag{5.4}$$

The local first-order reflectivity of an arbitrary surface point M_0 (with local angle of incidence χ_0) is given by:

$$\rho_{1,h_0,v_0}^{\text{local}}(\chi_0) = |r_{h_0,v_0}(\chi_0)|^2, \tag{5.5}$$

where r_{h_0,v_0} are the Fresnel reflection coefficients in local horizontal and vertical polarizations, respectively.

It is notable that, for 2D surfaces, the local polarization directions differ from one surface point to another. To describe the polarization state of the sea surface reflectivity, the average sea surface is considered, which is parallel to the horizontal plane ((X, Y) or (x, y)). The global horizontal polarization and the global vertical polarization are defined with respect to the average sea surface.

Consider an incident ray, with components in global H_i and V_i polarizations (defined with respect to the average sea plane and the incident ray $\hat{s}_i$), which intersects the sea surface at point M_0. Because the tangent plane of M_0 is not identical to the average sea surface in general, there is an angle α_i between the polarization directions H_i and $h_{0,i}$ (local horizontal polarization $h_{0,i}$ defined by the local tangent plane of M_0 and $\hat{s}_i$), or equally between V_i and $v_{0,i}$ (local vertical polarization $v_{0,i}$ defined by the local tangent plane of M_0 and $\hat{s}_i$). As a result, before performing the reflection, the components in global H_i and V_i polarizations have to be projected onto the local $h_{0,i}$ and $v_{0,i}$ polarization directions. In other words, cross-polarization occurs. This situation is very similar to that in Fig. 3.7, with the vector $\hat{s}$ replaced by $-\hat{s}'$, and α replaced by α_i.

We suppose that the incident ray is unpolarized, which means that its components in H_i and V_i polarizations have the same intensity ($I_{H_i} = I_{V_i} \equiv I$). The intensities of the components in $H_i h_{0,i}$ (global H_i polarization projected to local $h_{0,i}$ polarization), $V_i h_{0,i}$, $H_i v_{0,i}$ and $V_i v_{0,i}$ polarizations are given by:

$$I_{C_i p_{0,i}} = I f_i(\alpha_i), \tag{5.6}$$

with

$$f_i(\alpha_i) = \begin{cases} \cos^2\alpha_i, & \text{for } C_i,\, p_{0,i} \text{ stands for the same polarization,} \\ \sin^2\alpha_i, & \text{otherwise,} \end{cases} \tag{5.7}$$

where $C_i = \{H_i, V_i\}$ and $p_{0,i} = \{h_{0,i}, v_{0,i}\}$. Then, the components of the incident ray in local $h_{0,i}$ and $v_{0,i}$ polarizations are given for $I_{H_i} = I_{V_i} \equiv I$ by:

$$\begin{aligned} I_{h_{0,i}} &= I_{H_i h_{0,i}} + I_{V_i h_{0,i}} &&= I(\cos^2\alpha_i + \sin^2\alpha_i) &&= I, \\ I_{v_{0,i}} &= I_{V_i v_{0,i}} + I_{H_i v_{0,i}} &&= I(\cos^2\alpha_i + \sin^2\alpha_i) &&= I. \end{aligned} \tag{5.8}$$

It is notable that the intensity of the incident ray in $h_{0,i}$ and $v_{0,i}$ polarizations both equal the ones in H_i and V_i polarizations. In other words, the projection about α_i is not necessary. This is physical because the incident ray is unpolarized, which means that the intensities in any polarization are the same.

After the surface reflection, the intensity of the reflected ray in local h_0 and v_0 (defined by the local facet M_0 and $\hat{s}$) are given by:

$$\begin{aligned} I_{h_0} &= I_{h_{0,i}}|r_{h_0}(\chi_0)|^2 &= I|r_{h_0}(\chi_0)|^2, \\ I_{v_0} &= I_{v_{0,i}}|r_{v_0}(\chi_0)|^2 &= I|r_{v_0}(\chi_0)|^2. \end{aligned} \tag{5.9}$$

Note that the local h_0 and v_0 polarization directions are different from the global H and V (defined by the average surface and $\hat{s}$) polarization directions if the local facet is not identical to the average surface. As a result, there is an angle α between h_0 and H, or equally between v_0 and V. This is exactly the same situation as that discussed in Fig. 3.7. The components in local h_0 and v_0 polarizations are then projected onto the global H and V directions, given by:

$$I_{p_0C} = I_{p_0} f(\alpha), \tag{5.10}$$

with

$$f(\alpha) = \begin{cases} \cos^2\alpha, & \text{for } C, p_0 \text{ stands for the same polarization,} \\ \sin^2\alpha, & \text{otherwise,} \end{cases} \tag{5.11}$$

where $C = \{H, V\}$ and $p_0 = \{h_0, v_0\}$. The intensity of the components of the reflected ray $\hat{s}$ in global H and V polarizations are given for $I_{H_i} = I_{V_i} \equiv I$ by:

$$\begin{aligned} I_H &= I_{h_0H_i} + I_{v_0H_i} &= I(|r_{h_0}(\chi_0)|^2\cos^2\alpha + |r_{v_0}(\chi_0)|^2\sin^2\alpha), \\ I_V &= I_{h_0V_i} + I_{v_0V_i} &= I(|r_{h_0}(\chi_0)|^2\sin^2\alpha + |r_{v_0}(\chi_0)|^2\cos^2\alpha), \end{aligned} \tag{5.12}$$

Thus, the local polarized reflectivity of an arbitrary facet is given by:

$$\begin{aligned} \rho_{1,H}^{\text{local}} &= I_H/I_{H_i} &= |r_{h_0}(\chi_0)|^2\cos^2\alpha + |r_{v_0}(\chi_0)|^2\sin^2\alpha \\ \rho_{1,V}^{\text{local}} &= I_V/I_{V_i} &= |r_{h_0}(\chi_0)|^2\sin^2\alpha + |r_{v_0}(\chi_0)|^2\cos^2\alpha \end{aligned} \tag{5.13}$$

The polarized reflectivity of rough 2D surfaces is the average of the local reflectivity over all the surface, given by:

$$\rho_{1,H,V} = \left\langle \rho_{1,H,V}^{\text{local}}\, g_0^{\text{2D}}\, S_{\text{B}}^{1,\text{spe}} \right\rangle_{0,\text{2D}}, \tag{5.14}$$

where $\langle\cdots\rangle_{0,\text{2D}}$ stands for the statistical average over the heights ζ_0 and the slopes γ_{x_0} and γ_{y_0} of M_0, given by Eq. (3.16). The term g_0^{2D} results from projecting the surface area around the point M_0 onto the direction perpendicular to the observation direction $\hat{s}$. $S_{\text{B}}^{1,\text{spe}}$ is the bistatic illumination function with single surface reflection, which gives the probability density that M_0 is seen by both the receiver and the transmitter, with the slope in x and y directions $\gamma_{x_0} = \gamma_{x0}^{\text{spe}}$ and $\gamma_{y_0} = \gamma_{y0}^{\text{spe}}$ corresponding to the specular reflection from $\hat{s}_i$ to $\hat{s}$.

For a fully or partially polarized incident ray, it is difficult to define the polarized reflectivity. As the intensity of the incident ray in H_i and V_i polarizations are different, $\rho_{1,H}$ depends on I_{V_i}/I_{H_i} and $\rho_{1,V}$ depends on I_{H_i}/I_{V_i}. In other words, the polarized reflectivity depends on the polarization state of the incident ray. This case is not considered in this thesis.

5.1.3 Monte Carlo ray-tracing method

To evaluate the accuracy of the result, a Monte Carlo ray-tracing method is used. In the ray-tracing algorithm, 1D rough surfaces are generated, with Gaussian height and slope distributions (number of surfaces $N = 2000$, each surface with length $L = 100L_c$ in this chapter). Moreover, the surface points are assumed to be correlated with a Gaussian height autocorrelation function. After the generation of the rough surfaces, ray-tracing is performed. To be consistent with the model of surface emissivity, the inverse ray path is used. For a given observation direction $\hat{s}(\theta)$, an incident ray is put along the $-\hat{s}$ (inverse path) direction to find out all the points seen by the receiver. Then, the reflected rays at these points are traced. For the points whose reflected ray does not intersect the surface, the local reflectivity ρ_1^{local} of these points and the angle θ_i of the reflected rays are recorded.

For a given observation direction θ, the average surface (directional) reflectivity is given by:

$$\rho^{\text{spe}}_{1,\text{MC}}(\theta, \theta_i) = \frac{1}{N_s} \sum_{j=1}^{N_j} \rho_1^{\text{local},j} g_{0,i} \delta(\theta_i^j - \theta_i), \tag{5.15}$$

where N_s is the total number of the surface points, and N_j is the number of the surface points seen by the receiver and whose reflected ray $\hat{s}_i^{-,j}$ (inverse path) does not intersect the surface. The subscript "i" stands for "incident", and the superscript "j" is the index of the surface points selected by the ray-tracing algorithm. However, it is not possible to calculate the distribution of the reflectivity with respect to θ and θ_i by Eq. (5.15). As a numerical method, with a given θ, the ray-tracing algorithm is almost unable to obtain a reflection ray $\hat{s}_i^{-,j}$ in the exact θ_i direction. As a result, instead of using the Dirac delta function $\delta(\theta_i^j - \theta_i)$, a window function is used, given by:

$$W = \begin{cases} 1, & \text{for} \quad |\theta_i^j - \theta_i| \leq \triangle\theta_i \\ 0, & \text{otherwise} \end{cases}, \tag{5.16}$$

where $\triangle\theta_i$ is taken as $0.1°$ in this chapter. In other words, if the global angle of reflection θ_i^j is in a small region ($\theta_i \pm 0.1°$) around θ_i, it is considered that this reflected ray $\hat{s}_i^j$ reaches the transmitter (inverse path).

For a given θ, the hemispherical average reflectivity is also calculated, given by:

$$\rho^{\text{hemi}}_{1,\text{MC}} = \frac{1}{N_s} \sum_{j=1}^{N_j} \rho_1^{\text{local},j} g_{0,i}. \tag{5.17}$$

No restriction is put on the direction θ_i. Any reflected ray leaving the surface after one surface reflection contributes to the first-order surface reflectivity.

5.1.4 Numerical results

In this subsection, numerical results of the first-order reflectivity are presented. To be consistent with the Monte Carlo ray-tracing method, 1D surfaces (2D problems) are considered. The cross-polarization effect may be interesting to study, which involves 2D surfaces. This point is not study here, because of the complexity in programming and the lack of time.

The surface slope PDF is assumed to be Gaussian. The correlation between surface heights and slopes is taken into account, with a Gaussian height autocorrelation function. The average first-order reflectivity ρ_1^{spe} (bidirectional) is shown, as well as the hemispherical average reflectivity ρ_1^{hemi}. The results are compared with the Monte Carlo ray-tracing method.

5.1.4.1 Average first-order reflectivity ρ_1^{spe}

The average first-order reflectivity is obtained by Eq. (5.3), where the bistatic illumination function with one surface reflection $S_{\text{B}}^{1,\text{spe}}$ is involved. Recall that $S_{\text{B}}^{1,\text{spe}}$ involves the Dirac delta function $\delta(\gamma_0 - \gamma_0^{\text{spe}})$, which corresponds to considering specular reflections. However, to be consistent with the Monte Carlo ray-tracing method, this Dirac delta function is replaced by the window function given by Eq. (4.21), with $\triangle\theta_i = 0.1°$.

Figs. 5.2 and 5.3 show the results of the average first-order sea surface reflectivity ρ_1^{spe} in H and V polarizations. The up-wind direction is considered. Three observation angles $\theta = \{30°, 60°, 80°\}$ are studied, and the results are shown versus the angle of incidence θ_i. The wavelength is $\lambda = 10$ μm, and the wind speed u_{12} is 5 m/s in Fig. 5.2 and 10 m/s in Fig. 5.3.

It is shown that the model agrees very well with the Monte Carlo ray-tracing method. Taking into account the correlation between the surface heights and slopes hardly modifies the result. Its influence is visible only for $u_{12} = 10$ m/s and $\theta = 80°$.

It is shown that the H and V polarized reflectivities with one reflection ρ_1^{spe} do not equal each other. The V polarized ρ_1^{spe} is always smaller, which means that the surface reflection changes the global polarization state of the incident ray. The reflection of an unpolarized ray, whose intensity in any polarization is the same, would be partially polarized, with the intensity in H polarization being stronger.

It is notable that the location of the peaks of ρ_1^{spe} in H and V polarizations are different. In addition, they are not located in the global specular reflection direction. This effect is the most significant for $\theta = 60°$ shown in Figs. 5.2 (b) and 5.3 (b), where the peaks of ρ_1^{spe} are shifted to about $\theta_i \approx -75°$. This effect is reported in the measurements of the sea surface sun glitter [8, 45]. It is reported that the peak of the sun glitter was shifted toward the horizon ($|\theta_i|$ is larger).

5.1.4.2 Hemispherical average reflectivity ρ_1^{hemi}

The hemispherical average reflectivity with one surface reflection ρ_1^{hemi} is obtained in the same way as ρ_1^{spe}, with the window function being enlarged to $\theta_i \in [-90°, 90°]$. The new window function is given by Eq. (4.23), which is also used when calculating the hemispherical average bistatic illumination function.

Fig. 5.4 shows the hemispherical average reflectivity ρ_1^{hemi} versus θ. The wind speed is $u_{12} = 5$ m/s (left) and $u_{12} = 10$ m/s (right). The wavelength is $\lambda = 4$ μm (up) and $\lambda = 10$ μm (down).

The model generally agrees well with the result of the Monte Carlo ray-tracing method. For grazing angles $\theta > 80°$, the model slightly overestimates ρ_1^{hemi}. In general, the correlated model gives a better agreement with the Monte Carlo ray-tracing method, except for $\theta \approx 90°$. However, this discrepancy should be mainly caused by the large calculation error in the numerical method.

It is shown that the H polarized ρ_1^{hemi} monotonously increases with the observation zenith angle θ, while the V polarized ρ_1^{hemi} slightly decreases to a minimum value and then increases, because of the Brewster angle. Besides, the H polarized ρ_1^{hemi} is always larger than that in V polarization, which is opposite from the sea

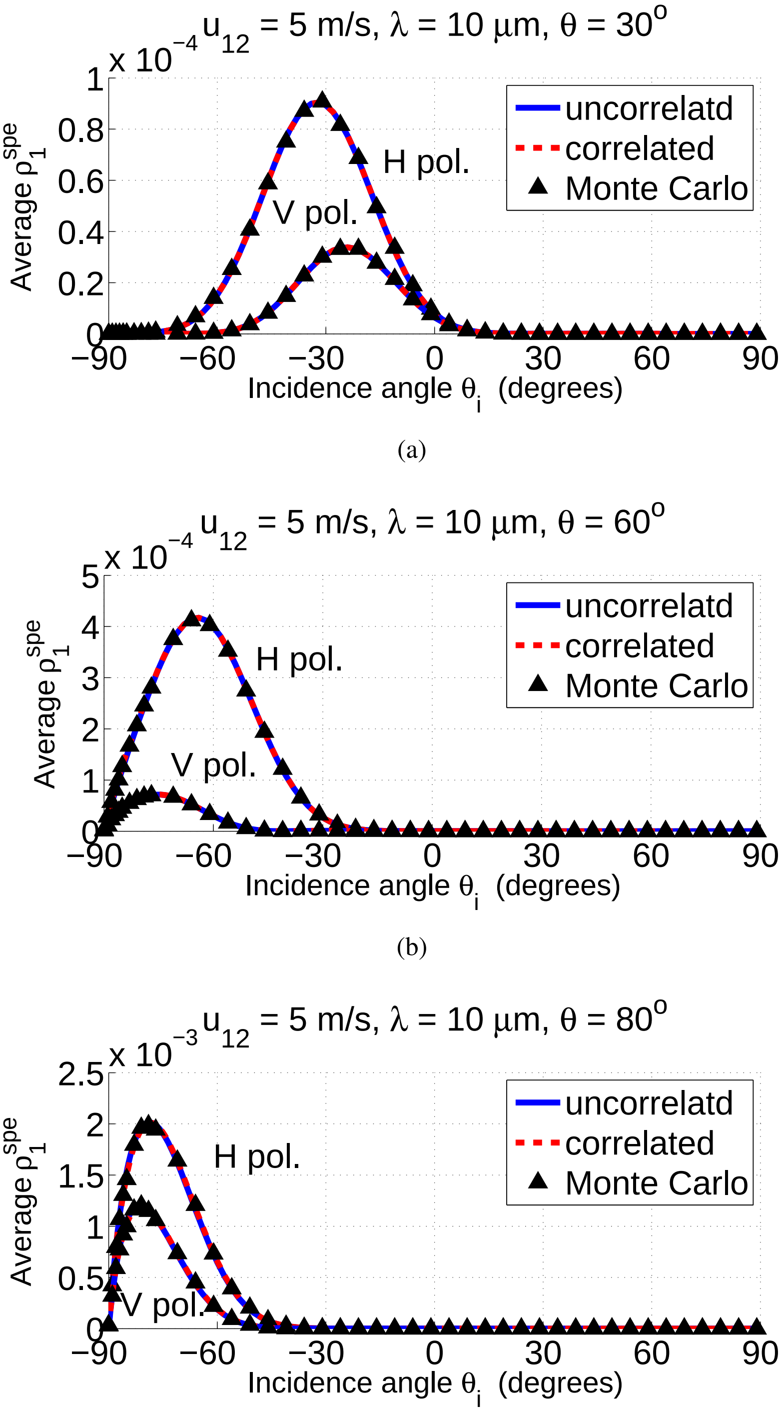

(a)

(b)

(c)

Figure 5.2: Average first-order reflectivity ρ_1^{spe} of the sea surface versus θ_i, with wavelength $\lambda = 10\ \mu$m. The observation angle is $\theta = 30^\circ$ in (a), $\theta = 60^\circ$ in (b), and $\theta = 80^\circ$ in (c). The wind speed $u_{12} = 5$ m/s.

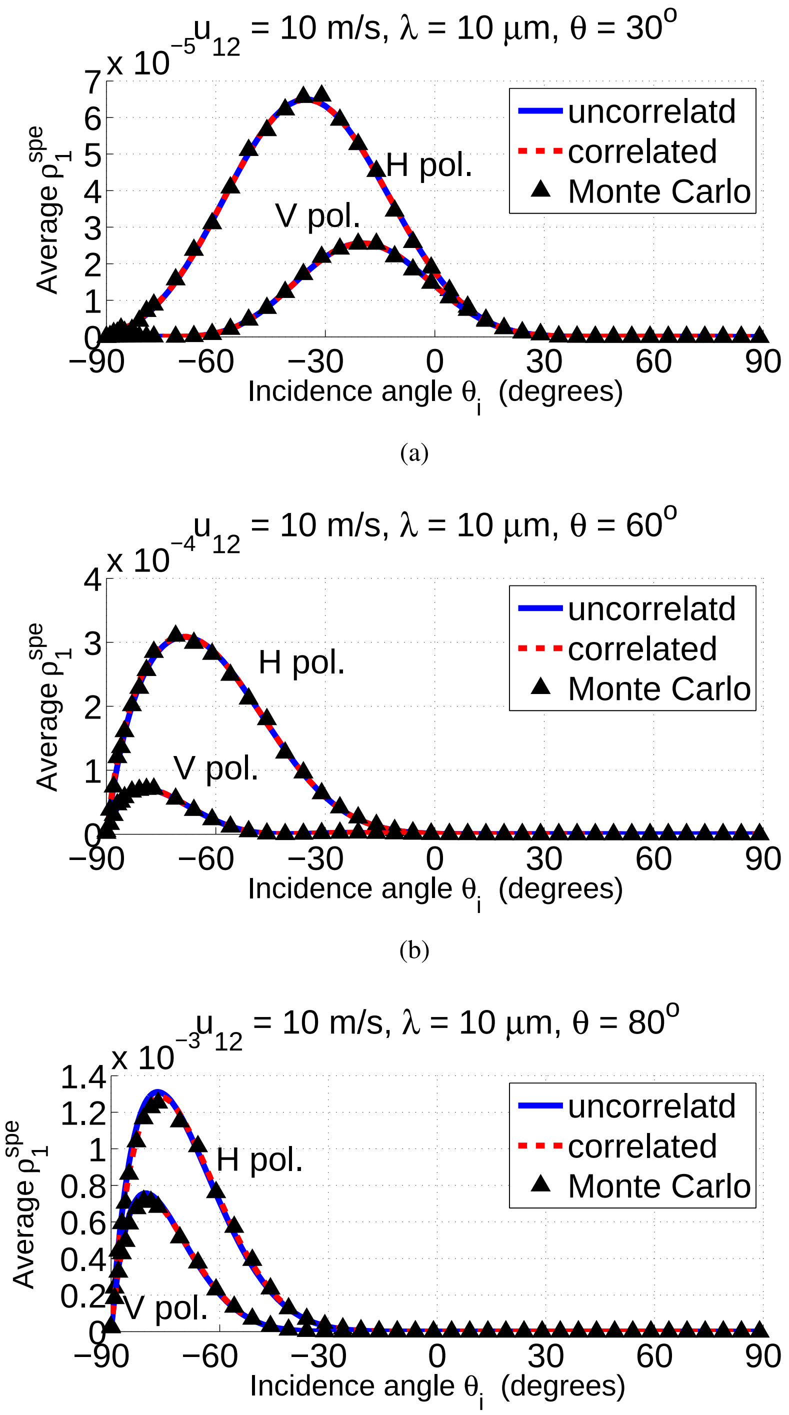

(a)

(b)

(c)

Figure 5.3: Average first-order reflectivity $\rho_1^{\rm spe}$ of the sea surface versus θ_i, with wavelength $\lambda = 10\ \mu$m. The observation angle is $\theta = 30°$ in (a), $\theta = 60°$ in (b), and $\theta = 80°$ in (c). The wind speed $u_{12} = 10$ m/s.

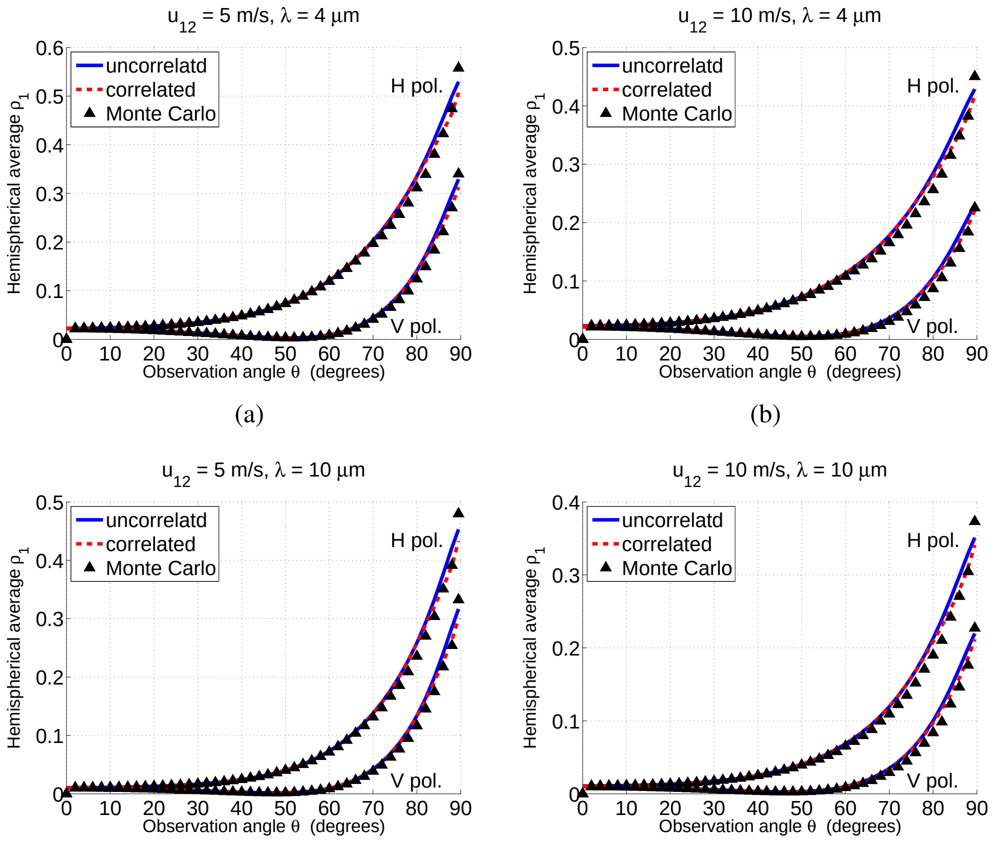

(a)

(b)

(c)

(d)

Figure 5.4: Hemispherical average first-order sea surface reflectivity ρ_1^{hemi} with respect to θ for $u_{12} = 5$ m/s (left) and 10 m/s (right), and for $\lambda = 4$ μm (up) and 10 μm (down).

surface emissivity ε_0, where $\varepsilon_{0,V}$ is always larger (see Fig. 3.5). This is physical, because more energy is reflected implies that less energy is absorbed (then re-emitted).

It is reported that, considering only the zero-order emissivity ε_0 and the first-order reflectivity ρ_1^{hemi} does not fulfill the energy conservation law [6]. The conclusion is also found latter in Figs. 5.12 and 5.12. The sum of reflected energy (ρ_1^{hemi}) and the absorbed energy (ε_0) does not equal the incident energy. Yoshimori *et al.* [6] stated that it was because multiple surface reflections are neglected. As a consequence, in the next section, sea surface reflectivity with two surface reflections is studied.

5.2 Reflectivity with two reflections

The second-order sea surface infrared reflectivity corresponds to the radiance from the sky (sun, atmosphere) which is reflected twice by the surface into the observation direction. Fig. 5.5 shows an emission ray from the sky reflected twice by the sea surface.

The receiver is located in the observation direction $\hat{s}(\theta, \phi)$, and the transmitter is located in the direction $\hat{s}_i^-(\theta_i, \phi_i)$. New systems of coordinates (X, Y, z), (X', Y', z) and (X'', Y'', z) are defined according to the directions of the receiver, of the reflec-

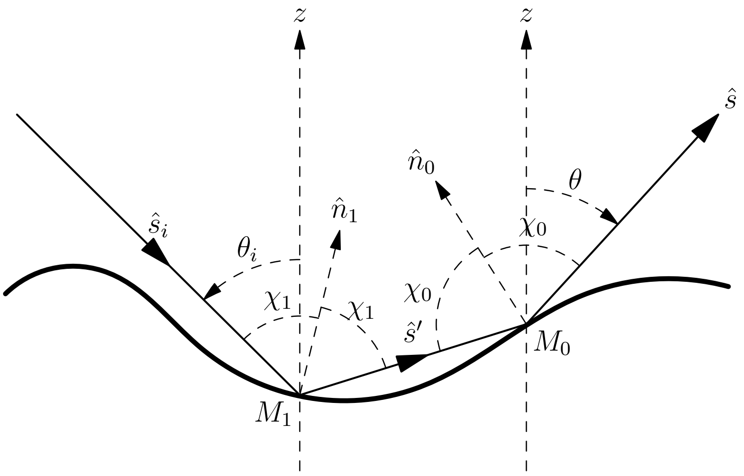

Figure 5.5: An incident ray intersects the surface at point M_0 and is reflected into the $\hat{s}'$ direction. The reflected ray $\hat{s}'$ intersects the surface again at M_0 and is then reflected to the observation direction $\hat{s}$. Illustration for 1D surfaces. Zenith angles are oriented with the direction of θ being the positive direction.

tion point M_1 and of the transmitter, respectively. The definitions of the angles and systems of coordinates are the same as the ones used in Chap. 4 (see Sec. 4.1.1 and Fig. 4.11 for details).

In this section, the bistatic illumination function with two surface reflections $S_{\text{B}}^{2,\text{spe}}$ developed in Sec. 4.2 is used to estimate the probability of the occurrence of double surface reflections.

5.2.1 Model for 1D surfaces

In this subsection, 1D surfaces (2D problem) are considered (see Fig. 5.5). For 1D surfaces, the zenith direction, and the rays $\hat{s}_i$, $\hat{s}'$ and $\hat{s}$ belong to the same plane, named (X, z) plane. In other words, cross-polarization never occurs. The local angle of incidence χ_0 at point M_0 is given by Eq. (3.2), and the one at point M_1 is given by Eq. (2.60).

Let the intensity of $\hat{s}_i$ in horizontal (noted H_1) and vertical (noted V_1) polarization directions being I_{H_1} and I_{V_1}, respectively. The intensity of the components of the ray $\hat{s}'$ in horizontal (noted H_1') and vertical (noted V_1') polarizations are given by:

$$I_{H_1'} = I_{H_1}|r_{H_1}(\chi_1)|^2, \qquad I_{V_1'} = I_{V_1}|r_{V_1}(\chi_1)|^2, \tag{5.18}$$

where r_{H_1,V_1} are the Fresnel reflection coefficients in horizontal and vertical polarizations. Similarly, the intensity of the ray $\hat{s}$ in horizontal (noted H) and vertical vertical (noted V) polarizations are given by:

$$\begin{array}{lllll} I_H & = & I_{H_1'}|r_H(\chi_0)|^2 & = & I_{H_1}|r_{H_1}(\chi_1)|^2|r_H(\chi_0)|^2, \\ I_V & = & I_{V_1'}|r_V(\chi_0)|^2 & = & I_{V_1}|r_{V_1}(\chi_1)|^2|r_V(\chi_0)|^2. \end{array} \tag{5.19}$$

The local polarized reflectivity with two surface reflections is then given by:

$$\begin{array}{lllll} \rho_{2,H}^{\text{local}} & = & I_H/I_{H_1} & = & |r_{H_1}(\chi_1)|^2|r_H(\chi_0)|^2, \\ \rho_{2,V}^{\text{local}} & = & I_V/I_{V_1} & = & |r_{V_1}(\chi_1)|^2|r_V(\chi_0)|^2 \end{array} \tag{5.20}$$

The polarized reflectivity $\rho_{2,H,V}$ of the sea surface with two surface reflections is the average of the local reflectivities over the whole surface, given by:

$$\begin{aligned} \rho_{2,H} &= \left\langle \rho_{2,H}^{\text{local}} g_0^{\text{1D}} S_{\text{B}}^{2,\text{spe}} \right\rangle_{1,1D}, \\ \rho_{2,V} &= \left\langle \rho_{2,V}^{\text{local}} g_0^{\text{1D}} S_{\text{B}}^{2,\text{spe}} \right\rangle_{1,1D}, \end{aligned} \tag{5.21}$$

where $\langle \cdots \rangle_{1,1D}$ stands for the statistical average over the slopes and the heights of the points M_1 and M_0, given by Eq. (3.22). $S_{\text{B}}^{2,\text{spe}}$ is the bistatic illumination function with two surface reflections for 1D surfaces, which is introduced in Sec. 4.2.3.3. The term g_0^{1D} results from projecting the area of the facet around M_0 onto the orthogonal direction of the observation direction θ, given by Eq. (3.9).

5.2.2 Model for 2D surfaces

In this subsection, 2D surfaces (3D problem) are considered. As stated before, for 2D surfaces, the local polarization directions are different from one surface point to another. To describe the polarization state, the average sea surface is considered, and the global horizontal H and vertical V polarizations are defined.

Consider an unpolarized incident ray with the same intensity I in any polarization direction. When the local tangent plane of M_1 is not identical to the average sea surface, there is an angle α_i between the global H_i (or V_i) and local $h_{1,i}$ (or $v_{1,i}$, defined by the local tangent plane of point M_1 and $\hat{s}_i$) polarization directions. However, this rotation angle α_i does not affect the polarized reflectivity if an unpolarized incident ray is considered, as discussed in Sec. 5.1.2. As a result, the intensities of the components of the incident ray in local $h_{1,i}$ and $v_{1,i}$ polarizations are

$$I_{h_{1,i}} = I_{v_{1,i}} = I. \tag{5.22}$$

After the surface reflection, the intensity of the reflected ray $\hat{s}'$ in local h'_1 and v'_1 polarizations (defined by the local tangent plane of M_1 and $\hat{s}'$) are given by:

$$\begin{aligned} I_{h'_1} &= I_{h_{1,i}} |r_{h_1}(\chi_1)|^2 &= I |r_{h_1}(\chi_1)|^2 \\ I_{v'_1} &= I_{v_{1,i}} |r_{v_1}(\chi_1)|^2 &= I |r_{v_1}(\chi_1)|^2 \end{aligned} \tag{5.23}$$

As the direction of the ray $\hat{s}'$ and the local normals $\hat{n}_1$ and $\hat{n}_0$ to M_1 and to M_0 are usually not in the same plane, there is an angle β between the local horizontal h'_1 and h'_0 (defined by the local tangent plane of M_0 and $\hat{s}'$) polarization directions. As a result, the intensity of the ray $\hat{s}'$ in h'_1 and v'_1 polarizations have to be projected onto the local h'_0 and v'_0 polarization directions. This case is exactly the same as that discussed in Fig. 3.19. The calculation of β is given in Appendix F. After the projection, the intensities of the ray $\hat{s}'$ in $h'_1 h'_0$ (local h'_1 project onto h'_0), $h'_1 v'_0$, $v'_1 h'_0$ and $v'_1 v'_0$ polarizations are given by:

$$\begin{aligned} I_{h'_1 h'_0} &= I_{h'_1} \cos^2\beta &= I |r_{h_1}(\chi_1)|^2 \cos^2\beta, \\ I_{v'_1 h'_0} &= I_{v'_1} \sin^2\beta &= I |r_{v_1}(\chi_1)|^2 \sin^2\beta, \\ I_{h'_1 v'_0} &= I_{h'_1} \sin^2\beta &= I |r_{h_1}(\chi_1)|^2 \sin^2\beta, \\ I_{v'_1 v'_0} &= I_{v'_1} \cos^2\beta &= I |r_{v_1}(\chi_1)|^2 \cos^2\beta. \end{aligned} \tag{5.24}$$

After the reflection from $\hat{s}'$ into $\hat{s}$, the intensity of $\hat{s}$ in h_0 and v_0 polarizations (defined by the local tangent plane of M_0 and $\hat{s}$) is given by:

$$\begin{array}{lllll} I_{h'_1h_0} & = & I_{h'_1h'_0}|r_{h_0}(\chi_0)|^2 & = & I|r_{h_1}(\chi_1)|^2|r_{h_0}(\chi_0)|^2\cos^2\beta, \\ I_{v'_1h_0} & = & I_{v'_1h'_0}|r_{h_0}(\chi_0)|^2 & = & I|r_{v_1}(\chi_1)|^2|r_{h_0}(\chi_0)|^2\sin^2\beta, \\ I_{h'_1v_0} & = & I_{h'_1v'_0}|r_{v_0}(\chi_0)|^2 & = & I|r_{h_1}(\chi_1)|^2|r_{v_0}(\chi_0)|^2\sin^2\beta, \\ I_{v'_1v_0} & = & I_{v'_1v'_0}|r_{v_0}(\chi_0)|^2 & = & I|r_{v_1}(\chi_1)|^2|r_{v_0}(\chi_0)|^2\cos^2\beta, \end{array} \tag{5.25}$$

or for short

$$I_{p'_1q_0} = I|r_{p_1}(\chi_1)|^2|r_{q_0}(\chi_0)|^2g(\beta), \tag{5.26}$$

where $p_1 = \{h_1, v_1\}$ and $q_0 = \{h_0, v_0\}$. The function $g(\beta) = \cos^2\beta$ if p_1 and q_0 are both horizontal or vertical polarizations. Otherwise, $g(\beta) = \sin^2\beta$.

As discussed previously, there is an angle α between the local and global horizontal polarization directions h_0 and H, or equally between the vertical polarization ones v_0 and V. The intensity is then projected onto the global H and V polarization directions, given by:

$$I_{p'_1q_0C} = I_{p'_1q_0}f(\alpha), \tag{5.27}$$

where $C = \{H, V\}$. The function $f(\alpha) = \cos^2\alpha$ if q_0 and C are both horizontal or vertical polarizations. Otherwise, $f(\alpha) = \sin^2\alpha$. The intensity of the ray $\hat{s}$ in H and V polarizations are given by:

$$\begin{array}{lll} I_H & = & \sum_{p'_1=\{h'_1,v'_1\},q_0=\{h_0,v_0\}} I_{p'_1q_0H} \\ I_V & = & \sum_{p'_1=\{h'_1,v'_1\},q_0=\{h_0,v_0\}} I_{p'_1q_0V} \end{array} \tag{5.28}$$

The local polarized reflectivity is then given by:

$$\begin{array}{l} \rho_H^{\text{local}} = I_H/I = \sum_{p'_1=\{h'_1,v'_1\},q_0=\{h_0,v_0\}} \rho^{\text{local}}_{p'_1q_0H}, \\ \rho_V^{\text{local}} = I_V/I = \sum_{p'_1=\{h'_1,v'_1\},q_0=\{h_0,v_0\}} \rho^{\text{local}}_{p'_1q_0V}, \end{array} \tag{5.29}$$

where

$$\begin{array}{l} \rho^{\text{local}}_{p'_1q_0H} = |r_{p_1}(\chi_1)|^2|r_{q_0}(\chi_0)|^2g(\beta)f(\alpha) \\ \rho^{\text{local}}_{p'_1q_0V} = |r_{p_1}(\chi_1)|^2|r_{q_0}(\chi_0)|^2g(\beta)f(\alpha) \end{array} \tag{5.30}$$

The polarized surface reflectivity is the average of the local polarized reflectivity over all the surface, given by:

$$\rho_{2,H,V} = \left\langle \rho^{\text{local}}_{2,H,V} g_0^{\text{2D}} S_{\text{B}}^{2,\text{spe}} \right\rangle_{1,2D}, \tag{5.31}$$

where the symbol $\langle\cdots\rangle_{1,2D}$ stands for the statistical average over the heights and the slopes of M_1 and M_0, given by Eq. (3.33). $S_{\text{B}}^{2,\text{spe}}$ is the bistatic illumination function with two surface reflections developed in Sec. 4.2.3.1.

5.2.3 Monte Carlo ray-tracing method

A Monte Carlo ray-tracing method is used to evaluate the accuracy of the model. For computational ease, 1D surfaces are considered (number of surfaces $N = 2000$, each surface with length $L = 100L_c$). The surface heights and slopes PDFs are assumed to be Gaussian, and the Gaussian height auto-correlation function is used. The same ray-tracing algorithm used in Sec. 4.2.4 is used here to find out the points seen by the receiver (M_0), and whose reflected rays $-\hat{s}'$ (inverse path) intersect the surface again (M_1) and then leave the surface. Each M_0 and its corresponding M_1

are called one pair. The slopes of these points (M_0 and M_1) are recored, as well as the direction of the ray $\hat{s}_i$.

The surface average reflectivity is firstly calculated, which is given by:

$$\begin{array}{rcl} \rho_{2,\mathrm{H,MC}} & = & \frac{1}{N_s}\sum_{j=1}^{N_j}|r_H(\chi_1)|^2|r_H(\chi_0)|^2 g_0^{\mathrm{1D}}\delta(\theta_i^j-\theta_i), \\ \rho_{2,\mathrm{V,MC}} & = & \frac{1}{N_s}\sum_{j=1}^{N_j}|r_V(\chi_1)|^2|r_V(\chi_0)|^2 g_0^{\mathrm{1D}}\delta(\theta_i^j-\theta_i), \end{array} \tag{5.32}$$

where N_s is the number of surface points, and N_j is the number of the pairs of M_0 and M_1.

For the same reason as stated in Sec. 5.1.3, it is meaningless to perform Eq. (5.32) in a numerical method, because of the Dirac delta function $\delta(\theta_i^j - \theta_i)$. As a result, the Dirac delta function is replaced by the same window function given by Eq. (5.16), with $\triangle\theta_i = 0.1°$.

For a given θ, the hemispherical average reflectivity is also calculated, given by:

$$\begin{array}{rcl} \rho_{2,\mathrm{H,MC}}^{\mathrm{hemi}} & = & \frac{1}{N_s}\sum_{j=1}^{N_j}|r_H(\chi_1)|^2|r_H(\chi_0)|^2 g_0^{\mathrm{1D}}, \\ \rho_{2,\mathrm{V,MC}}^{\mathrm{hemi}} & = & \frac{1}{N_s}\sum_{j=1}^{N_j}|r_V(\chi_1)|^2|r_V(\chi_0)|^2 g_0^{\mathrm{1D}}, \end{array} \tag{5.33}$$

where N_s is the total number of the surface points, and N_j is the number of pairs of M_0 and M_1. No restriction is put to the direction θ_i. Any reflected ray leaving the surface after two surface reflections contributes to the second-order hemispherical average surface reflectivity.

5.2.4 Numerical results

In this subsection, numerical results of the second-order reflectivity is presented. To be consistent with the Monte Carlo ray-tracing method, 1D surfaces (2D problems) are considered. The cross-polarization effect is not studied, because of the complexity in programming and the lack of time.

The surface slope PDF is assumed to be Gaussian. The correlation between surface heights and slopes is taken into account, with a Gaussian height autocorrelation function. The average second-order reflectivity ρ_2^{spe} and its hemispherical average ρ_2^{hemi} are calculated. Besides, the energy conservation is examined.

5.2.4.1 Average second-order reflectivity ρ_2^{spe}

The average second-order reflectivity ρ_2^{spe} is obtained by Eq. (5.21), where the bistatic illumination function with two surface reflections $S_{\mathrm{B}}^{2,\mathrm{spe}}$ is involved. Recall that $S_{\mathrm{B}}^{2,\mathrm{spe}}$ involves the Dirac delta function $\delta(\gamma_1 - \gamma_1^{\mathrm{spe}})$, which corresponds to considering specular reflections. For the same reason as stated before, the window function given by Eq. (4.21) is used to replace the Dirac delta function, with $\triangle\theta_i = 0.1°$.

Figs. 5.6 and 5.7 show the results of the average second-order sea surface reflectivity in H and V polarizations. The parameters are the same as the ones in Figs. 5.2 and 5.3.

It is shown that the model does not agree very well with the Monte Carlo ray-tracing method, especially for small observation angle $\theta = 30°$ and the moderate one $\theta = 60°$. For these two θ, the results of the present model have similar forms with the Monte Carlo ray-tracing results, but the locations of the peaks are different. A better agreement is obtained for $\theta = 80°$. Note that similar discrepancies between

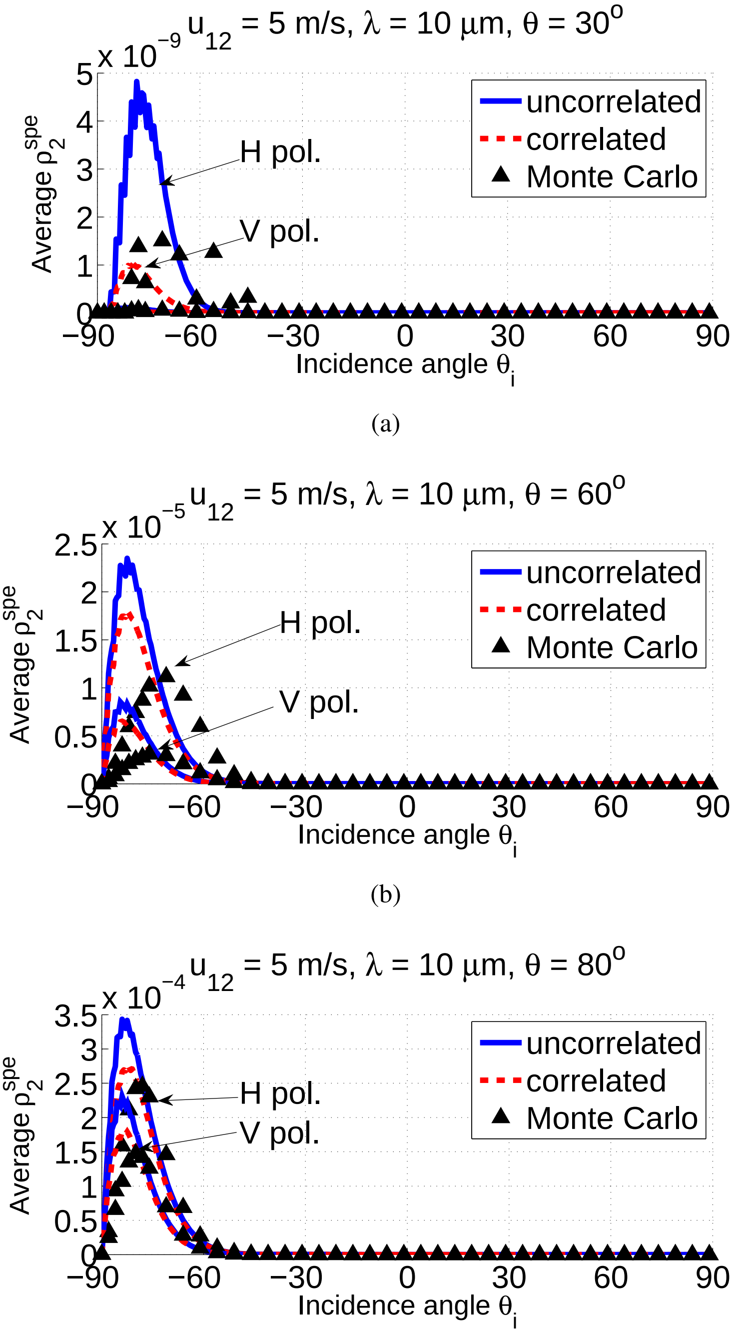

(a)

(b)

(c)

Figure 5.6: Average second-order reflectivity ρ_2^{spe} of sea surfaces versus θ_i, with the observation angle being $\theta = 30^\circ$ in (a), $\theta = 60^\circ$ in (b), and $\theta = 80^\circ$ in (c). The wavelength is $\lambda = 10\ \mu$m. The wind speed $u_{12} = 5$ m/s.

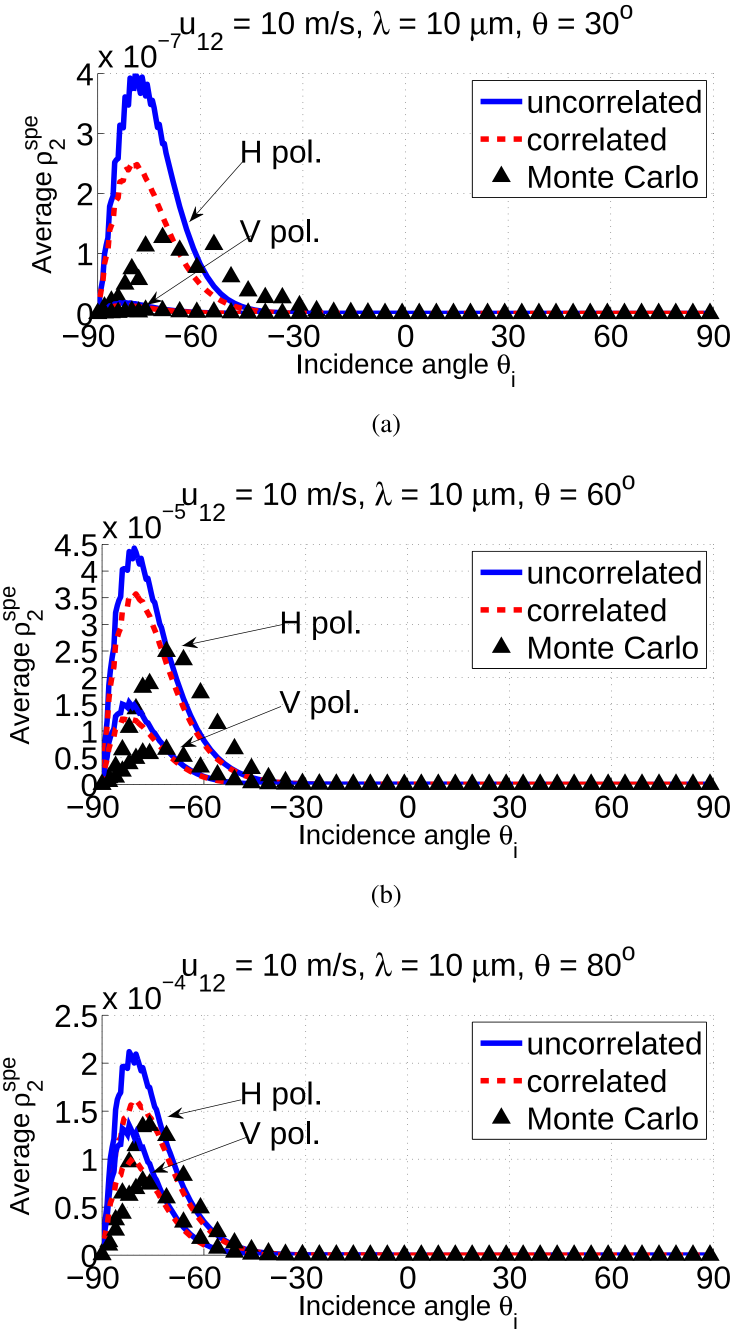

(a)

(b)

(c)

Figure 5.7: Average second-order reflectivity ρ_2^{spe} of sea surfaces versus θ_i, with the observation angle being $\theta = 30°$ in (a), $\theta = 60°$ in (b), and $\theta = 80°$ in (c). The wavelength is $\lambda = 10$ μm. The wind speed $u_{12} = 10$ m/s.

the bistatic illumination function $S_{\mathrm{B}}^{2,\mathrm{spe}}$ and the corresponding Monte Carlo ray-tracing results are found, as shown in Figs. 4.12 and 4.13. The reason may be that the slope of M_1 is not well calculated.

It is notable that the peaks of second-order reflectivity ρ_2^{spe} do not occur in the global specular directions. For $\theta = 30°$, $\rho_{2,H}^{\mathrm{spe}}$ reaches a maximum at $\theta_i \approx 60°$, and $\rho_{2,V}^{\mathrm{spe}}$ at $\theta_i \approx 80°$ although it is very small compared with $\rho_{2,H}^{\mathrm{spe}}$. For $\theta = 60°$, $\rho_{2,H}^{\mathrm{spe}}$ and $\rho_{2,V}^{\mathrm{spe}}$ both reach their maximum at $\theta_i \approx 75°$. But for $\theta = 80°$, the peak of $\rho_{2,H}^{\mathrm{spe}}$ and $\rho_{2,V}^{\mathrm{spe}}$ are found around the global specular reflection direction $\theta_i \approx -80°$. It can be concluded that double surface reflection shifts the peak of the surface reflectivity from the global specular reflection direction toward the horizon.

5.2.4.2 Hemispherical average reflectivity ρ_2^{hemi}

The hemispherical average reflectivity with two surface reflections ρ_2^{hemi} is obtained in the same way as ρ_2^{spe}, by enlarging the window function to the region $\theta_i \in [-90°, 90°]$. This window function is given by Eq. (4.23).

Fig. 5.8 shows the hemispherical average reflectivity ρ_2^{hemi} versus θ. The simulation parameters are the same as in Fig. 5.4.

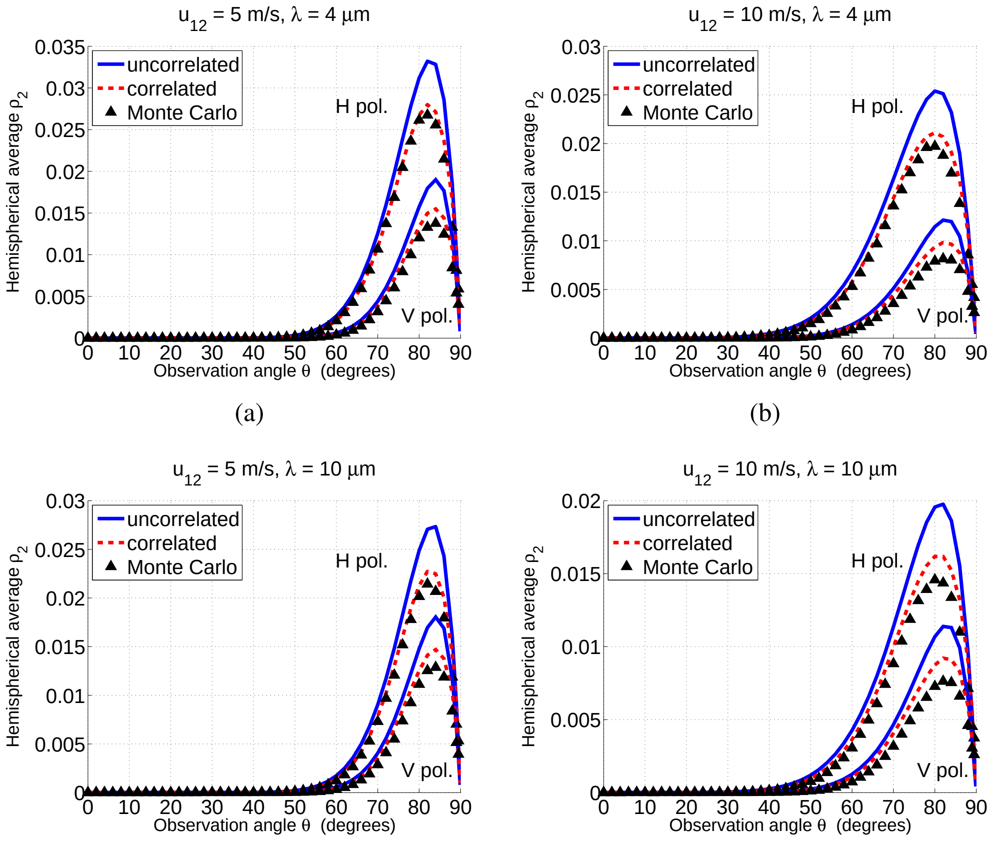

(a) (b)

(c) (d)

Figure 5.8: Hemispherical average second-order sea surface reflectivity ρ_2^{hemi} for wind speed $u_{12} = 5$ m/s (left) and $u_{12} = 10$ m/s (right), and for $\lambda = 4$ μm (up) and $\lambda = 10$ μm (down).

It is shown that the model agrees quite well with the Monte Carlo ray-tracing result. The uncorrelated model overestimates the surface reflectivity, which is largely overcome after taking into account the correlation between the surface heights and slopes. It is shown that the second-order hemispherical average surface infrared reflectivity is close to zero for small and moderate observation θ. It is relatively significant for large observation angles, e.g. $\theta > 70°$.

The second-order hemispherical average reflectivity in H polarization $\rho_{2,H}^{\text{hemi}}$ is larger than that in V polarization $\rho_{2,V}^{\text{hemi}}$. The maxima of $\rho_{2,H}^{\text{hemi}}$ are about $0.02 \sim 0.035$, while the ones of $\rho_{2,V}^{\text{hemi}}$ are smaller, about $0.01 \sim 0.02$. In general, as the wind speed increases, the lobes of ρ_2^{hemi} are wider, but the maxima are reduced.

5.2.4.3 Total surface reflectivity ρ_{tot}

The total surface reflectivity is studied in this subsection. Three and more surface reflections are neglected. As a result, the total surface reflectivity is the sum of the ones with one and two surface reflections, expressed as:

$$\rho_{\text{tot}}^{\text{spe,hemi}} = \rho_1^{\text{spe,hemi}} + \rho_2^{\text{spe,hemi}}. \tag{5.34}$$

Total average reflectivity $\rho_{\text{tot}}^{\text{spe}}$ The surface total average reflectivity $\rho_{\text{tot}}^{\text{spe}}$ is calculated. It corresponds to the bidirectional distribution of the sea surface reflectivity. It is obtained by the sum of ρ_1^{spe} and ρ_2^{spe}. The results are shown in Figs. 5.9 and 5.10, The up-wind direction is considered. Three observation angles $\theta = \{30°, 60°, 80°\}$ are studied. The wavelength is $\lambda = 10$ μm, and the wind speed u_{12} is 5 m/s in Fig. 5.9 and 10 m/s in Fig. 5.10.

Very similar results as the ones in Figs. 5.2, 5.3 (ρ_1^{spe} only) are obtained, except for the cases where $\theta = 80°$, where a significant increase is obtained. The reason is that, for $\theta = 30°$ and $60°$, the second-order average surface reflectivity ρ_2^{spe} is relatively weak. Take $u_{12} = 10$ m/s for example. The maximum of ρ_2^{spe} for $\theta = 30°$ is of the order of 10^{-7}, whereas that of ρ_2^{spe} is of the order of 10^{-5}, which is 100 times larger. As a result, in Figs. 5.9 (a) and 5.10 (a), we find almost the same results as in Figs. 5.2 (a) and 5.3 (a). For $\theta = 60°$, the same conclusion is obtained for the same reason. For $\theta = 80°$, taking into the second-order reflectivity ρ_2^{spe} significantly increase the surface total reflectivity.

In addition, very good agreements between the analytical models and the Monte Carlo ray-tracing method are obtained. The discrepancy of the second-order reflectivity between the model and the Monte Carlo ray-tracing method does not affect very much the total surface emissivity. The reason is that ρ_2^{spe} of the present model is weak compared with ρ_1^{spe}. Besides, when ρ_2^{spe} is relatively significant (e.g. for $\theta = 80°$), the present model agrees reasonable well with the Monte Carlo ray-tracing method.

Total hemispherical average reflectivity $\rho_{\text{tot}}^{\text{hemi}}$ The total hemispherical average reflectivity is the sum of the ones with one and two surface reflections. Fig. 5.11 shows the results for a wind speed $u_{12} = 5$ m/s (left) and $u_{12} = 10$ m/s (right), in H (up) and V (down) polarizations. The up-wind direction is chosen. The wavelength is $\lambda = 10$ μm. The results for $\lambda = 4$ μm is not shown, as they have a similar trend and lead to the same conclusion.

It is shown that the model is generally in good agreements with the Monte Carlo ray-tracing method. The first-order reflectivity ρ_1^{hemi} of the model overestimates the result. After taking into account the second-order reflectivity ρ_2^{hemi}, increases are found for large zenith angles, e.g. $\theta > 70°$. The present model also overestimates the total surface reflectivity for large zenith angles.

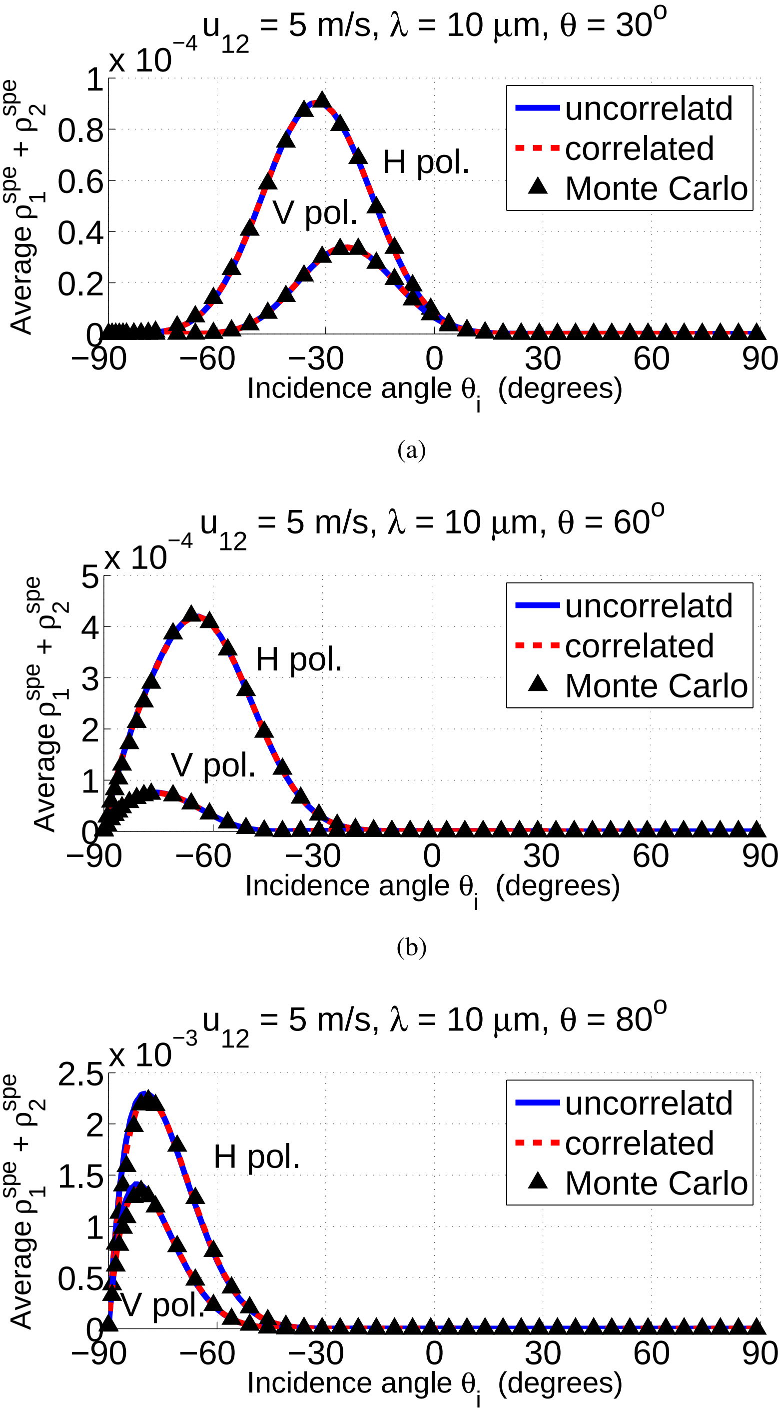

(a)

(b)

(c)

Figure 5.9: Average total reflectivity of the sea surface versus θ_i, with wavelength $\lambda = 10$ μm. The observation angle is $\theta = 30°$ in (a), $\theta = 60°$ in (b), and $\theta = 80°$ in (c). The wind speed $u_{12} = 5$ m/s.

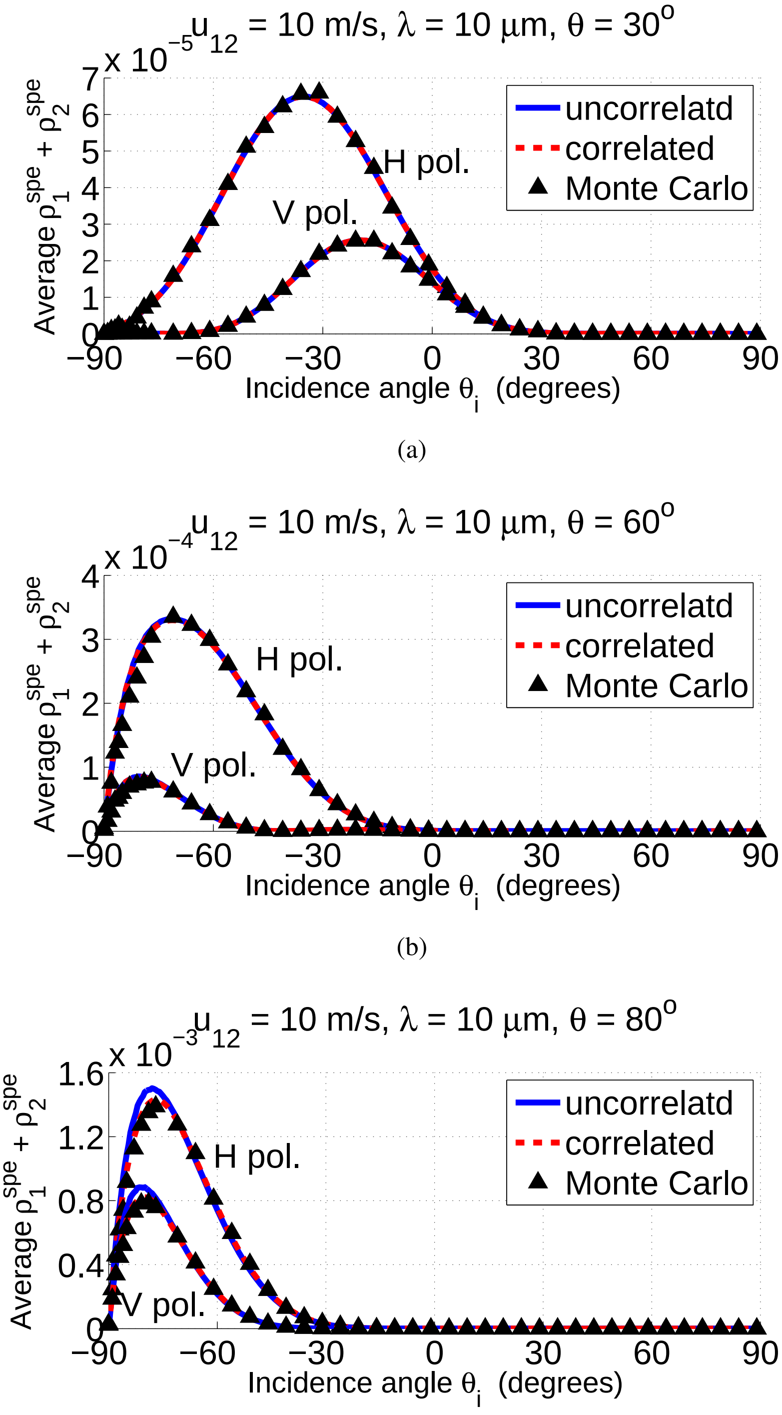

(a)

(b)

(c)

Figure 5.10: Bidirectional distribution of the polarized first-order reflectivity $\rho_1^{\rm spe}$ of the sea surface versus θ_i, with wavelength $\lambda = 10$ μm. The observation angle is $\theta = 30^\circ$ in (a), $\theta = 60^\circ$ in (b), and $\theta = 80^\circ$ in (c). The wind speed $u_{12} = 10$ m/s.

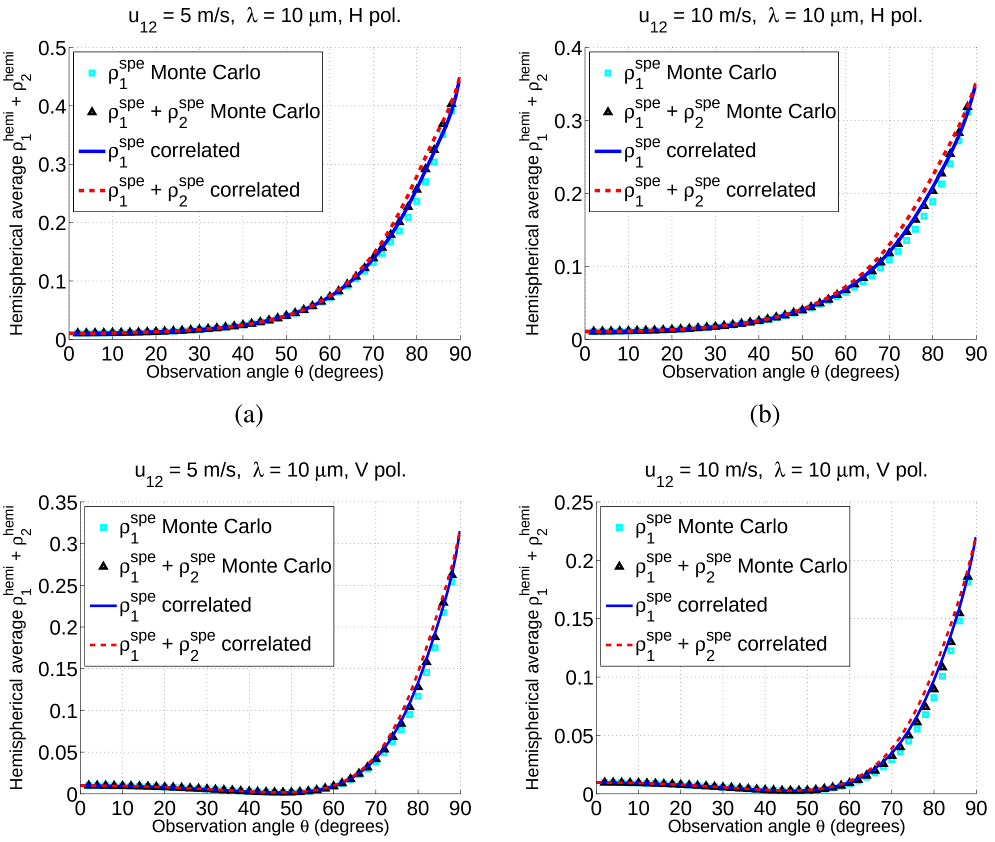

(a) (b)

(c) (d)

Figure 5.11: Total hemispherical average reflectivity of sea surfaces for wind speed $u_{12} = 5$ m/s (left) and $u_{12} = 10$ m/s (right), in H polarization (up) and in V polarization (down). The wavelength is $\lambda = 10$ μm.

5.2.4.4 Energy conservation

According to the law of energy conservation, under thermal equilibrium, the energy absorbed by the sea surface equals the energy it radiated. It is assumed that the sea surface is opaque, which means that all the energy of the refractive rays is absorbed by the sea. Then, the law of energy conservation can be expressed as that the sum of the surface emissivity and reflectivity equals 1, given by:

$$\varepsilon + \rho = 1. \tag{5.35}$$

It is reported that Eq. (5.35) is not fulfilled when only the direct emissivity ε_0 and the first-order reflectivity ρ_1^{hemi} are considered [6], with $\varepsilon_0 + \rho_1^{\text{hemi}} \leq 1$. In this subsection, Eq. (5.35) is examined, by taking into account the first-order emissivity ε_1 and the second-order reflectivity ρ_2^{hemi}.

The unpolarized emissivity and reflectivity are firstly calculated, which is the average of the ones in H and V polarizations, expressed as:

$$\varepsilon_{0,1} = \frac{\varepsilon_{0,1,H} + \varepsilon_{0,1,V}}{2} \qquad \rho_{1,2}^{\text{hemi}} = \frac{\rho_{1,2,H}^{\text{hemi}} + \rho_{1,2,V}^{\text{hemi}}}{2} \tag{5.36}$$

Fig. 5.12 shows the results for a wind speed at 12.5 m above the sea surface $u_{12} = 5$ m/s and Fig. 5.13 shows the results for $u_{12} = 10$ m/s. The wavelength is

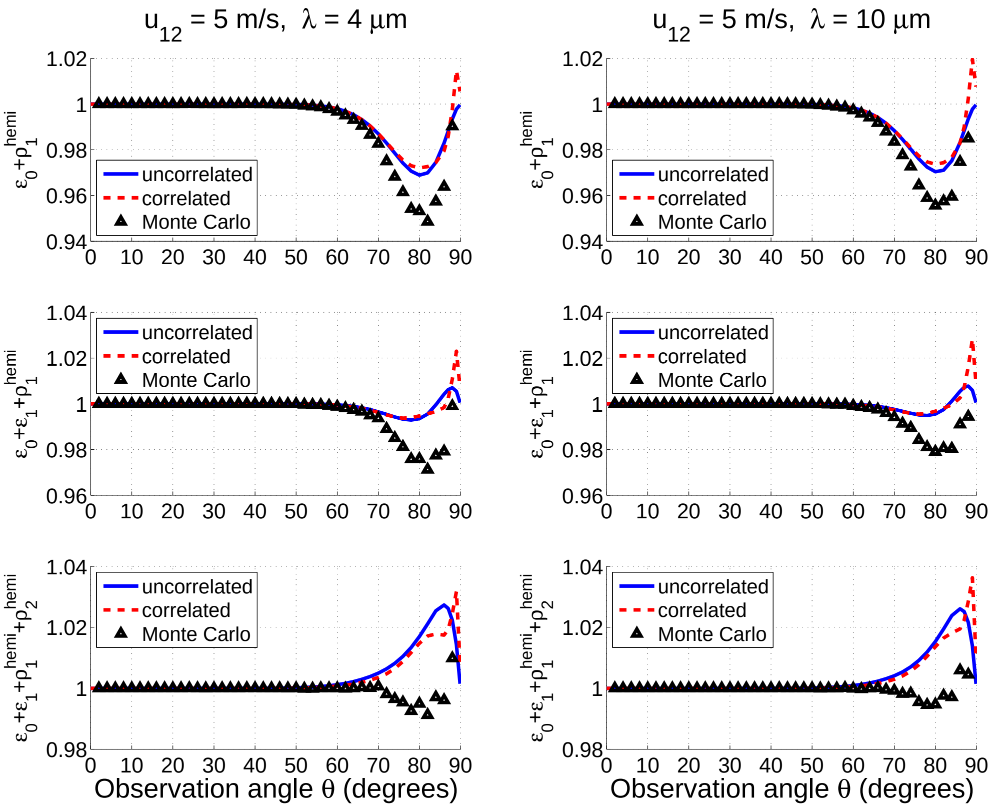

(a) (b)

Figure 5.12: Verification of the energy conservation. The sum of surface emissivity and reflectivity is shown. $\varepsilon_0 + \rho_1^{\text{hemi}}$ is firstly studied (top), then ε_1 is taken into account (middle), and last ρ_0^{hemi} is also added (bottom). $\lambda = 4$ μm on the left and $\lambda = 10$ μm on the right. The wind speed is $u_{12} = 5$ m/s.

$\lambda = 4$ μm (left) and $\lambda = 10$ μm (right). The analytical results are compared with the results of the Monte Carlo ray-tracing method. 1D surfaces are considered.

When the zero-order emissivity ε_0 and the first-order hemispherical average average reflectivity ρ_1^{hemi} are considered (top), $\varepsilon_0 + \rho_1^{\text{hemi}} = 1$ for $\theta < 50°$, which means that energy is conserved. This is because shadowing effect and surface reflections are not significant in this region (see Fig. 2.11 and Fig. 4.9). However, $\varepsilon_0 + \rho_1^{\text{hemi}} < 1$ for the region $50° < \theta < 90°$, which means that a loss of energy is found. This is because surface reflections are not considered [6]. The minimum is about 0.95 for $\theta \approx 80°$ shown by the Monte Carlo ray-tracing method, meaning that the peak of the loss of energy is about 0.05 (5% of the incident energy is "disappeared"). The analytical models, with or without considering the correlation of the surface heights and slopes, both overestimate the results, with the largest discrepancy with the Monte Carlo ray-tracing method being about 0.02 occurring for $\theta \approx 80°$. The correlated model shows a sharp peak exceeding 1 for $\theta \approx 88°$, which results from the large calculation error in calculating ε_0 when θ tends to $90°$ (see Fig. 3.4). This calculation error comes from the calculation of the correlated monostatic illumination function, which involves numerical integrations. This peak becomes the dominant error of the correlated model. For $u_{12} = 10$ m/s and $\lambda = 4$ μm, an energy gain is found for $\theta = 88°$ by the Monte Carlo ray-tracing method. This is

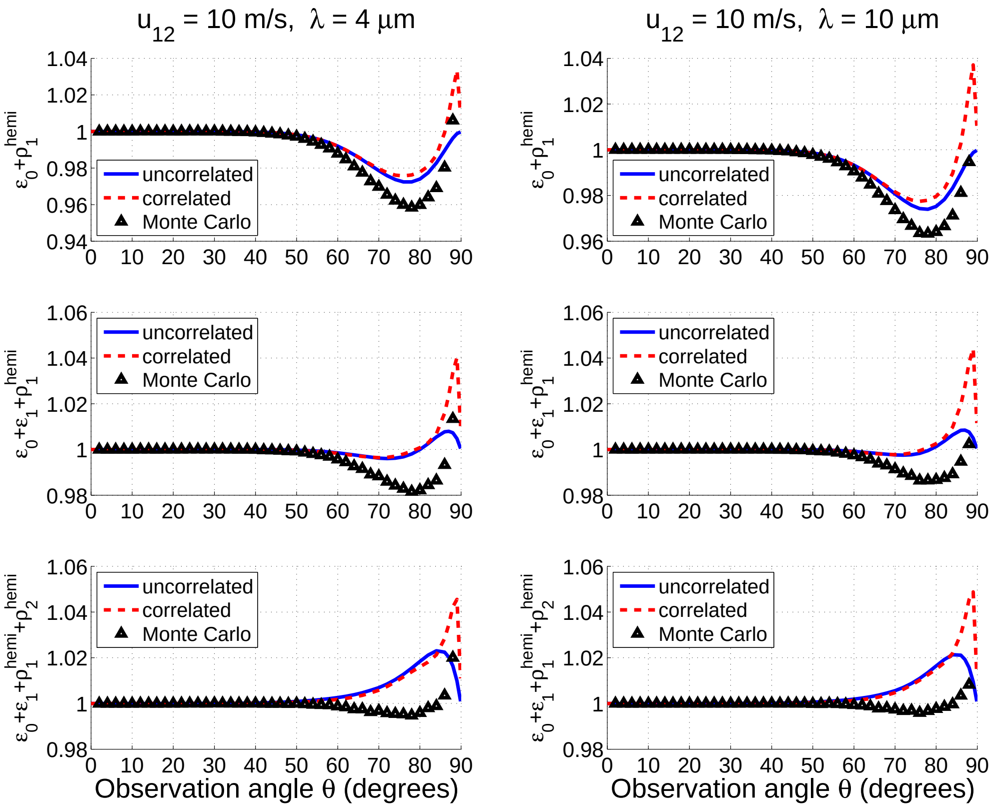

(a) (b)

Figure 5.13: Verification of the energy conservation. The sum of surface emissivity and reflectivity is shown. $\varepsilon_0 + \rho_1^{\text{hemi}}$ is firstly studied (top), then ε_1 is taken into account (middle), and last ρ_0^{hemi} is also added (bottom). $\lambda = 5$ μm on the left and $\lambda = 10$ μm on the right. The wind speed is $u_{12} = 10$ m/s.

mainly due to the error of the numerical method (lengths of generated surfaces are not infinity).

After taking into account the first-order surface emissivity ε_1 (middle), the minimum is about 0.97, with the peak of loss of energy being reduced by about 0.02. This is predictable, as the first-order emissivity ε_1 is of the order of 0.02 around $\theta = 80^\circ$ (see Fig. 3.15 and Fig. 3.16). The Monte Carlo ray-tracing method shows that an energy loss is still found, but the correlated and uncorrelated analytical models both show that energy conservation is nearly met. The uncorrelated model even shows an energy gain (larger than 1) for $\theta > 80^\circ$. However, ε_1 of the analytical models and the Monte Carlo ray-tracing method are of the same level. The difference of the sum $\varepsilon_0 + \rho_1^{\text{hemi}} + \varepsilon_1$ (middle) is mainly contributed by that of $\varepsilon_0 + \rho_1^{\text{hemi}}$ (top). Energy gain is predicted by the Monte Carlo ray-tracing method for $\theta = 88^\circ$ $u_{12} = 10$ m/s and $\lambda = \{4, 10\}$ μm $\theta = 88^\circ$ because of the error of the numerical method.

Then, the second-order surface reflectivity ρ_2^{hemi} is taken into account (bottom). It is shown by the Monte Carlo ray-tracing method that an energy loss is still predicted, with a minimum of about 0.995, which is also raised by about 0.02 compared with $\varepsilon_0 + \rho_1^{\text{hemi}} + \varepsilon_1$. The correlated and uncorrelated analytical models both suggest an energy gain (the sum is larger than 1), which is mainly due to the overestimation of $\varepsilon_0 + \rho_1^{\rm hemi}$ shown in the top sub-figure. The result of the uncorrelated model is larger than that of the correlated one, because $\rho_2^{\rm hemi}$ of the uncorrelated model is overestimated (see Fig. 5.8). The Monte Carlo ray-tracing method also shows an energy gain for $\theta = \{86°, 88°\}$ for both wind speeds and both wavelengths, which results from the error of the numerical method.

In general, taking into account multiple surface reflections shows that energy conservation is better fulfilled. The error of the analytical models results mainly from the overestimation of the zero-order surface emissivity ε_0 and the first-order hemispherical average surface reflectivity $\rho_1^{\rm hemi}$.

5.3 Conclusion

In this chapter, sea surface polarized reflectivity ρ is calculated by using bistatic illumination functions. Firstly, sea surface reflectivity with one reflection ρ_1 (first-order) is derived. The results for 1D surfaces are compared with a Monte Carlo ray-tracing method. Very good agreements are obtained for both the first-order average reflectivity $\rho_1^{\rm spe}(\theta_i, \theta)$ and the first-order hemispherical average reflectivity $\rho_1^{\rm hemi}(\theta)$. Then, the sea surface reflectivity with two surface reflections ρ_2 (second-order) is derived. The results for 1D surfaces are also compared with a Monte Carlo ray-tracing method. It is shown that the second-order average reflectivity $\rho_2^{\rm spe}$ does not predict well the distribution of the reflectivity versus θ_i and θ. However, $\rho_2^{\rm spe}$ is weak compared with $\rho_1^{\rm spe}$, and the total average reflectivity $\rho_1^{\rm spe} + \rho_2^{\rm spe}$ agrees very well with the Monte Carlo ray-tracing method. The second-order hemispherical average reflectivity $\rho_2^{\rm hemi}$ agrees quite well with the Monte Carlo ray-tracing method. Then, the energy conservation is examined by summing up the zero-order emissivity ε_0, the first-order emissivity ε_1, the first-order hemispherical average reflectivity $\rho_1^{\rm hemi}$ and the hemispherical average second-order reflectivity $\rho_2^{\rm hemi}$. It is shown that an energy loss is predicted if only zero-order emissivity ε_0 and first-order reflectivity $\rho_1^{\rm hemi}$ are considered ($\varepsilon_0 + \rho_1^{\rm hemi} \leq 1$), which is also reported by Yoshimori *et al.* [6]. The energy loss is due to neglecting the surface reflections. It is shown in thesis that by taking into the first-order emissivity ε_1 and the second-order reflectivity $\rho_2^{\rm hemi}$, the law of energy conservation is better met. The cross-polarization effect is not studied here, which involves 2D surfaces. This is left for future research.

6

Conclusion

Emissivity ε and reflectivity ρ are both dimensionless quantities ranging from 0 to 1. Emissivity is the measure of an object's ability to radiate absorbed energy. It equals the rate of energy absorption under thermal equilibrium for an opaque body (no energy is transmitted through the object), with $\varepsilon = 1$ being a perfect absorber or emitter (black body). Reflectivity relates to the rate of energy reflection, with $\rho = 1$ being a perfect reflector. According to the law of energy conservation, the sum of absorbed energy and reflected energy equals the incident energy, which implies:

$$\varepsilon + \rho^{\text{hemi}} = 1.$$

Sea surface emissivity and reflectivity are important parameters in oceanic remote sensing, for example, for deriving the sea surface temperature, estimating the sun glitter, detecting pollutions, etc. In application, their accuracy is of great importance [1, 37]. The aim of this thesis is to calculate the sea surface emissivity and reflectivity in the infrared atmospheric transmission windows ($\lambda \in [3, 5]$ and $\lambda \in [8, 12]$ μm) with accuracy.

Sea surface emissivity and reflectivity are both nearly constant for observation directions near zenith (small zenith angles θ), but they vary largely for high grazing angles (large zenith angles θ) because of the surface roughness [32, 10]. The appearance of sea waves leads to the shadowing effect and the surface reflections, which increases the difficulty in the prediction of sea surface emissivity and reflectivity. As a result, the accurate modeling of the sea surface emissivity and reflectivity have to be carried out by taking these two phenomena into account.

In the infrared atmospheric transmission windows, geometrical optics approximation is assumed to be valid, because the infrared wavelengths are small enough compared with the sea surface roughness. The sea surface is assumed to be single valued, which means that breaking waves are not considered. Besides, white caps are not dealt with. The sea surface is modeled as a ergodic random process. The probability density functions (PDFs) of the sea surface heights and slopes are firstly assumed to be Gaussian. Then, the skewness and kurtosis effects are considered [17]. The correlation between the surface heights ans slopes are taken into account by a Gaussian height auto-correlation function [26, 20].

In Chap. 2, the monostatic illumination function is studied, which corresponds to the intrinsic thermal radiation of the sea surface. The monostatic illumination function S_{M}^{0} of Smith [25] is adopted to deal with the shadowing effect. It is shown that shadowing does not show up ($S_{\mathrm{M}}^{0} = 0$) for observation directions near zenith (small zenith angle θ). But it is significant for grazing observation angles (large zenith angle θ, observation direction near the horizon). For an observation direction at the horizon (zenith angle $\theta = 90°$), $S_{\mathrm{M}}^{0} = 0$, meaning that all the surface is in the shadow of the receiver. An illumination function with one surface reflection S_{M}^{1} (first-order) is developed to deal with the surface reflection effect, which is significant for large zenith angles θ. The results show a good agreement with a Monte Carlo ray-tracing method. As the surface root mean square (RMS) slope increases, surface reflections become more and more significant for any zenith angle θ.

In Chap. 3, the sea surface infrared emissivity is calculated with the monostatic illumination functions developed in Chap. 2. The zero-order sea surface infrared emissivity is firstly studied by using the associated monostatic zero-order illumination function S_{M}^{0}. The sea surface is modeled as one-dimensional (1D surfaces, 2D problems) and then two-dimensional (2D surfaces, 3D problems). Polarization is also considered. It is shown that zero-order sea surface infrared emissivity ε_0 heavily depends on the wind speed and direction. As the wind speed increases, ε_0 significantly increases for large zenith angles (e.g. $\theta > 70°$). Besides, ε_0 is always larger in vertical polarization than in horizontal polarization, which means that the intrinsic infrared radiation of the sea surface is partially polarized. Cross-polarization (projection of local to global polarization directions) of ε_0 is significant for small zenith angles $\theta < 30°$, but is very weak for larger θ.

Then, one surface reflection is taken into account, and the sea surface infrared emissivity with one surface reflection ε_1 (first-order) is calculated by using the first-order monostatic illumination function S_{M}^{1}. It is shown that the first-order infrared emissivity ε_1 is significant for large zenith angles (e.g. $\theta > 50°$). The maximum contribution of ε_1 is found for $\theta \approx 80°$, with a value about 0.025. Cross-polarization of ε_1 is always weak for any zenith angle θ. Besides, considering one surface reflection reduces the magnitude of the degree of polarization of the surface infrared emissivity, meaning that the surface intrinsic infrared radiation is less polarized.

The skewness and the kurtosis effects are studied for both ε_0 and ε_1. It is shown that the skewness and the kurtosis effects are significant only for very large zenith angles (e.g. $\theta > 80°$). The surface emissivity with Gaussian surface slope PDF is symmetrical about the up-, down- and cross-wind directions. After taking account the kurtosis effect, this symmetry property still holds. However, after taking into account the skewness effect, the surface emissivity is symmetrical only about the up- and down-wind directions.

The results of the sea surface infrared emissivity are compared with measurements [37, 38]. It is shown that the zero-order emissivity ε_0 underestimates the sea surface emissivity for large zenith angles (65° in [38] and 73.5° in [37]). Taking into account one surface reflection reduces the underestimation.

From the beginning of Chap. 4, sea surface reflectivity is considered. The bistatic illumination function is studied in Chap. 4, which is an important parameter in the calculation of sea surface reflectivity. The bistatic illumination function of Smith [32] S_{B}^{1} is adopted to deal with one surface reflection, and a new model S_{B}^{2} is developed to take into account two surface reflections. The results are compared with a Monte Carlo ray-tracing method. It is shown that the Smith bistatic illumination function with one surface reflection S_{B}^{1} agrees very well with the Monte Carlo ray-tracing method. The bistatic illumination function with two surface reflections S_{B}^{2} does not predict very well the distribution of the directions of the reflected rays after two reflections, with a shift from the global specular direction toward the horizon. However, the hemispherical average of S_{B}^{2} agrees quite well with the Monte Carlo ray-tracing method, with a slight overestimation.

In Chap. 5, the sea surface reflectivity ρ is derived. Firstly, the sea surface reflectivity with one surface reflection ρ_1 is calculated by using the first-order bistatic illumination function S_{B}^{1}. The result agrees very well with the Monte Carlo ray-tracing method. Then two surface reflections are considered. Compared with a Monte Carlo ray-tracing method, the directional second-order reflectivity is not well predicted. However, the second-order hemispherical average reflectivity agrees well with the Monte Carlo ray-tracing method, especially when the correlation between the surface heights and slopes is considered.

Energy conservation is examined by summing up the sea surface emissivity and hemispherical average reflectivity. As mentioned previously, the sum should equal 1 according to the law of energy conservation. It is shown that when the zero-order emissivity ε_0 and the first-order hemispherical average reflectivity ρ_1^{hemi} are considered, an energy loss is found for large zenith angles θ, which is due to neglecting the surface reflections [6]. After taking into account the first-order emissivity ε_1 and the second-order hemispherical average reflectivity ρ_2^{hemi}, the law of energy conservation is better met. Because of the overestimation of the analytical models, an energy gain is reported, which is due to the error of calculation and the inaccuracy in modeling.

Several prospects to this work can be listed. First of all, cross-polarization of the surface reflectivity can be studied. Indeed, in Chap. 5, 1D surfaces are considered for simplicity, which does not involve cross-polarization. Cross-polarization can be interesting. It is not studied in this thesis because of the lack of time. The next step of this work is to calculate the reflectivity of 2D surfaces.

Secondly, more attention should be devoted to the second-order bistatic illumination function. The model presented here does not predict well the distribution of the direction of the reflected ray after two reflections, which is the main reason for the fact that the corresponding reflectivity does not agree well with the Monte Carlo method.

Thirdly, white caps and breaking waves of sea surfaces are not considered. In other words, the present model is valid only for sea surfaces with small to moderate wind speeds. As the wind speed increases, white caps show up, as well as breaking waves. These phenomena increase the difficulty in modeling the illumination functions.

Last but not least, the error of calculation of the zero-order emissivity ε_0 for θ close to 90° should be reduced. This error mainly results from the calculation of the correlated illumination function. Efforts have already been devoted to this subject in the simulations of this thesis, such as reducing the intervals in the numerical integrations. However, as the numerical calculation sometimes involves dividing very small numbers, the calculation must be rearranged carefully.

A

Non Gaussian Λ and Λ^-

Bourlier *et al.* [32] developed analytically the non-Gaussian marginal slope PDF of the sea surface basing on the slope PDF of Cox & Munk [17]. The integrations over the slopes in Eq. (2.20) for $\Lambda(\mu)$ and in Eq. (2.69) for $\Lambda^-(\mu_1)$ are then calculated analytically.

The integration result of the function $\Lambda(\mu)$ (Eq. (2.20)) is given by Bourlier *et al.* [32]:

$$\Lambda = \Lambda_G + \alpha_S \Lambda_S + \alpha_K \Lambda_K, \tag{A.1}$$

where

$$\begin{aligned}
\upsilon &= \frac{\mu}{\sigma_X \sqrt{2}}, \\
\Lambda_G &= \frac{\exp(-\upsilon^2) - \upsilon\sqrt{\pi}\text{erfc}(\upsilon)}{2\upsilon\sqrt{\pi}}, \\
\Lambda_S &= -\frac{\exp(-\upsilon^2)}{3\sqrt{2\pi}}, \\
\Lambda_K &= \frac{(2\upsilon^2 - 1)\exp(-\upsilon^2)}{6\upsilon\sqrt{\pi}}, \\
\alpha_S &= [c_{03}(\sigma_x \cos\phi)^2 + 3c_{21}(\sigma_y \sin\phi)^2] \\
&\quad \times(-\sigma_X \cos\phi)/(2\sigma_X^3), \\
\alpha_K &= \left[c_{04}(\sigma_x \cos\phi)^4 + c_{40}(\sigma_y \sin\phi)^4\right. \\
&\quad \left.+1.5c_{22}\sigma_x^2\sigma_y^2 \sin^2(2\phi)\right]/(8\sigma_X^4).
\end{aligned} \tag{A.2}$$

Subscripts G, S and K denote "Gaussian", "skewness" and "kurtosis", respectively, and $\text{erfc}(\upsilon)$ is the complementary error function, and c_{21}, c_{03}, c_{04}, c_{40}, c_{22} are the skewness and kurtosis coefficients derived by Cox & Munk [17]. σ_x, σ_y and σ_X are the RMS slope of the sea surface with respect to the x, y and X directions, respectively, which is related to the wind speed u_{12} at 12.5 m above the sea surface as [17, 32]:

$$\begin{aligned}
\sigma_x^2 &= 3.16u_{12} \times 10^{-3}, \\
\sigma_y^2 &= 1.92u_{12} \times 10^{-3} + 0.003, \\
\sigma_X^2 &= (\sigma_x \cos\phi)^2 + (\sigma_y \sin\phi)^2.
\end{aligned} \tag{A.3}$$

The non-Gaussian surface slope PDF along the direction X' can be obtained in the same way as that along X. Then, $\Lambda^-(\mu_1)$ (Eq. 2.69) with non-Gaussian slope

PDF is given by:

$$\Lambda^{-} = \Lambda_G^{-} + \alpha_S \Lambda_S^{-} + \alpha_K \Lambda_K^{-}, \tag{A.4}$$

where

$$\begin{array}{rcl} \Lambda_G^{-} & = & -1 - \Lambda_G, \\ \Lambda_S^{-} & = & -\Lambda_S, \\ \Lambda_K^{-} & = & -\Lambda_K. \end{array} \tag{A.5}$$

$\Lambda(\mu)$ and $\Lambda^{-}(\mu_1)$ with Gaussian slope PDF can be obtained by setting $\alpha_S = \alpha_K = 0$.

B

Correlated g

By substituting Eq. (1.17) into Eqs. (2.18), Bourlier *et al.* obtained the analytical expression of $g_{\mathrm{W}}^{\mathrm{co}}$ given by [20, 26]:

$$g_{\mathrm{W}}^{\mathrm{co}} = \frac{\sigma_{\gamma X}\sigma_{\zeta}\exp[-D-\mu(\mu A+2D)]}{4\pi A\sqrt{[|\,[C]\,|]}}\left[1-\exp(\kappa^2)\kappa\sqrt{\pi}\mathrm{erfc}(\kappa)\right], \qquad \text{(B.1)}$$

where

$$\begin{aligned}
A &= \frac{C_{i33}}{2\,|\,[C]\,|}, \qquad B = \frac{\zeta_0 C_{i14} - \zeta C_{i13} + \gamma_X C_{i34}}{2\,|\,[C]\,|} \qquad \zeta = \zeta_0 + \mu\tau, \\
D &= \frac{(\zeta_0^2+\zeta^2)C_{i11} + 2\zeta_0\zeta C_{i12} + 2\gamma_0(\zeta_0 C_{i13} - \zeta C_{i14}) + \gamma_X^2 C_{i13}}{2\,|\,[C]\,|} \\
&\quad -\frac{\zeta_0^2}{2\sigma_\zeta^2} - \frac{\gamma_X^2}{2\sigma_{\gamma X}^2},
\end{aligned} \qquad \text{(B.2)}$$

with the first index i in C_{inm} denoting the elements of the inverse matrix of $[C]$ (see Sec. 1.1.4.2). In the same way, the correlated $g_{\mathrm{S}}^{\mathrm{co}}$ is given by [20, 26]:

$$\begin{aligned}
g_{\mathrm{S}}^{\mathrm{co}} &= \frac{1}{\pi}\sqrt{\frac{A_1}{A}}\frac{\exp[-D-\mu(\mu A+2B)] - \dfrac{\zeta_0^2}{2\sigma_\zeta^2} - \dfrac{\gamma_X^2}{2\sigma_{\gamma X}^2}}{\exp\left(\dfrac{B_1^2}{A_1} - D_1\right)\mathrm{erf}\left(\dfrac{A_1\zeta + B_1}{\sqrt{A_1}}\right) + 1} \\
&\quad \times[1-\exp(\kappa^2)\kappa\sqrt{\pi}\mathrm{erfc}(\kappa)],
\end{aligned} \qquad \text{(B.3)}$$

where

$$\begin{aligned}
A_1 &= (C_{i11}C_{i33} - C_{i13}^2)E_1 \qquad E_1 = 1/(2C_{i33}\,|\,[C]\,|), \\
B_1 &= [\zeta_0(C_{i12}C_{i33} + C_{i14}C_{i13}) + \gamma_X(C_{i13}C_{i34} - C_{i14}C_{i33})]E_1, \\
D_1 &= [\zeta_0^2(C_{i11}C_{i33} - C_{i14}^2) + \gamma_X^2(C_{i33}^2 - C_{i34}^2) \\
&\quad +2\zeta_0\gamma_X(C_{i13}C_{i33} - C_{i14}C_{i34})]E_1.
\end{aligned} \qquad \text{(B.4)}$$

To further simplify Eqs. (B.1) and (B.3), the following changes of variables is performed:

$$R_0 = \sigma_\zeta^2 f_0 \qquad R_1 = -\sigma_{\gamma X}\sigma_\zeta f_1 \qquad R_2 = -\sigma_{\gamma X}^2 f_2. \qquad \text{(B.5)}$$

The elements of the inverse matrix of $[C]$ can be expressed as [26]:

$$\begin{array}{lll}
\dfrac{C_{i11}}{2\mid[C]\mid}=\dfrac{1}{2\sigma_\zeta^2}\dfrac{f_{11}}{f_M} & \dfrac{C_{i33}}{2\mid[C]\mid}=\dfrac{1}{2\sigma_{\gamma_X}^2}\dfrac{f_{33}}{f_M} & \dfrac{C_{i13}}{2\mid[C]\mid}=\dfrac{1}{2\sigma_\zeta\sigma_{\gamma_X}}\dfrac{f_{13}}{f_M}\\
\dfrac{C_{i12}}{2\mid[C]\mid}=\dfrac{1}{2\sigma_\zeta^2}\dfrac{f_{12}}{f_M} & \dfrac{C_{i34}}{2\mid[C]\mid}=\dfrac{1}{2\sigma_\sigma^2}\dfrac{f_{34}}{f_M} & \dfrac{C_{i14}}{2\mid[C]\mid}=\dfrac{1}{2\sigma_\zeta\sigma_{\gamma_X}}\dfrac{f_{14}}{f_M}\\
\mid[C]\mid=f_M(\sigma_\zeta\sigma_{\gamma_X})^4, & &
\end{array} \tag{B.6}$$

with

$$\begin{array}{lll}
f_{11}=1-f_2^2+f_1^2 & f_{33}=1-f_0^2-f_1^2 & f_{12}=f_1(f_0-f_2)\\
f_{12}=f_0f_2^2+f_1^2f_2-f_0 & f_{34}=f_0^2f_2+f_1^2f_0-f_2 & \\
f_{14}=f_1(1-f_1^2-f_0f_2) & f_M=(f_{33}^2-f_{34}^2)/(1-f_0^2). &
\end{array} \tag{B.7}$$

Together with the following changes of variables:

$$h_0=\frac{\zeta_0}{\sqrt{2}\sigma_\zeta}\qquad s_0=\frac{\gamma_X}{\sqrt{2}\sigma_{\gamma_X}}\qquad y=\frac{\tau}{L_c}\qquad \nu=\frac{\mu}{\sqrt{2}\sigma_{\gamma_X}}, \tag{B.8}$$

the correlated $g^{\mathrm{co}}_{\mathrm{W,S}}$ are presented in Tab. B.1, together with the correlated statistical illumination function. where y_tL_c is distance beyond which correlation can be neglected. Bourlier *et al.* indicated that $y_t=3$ is precise enough [26].

Table B.1: Wagner and Smith monostatic illumination function for a correlated Gaussian process.

Statistical illumination function	$S(\nu, h_0, s_0, y) = \Upsilon(\nu - s_0) \exp\left[-L_c \int_0^{y_t} g_{\mathrm{W,S}}^{\mathrm{co}} \, \mathrm{d}y + G_{W,S}\right]$
Wagner $L_c g_{\mathrm{W}}^{\mathrm{co}}$	$\frac{\eta\sqrt{f_M}}{2\pi f_{33}} \exp\left[-D - \nu(\nu A + 2B)\right] \left[1 - \exp(\kappa^2)\kappa\sqrt{\pi}\mathrm{erfc}(\kappa)\right]$ $\kappa = (B + \nu A)/\sqrt{A} \qquad \eta = \sigma_{\gamma_X} L_c/\sigma_\zeta = \sqrt{2}$ (Gaussian autocorrelation) $D = \frac{(h_0^2 + h^2) f_{11} + 2h_0 h f_{12} + 2s_0(h_0 f_{13} - h f_{14}) + s_0^2 f_{33}}{f_M} - h_0^2 - s_0^2$ $\nu(\nu A + 2B) = \frac{\nu^2 f_{33} + 2\nu(f_{34} s_0 + h_0 f_{14} - h f_{13})}{f_M} \qquad h = h_0 + y\nu\eta$ $\kappa = \frac{h_0 f_{14} - h f_{13} + s_0 f_{34} + \nu f_{33}}{\sqrt{f_{33} f_M}}$
Wagner G_W	$\Lambda(\nu)\mathrm{erfc}\frac{h_0 + y_t\nu\eta}{2}$
Smith $L_c g_{\mathrm{S}}^{\mathrm{co}}$	$\frac{\eta}{\pi} \frac{\sqrt{f_{11} f_{33} - f_{13}^2}}{f_{33}} \frac{\exp\left[-D - \nu(\nu A + 2B) - h_0^2 - s_0^2\right]\left[1 - \exp(\kappa^2)\kappa\sqrt{\pi}\mathrm{erfc}(\kappa)\right]}{\exp\left(\frac{B_1^2}{A_1} - D_1\right)\left[1 - \mathrm{erf}\left(\sqrt{A_1} h + \frac{B_1}{\sqrt{A_1}}\right)\right]}$ $D_1 = h_0^2 \frac{f_{11} f_{33} - f_{14}^2}{f_{33} f_M} + s_0^2 \frac{f_{33}^2 - f_{34}^2}{f_{33} f_M} + 2h_0 s_0 \frac{f_{13} f_{33} - f_{14} f_{34}}{f_{33} f_M}$ $\frac{B_1}{\sqrt{A_1}} = \frac{h_0(f_{12} f_{33} + f_{14} f_{13}) + s_0(f_{13} f_{34} - f_{14} f_{33})}{\sqrt{f_{33} f_M (f_{11} f_{33} - f_{13}^2)}}$ $\sqrt{A_1} = \sqrt{\frac{f_{11} f_{33} - f_{13}^2}{f_{33} f_M}}$
Smith G_S	$-\ln\left[1 - \mathrm{erfc}\frac{h_0 + y_t\nu\eta}{2}\right]$

C

Correlated g^-

For rays with slope μ_1 propagating toward the negative side of the X' direction, the conditional probability g^- is given by:

$$g^-(\mu_1|\gamma_{X'},\zeta_0;\tau) = \frac{\displaystyle\int_{-\infty}^{\mu_1} (\mu_1-\gamma)p(\zeta=\zeta_0+\mu_1\tau,\gamma|\zeta_0,\gamma_{X'};\tau)\mathrm{d}\gamma}{\displaystyle\int_{-\infty}^{\infty}\int_{-\infty}^{\zeta_0+\mu_1\tau} p(\zeta,\gamma|\zeta_0,\gamma_{X'};\tau)\,\mathrm{d}\gamma\,\mathrm{d}\zeta}, \tag{C.1}$$

With the neglect of the correlation between heights and slopes of different points, Eq. C.1 is simplified as:

$$g^-(\mu_1) = -\mu_1\Lambda^-(\mu_1)\frac{p_\zeta(\zeta=\zeta_0+\mu_1\tau)}{F(\zeta=\zeta_0+\mu_1\tau)}, \tag{C.2}$$

where

$$\Lambda^-(\mu_1) = \frac{1}{\mu_1}\int_{-\infty}^{\mu_1}(\gamma-\mu_1)p_\gamma(\gamma)\,\mathrm{d}\gamma. \tag{C.3}$$

For case 1 shown in Fig. 2.14, $\mu_1 > 0$ thus $\Lambda^-(\mu_1) < 0$ and $-\Lambda^-(\mu_1) > 0$. The integration over $\tau \in (-\infty, 0)$ is given by:

$$\begin{aligned}\int_{-\infty}^{0} g^-(\mu_1)\,\mathrm{d}\tau &= -\mu_1\Lambda^-(\mu_1)\int_{-\infty}^{0}\frac{p_\zeta(\zeta=\zeta_0+\mu_1\tau)}{F(\zeta=\zeta_0+\mu_1\tau)}\,\mathrm{d}\tau\\ &= -\Lambda^-(\mu_1)\,[\ln(F(\zeta_0)) - \ln(F(-\infty))]\\ &= -\Lambda^-(\mu_1)(+\infty)\\ &= +\infty\end{aligned} \tag{C.4}$$

Thus, from Eq. (2.65), the conditional probability $p(b|a)$ is given by:

$$p(b|a) = \exp\left[-\int_{-\infty}^{0} g^-(\mu_1)\,\mathrm{d}\tau\right] = \exp(-\infty) = 0. \tag{C.5}$$

For case 2 shown in Fig. 2.14, $\mu_1 < 0$. The integration over $\tau \in (-\infty, 0)$ is given by:

$$\begin{aligned}\int_{-\infty}^{0} g^-(\mu_1)\,\mathrm{d}\tau &= -\mu_1\Lambda^-(\mu_1)\int_{-\infty}^{0}\frac{p_\zeta(\zeta=\zeta_0+\mu_1\tau)}{F(\zeta=\zeta_0+\mu_1\tau)}\,\mathrm{d}\tau\\ &= -\Lambda^-(\mu_1)\,[\ln(F(\zeta_0)) - \ln(F(+\infty))]\\ &= -\Lambda^-(\mu_1)\ln(F(\zeta_0))\end{aligned} \tag{C.6}$$

Thus, from Eq. (2.65), the conditional probability $p(b|a)$ is given by:

$$p(b|a) = \exp\left[-\int_{-\infty}^{0} g^-(\mu_1)\,\mathrm{d}\tau\right] = \exp\left[\Lambda^-(\mu_1)\ln(F(\zeta_0))\right] = F(\zeta_0)^{\Lambda^-(\mu_1)}. \tag{C.7}$$

D

Least square method

The least square method is a standard approach to the approximate solution of overdetermined systems, i.e., sets of equations in which there are more equations than unknowns. The least square method is used to calculate the parameter C when calculating the empirical factor in Eq. (2.82). The solution of a linear least square problem is well known. But as the empirical factor defined in Eq. (2.82) is not a linear problem with respect to ν, it is firstly modified to a linear form, given by:

$$\begin{aligned} f &= (B-1)\exp\left[-C(\nu - s_0)\right] + 1, \\ 1 - f &= (1-B)\exp[C(s_0 - \nu)], \\ \ln(1-f) &= \ln(1-B) + C(s_0 - \nu), \\ \ln(1-f) - \ln(1-B) &= (s_0 - \nu)C. \end{aligned} \tag{D.1}$$

Here a linear form is obtained. The solution for a linear least square problem

$$y = Mx \tag{D.2}$$

is given by:

$$x = [M^T M]^{-1} M^T y. \tag{D.3}$$

Here, $M = s_0 - \nu$ and $y = \ln(1-f) - \ln(1-B)$.

E

Index of refraction of water

This thesis uses the complex index of refraction of water given by Hale $\&$ Querry [49]. It consists of a real part which corresponds to the index of refraction of water $n(\lambda)$, and an imaginary part which corresponds to the extinction coefficient $k(\lambda)$. The complex index of refraction is given by

$$\widetilde{n}(\lambda) = n(\lambda) - k(\lambda), \tag{E.1}$$

where λ is the wavelength of the incident ray.

The index of refraction of water $n(\lambda)$ and the extinction coefficient $k(\lambda)$ used in this thesis are listed in Table E.1. Note that these values are obtained for pure water at $25°C$ [49].

Table E.1: Complex index of refraction of water given by Hale $\&$ Querry.

$\lambda(\mu m)$	$k(\lambda)$	$n(\lambda)$	$\lambda(\mu m)$	$k(\lambda)$	$n(\lambda)$	$\lambda(\mu m)$	$k(\lambda)$	$n(\lambda)$
4.0	0.0046	1.351	8.0	0.0343	1.291	8.2	0.0351	1.286
8.4	0.0361	1.281	8.6	0.0372	1.275	8.8	0.0385	1.269
9.0	0.0399	1.262	9.2	0.0415	1.255	9.4	0.0433	1.247
9.6	0.0454	1.239	9.8	0.0479	1.229	10.0	0.0508	1.218
10.5	0.0662	1.185	11.0	0.0968	1.153	12.0	0.199	1.111
12.5	0.259	1.123	13.0	0.305	1.146	13.5	0.343	1.177

F

Rotation angles α and β

F.1 Derivation of α

The angle α is the one between the vectors $\hat{u}_V$ and $\hat{u}_{v_0}$. By definition, the vector $\hat{u}_{v_0}$ of the local vertical polarization direction belongs to the local incidence plane defined by the local normal $\hat{n}_0$ and the observation direction $\hat{s}$, and it is perpendicular to $\hat{s}$. As a result, $\hat{u}_{v_0}$ is in the same direction as the perpendicular projection of the local normal $\hat{n}_0$ to the plane perpendicular to $\hat{s}$ (the green plane in Fig. 3.7)

To derive α, a new system of coordinates (x', y', z') is defined, with $\hat{u}_H$, $\hat{u}_V$, $\hat{s}$ being the positive x', z' and y' directions, respectively.

The system of coordinates (x', y', z') can be obtained by rotating firstly (x, y, z) along $\hat{z}$ clockwise through an angle $90° - \phi$, then along the new $\hat{x}'$ anticlockwise through an angle $90° - \theta$. As a result, the normal $\hat{n}_0$ in (x', y', z') is expressed as:

$$\hat{n}'_0 = R_x(90° - \theta) R_z(\phi - 90°) \hat{n}_0, \tag{F.1}$$

where $R_x(\vartheta)$ and $R_z(\vartheta)$ are the rotation matries, given by:

$$\begin{aligned} R_x(\vartheta) &= \begin{bmatrix} 1 & 0 & 0 \\ 0 & \cos\vartheta & -\sin\vartheta \\ 0 & \sin\vartheta & \cos\vartheta \end{bmatrix}, \\ R_z(\vartheta) &= \begin{bmatrix} \cos\vartheta & -\sin\vartheta & 0 \\ \sin\vartheta & \cos\vartheta & 0 \\ 0 & 0 & 1 \end{bmatrix}. \end{aligned} \tag{F.2}$$

The angle α becomes the one between $\hat{z}'$ and the projection of $\hat{n}'_0$ onto the $x'z'$ plane. It is given by:

$$\begin{aligned} \cos\alpha &= \frac{(n'_{0,x'}\hat{x}' + n'_{0,z'}\hat{z}') \cdot \hat{z}'}{\|n'_{0,x'}\hat{x}' + n'_{0,z'}\hat{z}'\| \|\hat{z}'\|} \\ &= \frac{n'_{0,z'}}{\sqrt{n'^2_{0,x'} + n'^2_{0,z'}}} \end{aligned}, \tag{F.3}$$

where $n'_{0,x'}$ and $n'_{0,z'}$ are the x' and z' components of the vector $\hat{n}'_0$.

The angle α can be obtained by $\mathrm{acos}(\cos\alpha)$, which gives a result $0° < \alpha < 180°$. However, as emissivity links to intensity and the projection of intensity is considered while determining emissivity (see Eq. (3.13)), $\sin^2\alpha$ and $\cos^2\alpha$ are involved and their signs are not important. As a result, we take the effective value $\alpha = \mathrm{acos}(|\cos\alpha|)$ so that α never exceeds $90°$.

F.2 Derivation of β

The angle β is the one between the local planes of incidence of the points M_0 and M_1, or equally the one between $\hat{u}_{v_1}$ and $\hat{u}_{v_0'}$, or the one between $\hat{u}_{h_1}$ and $\hat{u}_{h_0'}$.

With the knowledge of $\hat{s}'$ and the normals $\hat{n}_0$ and $\hat{n}_1$ of these two points, the vectors $\hat{u}_{h_1}$ and $\hat{u}_{h_0'}$ are given by:

$$\begin{array}{rcl} \hat{u}_{h_1} & = & \hat{s}' \times \hat{n}_1 \\ \hat{u}_{h_0'} & = & \hat{s}' \times \hat{n}_0 \end{array} . \tag{F.4}$$

The angle β is then given by:

$$\cos\beta = \hat{u}_{h_1} \cdot \hat{u}_{h_0'} \tag{F.5}$$

For the same reason as stated at the end of F.1, the angle β is given by its effective value $\beta = \mathrm{acos}(|\cos\beta|)$.

Bibliography

[1] X. Wu and W. L. Smith. Emissivity of rough sea surface for 8–13 μm: modeling and verification. *Applied Optics*, 36(12):2609–2619, 1997. 1, 5, 12, 13, 14, 21, 25, 43, 54, 55, 56, 83, 84, 93, 120, 125, 193

[2] M. Sancer. Shadow-corrected electromagnetic scattering from a randomly rough surface. *IEEE Transactions on Antennas and Propagation*, 17(5):577 – 585, sep 1969. 4, 42, 144, 145

[3] R. J. Wagner. Shadowing of randomly rough surfaces. *The Journal of the Acoustical Society of America*, 41(1):138–147, 1967. 10, 11, 15, 17, 41, 52, 53, 57, 63, 65, 66, 67, 68, 143, 144, 145

[4] C. Bourlier, J. Saillard, and G. Berginc. Intrinsic infrared randiation of the sea surface. *Progress In Electromagnetics Research*, 27:185 –335, 2000. 4, 5, 6, 7, 15, 28, 31, 42, 43, 44, 47, 49, 57, 141, 143, 144, 145, 169

[5] N. Pinel and C. Bourlier. Scattering from very rough layers under the geometric optics approximation: further investigation. *J. Opt. Soc. Am. A*, 25(6):1293–1306, Jun 2008. 4, 42

[6] K. Yoshimori, K. Itoh, and Y. Ichioka. Thermal radiative and reflective characteristics of a wind-roughened water surface. *J. Opt. Soc. Am. A*, 11(6):1886–1893, Jun 1994. 4, 5, 9, 10, 12, 15, 23, 31, 33, 43, 51, 52, 53, 57, 58, 104, 169, 177, 188, 189, 191, 195

[7] K. Yoshimori, K. Itoh, and Y. Ichioka. Optical characteristics of a wind-roughened water surface: a two-dimensional theory. *Appl. Opt.*, 34(27):6236–6247, Sep 1995. 5, 12, 23, 43, 53, 104

[8] V. Ross, D. Dion, and G. Potvin. Detailed analytical approach to the gaussian surface bidirectional reflectance distribution function specular component applied to the sea surface. *J. Opt. Soc. Am. A*, 22(11):2442–2453, Nov 2005. 5, 15, 31, 32, 43, 58, 169, 174

[9] N. R. Nalli, P. J. Minnett, and P. Delst. Emissivity and reflection model for calculating unpolarized isotropic water surface-leaving radiance in the infrared. i: Theoretical development and calculations. *Appl. Opt.*, 47(21):3701–3721, Jul 2008. 9, 31, 51, 56, 169

[10] K. Masuda, T. Takashima, and Y. Takayama. Emissivity of pure and sea waters for the model sea surface in the infrared window regions. *Remote Sensing of Environment*, 24(2):313 – 329, 1988. 5, 9, 10, 12, 14, 17, 23, 45, 51, 52, 53, 54, 56, 63, 72, 103, 104, 105, 136, 193

[11] K. Masuda. Infrared sea surface emissivity including multiple reflection effect for isotropic Gaussian slope distribution model. *Remote Sensing of Environment*, 103(4):488 – 496, 2006. 13, 14, 55, 56, 83, 84, 125

[12] P. J. Lynch and R. J. Wagner. Rough-surface scattering: Shadowing, multiple scatter, and energy conservation. *Journal of Mathematical Physics*, 11:3032–3042, 1970. 15, 16, 29, 31, 57, 58, 157, 158, 159, 161, 169

[13] B. G. Henderson, J. Theiler, and P. Villeneuve. The polarized emissivity of a wind-roughened sea surface: A Monte Carlo model. *Remote Sensing of Environment*, 88(4):453 – 467, 2003. 5, 13, 14, 21, 43, 45, 54, 57, 73, 83, 89, 93

[14] J.A. Ogilvy. *Theory of wave scattering from random rough surfaces*. A. Hilger, 1991. 5, 44

[15] C. Bourlier. Unpolarized emissivity with shadow and multiple reflections from random rough surfaces with the geometric optics approximation: A pplication to gaussian sea surfaces in the infrared band. *Applied Optics*, 45(24):6241–6254, 2006. 5, 13, 14, 25, 45, 52, 55, 56, 57, 88, 121

[16] T. Elfouhaily, B. Chapron, K. Katsaros, and D. Vandemark. A unified directional spectrum for long and short wind-driven waves. *J. Geophys. Res.*, 102(C7):15781–15796, 1997. 5, 6, 45, 47

[17] C. Cox and W. Munk. Measurement of the roughness of the sea surface from photographs of the sun's glitter. *J. Opt. Soc. Am.*, 44(11):838–850, 1954. 5, 6, 12, 45, 46, 53, 103, 106, 193, 197

[18] A. Fung and K. Lee. A semi-empirical sea-spectrum model for scattering coefficient estimation. *IEEE Journal of Oceanic Engineering*, 7(4):166 –176, october 1982. 6, 47

[19] John R. Apel. An improved model of the ocean surface wave vector spectrum and its effects on radar backscatter. *J. Geophys. Res.*, 99(C8):16269–16291, 1994. 6, 47

[20] C. Bourlier, J. Saillard, and G. Berginc. Effect of correlation between shadowing and shadowed points on the Wagner and Smith monostatic one-dimensional shadowing functions. *IEEE Transactions on Antennas and Propagation*, 48(3):437 –446, mar 2000. 6, 7, 8, 11, 47, 49, 53, 68, 69, 71, 74, 193, 199

[21] C. Bourlier and G. Berginc. Shadowing function with single reflection from anisotropic gaussian rough surface. application to gaussian, lorentzian and sea correlations. *Waves in Random and Complex Media*, 13(1):27–58, 2003. 7, 48

[22] H. Li, N. Pinel, and C. Bourlier. Polarized infrared emissivity of one-dimensional Gaussian sea surfaces with surface reflections. *Appl. Opt.*, 50(23):4611–4621, Aug 2011. 7, 14, 25, 27, 34, 48, 52, 56, 84, 120, 138

[23] C. Bourlier, G. Berginc, and J. Saillard. Theoretical study on two-dimensional gaussian rough sea surface emission and reflection in the infrared frequencies

with shadowing effect. *IEEE Transactions on Geoscience and Remote Sensing*, 39(2):379 –392, feb 2001. 9, 10, 15, 31, 51, 52, 58, 169, 170

[24] S. Fauqueux, K. Caillault, P. Simoneau, and L. Labarre. Multiresolution infrared optical properties for gaussian sea surfaces: theoretical validation in the one-dimensional case. *Appl. Opt.*, 48(28):5337–5347, 2009. 10, 12, 52, 53

[25] B. Smith. Geometrical shadowing of a random rough surface. *IEEE Transactions on Antennas and Propagation*, 15(5):668 – 671, sep 1967. 10, 11, 12, 15, 17, 41, 52, 53, 54, 58, 63, 65, 66, 68, 70, 105, 143, 145, 194

[26] C. Bourlier, G. Berginc, and J. Saillard. Monostatic and bistatic statistical shadowing functions from a one-dimensional stationary randomly rough surface according to the observation length: I. single scattering. *Waves in Random and Complex Media*, 12(2):145–173, 2002. 10, 11, 14, 17, 52, 53, 56, 63, 66, 69, 71, 73, 75, 97, 193, 199, 200

[27] R. Brockelman and T. Hagfors. Note on the effect of shadowing on the backscattering of waves from a random rough surface. *IEEE Transactions on Antennas and Propagation*, 14(5):621 – 626, sep 1966. 11, 13, 52, 53, 55

[28] H. Li, N. Pinel, and C. Bourlier. A monostatic illumination function with surface reflections from one-dimensional rough surfaces. *Waves in Random and Complex Media*, 21(1):105–134, 2011. 11, 53, 101

[29] P. Beckmann. Shadowing of random rough surfaces. *IEEE Transactions on Antennas and Propagation*, 13(3):384 – 388, may 1965. 11, 53

[30] L. Ricciardi and S. Sato. On the evaluation of first passage time densities for Gaussian processes. *Signal Processing*, 11(4):339 – 357, 1986. 11, 17, 53, 63

[31] L. Ricciardi and S. Sato. A note on first passage time problems for Gaussian processes and varying boundaries. *IEEE Transactions on Information Theory*, 29(3):454 – 457, may 1983. 11, 17, 53, 63

[32] C. Bourlier. Unpolarized infrared emissivity with shadow from anisotropic rough sea surfaces with non-Gaussian statistics. *Appl. Opt.*, 44(20):4335–4349, 2005. 12, 23, 46, 53, 103, 104, 105, 193, 194, 197

[33] K. Caillault, S. Fauqueux, C. Bourlier, P. Simoneau, and L. Labarre. Multiresolution optical characteristics of rough sea surface in the infrared. *Appl. Opt.*, 46(22):5471–5481, Aug 2007. 12, 15, 53, 58

[34] P. M. Saunders. Radiance of sea and sky in the infrared window 800-1200 cm-1. *J. Opt. Soc. Am.*, 58(5):645–652, May 1968. 12, 17, 53, 56, 63, 72

[35] D. E. Freund, R. I. Joseph, D. J. Donohue, and K. T. Constantikes. Numerical computations of rough sea surface emissivity using the interaction probability density. *J. Opt. Soc. Am. A*, 14(8):1836–1849, Aug 1997. 12, 23, 54, 104

[36] J. Shaw and C. Marston. Polarized infrared emissivity for a rough water surface. *Opt. Express*, 7(11):375–380, 2000. 12, 24, 54, 103, 106

[37] W. L. Smith, R. O. Knuteson, H. E. Revercomb, W. Feltz, N. R. Nalli, H. B. Howell, W. P. Menzel, O. Brown, J. Brown, P. Minnett, and W. McKeown. Observations of the infrared radiative properties of the ocean implications for the measurement of sea surface temperature via satellite remote sensing. *Bulletin of the American Meteorological Society*, 77(1):41–51, 1996. 12, 27, 54, 103, 136, 141, 193, 194

[38] R. Niclòs, E. Valor, V. Caselles, C. Coll, and J. M. Sanchez. In situ angular measurements of thermal infrared sea surface emissivity–validation of models. *Remote Sensing of Environment*, 94(1):83 – 93, 2005. 12, 27, 54, 137, 194

[39] P. D. Watts, M. R. Allen, and T. J. Nightingale. Wind speed effects on sea surface emission and reflection for the along track scanning radiometer. *Journal of Atmospheric and Oceanic Technology*, 13(1):126–141, 1996. 13, 14, 25, 42, 55, 56, 84, 103, 120

[40] B. Ginneken, M. Stavridi, and J. J. Koenderink. Diffuse and specular reflectance from rough surfaces. *Appl. Opt.*, 37(1):130–139, Jan 1998. 15, 58

[41] C. Bourlier, G. Berginc, and J. Saillard. Monostatic and bistatic statistical shadowing functions from a one-dimensional stationary randomly rough surface: II. multiple scattering. *Waves in Random Media*, 12(2):175–200, 2002. 16, 58, 88

[42] P. Schott, N. de Beaucoudrey, and C. Bourlier. Reflectivity of one-dimensional rough surfaces using the ray tracing technique with multiple reflections. In *Geoscience and Remote Sensing Symposium, 2003. IGARSS '03. Proceedings. 2003 IEEE International*, volume 7, pages 4214 – 4216 vol.7, july 2003. 16, 58

[43] J. A. Shaw. Degree of linear polarization in spectral radiances from water-viewing infrared radiometers. *Appl. Opt.*, 38(15):3157–3165, 1999. 24, 103, 106

[44] H. Li, N. Pinel, and C. Bourlier. Polarized infrared emissivity of 2d sea surfaces with one surface reflection. *Remote Sensing of Environment*, accepted. 27, 34, 138

[45] W. Su, T. P. Charlock, and K. Rutledge. Observations of reflectance distribution around sunglint from a coastal ocean platform. *Appl. Opt.*, 41(35):7369–7383, Dec 2002. 31, 32, 169, 174

[46] A. Papoulis. *Probability, Random Variables, and Stochastic Processes*. McGraw-Hill Book Company, 1965. 43

[47] K. Yoshimori, K. Itoh, and Y. Ichioka. Statistical formulation for an inhomogeneous random water surface: a basis for optical remote sensing of oceans. *J. Opt. Soc. Am. A*, 11(2):723–730, Feb 1994. 44

[48] Y. Dodge and D. Cox. *The Oxford Dictionary of Statistical Terms*. Oxford University Press, 2006. 46

[49] G. M. Hale and M. R. Querry. Optical constants of water in the 200-nm to 200-μm wavelength region. *Appl. Opt.*, 12(3):555–563, 1973. 106, 129, 138, 207

[50] K. E. Torrance and E. M. Sparrow. Theory for off-specular reflection from roughened surfaces. *J. Opt. Soc. Am.*, 57(9):1105–1112, Sep 1967. 141, 142

Contents

List of Tables

List of Figures

l'université nantes angers le mans
PÔLE DE RECHERCHE ET D'ENSEIGNEMENT SUPÉRIEUR

UNIVERSITÉ DE NANTES

Thèse de Doctorat

Hongkun LI

Émissivité et réflectivité infrarouges de la surface de mer avec ombre et réflexions multiples
Infrared emissivity and reflectivity of sea surfaces with shadowing effect and surface reflections

Résumé

L'émissivité et la réflectivité infrarouges d'une surface de mer sont des paramètres clés pour le calcul de la température apparente d'une surface de mer. Pour des angles d'observation rasants (proches de l'horizon), elles dépendent fortement de la rugosité de la surface de mer. Cette thèse a pour but de modéliser l'émissivité et la réflectivité d'une surface de mer dans le domaine infrarouge avec précision. De plus, la polarisation de l'onde est prise en compte dans la modélisation. En effet, les phénomènes d'ombrage et de réflexions multiples par la surface sont pris en compte dans les modèles via les fonctions d'illumination monostatique et bistatique sans et avec réflexions. Pour tester la validité de ces modèles, une méthode de référence, basée sur une méthode de tracé de rayons de Monte Carlo, est mise en œuvre. Des simulations montrent alors de bons accords entre les modèles avec ombrage et réflexions multiples développés et la méthode de tracé de rayons. De plus, l'accord avec des mesures de l'émissivité issues de la littérature est meilleur lorsqu'une réflexion sur la surface est prise en compte. Le critère de la conservation de l'énergie est également mieux vérifié en prenant en compte les réflexions multiples par la surface de mer. Ainsi, ces résultats montrent clairement l'intérêt de prendre en compte l'ombrage et les réflexions multiples dans la modélisation.

Mots clés

Optique géométrique, Surface de mer, Émissivité infrarouge, Réflectivité infrarouge, Ombrage, Réflexions multiples

Abstract

Sea surface infrared emissivity and reflectivity are important parameters in oceanic remote sensing, e.g. for deriving the sea surface temperature. They are both nearly constant for observation directions near zenith, but they vary largely for large grazing angles, because of the surface roughness. This thesis aims at calculating the sea surface infrared emissivity and reflectivity with accuracy. In addition, polarization is taken into account. Indeed, the phenomena of shadowing and multiple surface reflections are taken into account in the models through illumination functions without and with surface reflections. In order to validate developed models, a reference method, based on a Monte Carlo ray tracing algorithm, is used. Simulation results show very good agreements of the models with the ray tracing algorithm. Moreover, the agreement with emissivity measurements of the literature is improved if one surface reflection is considered. The criterion of energy conservation is better met by taking the sea surface reflections into account in the model. Thus, these results clearly show the usefulness of considering shadowing and surface reflections in the modeling.

Key Words

Geometrical optics, Sea surfaces, Infrared emissivity, Infrared reflectivity, Shadowing, Surface reflections